FACULTY OF SCIENCES

Sputter deposition on composites:
Interplay between film and substrate properties

Florian Guy Cougnon

Promotors: prof. dr. D. Depla and prof. dr. ir. W. Van Paepegem
Thesis submitted for the degree
Doctor of Science: Physics
January 2020

UNIVERSITEIT GENT

This page is intentionally left blank.

UNIVERSITEIT GENT

FACULTY OF SCIENCES

Sputter deposition on composites: Interplay between film and substrate properties

Florian Guy Cougnon

Promotors prof. D. Depla and W. Van Paepegem

Ghent University
Faculty of Sciences
Department of Solid State Sciences
Krijgslaan 281 (S1)
B-9000 Ghent, Belgium


+32 9 264 43 42


diederik.depla@ugent.be


draft.ugent.be

Examination Board:

Prof. Nicolas Martin (FEMTO-ST, voting member)
Prof. Stéphane Lucas (UNamur, voting member)
Prof. Mathias Kersemans (UGent, voting member)
Prof. Jolien Dendooven (UGent, voting member)
Prof. Diederik Depla (UGent, promotor)
Prof. Wim Van Paepegem (UGent, promotor)
Prof. Natalie Jachowicz (UGent, secretary)

Thesis submitted for the degree of Doctor of Science: Physics

This page is intentionally left blank.

Table of contents

This page was intentionally left blank.

Acknowledgments

In analogy to the process of diffusion and nucleation of adatoms on a substrate, people like to settle on preferential positions on the earth's surface. The better you are surrounded by strongly bounded factors, the higher the likelihood you remain on this location. In my case, I landed on the world surface in Brussels, Belgium, where I was strongly bound to a warm and comforting island, called home. It is here that I spent the major part of my current life and where we find the fundamental layer of my acknowledgments:
A mon père, Jean-Marie Cougnon

Des batailles franco-anglaise ou de la peinture classique et contemporaine à la littérature russe ou les projections de Mercator, le désir de savoir n'a pas de limite. Tu es un vrai exemple pour moi.

Aan mijn moeder, Marleen van den Berge

Je alledaagse inzet en onvoorwaardelijke steun en liefde zijn onevenaarbaar. Je bent de held van vele, en zeker ook de mijne.

Under bombardment of the opportunity to go to university, and given the high probability for island desorption for young adolescents, I diffused from Brussels to Ghent to settle in an environment of education and self-development. It is here, at Ghent University, after obtaining my Master degree in Engineering Physics, that I was given the opportunity to fulfill a doctoral research at the DRAFT research group in collaboration with the Mechanics of Composite Materials research group. Of course, many people, either in a direct or indirect way, have contributed to this.

The highest amount of gratitude is reserved for my promotor Diederik Depla. His continuous availability, dedicated enthusiasm, and scientific integrity are to my opinion very inspiring. Also the large amount of fundamental knowledge present within the DRAFT research group on this niche field of magnetron sputtering has been of great value to the accomplishment of this work. In this respect, I also want to acknowledge the collaborative effort of the entire - present and past - DRAFT team. From a personal point of view, some members deserve a special atten-

tion. Roeland Schelfhout, Francis Boydens, Bert Braeckman, and Koen Strijckmans for their willingness and patience to train me as a starter in sputter deposition, Robin Dedoncker and Dulmaa Altangerel for their assistance in the lab and being such a friendly colleagues, Roger De Gryse for the relaxing breaks with a perfect mix of coffee and magnetrons, Olivier Janssens for his contributions to all SEM and XRD related results, Jo Sys and Stefaan Broekaert for their professional assistance during the experimental setup, Nico De Roo for solving the most persistent problems of all (print a paper), and Wouter Leroy for the punctual administration.

Also the assistance provided in the composite lab at the research group Mechanics of Composite Materials was of great value for this work. In this respect, I would like to thank my co-promotors Wim Van Paepegem and Joris Degrieck for their input and ideas related to sensing in composite materials, Ives De Baere and Alfredo Lamberti for the production and testing of the composite materials, and Mathias Kersemans, Saeid Hedayatrasa, and Gaetan Poelman for their assistance and ideas related to the experiments on the infrared thermography of composites.

The last paragraph is dedicated to special people who, strangely enough, at some times rather obstructed than contributed to the advancements of this PhD thesis. However, they have proven to be the most valuable players (MVPs). As previously stated by Georges Brassens, Doctor of Life:

Des bateaux j'en ai pris beaucoup
Mais le seul qui'ait tenu le coup
Qui n'ai jamais viré de bord
Naviguait en père peinard
Sur la grand-mare des canards
Et s'appelait Les Copains d'abord
Les Copains d'abord

I hereby want to thank my friends for being awesome.

My left and right hand:

Dries Minoodt and Koen van den Berge

Every member of Bankteam Wemmel:

Benoit and Thibaut Struys, Jules Smits, Stef De Wit,
Gerre Debraekeleer, Sebastien Meunier, Mickael Moyeart,
Koen Corneille, Maxime Broeckaert, Laurent Delbar,
Pieter 'de Prins' Gerits, and Jonas 'de Kunick' Fratarri

These four strangers I met in Ghent:

Michael Bulthé, Mathias Boeck,
Matthias Bilteryst, and Rémi Krick

My brothers:

Thomas, Mathias, and Nicolas Cougnon

Because he is funny:

Balthazar Boma,
general director,PDG of the Boma flesh industry N.V.

For being nice:

Vogel and Ballie

For being simply the best:

Eva Demaré

Ghent, December 2019
Florian Guy Cougnon

This page was intentionally left blank.

Summary

A composite refers to a material in which two or more constituents can be distinguished. New materials with optimized properties can be created when the favorable properties of the different constituents are combined. Typically, we can distinguish between the reinforcement and the matrix. The reinforcement acts as the load carrying medium, whereas the matrix holds the reinforcement in position, protects the reinforcement from the environment and acts as a load transporting medium. Classical examples of composite materials are wood (bundles of cellulose fibers embedded in a matrix of lignin and hemicellulose), bones (hydroxyapatite crystals suspended in a fibrous collagen matrix), or concrete (stones in a matrix of cement). Over the years, fiber-reinforced polymers (FRPs), for example glass or carbon fibers suspended in a polymeric matrix, have taken a strong position as a material choice for advanced applications and all-day use. FRPs exhibit some unique properties such as very high specific stiffness and strength, good fatigue durability, and good resistance against corrosion. Compared to metals, composites are an interesting alternative material choice with regard to weight savings, for example, for fuel efficiency in transport and aerospace industry. Other examples are the use of composite materials for sports equipment such as lightweight racing bikes or tennis rackets, or for big engineering structures such as bridge decks or wind turbine blades.

However, during both the production cycle and the exposure to impact and fatigue while in service, FRPs are prone to defects and internal damage. Of course, with the cost of material failure within these big and critical structures being unacceptably high, the widespread use of FRPs has pushed the demand for monitoring the production cycle, the structural health, and the environmental conditions during operation. Failure of composite structures mostly originates in the bulk of the material. The anomalies, deteriorations or damage in the material can mostly not be observed at the surface. In light of structural health monitoring, it is therefore essential to gather data from the interior of the material. As such, in order to reduce maintenance costs and to allow inspection during operation, an approach of embedded sensor networks or functionalities in

the bulk of the composite is very attractive. A major constraint however is that the embedded sensor can only add value or functionality, but cannot compromise on the structural properties of the host material. Therefore, it is necessary for the sensors to have restricted out-of-plane dimensions in order not to deteriorate the material structure.

Due to their restricted thickness, thin films have the potential to address this constraint and are presented as an approach for embedded functionalities in composite materials. Furthermore, with the use of embedded thin films in composite materials, a range of new possible applications arises. However, many questions and challenges precede these opportunities. It is necessary to study these questions in great detail in order to develop a thorough understanding of the involved and underlying mechanisms and to evaluate the feasibility of embedded thin films in composites with respect to future applications. Two main research questions are addressed. At first, the hypothesis of a restricted impact of the embedded films on the structural integrity of the composite is evaluated. Secondly, the constraints on the deposition process, related to the presence of the composite substrate, are studied.

The impact of embedded thin films on the mechanical properties of a composite laminate is evaluated in Chapter 2. The mechanical properties of the composite are influenced by the vacuum exposure related to the deposition process, the film thickness, and the fractional coverage of the substrate, causing the composite to fail at lower loads. In general however, the impact of the embedded films remained limited, especially in the elastic regime. Therefore, embedded thin films are an attractive candidate for sensing applications in composites as they fulfill the requirement not to compromise on the structural integrity of the host material.

Among the different techniques available for thin film deposition, this work focuses on the growth of thin films by means of direct-current magnetron sputtering. Magnetron sputter deposition, as introduced in Chapter 3, is a vacuum coating technique which allows the growth of metallic and ceramic films. As magnetron sputtering is based on a magnetically enhanced glow discharge, the substrate is exposed to a flux of energetic particles. The specific characteristics of the deposition technique involve two main challenges for film deposition on polymeric substrates.

Firstly, polymeric substrates are temperature-sensitive. Hence, the heat load during deposition must be restricted in order not to deteriorate the polymer. A too high heat load towards the composite prepreg substrate during deposition can cause local curing or deteriorate the adhesion between prepreg sheets in a laminate. This introduces weak spots which are prone to delamination. As the impact of the deposition on the structural properties of the laminate must be limited as much as possible, it is important to study the heat flux during sputter deposition in order to

control the heat load towards the substrate. A characterization of the heat load during sputtering is given in Chapter 4. The restriction of a limited heat flux towards the substrate imposes constraints on the available deposition conditions for film growth on composites.
Secondly, when the substrate is introduced in the vacuum chamber for deposition, outgassing of the polymer introduces impurities in the vacuum. Impurities during film growth can severely affect the film growth. An introduction to thin film growth is given in Chapter 5. The influence of impurities on the film growth is thoroughly studied, by means of experiments and simulation, in Chapter 6. Here, it is demonstrated how the impact of impurities on the film growth can be evaluated from the ratio τ between the impurity impingement flux to the material flux arriving on the substrate, i.e. the relative amount of impurities impinging on the surface per arriving sputtered atom. It was shown that, in the low-impurity regime, i.e. when $\tau < 1$, the domain size was not significantly or consistently affected by the presence of impinging impurities. This was understood as the spatial distribution between chemisorbed impurity species is larger than the characteristic length of the metal adatoms. For larger impurity-to-metal ratios, i.e. $\tau > 1$, the spatial distribution between the chemisorbed species will be smaller than the characteristic length of the diffusing adatoms. In this case, the explored diffusion area of the adatom is restricted by the presence of different nucleation sites within this area, promoting nucleation and consequently grain-refinement. A power-law behavior $D \sim \tau^{\alpha}$ is observed, which describes the decrease in domain size with increasing impurity-to-metal ratio τ for seven studied materials ($Ni_{90}Cr_{10}$, $Cu_{55}Ni_{45}$, Cu, Ag, Al, Cr, CoCrCuFeNi). When the exponent α was averaged over the different materials, a value $\alpha = -0.50 \pm 0.07$ was found. This material-independent power-law behavior was also successfully simulated by means of a kinetic Monte Carlo code for a nucleation-dominated growth model. Also a coalescence-hindered growth model could explain this observed power-law behavior. However, for as-sputter deposited films, i.e. deposited without any additional heating contribution to the substrate, the conditions for impurity segregation are less favorable and its occurrence is debatable. This was illustrated by means of the observed texture changes and lattice expansions which are not in line with the idea of impurity segregation.

Finally, with regard to applications, a thorough study of the electrical (resistivity) and the thermoelectric properties (Seebeck coefficient) is given in Chapter 7 and 8, respectively. In both cases, it was shown that a proper evaluation of the impurity-to-metal ratio is essential in order to disentangle the influence of energy effects from impurity effects on the film properties. Within the studied experimental range, the changes in film properties under influence of varying deposition conditions could not be related to energetic effects, but rather to the effect of impurities. The

effect of different deposition conditions on the film properties can, in good approximation, be evaluated by projecting the conditions on the corresponding τ value. The (electrical) film properties are not significantly affected by the deposition conditions as long as the impurity-to-metal ratio is low. In the high-impurity regime, enhanced grain-boundary scattering due to the grain-refinement was shown to be a crucial mechanism in understanding the variations in electrical film properties. In Chapter 9, the different insights obtained during this work are acquired to present some new perspectives and evaluate the feasibility of some applications based on embedded thin films in composite laminates. As an example, a new approach for the development of a single-metal thin film thermocouple is proposed. The outgassing products of the composite were employed to tune the thermoelectric properties of the metallic film.

As such, it is clear that - in the specific case of a composite substrate on the one hand, and the metal film on the other hand - an interplay exists between film and substrate properties. The presence of the substrate influences the film properties, and the specific requirements for the film imposes, via the substrate, constraints on the deposition process. Given the insights provided in the interplay between substrate properties and metallic film growth in this work, a much better evaluation of the critical aspects regarding sensor development for composite materials can be made and consequently, refined solutions can be proposed.

Nederlandstalige samenvatting

Een composiet is een materiaal waarin twee of meer componenten kunnen worden onderscheiden. Nieuwe materialen met geoptimaliseerde eigenschappen kunnen worden gecreëerd wanneer de gunstige eigenschappen van de verschillende componenten worden gecombineerd. Typisch kunnen we onderscheid maken tussen de wapening en de matrix. De wapening fungeert als draagkrachtmedium, terwijl de matrix de wapening op zijn plaats houdt, beschermt tegen de omgeving en fungeert als dissiperend medium voor de draagkracht. Klassieke voorbeelden van composietmaterialen zijn hout (bundels cellulosevezels ingebed in een matrix van lignine en hemicellulose), beenderen (hydroxyapatietkristallen gesuspendeerd in een vezelige collageenmatrix) of beton (stenen in een matrix van cement). In de loop der jaren hebben vezelversterkte polymeren (VVPs), bijvoorbeeld glas- of koolstofvezels gedispergeerd in een polymeer matrix, een sterke positie ingenomen als materiaalkeuze voor zowel geavanceerde als alledaagse toepassingen. VVPs vertonen enkele unieke eigenschappen zoals een zeer hoge specifieke stijfheid en sterkte, een goede vermoeiingsduurzaamheid en een goede weerstand tegen corrosie. Vergeleken met metalen zijn composieten een interessante alternatieve materiaalkeuze met betrekking tot gewichtsbesparingen, bijvoorbeeld voor brandstofefficiëntie in de transport- en ruimtevaartindustrie. Andere voorbeelden zijn het gebruik van composietmaterialen voor sport toepassingen zoals lichtgewicht racefietsen of tennisrackets, of voor grote technische constructies zoals brugdekken of windmolenbladen.

VVPs zijn echter gevoelig voor defecten en inwendige schade, zowel tijdens het productieproces als onder invloed van blootstelling aan impact en vermoeidheid tijdens de dienst. Aangezien de kost van materiaalfalen binnen deze grote en kritische structuren onaanvaardbaar hoog is, heeft het wijdverspreide gebruik van VVPs de vraag naar de controle van de productiecyclus, de structurele integriteit en de omgevingsfactoren tijdens de dienst gestimuleerd. Het falen van composiet constructies vindt zijn oorsprong meestal in het inwendige van het materiaal. De defecten of beschadigingen in het materiaal kunnen meestal niet aan het oppervlak worden waargenomen. In het kader van structurele integriteitscontrole is

het daarom essentieel om data te verzamelen uit de bulk van het materiaal. Om de onderhoudskosten te drukken en om inspectie tijdens de dienst mogelijk te maken, is een benadering van sensornetwerken, geïntegreerd in de bulk van het composiet, zeer aantrekkelijk. Een belangrijke beperking is echter dat de ingebouwde sensor alleen een toegevoegde waarde kan hebben, maar geen afbreuk kan doen aan de structurele eigenschappen van het composiet. Daarom is het noodzakelijk dat de sensoren een beperkte dikte hebben om de materiaalstructuur niet aan te tasten.

Door hun beperkte dikte hebben dunne lagen het potentieel om te voldoen aan deze eis. Bovendien ontstaan er met het gebruik van ingebedde dunne films in composietmaterialen, een hele reeks aan nieuwe mogelijke toepassingen. Aan deze opportuniteiten gaan echter veel vragen en uitdagingen vooraf. Het is noodzakelijk om deze vragen in detail te bestuderen om een grondig inzicht te krijgen in de betrokken en onderliggende mechanismen, en om de haalbaarheid van ingebedde dunne lagen in composieten, met het oog op toekomstige toepassingen, te evalueren. Twee belangrijke onderzoeksvragen komen aan bod. In eerste instantie wordt de hypothese van een beperkte impact van de ingebedde lagen op de structurele integriteit van het composiet geëvalueerd. Ten tweede worden de beperkingen op het depositieproces, gerelateerd aan de aanwezigheid van het composiet substraat, bestudeerd.

De impact van ingebedde dunne films op de mechanische eigenschappen van een composietlaminaat wordt geëvalueerd in Hoofdstuk 2. De mechanische eigenschappen van het composiet worden beïnvloed door de vacuümblootstelling gerelateerd aan het depositieproces, de laagdikte en de fractionele bedekking van het substraat, waardoor het composiet bij lagere belastingen faalt. Echter, in het algemeen bleef de impact van de ingebedde lagen beperkt, vooral in het elastische regime. Daarom zijn ingebedde dunne lagen een aantrekkelijke kandidaat voor sensortoepassingen in composieten omdat ze voldoen aan de eis om de structurele integriteit van het dragermateriaal niet te schaden.

Een van de verschillende technieken die beschikbaar zijn voor dunne filmdepositie, is de groei van dunne lagen door middel van gelijkstroom magnetron sputteren. Magnetron sputter depositie, zoals geïntroduceerd in Hoofdstuk 3, is een vacuüm coating techniek die de groei van metalen en keramische lagen mogelijk maakt. Aangezien magnetron sputteren gebaseerd is op een magnetisch geassisteerde glimontlading, wordt het substraat blootgesteld aan een flux energetische deeltjes. De specifieke kenmerken van deze depositietechniek houden twee belangrijke uitdagingen in voor film depositie op polymeer substraten.

Ten eerste zijn polymeer substraten temperatuursgevoelig. Daarom moet de warmtebelasting tijdens de depositie beperkt worden om het polymeer niet te beschadigen. Een te hoge warmtebelasting naar het composiet

substraat tijdens de afzetting kan lokale uitharding veroorzaken of de hechting in een laminaat aantasten. Dit introduceert zwakke plekken die gevoelig zijn voor delaminatie. Omdat de impact van de depositie op de structurele eigenschappen van het laminaat zoveel mogelijk beperkt moet worden, is het belangrijk om de warmteflux tijdens het sputteren te bestuderen, zodoende de warmtebelasting naar het substraat te beheersen. Een karakterisering van de warmtebelasting tijdens het sputteren wordt gegeven in Hoofdstuk 4. De warmteflux naar het substraat legt echter beperkingen op aan de beschikbare depositiecondities voor dunne laaggroei op composieten. Ten tweede, wanneer het substraat wordt ingevoerd in de vacuümkamer voor depositie, zorgt het ontgassen van het polymeer voor de introductie van onzuiverheden in het vacuüm. Onzuiverheden tijdens de filmgroei kunnen ernstige impact hebben op de laaggroei. Een inleiding tot dunne laaggroei wordt gegeven in Hoofdstuk 5. De invloed van onzuiverheden op de dunne laaggroei wordt grondig bestudeerd, door middel van experimenten en simulatie, in Hoofdstuk 6. Hier wordt aangetoond hoe het effect van onzuiverheden op de dunne laaggroei kan worden geëvalueerd uit de verhouding τ tussen de inslaande onzuiverheidsflux tot de materiaalflux die toekomt op het substraat, i.e. de relatieve hoeveelheid onzuiverheden op het oppervlak per aankomende adatoom. Er werd aangetoond dat, in het lage onzuiverheidsregime, dat wil zeggen wanneer $\tau < 1$, de domein grootte niet significant of consequent werd beïnvloed door de aanwezigheid van onzuiverheden. Dit kunnen we begrijpen vanuit het perspectief dat de ruimtelijke verdeling tussen de gechemisorbeerde onzuiverhedenssoorten groter is dan de karakteristieke lengte van de adatomen. Voor grotere onzuiverheid-op-metaal verhoudingen, d.w.z. $\tau > 1$, zal de ruimtelijke verdeling tussen de gechemisorbeerde deeltjes kleiner zijn dan de karakteristieke lengte van de adatomen. In dit geval wordt het diffusie-oppervlak van het adatoom beperkt door de aanwezigheid van verschillende nucleatiecentra binnen dit gebied, wat de nucleatie en bijgevolg de korrelverfijning bevordert. Een machtsrelatie $D \sim \tau^{\alpha}$ wordt waargenomen, die de daling van de domeingrootte met toenemende onzuiverheid-metaal verhouding τ voor zeven verschillende materialen ($Ni_{90}Cr_{10}$, $Cu_{55}Ni_{45}$, Cu, Ag, Al, Cr, CoCrCuFeNi) beschrijft. Een gemiddelde waarde voor de exponent $\alpha = -0,50 \pm 0,07$ werd gevonden. Dit materiaal-onafhankelijk gedrag werd ook succesvol gesimuleerd door middel van een kinetische Monte Carlo code voor een door nucleatie gedomineerd groeimodel. Ook een "coalescence"-verhinderd groeimodel zou deze waargenomen machtsrelatie kunnen verklaren. Echter, voor films afgezet door sputter depositie, zijn de voorwaarden voor onzuiverheidssegregatie minder gunstig en het optreden ervan is onzeker. Dit werd geïllustreerd door middel van de waargenomen structuurveranderingen en roosteruitbreidingen die niet in overeenstemming zijn met het idee van onzuiverheidssegregatie.

Ten slotte, met betrekking tot toepassingen, wordt een grondige studie van de elektrische (weerstand) en de thermo-elektrische eigenschappen (Seebeck-coëfficiënt) gegeven in Hoofdstukken 7 en 8. In beide gevallen werd aangetoond dat een goede evaluatie van de onzuiverheid-metaal verhouding essentieel is om de invloed van energie-effecten van onzuiverheids-effecten op de laageigenschappen te ontrafelen. Binnen het bestudeerde experimentele bereik konden de veranderingen in laageigenschappen onder invloed van wisselende depositieomstandigheden niet worden gerelateerd aan energetische effecten, maar eerder aan het effect van onzuiverheden. Het effect van verschillende depositiecondities op de laageigenschappen kan, bij goede benadering, geëvalueerd worden door de depositie omstandigheden op de overeenkomstige τ waarde te projecteren. De (elektrische) filmeigenschappen worden niet significant beïnvloed door de depositieomstandigheden zolang de onzuiverheid-metaalverhouding laag is. In het hoog-zuiverheidsregime is de toenemende korrel-grens verstrooiing, als gevolg van de korrelverfijning, een cruciaal mechanisme in het begrijpen van de variaties in elektrische laageigenschappen. In Hoofdstuk 9 worden de verschillende inzichten die tijdens dit werk werden verkregen, aangewend om enkele nieuwe perspectieven te presenteren en de haalbaarheid van sommige toepassingen op basis van ingebedde dunne lagen in composietlaminaten te evalueren. Als voorbeeld wordt een nieuwe aanpak voorgesteld voor de ontwikkeling van een enkel-metaal thermokoppel. In dit geval werden de ontgassingsproducten van het composiet gebruikt om de thermo-elektrische eigenschappen van de metaalfilm aan te passen.

Het is dus duidelijk dat er - in het specifieke geval van een composiet substraat enerzijds en een dunne metaallaag anderzijds - een wisselwerking bestaat tussen de laag- en de substraateigenschappen. De aanwezigheid van het substraat heeft invloed op de filmeigenschappen, en de specifieke eisen die aan de laag worden gesteld, leggen - via het substraat - beperkingen op aan het depositieproces. Op basis van de verworven inzichten in de wisselwerking tussen de substraateigenschappen en de groei van de metaallaag, kan een veel betere evaluatie van de kritische aspecten met betrekking tot sensorontwikkeling voor composietmaterialen worden gemaakt, en kunnen bijgevolg spitsvondige oplossingen worden voorgesteld.

1 Outline

Over the years, fiber-reinforced polymers (FRPs) have taken a strong position as a material choice for advanced applications and all-day use. FRPs are composite materials and exhibit some unique properties such as very high specific stiffness and strength, good fatigue durability, and good resistance against corrosion. Compared to metals, composites are an interesting alternative material choice with regard to weight savings, for example, for fuel efficiency in transport and aerospace industry. The Boeing 787 Dreamliner or Airbus A350 are passenger airliners for which the primary structure is composed - in addition to the more common materials such as titanium, aluminum and steel - for 50% out of FRPs [5, 7]. Other examples are the use of composite materials for sports equipment such as lightweight racing bikes or tennis rackets, or for big engineering structures such as bridge decks [1] or wind turbine blades [4, 6, 15]. However, during both the production cycle and the exposure to impact and fatigue while in service, composite materials are prone to defects and internal damage. Of course, with the cost of material failure within these big and critical structures being unacceptably high, the widespread use of composite materials has pushed the demand for monitoring the production cycle, the structural health, and the environmental conditions during operation. Nowadays, sensors are used to monitor the curing cycle in the autoclave, or the environmental conditions during operation such as temperature, humidity, or mechanical strain. Some examples of embedded sensor approaches are optical fibers with Bragg gratings [8, 11, 17], polymer waveguides [9] to measure strain and temperature, or capacitive sensors [16] to monitor the dielectric properties of the polymer matrix during curing. A major constraint is that the embedded sensor can only add value or functionality, but cannot compromise on the structural properties of the host material. Therefore, it is necessary for the sensors to have restricted out-of-plane dimensions in order not to deteriorate the

material structure. Thin films have the potential to address this constraint. Furthermore, as illustrated by the following example, the use of embedded thin films in composite materials is accompanied by a range of possible applications.

The in-plane deformation of a specimen under influence of an external load can be measured by means of digital image correlation (DIC). DIC [10] provides stress and strain fields of a specimen by correlating digital images of a unique reference pattern on the surface of the test object before and after deformation. When a random gray intensity distribution is present, the natural surface texture can simply be used as a reference pattern, but quite often a speckle pattern is applied on the surface. Even the feasibility of thin film patterns was already evaluated in this context [13]. DIC only allows to derive the in-plane components but provides no information on the field components in the bulk of the material. Failure of composite structures mostly originates in the bulk of the material. However, anomalies, deteriorations or damage in the bulk can mostly not be observed at the surface. In light of structural health monitoring, it is therefore essential to gather data related to the interior of the material. Digital volumetric image correlation [2, 3] (DVC) is the three-dimensional extension of DIC. X-ray micro-computed tomography is used to generate digital volume images of a sample. The material microstructure itself or internal markers such as the cross-sectional arrangement of the fibers, or pores within the sample can be used to provide a unique reference subset [12]. However, the visualization of the internal structure with X-ray micro-CT suffers from poor contrast [14], and the less artifacts present in the composite, the more challenging it becomes to obtain a reference subset sufficient in size and contrast. Furthermore, it is generally hard to distinguish between the indications of porosities and those given by the formation of cracks [12]. This is understood since the images obtained in computed tomography basically represent variations in the volumetric density. In order to facilitate the allocation of a reference subset with an enhanced contrast within the CT-images, a thin film speckle pattern of a high-density material could be embedded in the material. With the thickness dimension of thin films in the range of nanometers up to a micron, thin films are an attractive candidate of being embedded with a restricted impact on the structural properties of the final composite. Figure 1.1 a) and b) show a 300 nm thin film pattern of tantalum deposited on dry glass fibers, and figures c) and d) show their respective reconstructed patterns from the CT-scans after the patterned fibers are integrated in a 1.2 cm thick composite plate. Clearly, this approach is promising as the patterns - even with sub-millimeter in-plane dimensions - appear with high contrast, are geometrically stable, and can be easily extracted from the reconstructed CT-images. The illustration of the DVC-application shows the general potential of embedded thin films for enhanced functionalities

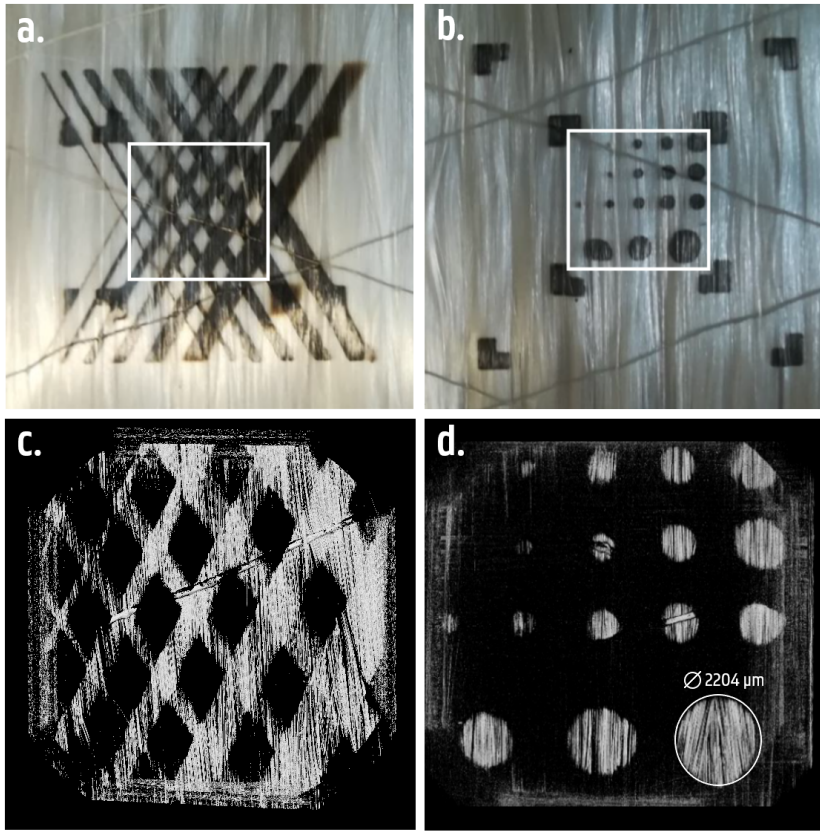

Figure 1.1. *a) and b) show a 300 nm thin film pattern of tantalum deposited on dry glass fibers. The adherence of the films on the fibers was good, and the patterns remained geometrically stable along the resin infusion and curing process. c) and d) show their respective reconstructed patterns from the CT-scans after the patterned fibers are integrated in a 1.2 cm thick composite plate. Figures adapted from [14].*

in composite materials. Besides speckle patterns for DVC, many other promising applications can be thought of, such as thin film heating elements for in-flight deicing of aerospace components or thin film antenna network for wireless power transfer, inductive heating and remote sensing. As such, in order to reduce maintenance costs and to allow inspection during operation, an approach of embedded sensor networks or functionalities in the bulk of the composite is very attractive. However, many questions and challenges precede these opportunities. It is necessary to study these questions in great detail in order to develop a thorough understanding of the involved processes and to evaluate the feasibility of this approach with respect to future applications. Thin films are presented as an approach for embedded functionalities in composite materials as they

are thought to have a restricted impact on the structural properties of the host material. In this light, the research is focused on an evaluation of the feasibility of this approach, based on a fundamental understanding of the involved and underlying mechanisms. Two main research questions are addressed. At first, the hypothesis of a restricted impact of the embedded films on the structural integrity of the composite is evaluated. Secondly, the constraints on the deposition process, related to the presence of the composite substrate, are studied. Advanced insights allow to uncover an interplay between the substrate properties and film properties which can be exploited for proposing refined solutions for sensor development for composite materials.

The impact of embedded thin films on the mechanical strength of a composite laminate is addressed in Chapter 2, together with an introduction to composite materials and their production methods and failure mechanisms. In this work, films are deposited by magnetron sputtering, a vacuum coating technique which allows the deposition of metallic and ceramic films. An introduction to thin films and magnetron sputtering as a deposition technique is given in Chapter 3. In the illustration above, the thin film patterns were deposited on dry glass fibers which were consequently impregnated with resin. Very often however, the starting product for composite production are fibers already pre-impregnated with resin. In this case, the approach for embedded thin films requires deposition on polymeric substrates. Two main challenges are encountered with the sputter deposition on polymeric substrates. Firstly, as thin films are grown on temperature-sensitive substrates, the heat load during deposition must be restricted in order not to deteriorate the polymer. A characterization of the heat load during sputtering is given in Chapter 4. Secondly, when the substrate is introduced in the vacuum chamber for deposition, outgassing of the polymer introduces impurities in the vacuum. Impurities during film growth can greatly affect the film growth and properties. An introduction to thin film growth is given in Chapter 5. The influence of impurities on the film growth is studied by means of experiments and simulation in Chapter 6. With regard to the use of thin films for application, a thorough study of the electrical properties (resistivity) and the thermoelectric properties (Seebeck coefficient) is given in Chapter 7 and 8 respectively. Finally, Chapter 9 summarizes different feasibility studies with regard to applications based on embedded thin films in composite laminates.

References

[1] CE Bakis, LC Bank, VL Brown, E Cosenza, JF Davalos, JJ Lesko, A Machida, SH Rizkalla, and TC Triantafillou, Fiber-Reinforced Polymer Composites for Construction—State-of-the-Art Review, Journal of Composites for Construction **6** (2002), no. 2, 73–87.

[2] BK Bay, Methods and applications of digital volume correlation, The Journal of Strain Analysis for Engineering Design **43** (2008), no. 8, 745–760.

[3] BK Bay, TS Smith, DP Fyhrie, and M Saad, Digital volume correlation: three-dimensional strain mapping using X-ray tomography, Experimental mechanics **39** (1999), no. 3, 217–226.

[4] P Brøndsted, H Lilholt, and A Lystrup, Composite materials for wind power turbine blades, Annu. Rev. Mater. Res. **35** (2005), 505–538.

[5] GH Gaynor, Boeing and the 787 Dreamliner, Decisions, John Wiley & Sons, Inc., jan 2015, pp. 187–218.

[6] DA Griffin and MD Zuteck, Scaling of composite wind turbine blades for rotors of 80 to 120 meter diameter, Journal of solar energy engineering **123** (2001), no. 4, 310–318.

[7] B Jens, C Hidalgo, and S Bricout, Environmental analysis of innovative sustainable composites with potential use in aviation sector—A life cycle assessment review, Science China Technological Sciences **60** (2017), no. 9, 1301–1317.

[8] G Luyckx, E Voet, N Lammens, and J Degrieck, Strain measurements of composite laminates with embedded fibre Bragg gratings: Criticism and opportunities for research, Sensors **11** (2011), no. 1, 384–408.

[9] J Missinne, BN Teigell, A Lamberti, G Chiesura, G Luyckx, MA Mattelin, W Van Paepegem, and G Van Steenberge, Thin and flexible polymer photonic sensor foils for monitoring composite structures, Advanced Engineering Materials **20** (2018), no. 6, 1701127.

[10] B Pan, K Qian, H Xie, and A Asundi, Two-dimensional digital image correlation for in-plane displacement and strain measurement: a review, Measurement science and technology **20** (2009), no. 6, 062001.

[11] MA Rumsey, An evaluation of sensing technologies in a wind turbine blade: some issues, challenges and lessons learned, Industrial and Commercial Applications of Smart Structures Technologies 2011, vol. 7979, International Society for Optics and Photonics, 2011.

[12] MGR Sause, In situ monitoring of fiber-reinforced composites: theory, basic concepts, methods, and applications, vol. 242, Springer, 2016.

[13] D Schroyen, Application of Digital Image Correlation on the micro-scale of composites, Master's thesis, TU Delft, 2018.

[14] L Sioen, Assessment of embedded metallic substances for the enhancement of micro-computed tomography images of fibre reinforced composites, Master's thesis, Ghent University, 2019.

[15] PS Veers, TD Ashwill, HJ Sutherland, DL Laird, DW Lobitz, DA Griffin, JF Mandell, WD Musial, K Jackson, and M Zuteck, Trends in the design, manufacture and evaluation of wind turbine blades, Wind Energy **6** (2003), no. 3, 245–259.

[16] Y Yang, G Chiesura, T Vervust, F Bossuyt, G Luyckx, J Degrieck, and J Vanfleteren, Design and fabrication of a flexible dielectric sensor system for in situ and real-time production monitoring of glass fibre reinforced composites, Sensors and Actuators A: Physical **243** (2016), 103–110.

[17] G Zhou and LM Sim, Damage detection and assessment in fibre-reinforced composite structures with embedded fibre optic sensors-review, Smart Materials and Structures **11** (2002), no. 6, 925.

This page was intentionally left blank.

2 Composite materials

Composite materials cover a broad range of materials. A composite refers to a material in which two or more constituents can be distinguished. New materials with optimized properties can be created when the favorable properties of the different constituents are combined. Typically, we can distinguish between the reinforcement and the matrix. The reinforcement acts as the load carrying medium, whereas the matrix holds the reinforcement in position, protects the reinforcement from the environment and acts as a load transporting medium. Classical examples of composite materials are wood (bundles of cellulose fibers embedded in a matrix of lignin and hemicellulose), bones (hydroxyapatite crystals suspended in a fibrous collagen matrix), or concrete (stones in a matrix of cement).

2.1. Polymeric fiber-reinforced materials

Nowadays, the term composite material is mostly used to refer to fiber-reinforced polymers (FRPs). Here, the fibers are the reinforcement and are embedded in a polymeric matrix. A cross-sectional SEM image of a glass-fiber/epoxy composite is presented in Figure 2.1a. The diameter of the glass fibers is around 15 μm, but generally varies in the range of 5 up to 25 μm. The most commonly used types of fibers are carbon, glass or aramid fibers, but also silicon carbide or inorganic oxide fibers (alumina/silica) can be encountered. Figure 2.1 shows a SEM micrograph of a carbon (b) and glass (c) fiber fractured in tension. Carbon fibers have a high tensile strength, high stiffness, low density, and a high chemical resistance compared to glass fibers, but are more brittle, and have a lower interfacial bonding strength with the resin matrix [14, 17].
In FRPs, the fibers are suspended in a polymeric matrix by impregnation of the fibers with a resin. We can distinguish between thermosetting and thermoplastic resins [9]. The most common thermosetting resins are

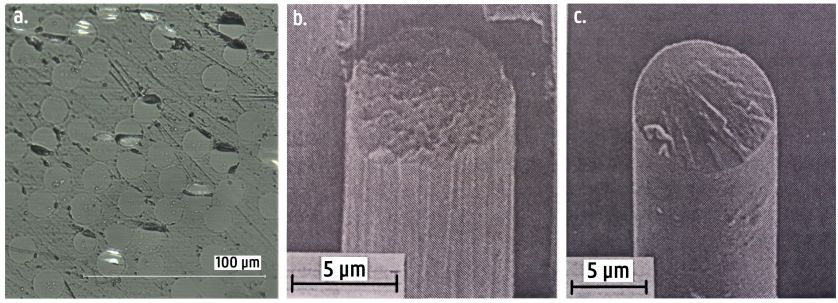

Figure 2.1. *(a) Cross-sectional SEM image of glass-fibers suspended in an epoxy matrix. The diameter of the glass fibers is around 15 µm. (b) SEM micrograph of carbon fiber and (c) glass fiber fractured in tension. Figures (b) and (c) adapted from Ref. [9].*

based on polyesters, vinyl esters and epoxy resins. They are the most commonly used resins in composites and must be "cured", i.e. the transition from a liquid into a solid state. This curing process is typically initiated by applying heat, but can also be induced under influence of light [12], radiation [7], or chemical additives [13] called hardeners. The process of polymer-hardening is referred to as polymerization or cross-linking, and is the consequence of the entanglement of long polymeric chains. The process of solidification of the polymer is however not reversible. When heated, the epoxy does not melt or reflow, but undergoes a phase change. As the mobility of the polymer chains increases significantly, a slight softening of the cured epoxy occurs. The glass transition temperature is a temperature range where a thermosetting polymer changes from a rigid or "glassy" state to a more flexible or "rubbery" state [11]. Thermoplastic resins on the other hand do not show any cross-linking between polymeric chains, and can therefore be re-melted after formation. Typical thermoplastics are polyethylene, polypropylene, polyamide, and polycarbonates. In this work however, only thermosetting epoxy resins are used.
Figure 2.2 shows a comparison of the elastic Young's modulus E, plotted against density ρ, between composite materials and some common engineering materials, i.e. wood, polymers, concrete, metals and ceramics. Ceramics typically have a very high elastic modulus but do also have high material densities. Wood on the other hand has a low density but has an elastic modulus restricted to 20 GPa. When comparing fiber-reinforced composites to metals, it is clear that they provide a much higher specific stiffness, i.e. the elastic modulus per mass density. As an example, carbon fiber composites offer a stiffness comparable to steel but with only a fourth of the material density. As composite materials are anisotropic materials, they exhibit anisotropic material properties. This is especially true in the case of unidirectional composites. They show very strong material properties in the direction of the fibers, but are weak in the

transverse direction of the fiber. Figure 2.2 compares the Young modulus of wood and carbon fiber composites in both fiber directions. The values for the elastic modulus along the fiber directions differ by more than an order of magnitude from the values perpendicular to the fiber direction. By stacking fibers in specific directions into a laminate, it is possible to create a laminate with specific, enhanced mechanical properties in a given direction.

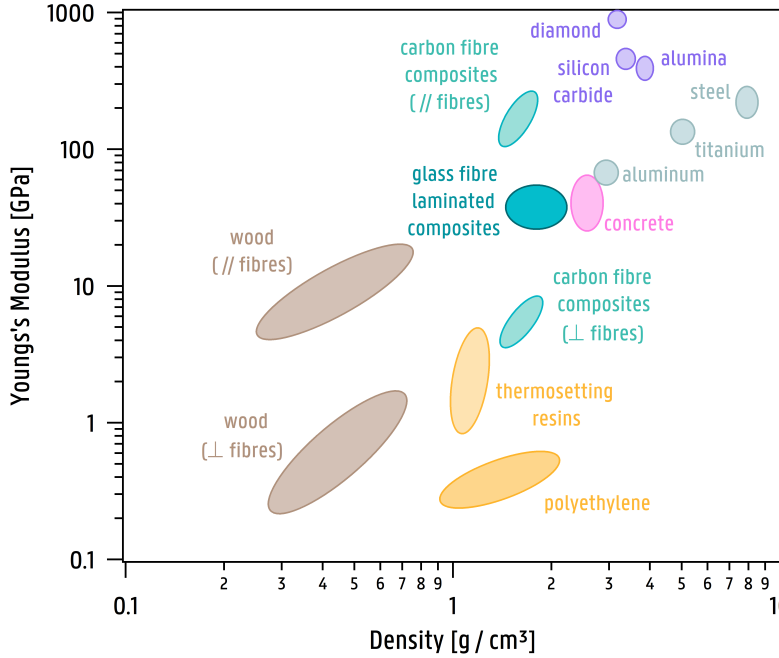

Figure 2.2. *Comparison of the Young's modulus E, plotted against density ρ, between composite materials and some common engineering materials. Figure adapted from Ref. [9].*

2.2. Manufacturing processes

Different fabrication procedures for the production of polymer composites are available. The main objective during production is to ensure that the fibers are uniformly distributed, properly aligned and well wetted by the resin. The main approaches with respect to the production of thermoset composites are liquid resin impregnation, or consolidation of a stacking of prepregs plies, i.e. sheets of fibers pre-impregnated with partially cured resin. During resin impregnation, the fibers can be impregnated by the resin in several ways. Either they can be manually impregnated (as is the case for small-scale repairs of for example car bodies), impregnated by pulling the fibers through a bath of resin, a process referred to as fil-

ament winding (well suited for the production of simple shapes such as tubes), or the resin can be sucked into a mould (mostly pressure-driven) in which the fibers are already placed in position, a process referred to as vacuum-assisted resin transfer moulding (VARTM). Relatively large moulds are applied for the production of parts in automobile or windmill industry. An example of a RTM process for the production of a windmill blade is shown in Figure 2.3. The composite is cured inside the mould and after solidification of the resin, the mould is removed. Resin transfer moulding allows to produce complex geometries with a low concentration of porosities or other defects.

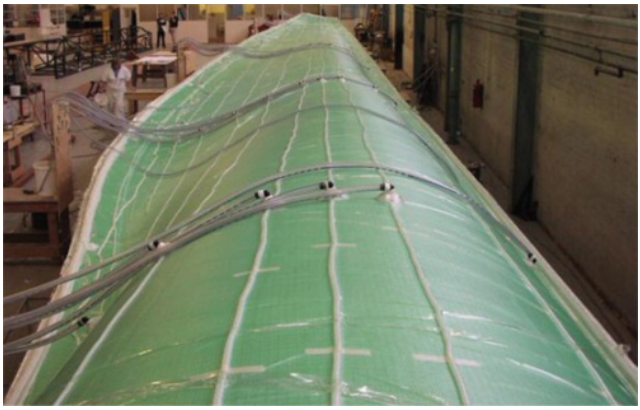

Figure 2.3. *Infusion pipework for the impregnation of fibers placed on the windmill blade mould. Picture taken from Ref. [1] (September 2019).*

Plies of prepreg can be stacked into a laminate in which the fiber direction of each lamina can be chosen. The laminate is then consolidated into a single piece by applying heat, often assisted by an over-pressure environment which compacts the composite laminate and disables the formation of voids and bubbles in the resin. For high-quality materials, curing is preferentially done in an autoclave, a closed chamber used to cure the resin at high temperatures and in a pressurized atmosphere.
The stacking of prepreg plies into a laminate is used for the production of composite laminates in this work. An overview of the different steps during production is shown in Figure 2.4. Figure 2.4a presents the different attributes needed during curing of the laminate: equally shaped sheets of (glass/epoxy) prepreg material (Castro Composites), a vacuum bag forseen of a sealant at the edges, a bottom plate and a top plate in order to guarantee a flat finish of the produced laminate, a release film to prevent sticking of the resin onto other surfaces in the vacuum bag, a distribution mesh to allow different paths for pumping, and a pumping outlet where the vacuum bag can be connected. At first, a lay-up of the

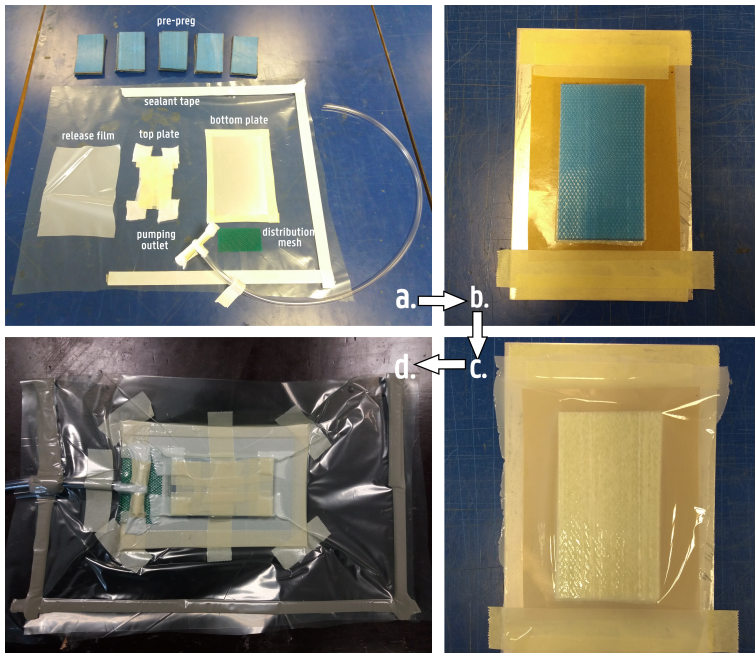

Figure 2.4. *a. The different attributes needed during curing of the laminate b. A lay-up of the prepreg plies on top of the bottom plate. c. The uncured laminate stacking after removing the blue protection layer and covered with a release film. d. The uncured laminate placed in a closed vacuum bag and ready for curing in the oven.*

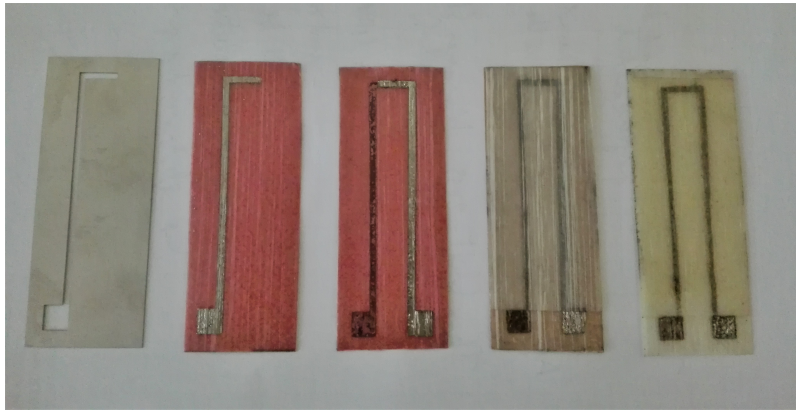

Figure 2.5. *Illustration of the different steps during the production of an embedded thermocouple. From left to right: a mask used for pattering, deposition of a first thermocouple leg, deposition of a second thermocouple leg, embedding the thermocouple by stacking prepreg plies, a cured composite sample with an embedded thin film thermocouple.*

prepreg plies is made on top of the bottom plate (see Figure 2.4b). In total, the laminate constisted of a stacking of 32 or 36 prepreg sheets. The blue finish on top of the prepreg plies is a protective release film against dirt and moisture. The bottom plate is forseen by a layer of Kapton®. As Kapton does not bind with the resin, this finish causes a good release of the composite from the bottom plate after curing. Figure 2.4c shows the laminate after removing the blue protection layer from the top ply. The whole laminate is now covered with a release film to prevent any excess resin to flow out of the laminate and to stick onto other surfaces during curing. Finally, a top plate is placed on top of the - with release film covered - laminate and the vacuum bag is properly closed. When the vacuum is applied, the atmospheric pressure applies a load onto the vacuum bag (Figure 2.4d). The top plate must prevent any deformation of the laminate surface under influence of this external force. When it is verified that there are no leaks and the vacuum bag keeps its pressure, the sample is ready for curing. Not all prepregs however require curing in the autoclave. During this study, we worked with MTC275 out-of-autoclave prepreg by Castro Composites (Spain). The out-of-autoclave indicates that the composite can be cured without autoclave, but simply by following a well-defined temperature cycle in the oven. The recommended temperature cycle for curing this specific prepreg is given by a dwell step at 85°C for 2±0.5 hours at a ramp rate of 1°C per minute, followed by 1 hour at 130°C with a ramp rate of 2°C per minute.
As an example, a visualization of the production - in its simplest form - of an embedded thin film thermocouple in the bulk of a composite laminate is shown step by step in Figure 2.5. From left to right we can see the mask used for pattering of the thin films, the deposition of a first thermocouple leg, the deposition of a second thermocouple leg, embedding the thermocouple by stacking prepreg plies, and finally a cured composite sample with an embedded thin film thermocouple. A sputter mask is used for patterning because processes as used in photo-lithography are not compatible with the composite substrate. Although the laminate only consists of a stacking of two plies of prepreg, this suffices as an illustrative example. The pink foil on top of the prepreg plies is a release film which is present to prevent sticking of the mask to the resin.

2.3. Mechanical strength

Damage development and failure mechanisms in composite materials are complex, but mostly originate at sites of enhanced stress. This can take the form of a local or distributed material defect (for example induced during production), a structural or geometrical feature (such as a notch), or damage (such as induced under impact) [8]. For a defect to be critical, it must be located such that the local stress conditions during service are severe enough to initiate damage growth and failure. Some of the

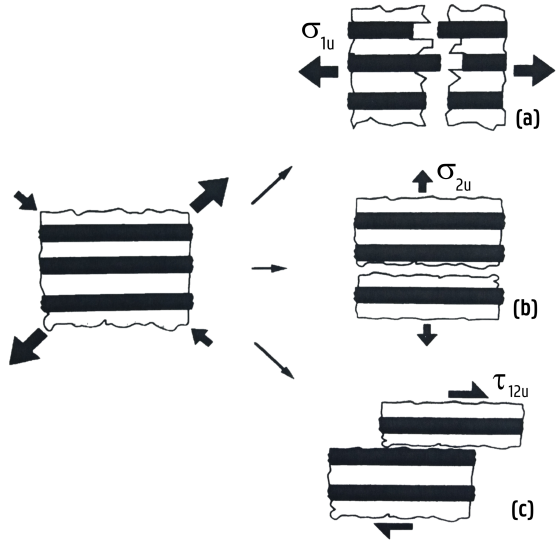

Figure 2.6. *Failure mechanisms in a laminate under a) axial tensile stress, b) transverse tensile stress, and c) shear stress. Figure reproduced from Ref. [10]*

.

more common defects include the presence of voids and porosities, matrix cracks, matrix-fiber debonding, or delaminations. The latter is mainly applicable to laminated composite structures where the adhesion between subsequent laminae in the laminate stacking fails, resulting in separation of the adjacent plies. Failure of unidirectional laminates under influence of mechanical stress can be ascribed to three basic failure mechanisms as shown in Figure 2.6 [10]. Under large axial tensile stresses σ_{1u} (Figure 2.6a), i.e. along the fiber direction, fracture of fibers and matrix leads to a fracture path perpendicular to the fiber direction. Due to the high degree of anisotropy in an unidirectional laminate, the fracture mechanism differs when transverse tensile stress σ_{2u} is applied perpendicular to the fiber direction (Figure 2.6b), or shear stress τ_{12u} is applied along the fiber direction (Figure 2.6c). The stresses are now located in the ply-to-ply interface and crack propagation occurs parallel to the fiber direction and thus in the laminate plane. Transverse tensile stresses tend to separate the laminae from each other, whereas shear stresses tend to slide one lamina over adjacent ones. Both transverse and shear stresses can cause interlaminar separation or delamination.

In light of this thesis, it is essential to evaluate the impact of interlaminar embedded thin films - produced according to the approach presented in Figures 2.4 and 2.5 - on the mechanical properties of a laminate. Different

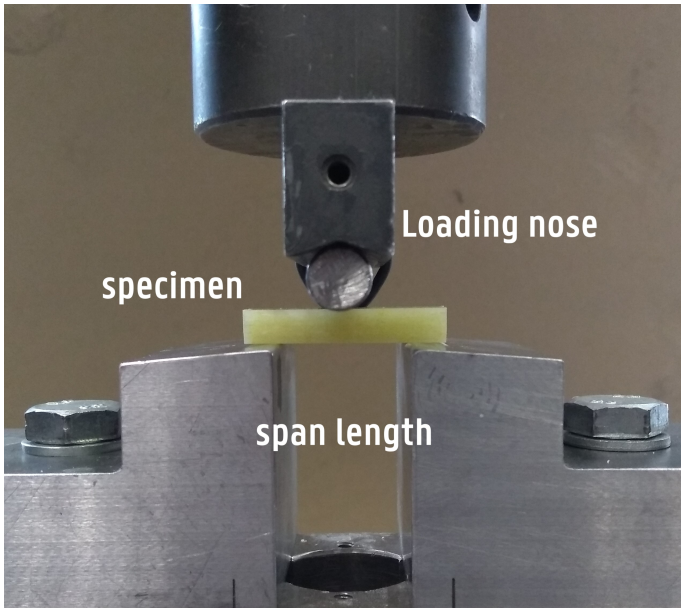

Figure 2.7. *Visualization of the short-beam-shear test-setup. The specimen with dimensions (w×l×h) of 12 mm×32 mm×6 mm, rests on two supports that allow lateral motion. The span length is 24 mm. The laminate specimen is oriented with the fiber direction in the span direction, and is center-loaded until fracture occurs. The load is applied by means of a loading nose directly centered on the midpoint of the test specimen.*

standardized test methods are available for measuring the fracture toughness of laminates under stimulation of different failure modes [4–6]. Here, a standard test method (ASTM D2344) [3] was used to compare the interlaminar shear strength of laminates with different coating coverage area of the midplane ply. As a short-beam strength test is a relatively simple test with regard to experimental setup and specimen production, this test is attractive as quality control for comparative testing [3]. During a short-beam test, a specimen rests on two supports that allow lateral motion, oriented with the fiber direction in the span direction, and is center-loaded, as shown in Figure 2.7, until fracture occurs, i.e. destructive testing. The load is applied by means of a loading nose directly centered on the midpoint of the test specimen. The small specimens' length-to-thickness ratios prescribed for the short beam shear test minimizes the bending stresses and maximizes the induced shear stress [2]. According to elementary beam theory, the bending stresses are maximum on the surface, varying linearly to zero in the midplane, while the shear stress varies parabolically over the specimen's thickness and is maximized at the midplane [15]. By embedding the thin films in the midplane, it is very likely that fracture originates in the interlaminar region between the

coated and the uncoated laminae. As such, the impact of embedded films on the mechanical properties of the composite laminate can be quantified by comparison of the variation in shear strength.

2.3.1. Experimental

Four unidirectional laminates are produced with different conditions for the mid-plane prepreg ply as presented in Figure 2.8. From left to right, we have a) a reference ply, b) a fully coated prepreg ply, c) a prepreg ply coated with lines of 2 mm width, and d) a prepreg ply without any deposition but with an exposure to vacuum for the same amount of time as the coated samples, i.e. 300 s pre-vacuum at $\sim$ 1 Pa and 210 s in a high vacuum at $\sim 1{\times}10^{-4}$ Pa. The applied coatings were 150 $\pm$ 30 nm thick sputter-deposited constantan ($Cu_{55}Ni_{45}$) films. All laminates were produced by a unidirectional lay-up of 32 plies of prepreg where the treated prepreg plies (a - d) occupy the mid-plane. From the different laminates, representative samples were cut as presented by the white rectangle in Figure 2.8. The methodology as prescribed by the standard [3] requires a span-to-thickness ratio of 4, and test specimens with a length of 6 $\times$ thickness and a width of 2 $\times$ thickness. With the thickness of the laminates $\sim$6 mm, the span length was 24 mm and the dimensions of the specimens in our case were 12 mm$\times$36 mm. The coated surface area fractions within the test samples are 0, 100, 17, and 0 % respectively.
An overview of all the results of the mechanical tests is presented in Figure 2.10. Each sample was tested multiple times to verify the reproducibility of the results. In the elastic regime, i.e. the regime where the applied load increases linearly with the beam displacement, the behavior between the different samples is very comparable. The onset for fracture

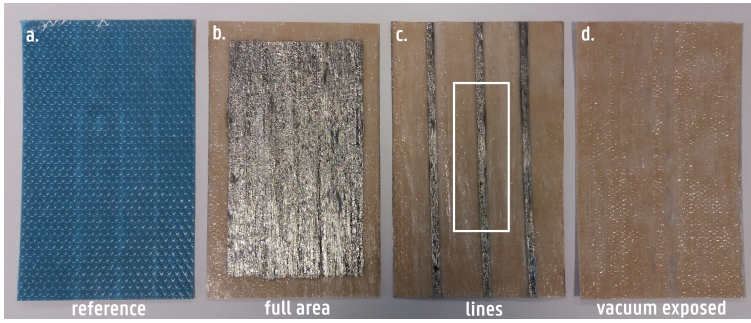

Figure 2.8. *Representation of the different treatments for the mid-plane prepreg ply of the laminates used for mechanical testing: a) reference sample (still covered by the blue release film to symbolize the prepreg itself is untreated) b) fully coated area, c) line pattern (line width 2 mm), and d) uncoated prepreg but exposed to vacuum for the same duration as the coated samples. The coatings are constantan films with a thickness of 150 $\pm$ 30 nm.*

however is different. The fracture load, interpreted as the first attained maximum load, is taken as a measure for the apparent shear strength of the material. The insert in Figure 2.10 compares the average short-beam-shear (SBS) strength values obtained for the reference, the vacuum exposed, the line patterned and full area coated samples and are respectively given by 42.6, 39.6, 37.9, and 34.2 MPa. It is clear that there is an influence for both the presence of a coating on the prepreg (b, c) as for the exposure of the prepreg to vacuum (d). The mechanical behavior and the SBS-values obtained for both the uncoated (vacuum exposed) sample and the sample with lines are however very comparable. This indicates that the exposure of the prepreg to the vacuum has a distinct influence on the SBS-value compared to the reference, but the influence of the limited surface coverage ($\sim$17 %) of the coating on the prepreg does not significantly affect the SBS-value. A possible explanation for the reduced short-beam strength after vacuum exposure is the reduced adhesion to other prepreg plies due to dehydration of the epoxy in the vacuum. When we increase the surface coverage from 17 % to 100 %, the mechanical behavior is remarkably different. A relaxation occurs at around 75 % of the SBS-value of the reference. This relaxation can be attributed to the onset of delamination under influence of interlaminar shear. Figure 2.9 shows an example of interlaminar shear at the mid-plane between the (fully) coated (sample b) and the uncoated prepreg plies. Basically, after relaxation, the sample can be seen as two separate samples with only half the thickness placed on top of one another. The cross-sectional moment of inertia I of the beam-like specimen determines the resistance to displacement under influence of stress or torque, and depends on the laminate thickness h as $I \sim h^3$. As a delamination grows through the midplane, the moment of

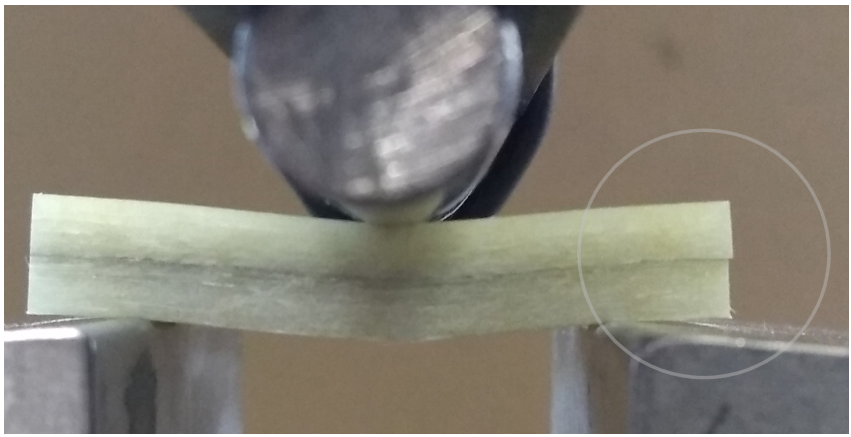

Figure 2.9. *(top) Delamination due to interlaminar shear at the mid-plane between the fully coated and the uncoated laminae.*

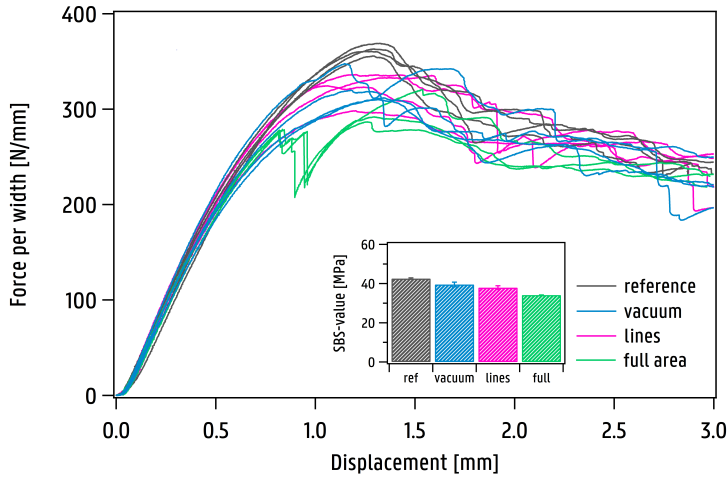

Figure 2.10. *Overview of the load-displacement curves of the short beam shear test for laminates with different conditions for the midplane prepreg ply (reference, fully coated by a 150 nm constantan ($Cu_{55}Ni_{45}$) film, partially (17 %) coated by lines of constantan of 2 mm width and 150 nm thick, and uncoated but vacuum exposed). Each sample was tested multiple times.*

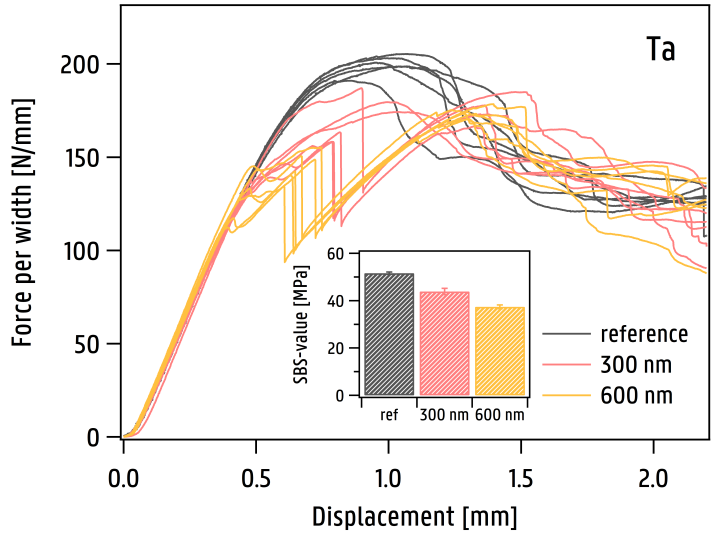

Figure 2.11. *Overview of the load-displacement curves of the short beam shear test for laminates produced by VARTM [16] with different conditions for the midplane fiber mat: untreated reference, fully coated by a 300 nm tantalum film, fully coated by a 600 nm tantalum film. Each sample was tested at least four times.*

inertia of the specimen is strongly affected and offers less resistance against deformation. This is marked by the sudden drop in the load-displacement curve.

A similar experiment was performed by L. Sioen for laminates produced by VARTM [16]. Three sets of laminates were tested, consisting of a layup of six unidirectional fiber mats impregnated in epoxy with different conditions for the fiber mat in the midplane: a reference set, a set with a 300 nm Ta film applied over the entire fiber-surface in the midplane, and a set with a 600 nm Ta film, also applied over the entire fiber-surface in the midplane. The results are presented in Figure 2.11 and the obtained SBS-values are respectively given by 51.6, 43.9, and 37.4 MPa. The failure behavior of the samples with the fully coated fibers is very similar to the behavior of sample (b) with the fully coated prepreg surface, indicating failure due to the formation of a delamination in the midplane. The samples however show a remarkable post-critical strength recovery as the sustained load increases above the fracture load. The decrease in SBS-value for the samples with increased layer thickness can probably be related to the decreased interdiffusion of the epoxy through porosities in the coating causing a restricted adhesion.

2.4. Conclusion

The scope of this chapter covers an introduction to fiber-reinforced composite materials and their production methods. Also the impact of embedded thin films, either deposited on dry fibers or on a prepreg surface, and the exposure of the prepreg to the vacuum on the mechanical properties of a glass/epoxy composite was evaluated. In the elastic regime, the mechanical behavior of the different samples is very comparable and neither the embedded films, nor the vacuum exposure seems to have a significant effect on the mechanical behavior. This is observed, irrespective if the deposition was performed on the dry fibers prior to resin impregnation or on the uncured prepreg surface. The behavior during failure is however different. The highest SBS-values are obtained for the untreated reference samples. A clear influence is however observed from the vacuum exposure and the surface coverage of the film. For low surface coverages, the deteriorated mechanical properties are rather attributed to the vacuum exposure than to the embedded film. For high surface coverages, there is a clear influence of the embedded film on both the interlaminar shear strength and the failure mechanism. The onset of a delamination caused by an increased interlaminar shear is observed and accompanied by a sudden relaxation in the displacement-force curve. This same failure behavior is also noticed for the samples which were coated on the fibers and is the result from a decreased moment of inertia of the samples. From these latter test samples, also the deteriorative effect of an increased layer thickness on the SBS-value could be evaluated. In general, the impact of

the embedded films remained limited, especially in the elastic regime. Therefore, embedded thin films are an attractive candidate for sensing applications in composites as they fulfill the requirement not to compromise on the structural integrity of the host material.

References

[1] http://www.renewableenergyfocus.com/view/1149/tooling-up-for-large-wind-turbine-blades/.

[2] DF Adams, The short beam shear test, High Perform Compos **14** (2006).

[3] ASTM D2344 / D2344M-16, Standard Test Method for Short-Beam Strength of Polymer Matrix Composite Materials and Their Laminates, 2016.

[4] ASTM D5528-01, Standard Test Method for Mode I Interlaminar Fracture Toughness of Unidirectional Fiber-Reinforced Polymer Matrix Composites, 2007.

[5] ASTM D6671 / D6671M-04, Standard Test Method for Mixed Mode I-Mode II Interlaminar Fracture Toughness of Unidirectional Fiber Reinforced Polymer Matrix Composites, 2004.

[6] ASTM D7905 / D7905M-14, Standard Test Method for Determination of the Mode II Interlaminar Fracture Toughness of Unidirectional Fiber-Reinforced Polymer Matrix Composites, 2014.

[7] A Endruweit, MS Johnson, and AC Long, Curing of composite components by ultraviolet radiation: A review, Polymer composites **27** (2006), no. 2, 119–128.

[8] E Greenhalgh, Failure analysis and fractography of polymer composites, Woodhead Publishing Limited, 2009.

[9] D. Hull and T. W. Clyne, General introduction, An Introduction to Composite Materials, Cambridge University Press, pp. 1–8.

[10] ———, Strength of composites, An Introduction to Composite Materials, Cambridge University Press, pp. 158–207.

[11] Epotek Epoxy Technology Inc.

[12] N Kramer, U Lohbauer, F García-Godoy, and R Frankenberger, Light curing of resin-based composites in the LED era, American Journal of Dentistry **21** (2008), no. 3, 135.

[13] NR Paluvai, S Mohanty, and SK Nayak, Synthesis and modifications of epoxy resins and their composites: a review, Polymer-Plastics Technology and Engineering **53** (2014), no. 16, 1723–1758.

[14] J Pusch and B Wohlmann, Carbon Fibers, Inorganic and Composite Fibers, Elsevier, 2018, pp. 31–51.

[15] F Rosselli and MH Santare, Comparison of the short beam shear (SBS) and interlaminar shear device (ISD) tests, Composites Part A: applied science and manufacturing **28** (1997), no. 6, 587–594.

[16] L Sioen, Assessment of embedded metallic substances for the enhancement of micro-computed tomography images of fibre reinforced composites, Master's thesis, Ghent University, 2019.

[17] RM Wang, SR Zheng, and YP Zheng, Elementary mechanical properties of composite materials, Polymer Matrix Composites and Technology, Elsevier, 2011, pp. 357–548.

This page was intentionally left blank.

3 Magnetron sputtering

Among the different deposition techniques available for the growth of thin films, this work focuses on the growth of thin films by means of magnetron sputtering. In this chapter, the fundamentals of magnetron sputtering are introduced, together with an experimental determination of the sputter yield of two nickel-based alloys, i.e. chromel and constantan. Details regarding the experimental setup of the sputter process and film analysis techniques can be found at the end of this chapter.

3.1. Thin film deposition

Already for thousands of years, thin films - or also called coatings - have been part of our daily lives. An instructive overview of more than 5000 years of documented history on thin film growth is given by J.E. Greene [20]. Accordingly, the first documented thin films were chemo-mechanically produced gold films for decorative use by the Egyptians more than 5000 years ago. The minted gold was purified by melting it in a chemical mixture and afterwards mechanically flattened by the use of stones, animal skin, parchment, and vellum. Gold films with thicknesses smaller than 300 nm ($\sim$ 1465 atomic layers) have been found in tombs in Egypt [21]. In Peru, artifacts ($\sim$100 BC) were found with gold coatings ($\sim$200 nm - 1 μm) produced by oxidation/reduction reactions and which show clear evidence of post-deposition heat treatment, i.e. annealing, to obtain an inter-diffusion zone between film and substrate to enhance adhesion. Typically, thin films are used to enhance or to functionalize the physical and chemical properties of a surface [21]. Examples in today's use are low-emissivity coatings on architectural glass [7, 33], hard coatings on cutting tools to increase the life time of the tool [29], tribological coatings for low friction in automotive parts [43], copper interconnects between transistors in integrated-circuits [11], transparant conductive ox-

ide (and absorber) layers for solar cells and displays [19, 28], catalytic layers for gas-sensing [6, 38], anti-reflection coatings on sunglasses [37], and many more. Different thin film deposition techniques exist. In first instance, we can distinguish between chemical and physical deposition processes. Chemical depositions either originate from the liquid phase, such as electrodeposition or sol-gel methods, or from the vapor phase, such as atomic layer deposition. Physical deposition techniques originating from the vapor phase are evaporation, laser ablation or sputtering. In this work, we focus on thin films grown by sputter deposition. Sputtering is a vacuum-assisted deposition technique in which atoms are ejected from a source, called the target, under influence of ion bombardment. Although the etymology of the word 'sputtering' is unclear, the term "spluttering", meaning "to spit with explosive sounds" or "to spit out a spray of particles in noisy bursts" (a cognate for the Dutch word "sputteren") [20], seems to be a legitimate approach as the term covers, with exception of the noise, a representation of the process on the atomic scale. Sputter deposition is a process which takes place in a vacuum chamber. Typically these chambers are made out of stainless steel and can have different sizes, from small ($\sim 10^{-2}$ m^3) laboratory set-ups, up to very large ($\sim 10^3$ m^3) industrial glass coaters. The chambers are pumped, mostly by a turbomolecular or a cryogenic pump, in combination with a rotation pump. The need for a high vacuum is mainly driven by the need of a decreasing impurity content in the films grown from the vapor phase, increased mean-free paths for the particles in the gas phase, and higher deposition rates. The ions needed for the ion bombardment of the target are provided by a gas discharge. For this, a sputter gas has to be introduced into the chamber. As sputter gas, mainly the inert gases are used since they do not react with the sputtered material. These are helium (He), neon (Ne), argon (Ar), krypton (Kr) and xenon (Xe). Argon is the most commonly used sputter gas as it is abundant and thus inexpensive, and the mass of argon (Z = 18) results in a acceptable momentum transfer with most of the deposited metals (see Chapter 4). A very small fraction of the argon gas atoms initially present in the chamber will already be ionized, for example, by gamma-ray radiation. By application of a DC voltage between the cathode, i.e. the target at negative potential, and the anode, i.e. the chamber walls at ground potential, a small fraction of free electrons in the gas will get accelerated by the electric field. As soon as enough energy can be gained from the electric field for the electrons to ionize another neutral argon atom during collision, an avalanching ionization effect occurs. When the number of ions produced by ionization processes is sufficient to self-reproduce the discharge, a transition towards a self-sustained electrical glow discharge of the working gas occurs [9]. A glow is observed due to emitted photons caused by atomic relaxation of excitation collisions. While electrons are attracted towards the anode, i.e. the chamber walls and the substrate if grounded, the inert gas ions are

accelerated towards the target, i.e. the cathode. When the ions impinge on the target surface, atoms are ejected under momentum transfer, or sputtered, from the target. When the material vapor makes contact with a surface, either a provided substrate or the chamber walls, the target material condenses and a film of sputtered target material starts to grow. The process briefly described here, presents the direct-current (DC) sputter process in its simplest form. However, DC sputtering has turned out to be unsuitable for many industrial applications since the deposition rates are low, the ionization efficiency in the plasma is low, the working pressures high and there is a high thermal load towards the substrate, making depositions on temperature-sensitive materials, like plastics, difficult [8]. However, these inconveniences may be overcome by the application of a properly defined magnetic field at the target.

3.2. Magnetron sputtering

A cathode accompanied by a properly shaped magnetic field is called a magnetron. A sketch of a typical setup for magnetron sputtering is presented in Figure 3.1a and b. Mostly, the magnetic fields, in the range of hundreds of Gauss, are generated by permanent magnets. When a magnetic field is present near the target surface, electrons will bend their trajectories into helices around the magnetic field lines, increasing the length of the electron paths and consequently enhancing the ionization efficiency by electron-neutral gas collisions. This in turn, leads to a denser plasma near the target surface and therefore an increase of ion bombardment on the target with an increase in deposition rate on the substrate as a result. The increased ionization probability allows to operate at much lower pressure levels and discharge voltages. For magnetron sputtering, the pressure and discharge voltage are typically in the range of 0.1 to 2 Pa (compared to 100 Pa for diode sputtering) and 300-700 V respectively [44]. A low pressure is usually desirable since the sputtered particles have a larger mean-free path in a low pressure gas discharge – in the range of 0.02 to 0.5 m at standard temperature for the pressure range mentioned above – and can therefore retain some of their kinetic energy as they traverse the process chamber towards the substrate.

When the plasma, i.e. the conductive medium between the anode and cathode, makes contact with the magnetron, most of the voltage drop between anode and cathode appears adjacent to the cathode in a region called the cathode sheath. The cathode sheath thickness is around one or two millimeters and is of great importance to sustain the discharge [10]. While the electron movement is constrained by the presence of the magnetic field lines, the trajectories of the ions are mostly insensitive to the magnetic field. Under influence of the electric field, the ions are directed towards the target where they are accelerated over the steep voltage gradient in the cathode sheath before impact on the target surface. As the

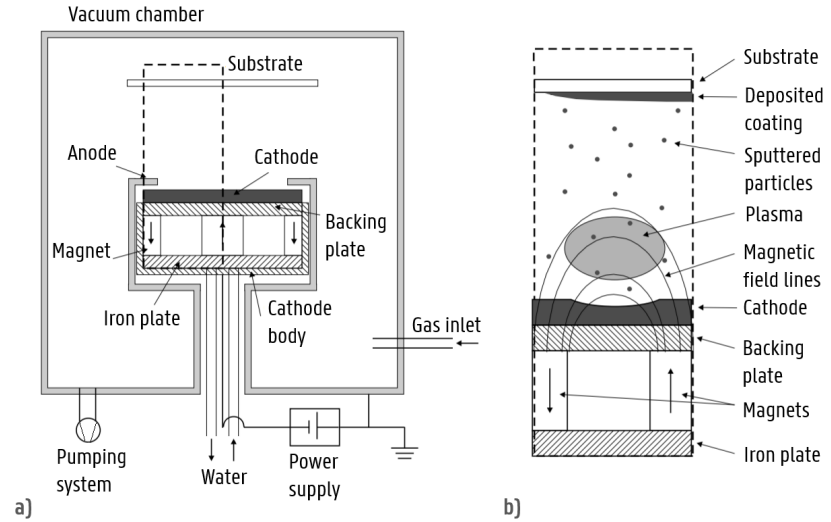

Figure 3.1. *a) A sketch of a typical setup for magnetron sputtering. The magnetron consists of a cathode body which contains the target, the magnets and the cooling system. It is surrounded by an anode housing. Also the substrate, vacuum chamber, electrical power supply, gas inlet and pumping system are presented. b) Sketch of a magnetron discharge (enlargement of enclosed region in a)). Figure adapted from G. Buyle in Ref. [10]*

ion energies are small before entering the cathode sheath, the dominant component of the momentum vector of the ion is normal to the target surface and therefore most of the ions will bombard the target surface under normal incidence. As the target gets heated by ion bombardment, it needs to be cooled to prevent undesired effects like melting or evaporation of the target material, or demagnetization of the magnets. Under ion impact, atoms and electrons are released from the target surface. The latter are referred to as secondary electrons. The mean number of ejected atoms per impinging ion is defined as the sputter yield Y, whereas the amount of ejected secondary electrons per impinging ion is defined as the ion-induced secondary electron yield γ_e, both material dependent parameters. Whereas the former is important with respect to the deposition rate, the latter is important for sustaining the discharge.

3.2.1. A self-sustaining glow discharge

Electron emission from solid surfaces when bombarded by energetic ions is a well-known phenomenon [22]. Under influence of the high electric field in the cathode sheath, the emitted electrons are accelerated away from the target, into the plasma. Here they can make an ionizing collision with neutral species present in the plasma. The average distance the electron can travel between two successive collisions is referred to as the

mean-free path of the electron. As the sputter gas pressure defines the average free space in the vacuum chamber, the rate of collision between the emitted electrons and the (neutral) sputter gas atoms scales with the sputter gas pressure. As an example, in a high vacuum ($10^{-3} - 10^{-7}$ Pa) a mean-free path between 10 cm and 1 km can be expected, and in the range of 0.1 - 100 mm in the case of a medium vacuum ($1 - 10^{-3} Pa$). It is in the latter pressure range that we typically find the sputter gas pressures during magnetron sputtering (between 0.3 and 1.2 Pa in this work). The role of the secondary electrons is essential for sustaining the magnetron discharge. An important ionization mechanism is the ionization of argon atoms by high energy electron impact. This inelastic process lowers the kinetic energy of the electron by an amount equal to the sum of the ionization energy of the argon atom and the kinetic energy of the ejected electron. Another inelastic process is argon excitation by electron impact. Here, an electron from an argon atom gains energy in the collision and gets excited towards a higher energy level. When the latter electron returns to lower energy states, photon emission occurs which is partly sensitive to the human eye. Excited argon atoms can also be ionized by electron impact, requiring less energy transfer. The discharge is defined as sustainable when a closed loop of events can be identified, i.e. begin with a selected starting event in the loop, and then require that exactly one new event, of the type started with, is reproduced after one passage through the loop [9]. Therefore, the conditions for a self-sustained discharge can be derived starting with the emission of a secondary electron from the target, starting with the bombardment of an ion on the target, or starting with an ionization event. As an example, if the bombardment of an ion on the target is considered as a starting point, the condition for a sustained discharge is fulfilled when the amount of secondary electrons γ_e generated by impact of one argon ion, suffices to generate a new argon ion. With γ_e electrons released per incident argon ion, the total electron energy after acceleration over the cathode sheath becomes $\gamma_e e V_d$, with V_d the discharge voltage or, approximately, the voltage drop over the cathode sheath. With the average electron energy loss per ionization noted as W, in the order of 30 eV for argon, enough energy is available to ionize γ_e eV_d / W argon atoms. However, electrons can be lost before generating the maximal number of ionizations, for example, if a magnetic field line crosses an anode surface, or ions could be lost when they are created too far from the target. Therefore, with ϵ_i the probability that the average secondary electron will make the maximum number of ionizing collisions and ϵ_e the probability that a created ion effectively reaches the cathode, the number of generated ions effectively reaching the target becomes $\epsilon_e \epsilon_i \gamma_e e V_d / W$. For magnetrons, one can state that $\epsilon_e \epsilon_i \approx 1$ [39]. At strong magnetic fields however, the electron paths are close to the target and therefore sheath ionization becomes important. Ionization in the sheath can be seen as a multiplicative process for the initial elec-

tron fraction γ_e. Therefore, sheath ionisation can be accounted for by multiplying the initial electron fraction γ_e with a multiplication factor m. Additionally, secondary electrons that made no collisions with the sputter gas can either be reflected back at the target, continuing their gyrating orbit in the reverse way, or either be recaptured at the target. When the secondary electron is recaptured by the target, the electron is lost from the system and can no more contribute in the ionization process. With f the effective ionization probability, $(1 - f)$ becomes the probability a secondary electron gets recaptured at the target. The effective secondary electron yield can be defined as $\gamma_{eff} = m\ f\ \gamma_e$. Therefore, the condition for sustaining a magnetron discharge can be formulated as:

$$\frac{\epsilon_e \epsilon_i \gamma_{eff} e V_d}{W} = 1 \tag{3.1}$$

By solving this equation for the discharge voltage V_d, we find a formula estimating the minimal discharge voltage for magnetron sputtering [10]:

$$V_d = \frac{W}{\epsilon_e \epsilon_i \gamma_{eff} e} \qquad [V] \tag{3.2}$$

The effective secondary electron yield $\gamma_{eff} \approx 0.1$ [15]. With the ionization energy for argon W $\approx 30\ eV$, the discharge voltage for magnetron sputtering in an argon environment is around $V_d \approx 300\ V$. Note that, at a too low pressure, the effective ionization probability f will be very small as most of the secondary electrons make no collisions and are recaptured by the target. Therefore, higher discharge voltages are needed when working at lower pressures, otherwise the discharge will extinct.

The sustaining mechanism described above is based on high-energy electrons in a magnetron discharge due to sheath energization of the emitted secondary electrons. Low energy electrons, originating from ionizations in the pre-sheath or from high-energy electrons reentering the cathode sheath after several ionizations, are not considered to participate in the sustaining mechanism of the discharge. Although the model of a self-sustaining discharge driven by the emission of secondary electrons was accepted for a long period of time, today, its generality is however the topic of debate. More recently, Huo et al. [23] observed for high-power impulse magnetron sputtering (HiPIMS) of Al an increased amount of self-sputtering, i.e. sputtering by bombardment of Al^+ on Al. The secondary electron emission yield for bombardment of single charged metal ions on a target of the same material is however close to zero [4, 9, 16]. It is thus clear that the model based on ionizations due to high-energetic secondary electrons is insufficient for describing the discharge. Therefore, an additional electron energization mechanism based on low-energy electrons was proposed [23]. Low-energy electrons are thought to be energized due

to Ohmic heating, i.e. the dissipation of local electric energy to the electrons [9]. Investigations of DCMS and HiPIMS discharges demonstrated that the plasma above the erosion groove or race-track is not uniform, but has regions of high plasma potential, i.e. potential humps, compared to its surrounding region [30]. These plasma structures are called spokes and were first reported in HiPIMS discharges [5, 18, 25, 31]. Spokes sweep over the racetrack and low-energy electrons gain energy as they drift from the low-potential side to the high-potential side of the spoke [30]. As such, low-energy electrons in a DCMS discharge can gain more than 50 eV [31] and exceed the energy threshold for ionization and/or excitation processes. Strictly speaking, the spokes are zones of enhanced light emission, caused by the inelastic collisions of the energy-enhanced electrons with atoms and ions in the plasma [31]. However, as the cross-sections for ionization and excitation as a function of the electron energy are very similar, the spokes are also zones of enhanced ionization. Ohmic heating is found to be a more important contribution to the ionization events than sheath energization for secondary electron emission yields lower than 0.1 [9].

3.2.2. Sputter yield

The number of sputtered atoms per incident ion can be calculated from the mass difference before and after sputtering for a given time, while the number of incident ions can be calculated based on the measured discharge current delivered by the power supply. A detailed description of this method can be found in Ref. [13]. During this work, five different target materials are mainly used: chromel ($Ni_{90}Cr_{10}$) and constantan ($Cu_{55}Ni_{45}$), two common Ni-alloys used for the production of thermocouples, silver (Ag) and copper (Cu), two good conductors, and tantalum (Ta), a high-density material. Values for the sputter yield of Ag, Cu, and Ta are already reported in Ref. [13] and - at a discharge voltage of 400 V - respectively given by 2.26, 1.74, and 0.48 atoms per incident argon ion. Values for the sputter yield of both chromel and constantan are however not yet available and therefore determined in this section.
As the ion energy, and thus the amount of ejected particles from the target, depends on the discharge voltage, the discharge voltage must be kept constant during the measurement. The target was sputtered for 4 hours at a constant voltage of 400 V, resulting in an incident argon ion energy of 400 eV. The target was weighted before and after these four hours of operation. The current was measured in detail by placing three 12 Ω (10 W) resistors in parallel over the voltage pin and the ground of the power supply (Huttinger 1500 DC) and consequently logging the voltage over the resistor by means of a data acquisition unit. This voltage signal is afterwards recalculated to the corresponding current value using Ohm's law. The acquired data from this experiment are presented in Figure 3.2. The number of incident ions can be obtained after integration of the mea-

sured current data over time. The total current is the sum of the incident ion current and the emitted secondary electron current. As γ_e electrons are generated per incident ion, the total current can be written as

$$I_{total} = I_{ion} + I_e = I_{ion}(1 + \gamma_e) \qquad [A] \tag{3.3}$$

After integration over the sputter time, the total amount of associated charges is given by

$$\begin{aligned} N_{total} &= \int I_{tot}\ dt \\ &= N_{ion}(1 + \gamma_e) \end{aligned} \tag{3.4}$$

with N_{total} the total amount of elementary charges, γ_e the secondary electron yield and N_{ion} the amount of incident Ar^+-ions. Consequently, the effective sputter yield can thus be given by

$$Y = \frac{(\Delta\ m/M)N_a}{\int I_{tot}(t)/(1 + \gamma_e)dt} \qquad [atoms/ion] \tag{3.5}$$

which represents the ratio of the number of atoms leaving the target and the number of ions bombarding the target, with $\Delta\ m$ the measured mass difference of the target, M the molar mass of the target material, N_a Avogrado's number, and I_{tot} as described in Eq. 3.3.

In what follows, we give an overview of the different steps encountered for the determination of the sputter yield of both chromel and constantan. In order to find a value for the amount of incident ions, we need to find a value for the secondary electron emission coefficient γ_e for both materials. As no data could be found in literature for the γ_e of both chromel and constantan, an estimation was made. Within an acceptable degree of error, one can approximate the γ_e of chromel ($Ni_{90}Cr_{10}$) by

$$\gamma_{e,chromel} \approx 0.9 \times \gamma_{e,Ni} + 0.1 \times \gamma_{e,Cr} \tag{3.6}$$

Strictly speaking, the simple approximation for the secondary electron yield of an alloy given above can only be considered valid in the case that the constituent materials are distinguishable within the target [17]. In case of alloy mixtures, it was found that this relation is no longer evident as the work function, i.e. the energy needed to release an electron completely from a metal surface, of a mixture of metals is not necessarily given by the linear combination of the work functions of the constituents. However, in many cases, the approximation based on the compositional weight of the respective constituents to determine the secondary electron yield in absence of reported values is a common approach [32]. In general, reliable data on the ion induced secondary electron emission yield are scarce. The γ_e of chromium, reported by Depla et al. [15], is found to be

Table 3.1. *Intermediate results for the calculation of the sputter yield of both chromel and constantan.*

Material	Δ m [g]	M [g mol^{-1}]	N_{tot} [# charges]	γ_e [e$^-$/ion]	N_{ion} [# ions]	Y [atoms/ion]
$Ni_{90}Cr_{10}$	3.078	58.02	3.10×10^{22}	0.1	2.82×10^{22}	1.13
$Cu_{55}Ni_{45}$	3.295	61.36	2.48×10^{22}	0.09	2.27×10^{22}	1.42

$\gamma_{e,Cr} = 0.091$. No value for $\gamma_{e,Ni}$ was found. However, the bulk modulus of a metal, as a measure for the material's resistance to uniform compression, can be used as an indicator for the secondary electron emission yield [14]. The metal bulk moduli for nickel and chromium are reported by Makino et al. [26] and respectively given by 186.3 GPa and 190.3 GPa. The values of the bulk moduli of both materials are comparable, a result understood based on their similar $3d$-bond character. Therefore, it is acceptable to approach the γ_e for both materials as being equal, i.e. $\gamma_{e,Ni} \approx \gamma_{e,Cr}$, and thus, $\gamma_{e,chromel} \approx 0.1$. All the parameters and intermediate results used to calculate the sputter yield are presented in Table 3.1. The calculation was also repeated for constantan, but only the intermediate results are reported in Table 3.1. The secondary electron emission yield was approximated in analogy to the case of chromel, with a value for $\gamma_{e,Cu} = 0.084$ [15]. For chromel and constantan, we find a sputter yield of 1.13 and 1.42 atoms per incoming ion respectively. We can compare this value with other predictions. Comparison based on a weighted average of the metallic sputter yields with TRYDIN-values [1, 27], Seah-values [35, 36] and SRIM-values [3, 45] results in 0.95, 1.06, and 1.56 for chromel and 1.12, 1.31 and 1.88 respectively in the case of constantan.

During the experiment, the discharge voltage was fixed at 400 V and the discharge current varied in time in the range of 0.2 - 0.5 A as can be seen in Figure 3.2. The reason why the discharge current increases can be understood from the self-sustaining discharge model of Buyle (see section 2.1). As the target is sputtered, the target is eroded in time. During erosion, the target surface moves in the direction of the magnets and thus the magnetic field strength at the surface increases. By trapping the plasma within the static magnetic field lines, most of the ionization and consequently target bombardment happens in this region. As the surface of the target erodes in the direction of the magnets, the magnetic field strength above the surface, and thus within the cathode sheath, increases. This causes a more efficient ionization efficiency of the electrons. The deposition current and discharge voltage are related by the impedance of the plasma through an IV-curve. Typically, an IV-curve for a magnetron discharge is given by $I = k(V - V_d)^n$ [41], with n a measure for the electron confinement in the vicinity of the erosion groove [12]. Values for the exponent n during magnetron sputtering are in the range of 2 - 5 (poorly designed magnetron) up to 12 (extremely high electron

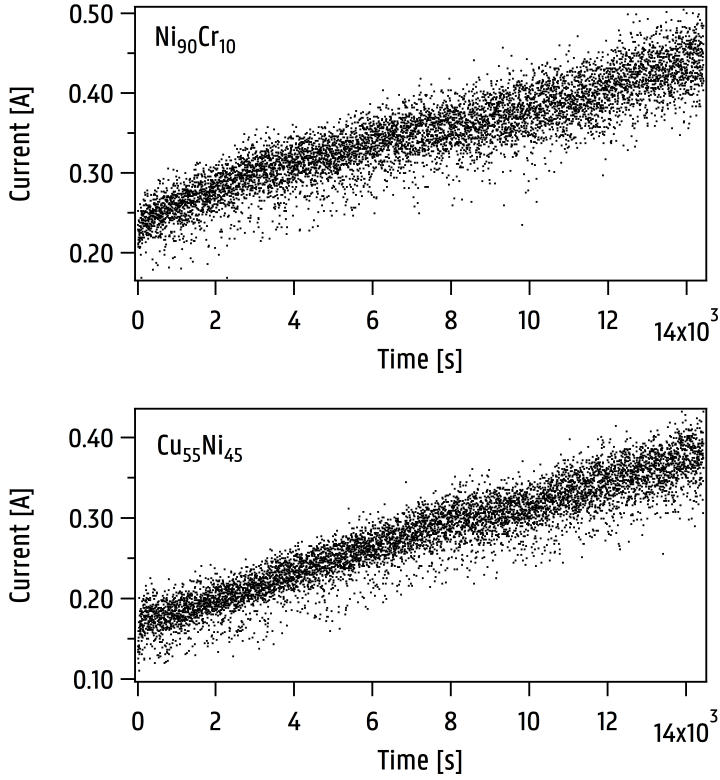

Figure 3.2. *Acquired current-time data for the determination of the sputter yield. The argon pressure was set to 0.6 Pa and the background pressure lower than* $5 \times 10^{-4} Pa$.

confinement) [12]. It is understood that, with increasing erosion of the race track and thus with enhanced electron ionization efficiency, the IV-characteristic becomes more steep. Therefore, when eroding the target at a fixed discharge voltage, the corresponding value for the discharge current on the IV-curve will increase. A picture of a typical erosion groove in a planar target is shown in Figure 3.3. In cross-section, the erosion groove can be described by a Gaussian distribution. The circular shape of the erosion groove is a consequence of the circular magnets used for the magnetic configuration in the magnetron. The static, non-uniform plasma density above the surface causes a non-uniform erosion of the target and consequently a limited material utilization of only ±30%. Other magnetron designs such as rotatable magnetrons have a rotating target surface in a static magnetic field configuration, causing a more uniform erosion profile and target utilization up to 90% [12]. The circular black ring which is observed on the target is formed by redeposited particles. As these particles are reflected towards the (water-cooled) target by col-

lisions with the gas phase, they typically have low energy and the formed layer is thus porous in nature (see Chapter 5). Although the redeposition is uniform on the target surface, the observed ring is due to the circular erosion groove (inner ring) and a circular clamping of the target to the magnetron (outer ring).

From the calculations above, we learn that on average 1.96×10^{18} ions bombarded the target per second, or with the sputter yield of chromel $Y_{chromel} = 1.13$, this results in 2.21×10^{18} sputtered particles leaving the target every second! In the simple assumption that the sputtered particles are emitted as an omnidirectional isotropic point source, i.e. the particles are evenly distributed over half a sphere (sputtered particles have momentum vector out of the target), and no sputter gas is present, a first approximation of the flux arriving at a distance r from the target can be given by

$$F_m = \frac{2.21 \times 10^{18}}{2\pi r^2} \qquad [\frac{atoms}{cm^2 s}] \tag{3.7}$$

This yields a particle flux of around 1.4×10^{16} (particles cm^2 s^{-1}) arriving at a substrate placed at a distance of 5 cm and 1.6×10^{15} at a distance of 15 cm from the sputter source (see Figure 4.3 Chapter 4). Note that the obtained values are only a crude estimation of the arriving material flux and do not account for the angular distribution of the sputtered particles, nor for the presence of a sputter gas. In order to develop a better and more realistic understanding of the propagation of the sputtered particles through the gas phase, simulation tools can be used. SiMTra [42] is a kinetic Monte Carlo code which allows to simulate the transport of particles leaving the target surface through the gas phase. The software gives viable results and is subject to an increasing interest for use in magnetron sputtering simulation models. In the next chapter, SiMTra simulations are presented in comparison to experimentally measured material fluxes. The code can be freely downloaded at the website of the DRAFT research group [2].

3.3. Process variables and Equipment

3.3.1. Magnetron

During this work, five different target materials are mainly used: chromel ($Ni_{90}Cr_{10}$), and constantan ($Cu_{55}Ni_{45}$), two common Ni-alloys used for the production of thermocouples, silver (Ag) and copper (Cu), two good conductors, and tantalum (Ta), a high-density material. All targets were planar and circular with a two-inch diameter which were clamped on an unbalanced magnetron.

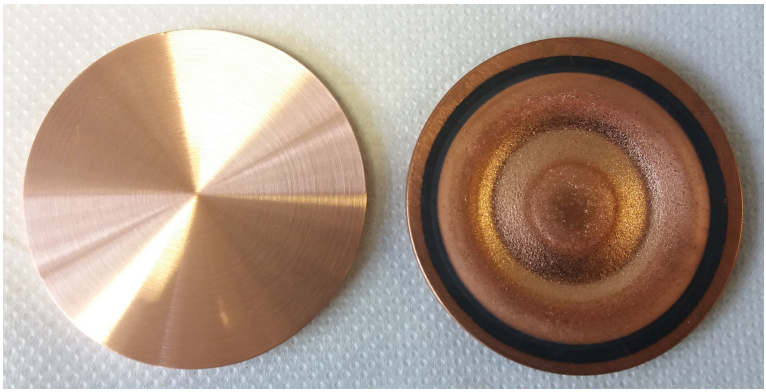

Figure 3.3. *(left) New unused 2-inch planar copper target. (right) Erosion groove in a planar target. The circular shape of the erosion groove is a consequence of the circular magnets used for the magnetic configuration in the magnetron. The circular black ring as well as the small centered circle are formed by redeposited particles.*

3.3.2. Substrate

Depositions are performed on three different types of substrates. Depositions for film analysis are typically performed on a silicon substrate. Prior to deposition, the silicon wafer is RCA cleaned, i.e. a procedure for the removal of organic and ionic contaminants. As silicon reacts with oxygen, a native silicon oxide layer will always be present on the top surface. For the electrical characterization, i.e. film resistivity and thermoelectric properties, deposition is mostly performed on glass. Finally, for application purposes, depositions are also performed on (glass/epoxy) prepreg.

3.3.3. Vacuum chamber

The depositions in this work are performed in two different vacuum chambers. One chamber, referred to as chamber A, is a stainless steel cuboid with a volume of 0.259 m^3, the other chamber, referred to as chamber B, is a stainless steel cylindrical shaped chamber with a volume of 0.052 m^3. Some experiments were only done in chamber A or B, others were done in both in order to exclude a possible influence of the deposition set-up.

3.3.4. Sputter gas pressure

As sputter gas, Argon (5.0) from Praxair was used. The sputter gas pressure in the vacuum chamber is measured by means of a capacitance gauge (CMR 274, Pfeiffer Vacuum). All depositions in this work are performed at an argon pressure in the range of 0.3 Pa to 1.2 Pa.

3.3.5. Background pressure

The background pressure or the residual gas pressure inside the deposition chamber is measured by means of a Compact FullRange Gauge (PKR 251). The PKR251 is a combination of a Pirani gauge and a Compact cold cathode gauge (IKR) combined into a single measurement device. The PKR is designed for vacuum measurements in the range of 10^5 Pa down to 10^{-2} Pa, whereas the IKR is designed to operate in a pressure range of 1 Pa down to $5\times\ 10^{-9}$ Pa.

3.3.6. Current and voltage

The power to the magnetron is delivered by a Hüttinger 1500 DC power supply. All depositions in this work are performed in a current-controlled way with a current between 0.1 A and 1 A. The discharge voltage is a variable mainly depending on the material, the sputter gas pressure, and the erosion of the target (see subsection 2.1).

3.3.7. Target-to-substrate distance

The target-to-substrate distance indicates the perpendicular distance between the target surface and the substrate surface. This distance can be changed without breaking the vacuum by means of a linear transfer which moves the magnetron up and down. All depositions in this work are performed at target-to-substrate distances between 5 cm and 15 cm.

3.4. Process and thin film analysis

3.4.1. Thermal Probe

The energy flux towards the substrate during the DC magnetron sputtering process was measured using a calorimetric probe [40]. This probe consists of a K-type thermocouple welded on the back of a sensing element with a diameter of 10 mm. The heat capacity of the sensor was 0.048 J/K. The output of the calorimetric probe is connected to the computer through a data-acquisition unit (National Instruments) and a software package determines the energy flux towards the substrate by fitting the heating and cooling temperature curves with the Levenberg-Marquardt algorithm. The probe was installed in front of the cathode surface and energy fluxes were measured for different deposition conditions. Figure 3.4 shows an example of a thermal probe measurement with the typical heating/cooling curve during the magnetron discharge. At first, there is no plasma and the probe just measures the background temperature. When the plasma is on, we see an exponential increase of the temperature as function on time. When the discharge is turned off, an exponential cooling curve is observed. The standard deviation on the measurements is 1 mW/cm^2.

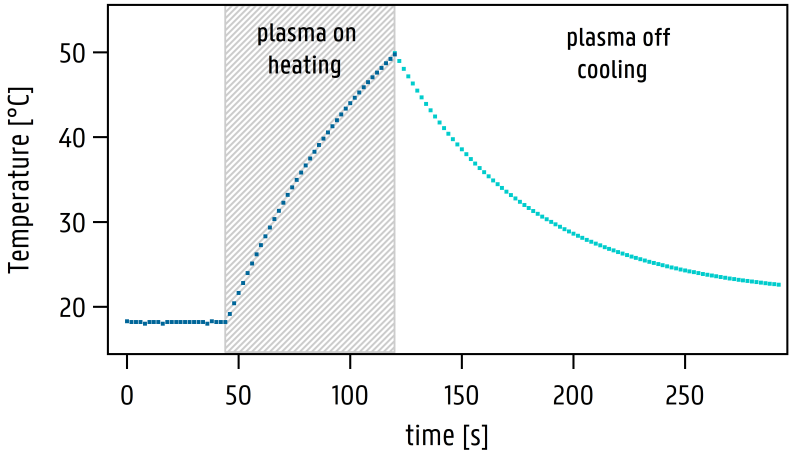

Figure 3.4. *Example of a temperature profile measured by the thermal probe during deposition. The thermal power is retrieved by fitting the heating and cooling curves.*

3.4.2. Contact Profilometry

The film thickness was measured by means of contact profilometry (Talystep Taylor-Hobson). The profilometry is performed on a partially coated (RCA cleaned) silicon substrate. The step between the coated and the uncoated substrate is measured by the profilometer tip and determines the thickness of the layer. The thickness was always measured at four different steps on the sample and afterwards the different measurements are averaged. The standard deviation on the thickness measurements is around 30 nm.

3.4.3. X-ray analysis

X-ray diffraction is used to study the crystallographic orientation and crystallite size in thin films. The X-ray beam is a Cu K-α 154 pm line. Crystallites or crystallographic units in a material diffract the incoming bundle in phase. This allows to determine the out-of-plane texture. X-ray diffraction (XRD) was performed with a Bruker D8, equipped with a line detector (LynxEye). Most measurements are performed in a classical Bragg-Brentano configuration, however, to exclude any influence of the configuration, some measurements were repeated with a parallel beam configuration (Göbel mirror). The peak width, or FWHM, is inversely proportional to the crystallite size [34]. Based on the determined integral breadth, the domain size is calculated with the Debye-Scherrer equation. Peak broadening is inherent to the instrumentation, but also finds contributions from crystallite size, microstrain (due to dislocations, lattice distortions, ...) or temperature effects. The instrumental broadening was

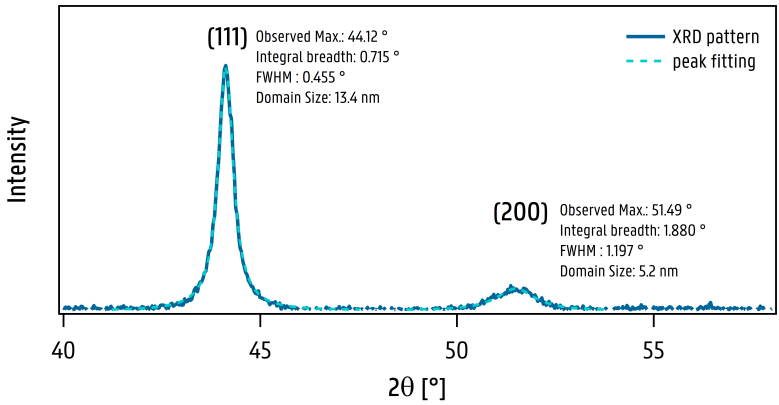

Figure 3.5. *An XRD pattern obtained for a chromel thin film. A preferential 111 out-of-plane orientation is observed. The domain size is determined from the XRD pattern by fitting the peak broadening to a Pearson VII peak shape. Based on the determined integral breadth and FWHM, the domain size is calculated with the Debye-Scherrer equation.*

determined by measuring the XRD pattern for Cu and Al powder. The domain size is determined from the XRD pattern by fitting the broadening of a particular peak associated with a particular planar reflection to a Pearson VII peak shape as described by Ida [24]. Based on the determined integral breadth, the domain size was calculated according to the Debye-Scherrer equation. X-ray reflectivity (XRR) can be used to gather information about layer thickness, surface roughness and film density. During XRR, the reflection of X-rays on a sample is measured around the critical angle for total internal reflection. When the electron density on the interface changes, the reflected X-ray intensity will also change. From the deviation between the predicted and the measured reflected intensity, the layer thickness or film density can be determined. The error on the obtained density is $\pm$ 2%.

3.5. Conclusion

In this chapter, the fundamentals of magnetron sputtering were introduced. The mechanisms and conditions for sustaining a magnetron discharge are discussed in great detail. Also the sputter yield for chromel and constantan are experimentally determined based on the monitored mass difference of a fresh target after sputtering for a given time frame in voltage-controlled mode. The procedure yields a sputter yield for chromel and constantan of 1.13 and 1.42 atoms per incident ion respectively.

References

[1] Download from https://www.hzdr.de/db/Cms?pOid=21578&pNid=0&pLang=en.

[2] Download SiMTra from www.draft.ugent.be.

[3] Downloaded from http://www.srim.org.

[4] A Anders, Self-sputtering runaway in high power impulse magnetron sputtering: The role of secondary electrons and multiply charged metal ions, Applied Physics Letters **92** (2008), no. 20, 201501.

[5] A Anders, P Ni, and A Rauch, Drifting localization of ionization runaway: Unraveling the nature of anomalous transport in high power impulse magnetron sputtering, Journal of Applied Physics **111** (2012), no. 5, 053304.

[6] K Arshak, E Moore, GM Lyons, J Harris, and S Clifford, A review of gas sensors employed in electronic nose applications, Sensor review **24** (2004), no. 2, 181–198.

[7] G Bräuer, Large area glass coating, Surface and Coatings Technology **112** (1999), no. 1-3, 358–365.

[8] G Bräuer, B Szyszka, M Vergöhl, and R Bandorf, Magnetron sputtering–Milestones of 30 years, Vacuum **84** (2010), no. 12, 1354–1359.

[9] N Brenning, JT Gudmundsson, D Lundin, T Minea, MA Raadu, and U Helmersson, The role of Ohmic heating in dc magnetron sputtering, Plasma Sources Science and Technology **25** (2016), no. 6, 065024.

[10] G Buyle, D Depla, K Eufinger, J Haemers, W De Bosscher, and R De Gryse, Simplified model for the DC planar magnetron discharge, Vacuum **74** (2004), no. 3-4, 353–358.

[11] A Chaudhry, Interconnects for nanoscale MOSFET technology: a review, Journal of Semiconductors **34** (2013), no. 6, 066001.

[12] W De Bosscher and H Lievens, Advances in magnetron sputter sources, Thin Solid Films **351** (1999), no. 1-2, 15–20.

[13] D Depla, On the effective sputter yield during magnetron sputter deposition, Nuclear Instruments and Methods in Physics Research Section B: Beam Interactions with Materials and Atoms **328** (2014), 65–69.

[14] ———, Magnetrons, reactive gases and sputtering, 2017.

[15] D Depla, G Buyle, J Haemers, and R De Gryse, Discharge voltage measurements during magnetron sputtering, Surface and Coatings Technology **200** (2006), no. 14-15, 4329–4338.

[16] D Depla, S Mahieu, and R De Gryse, Magnetron sputter deposition: Linking discharge voltage with target properties, Thin Solid Films **517** (2009), no. 9, 2825–2839.

[17] D Depla, H Tomaszewski, G Buyle, and R De Gryse, Influence of the target composition on the discharge voltage during magnetron sputtering, Surface and Coatings Technology **201** (2006), no. 3-4, 848–854.

[18] AP Ehiasarian, A Hecimovic, T De Los Arcos, R New, V Schulz-Von Der Gathen, M Böke, and J Winter, High power impulse magnetron sputtering discharges: Instabilities and plasma self-organization, Applied Physics Letters **100** (2012), no. 11, 114101.

[19] K Ellmer, A Klein, and B Rech, Transparent conductive zinc oxide: basics and applications in thin film solar cells, vol. 104, Springer Science & Business Media, 2007.

[20] JE Greene, Tracing the 5000-year recorded history of inorganic thin films from 3000 BC to the early 1900s AD, Applied Physics Reviews **1** (2014), no. 4, 041302.

[21] ———, Tracing the recorded history of thin-film sputter deposition: From the 1800s to 2017, Journal of Vacuum Science & Technology A: Vacuum, Surfaces, and Films **35** (2017), no. 5, 05C204.

[22] D Hasselkamp, Kinetic electron emission from solid surfaces under ion bombardment, Particle Induced Electron Emission II, Springer Berlin Heidelberg, 1992, pp. 1–95.

[23] C Huo, D Lundin, MA Raadu, A Anders, JT Gudmundsson, and N Brenning, On sheath energization and Ohmic heating in sputtering magnetrons, Plasma Sources Science and Technology **22** (2013), no. 4, 045005.

[24] T Ida, New measures of sharpness for symmetric powder diffraction peak profiles, Journal of Applied Crystallography **41** (2008), no. 2, 393–401.

[25] AV Kozyrev, NS Sochugov, KV Oskomov, AN Zakharov, and AN Odivanova, Optical studies of plasma inhomogeneities in a high-current pulsed magnetron

discharge, Plasma Physics Reports **37** (2011), no. 7, 621–627.
[26] Y Makino and S Miyake, Estimation of bulk moduli of compounds by empirical relations between bulk modulus and interatomic distance, Journal of alloys and compounds **313** (2000), no. 1-2, 235–241.
[27] W Möller and W Eckstein, Ion mixing and recoil implantation simulations by means of TRIDYN, Nuclear Instruments and Methods in Physics Research Section B: Beam Interactions with Materials and Atoms **7** (1985), 645–649.
[28] J Müller, B Rech, J Springer, and M Vanecek, TCO and light trapping in silicon thin film solar cells, Solar energy **77** (2004), no. 6, 917–930.
[29] S PalDey and SC Deevi, Single layer and multilayer wear resistant coatings of (Ti, Al) N: a review, Materials Science and Engineering: A **342** (2003), no. 1-2, 58–79.
[30] M Panjan, Self-organizing plasma behavior in RF magnetron sputtering discharges, Journal of Applied Physics **125** (2019), no. 20, 203303.
[31] M Panjan and A Anders, Plasma potential of a moving ionization zone in DC magnetron sputtering, Journal of Applied Physics **121** (2017), no. 6, 063302.
[32] L Pekker, Plasma chemistry model of DC magnetron reactive sputtering in ArO2 gas mixtures, Thin Solid Films **312** (1998), no. 1-2, 341–347.
[33] C Schaefer, G Bräuer, and J Szczyrbowski, Low emissivity coatings on architectural glass, Surface and Coatings Technology **93** (1997), no. 1, 37–45.
[34] P Scherrer, Bestimmung der inneren Struktur und der Größe von Kolloidteilchen mittels Röntgenstrahlen, Kolloidchemie Ein Lehrbuch, Springer Berlin Heidelberg, 1912, pp. 387–409.
[35] MP Seah, Pure element sputtering yields using 500–1000 eV argon ions, Thin Solid Films **81** (1981), no. 3, 279–287.
[36] MP Seah and TS Nunney, Sputtering yields of compounds using argon ions, Journal of Physics D: Applied Physics **43** (2010), no. 25, 253001.
[37] JH Sternbergh, Multilayer anti-reflective and ultraviolet blocking coating for sunglasses, December 2 1997, US Patent 5,694,240.
[38] YF Sun, SB Liu, FL Meng, JY Liu, Z Jin, LT Kong, and JH Liu, Metal oxide nanostructures and their gas sensing properties: a review, Sensors **12** (2012), no. 3, 2610–2631.
[39] J Thornton, Magnetron sputtering: basic physics and application to cylindrical magnetrons, Journal of Vacuum Science and Technology **15** (1978), no. 2, 171–177.
[40] ———, Substrate heating in cylindrical magnetron sputtering sources, Thin Solid Films **54** (1978), no. 1, 23–31.
[41] J Thornton and A Penfold, Cylindrical magnetron sputtering, Thin film processes **4** (1978), 75–113.
[42] K Van Aeken, S Mahieu, and D Depla, The metal flux from a rotating cylindrical magnetron: a Monte Carlo simulation, Journal of Physics D: Applied Physics **41** (2008), no. 20, 205307.
[43] J Vetter, J Crummenauer, G Barbezat, and J Avissar, Surface Treatments of Automotive Parts - Research and Applications, Vakuum in Forschung und Praxis **20** (2008), no. S1, 47–52.
[44] RK Waits, Planar magnetron sputtering, Journal of Vacuum Science and Technology **15** (1978), no. 2, 179–187.
[45] JF Ziegler, MD Ziegler, and JP Biersack, SRIM–The stopping and range of ions in matter (2010), Nuclear Instruments and Methods in Physics Research Section B: Beam Interactions with Materials and Atoms **268** (2010), no. 11-12, 1818–1823.

This page was intentionally left blank.

4 Heat Flux

A too high heat load towards the composite prepreg substrate during deposition can cause local curing or deteriorate the adhesion between prepreg sheets in a laminate. This introduces weak spots in the laminate which are prone to delamination. As the impact of the deposition on the structural properties of the laminate must be limited as much as possible, it is important to study the heat flux during sputter deposition in order to control the heat load towards the substrate.

4.1. Energy Flux

During sputter deposition, it is possible to categorize the energy flux towards the substrate by different contributions such as from incident sputtered particles, energetic ions, reflected neutrals and electrons (kinetic contributions), from heat of condensation and the reaction energy of the deposited sputtered flux (thermodynamic contributions), or from photons emitted from the plasma (radiative contributions).

4.1.1. Sputtered Particles

When an energetic sputter gas ion with energy E_{ion} and mass m bombards the target, the transferred energy is maximized in a head-on collision with a target atom (mass M), and given by γE_{ion}, with

$$\gamma = 4\frac{mM}{(m+M)^2} \tag{4.1}$$

the energy transfer factor. As an example, a head-on collision from an argon ion on a copper atom yields an energy transfer factor $\gamma = 0.94$, whereas for xenon or helium lower values of 0.88 and 0.22 respectively are found. This relatively high value for γ for bombardment of argon on most

common sputtered materials is one of the main reasons for its popularity as sputter gas (see Chapter 3). After bombardment, an atomic collision cascade propagates through the bulk of the target. Due to energy transfer by the collisions between neighboring atoms, some of the surface atoms gain enough energy to escape the target surface. Most of the energy of the collision cascade is however dissipated in the target. As a good thermal contact is facilitated - by means of thermal paste - between the target and the water-cooled cathode, the heat is dissipated to the cooling water. As such, the target is prevented from melting and contributions to the material flux due to evaporation are excluded. The energy of the atoms that leave the target can be described by the Thompson distribution for low impact energies

$$f(E) \approx A\frac{E}{(E+U_{sb})^3} \tag{4.2}$$

where E denotes the kinetic energy of the ejected atom, U_{sb} the surface binding energy of the sputtered material and A a normalization constant. The maximum of the distribution, i.e. $\frac{df(E)}{dE} = 0$, is found at $E = U_{sb}/2$ and represents the most common energy. In the case of copper this yields an energy of 1.74 eV [10]. The most common energy is however not the same as the average energy. The average energy is found by

$$E_{av} = \int_0^{\gamma E_{ion}} Ef(E)dE = 2U_{sb}ln(\frac{\gamma E}{U_{sb}}) \tag{4.3}$$

In the case of copper, this yields $E_{av} = 20.7eV$. These energies are much larger compared to the energy corresponding to a thermalized particle at room temperature, i.e. $(3/2)kT \approx 0.037\ eV$. This enhanced energy of the sputtered particles is one of the main advantages of sputter deposition over evaporation and allows for well adherent, dense and self-organized microstructures (see Chapter 5) [20].
After a particle is released from the target surface, it moves with a given energy and a given direction through the gas phase. Typically, we approximate the angular distribution of the particle as cosine. The particle will either find a surface on which it will condensate or either it will collide with a sputter gas atom. The chances for collision with a gas atom increase with both the sputter gas pressure P and the distance from the target surface d, i.e. with $P \times d$. Collisions with a sputter gas atom create energy losses, a process referred to as thermalization. This is shown in Figure 4.1.

4.1.2. Condensation Energy

When a particle is in the close vicinity of a surface, a physisorption process can occur. The particle is then physically adsorbed on the surface but not yet chemically. The interaction energy for physisorption is low (order meV). When a particle is physisorbed and excess energy is avail-

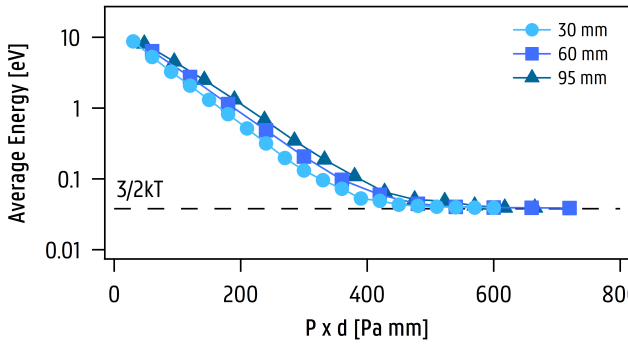

Figure 4.1. *Thermalization of sputtered atoms as function of P×d. The simulation was performed at T=300K. Sputter conditions in analogy to Ref. [3]*

able, it can still diffuse over the surface. During this diffusion process, the particles will be attracted to energetically preferential positions on the surface, and finally settle in by forming a chemical bond. This process is referred to as chemisorption. In case of metals, the energy released to the substrate during chemisorption can be given by the sublimation energy, i.e. the exchange energy for a transition from the gas phase into the solid phase. As an example, the sublimation energy for copper is 3.52 eV and 8.10 eV for tantalum [10], values much higher than the physisorption energy.

4.1.3. Radiation

A magnetron discharge is sustained by ionization processes as described in Chapter 3. It was mentioned that secondary electrons can be lost before generating the maximal number of ionizations, for example, by capture at an anode surface or when the ionization occurs too far from the target, or when the collision simply did not result in an ionization. In the two latter cases, the energy dissipated in the gas phase causes a heating of the plasma and excitation-relaxation mechanisms of the sputter gas atoms. Also, the average energy loss per ionization event is about 30 eV [4, 11, 21] while the ionization energy is only 15.76 eV. Approximately 14 eV is thus transferred to the plasma per sputter gas ionization [14]. These mechanisms are the origin of the radiative energy contributions towards the chamber walls and the substrate during the sputter process. As most ionization processes are located in the vicinity of the cathode surface, the energy density decreases approximately quadratically with the distance from the cathode, i.e. $E_{pl} \sim d_{TS}^{-2}$ [14].

4.1.4. Electronic contributions

As already mentioned above, besides participating in ionization and excitation processes, electrons are also captured by the anode, i.e. chamber

walls and substrate. The same holds for sputter gas ions. When created too far from the target surface, the ions do not feel the presence of the potential sheath and can recombine at the substrate. Ions are attracted to the substrate to sustain the grounding of the substrate. The energetic contribution due to ion impingement on a grounded substrate is however small compared to the energy required for displacement of chemisorbed adatoms ($\approx$ 20 - 30 eV for metals [2, 6, 9, 14, 24]). Therefore, with exception of a small fraction of high-energetic species, impingement of ions on the substrate will not significantly contribute to the breaking of bonds between adatoms, and thus enabling restructuring of the formed islands. Rather, because of the large amount of incident electrons and ions, the substrate temperature increases due to Joule heating. This additional energetic contribution caused by charged particles is referred to as the electronic contribution. Depending on the balance of the incident ions and electrons, a floating potential can arise in case the substrate is isolated from the ground, i.e. in absence of a conductive path. Sometimes, a positive or negative voltage is applied on purpose in order to tune this charged particle flux and the associated heat contribution to the substrate.

4.1.5. Reflected Neutrals

When a heavy ion with mass M is accelerated (typical values for magnetron sputtering $\sim$ 300 - 500 eV) towards a sputter target of a lighter material with mass m, i.e. $M \gg m$, the laws of momentum transfer dictate that the projectile with mass M will keep its momentum and will be implanted inside the sputter target. On the other hand, when the mass of the incident ion is much lighter than the target material, i.e. $M \ll m$, the ion is neutralized and can be reflected at the target surface. An energetic (neutralized) massive particle now propagates through the gas phase, referred to as a reflected neutral. Upon incidence on the substrate, momentum is transferred to the substrate and the growing film. As it is the case for sputtered particles, chances for collision and thus energy dissipation are expected to scale with $P \times d$ [7, 12, 16]. In most cases however, the atomic mass of the sputter gas is comparable to the atomic mass of the target materials and the ratio m/M is not identified by one of the extreme cases. Therefore, a mixture of implantation and reflection processes can be expected during common operation.
It is important here to properly distinguish energy transfer from momentum transfer. Because of their very small mass, electrons can transfer energy but do not have significant momentum. Also photons only transfer energy towards the substrate. Momentum is carried by massive particles, such as sputtered particles, incident ions or reflected neutrals. Upon incidence on the substrate, momentum transfer can cause re-sputtering, or densification of the growing film. Densification is the consequence of reorganizing particles and filling voids within the film under influence of mo-

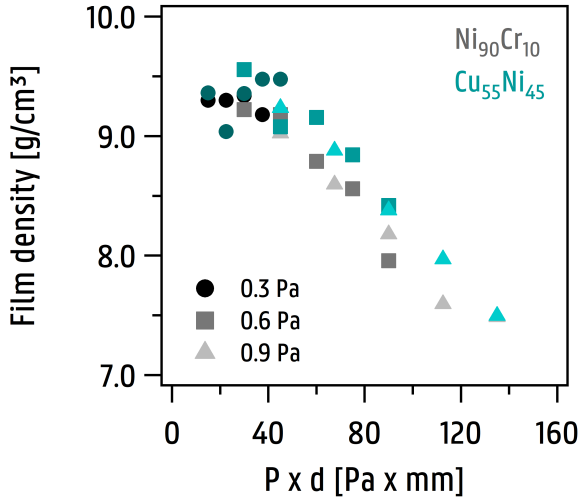

Figure 4.2. *The film density as a function of the product of the argon pressure times the target-to-substrate distance, i.e. P×d. All depositions are performed at a discharge current of* $I = 0.3$ *A, a background pressure* $< 4 \times 10^{-4}$ *Pa, and the deposition rate varied in the range from 0.2 to 1.5 nm/s.*

mentum flux [13, 18]. Also impingement of negative oxygen, specifically during reactive magnetron sputtering (see Chapter 9), can be responsible for large amounts of momentum transfer towards the substrate [23]. Figure 4.2 shows how the film density of chromel and constantan decreases as a function of P × d. It is a common misconception that densification is related to the energy flux towards the film. Of course, both quantities will scale but not every contribution to the energy flux contributes to the momentum flux.

4.2. Experiment

The energy flux during deposition was measured by means of a calorimetric probe. This probe consists of a sensing element with a diameter of 10 mm with a K-type thermocouple welded on the back of the sensing element. The heat capacity of the sensor is 0.048 J/K. The probe was installed in front of the cathode surface and the energy flux during deposition was measured for different target-to-substrate distances, discharge currents and working pressures.
The results are presented in Figure 4.3. When the discharge current is doubled, the energy flux or dissipated power at the substrate is in good approximation doubled. We can understand this behavior based on the description of the IV-characteristic discussed in Chapter 3. For a magnetron discharge, the IV-curve is steep and therefore when the current is doubled, the discharge voltage only varies over a small amount. As an

example, for a given argon pressure of 0.3 Pa and a target-to-substrate of 10 cm, the discharge voltage varied respectively from 392 V to 416 V in the case of chromel and from 396 V to 419 V in the case of constantan, when the discharge current was varied from 0.3 A to 0.6 A. From this, we calculate the variation in dissipated power from 118 W to 250 W for chromel and from 119 W to 251 W for constantan. This calculation confirms that the dissipated power in the vacuum system approximately doubles when the discharge current is doubled. Therefore, also the power density, or energy flux, at the substrate will be doubled. Also the target-to-substrate distance has a clear influence on the energy flux. For a target-to-substrate distance varying over a factor three, i.e. from 5 cm to 15 cm, the energy flux measured at a discharge current of 0.3 A almost decreased over an order of magnitude, i.e. from approximatly 100 mW/cm^2 to 10 mW/cm^2 and in the range of 200 mW/cm^2 to 20 mW/cm^2 at a discharge current of 0.6 A. This strong effect of the target-to-substrate distance on the energy flux is expected as on the one hand, the target-to-substrate distance plays a role in the thermalization process and on the other hand, the dissipated energy originating from the vicinity of the target surface is distributed over the solid-angle for which the area holds a quadratic relationship to the distance from the target (see subsection 1.3). This quadratic relationship with the target-to-substrate distance can - by approximation - be found in the data. Within our experimental range, the influence of the argon pressure on the overall energy flux is small. For an argon pressure varied over a factor three, i.e. from 0.3 Pa to 0.9 Pa, the total energy flux decreased maximally by 25 percent for the largest $P \times d$ combinations.

Furthermore, whereas the variation of the total energy with $P \times d$ is rather inconclusive, the results in Figure 4.2 however indicate a consistent and substantial influence of $P \times d$ on the film density. This again emphasizes that energy is not a good measure for the film density. Indeed, the inconclusive trend of $P \times d$ on the total energy flux results from the fact that $P \times d$ only affects a fraction of the total energy flux, i.e. the energetic contributions related to massive particles. In order to properly understand the film density, it is essential to disentangle energy effects and effects related to momentum transfer [15].

Figure 4.3b and d represent the sputtered particle flux as function of the target-to-substrate distance, the argon pressure and the discharge current. The material flux was calculated as

$$F_M = \frac{v_d \rho N_A}{M} \qquad [\frac{atoms}{cm^2 s}] \tag{4.4}$$

with v_d the deposition speed, ρ the film density, M the molar mass of the sputtered material, and N_A Avogadro's number. The dependencies of the sputtered particle flux on the process conditions are very similar to the

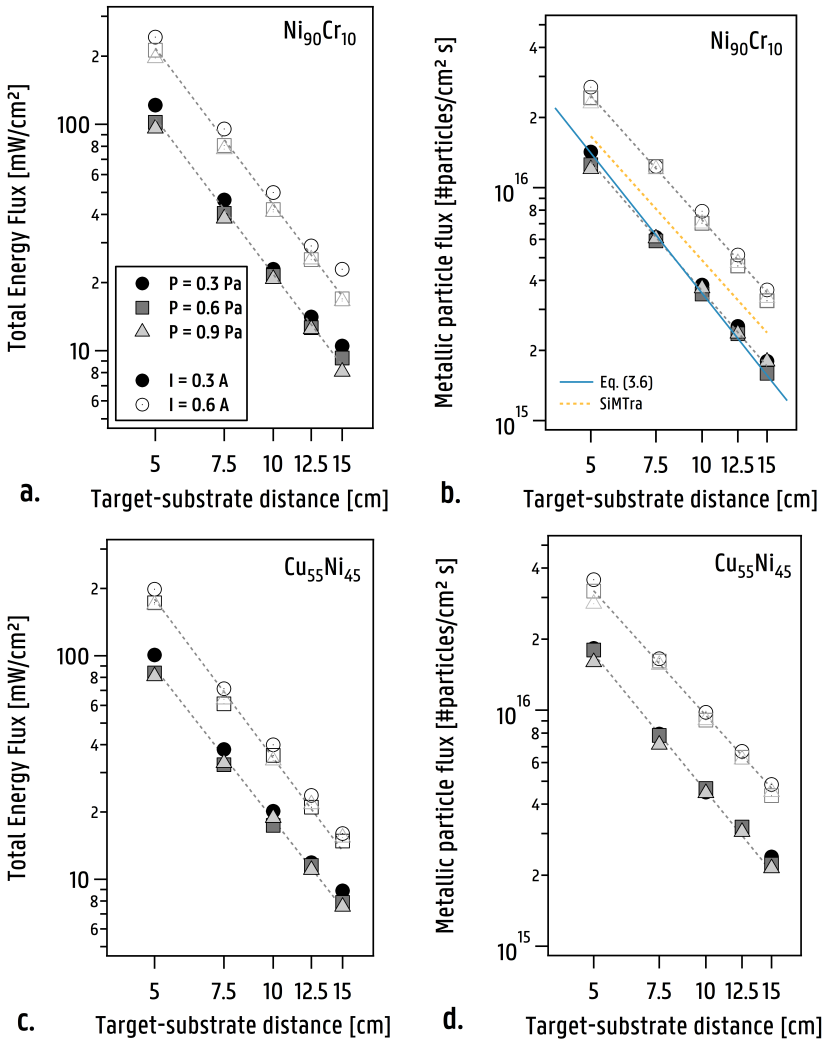

Figure 4.3. *The total energy flux and material flux as function of the target-to-substrate distance for three argon pressures (0.3, 0.6, and 0.9 Pa) and two discharge currents (0.3 A (closed markers) and 0.6 A (open markers)). a) Total energy flux, and b) arriving material flux for chromel. The blue line represents the prediction from Chapter 3 Eq. (3.7). The yellow striped line represent a SiMTra simulation for* 10^7 *particles leaving the target at an argon pressure of 0.6 Pa and the coefficients for the angular distribution* $c_1 = 1$ *and* $c_3 = -0.8$*. The results of the simulation are rescaled to meet the condition of* 2.21×10^{18} *particles leaving the target per second as derived in Chapter 3. c) The total energy flux and d) material flux for constantan. The lines are a guide for the eye.*

case of the energy flux discussed above. Doubling the discharge current doubles the amount of ionic bombardment events per second on the target. The associated change in discharge voltage is limited because of the steep IV-curve (see Chapter 3). As the sputter yield Y depends in good approximation linearly on the discharge voltage in a restricted voltage range [17, 19, 25], only a small variation in sputter yield is expected when the discharge current is doubled. Therefore, at doubled discharge current, the rate of particles ejected from the target is in good approximation also doubled. The particles are ejected from the target surface according to a (under-)cosine distribution. If there were no gas atoms present, the particle density in a given direction θ at a distance r from the (center) of the target surface would approximately be $\sim cos(\theta)/r^2$. Again, this quadratic relation with the distance from the origin is approximately found in the experimental data. Due to collision events with the atoms of the sputter gas during transport of the sputtered atoms towards the substrate, the initial angular distribution of the sputtered particles evolves towards a more uniform angular distribution of the particles arriving at the substrate. Within our experimental range, however, the observed effect of the argon pressure on the deposition rate is small. When the pressure is increased over a factor 3, from 0.3 Pa to 0.9 Pa, the material flux decreases at maximum by 15 percent again for the largest $P \times d$-value, whereas an increase of the target-to-substrate distance over a factor 3, from 5 cm to 15 cm, approximately decreases the arriving material flux by an order of magnitude, i.e. 90 %. When the particle flux is uniformly distributed in any angular direction, the expected particle flux would behave as $F_M \sim 1/2\pi r^2$. This relation corresponds to the prediction as prescribed by equation (3.7), which is shown by the blue line in Figure 4.3 b. Based on the calculation of the amount of sputtered particles and the assumption of a uniform angular distribution (Chapter 3), already a good agreement can be observed with the experimental data. The yellow striped line represents a SiMTra simulation. The simulation was performed for both Ni and Cr as target material and afterwards the results were weighted in order to meet the stoichiometry of chromel, i.e. $Ni_{90}Cr_{10}$. A cuboid chamber with the same spatial dimensions as the original was used, the argon pressure was set to 0.6 Pa, the coefficients c_1 and c_3 for the angular distribution set to 0 and -0.8 respectively, and a Molière screening function was used. In total 10^7 particles leaving the target were simulated and afterwards rescaled in order to meet the condition of 2.21×10^{18} particles leaving the target per second as derived in Chapter 3.

4.3. Energy per arriving adatom

The experimental observations of the total energy flux and the material flux allow to calculate an average energy per arriving particle (EPA) on the substrate surface. The EPA is defined by the ratio between the energy

flux and the material flux and is a measure for the diffusivity of an adatom on the substrate surface. We will come back on this topic in the next chapter.

The EPA as function of process parameters is presented in Figure 4.4. In the case of chromel, the EPA varies in the range of 35 eV/at up to 55 eV/at within our experimental space and between 20 eV and 40 eV in the case of constantan. The EPA for constantan is lower than for chromel as for the latter, the measured energy fluxes are slightly lower and the material flux slightly higher for a given discharge current. As the EPA is the result of both measurements of the energy and material flux, the experimental error on the resulting values is quite large. The error on the EPA is defined by the measurements of layer thickness, density and thermal probe measurements. In the plots in Figure 4.4 the error bars are valid for all data points but only presented, for the sake of clarity, on one series ($P = 0.6\ Pa$ at $I = 0.3\ A$). Despite the error on the data, some trends can be revealed. As both energy flux and material flux scale in a comparable, but non-equal way, with the target-to-substrate distance, the EPA will still hold a main dependency for the target-to-substrate distance. This is presented by the gray dotted lines in Figure 4.4. The effects of argon pressure and discharge current are not very consistent or strongly expressed. This indicates that the EPA is not strongly affected by variations of these latter deposition conditions. For the case of the argon pressure, this is understood as the pressure didn't have a distinct influence on the energy flux or the material flux within our experimental

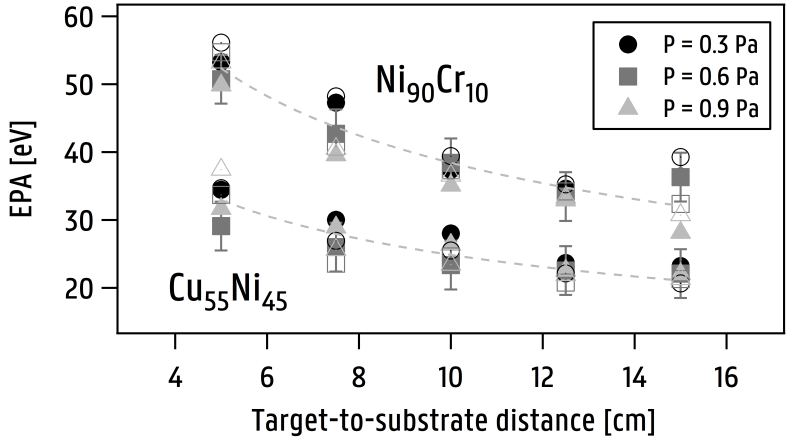

Figure 4.4. *The average energy per arriving particle (EPA) for chromel and constantan as function of the target-to-substrate distance for different argon pressures, and discharge currents (closed markers: 0.3 A, open markers: 0.6 A). As a guideline, the entire dataset is approximated by EPA* $\sim d_{TS}^{\alpha}$*, with* $\alpha = -0.44 \pm 0.03$ *and* $\alpha = -0.41 \pm 0.03$ *for chromel and constantan respectively.*

range. The discharge current, or power, on the other hand did have a strong effect on both the material flux and the energy flux, but as both fluxes scaled in a similar linear way with the discharge current, the EPA, defined as the ratio between both fluxes, is not distinctively affected by the discharge current or power. Our observations with respect to the EPA are also in line with the reports of Thornton [22]. He reports that the EPA varies from 15 to 25 eV for light metals and over 50 eV for heavier metals with moderate sputtering yields. Furthermore, in line with our results, Thornton reports that the EPA is independent of the deposition rate, or analogous the discharge current or power, and the sputter gas pressure. However, it is important to emphasize that these results can only be generalized with great care as they are strongly dependent on the experimental range in which the experiments are performed. As an example, Drüsedau et al. [5] studied the influence of pressure and power on the EPA for the deposition of Al and Mo, and found an increase of the EPA with increasing pressure, and with decreasing power. This conclusion differs from ours as the experimental range in which the pressure was varied goes up to 6 Pa. Our observations and the reports of Thornton are however consistent with the latter work when comparing within a similar experimental range, i.e. $P < 1\ Pa$.

4.4. Composite Curing

Based on the previous sections, it is clear that during sputter deposition, the substrate is bombarded by different energetic species which results in a heat flux towards the substrate. A sheet of pre-preg in its uncured state is however a temperature sensitive material. When it is used as a substrate for deposition, it is therefore important to restrict the heat load towards the substrate. A too high heat load can cause local curing of the resin. This results in a bad adhesion in between the different sheets of uncured pre-preg when integrated in a lay-up, and consequently a cured laminate is produced which is prone to delamination. As we measured the heat loads coupled to different deposition condition, it is possible to estimate the temperature increase of a prepreg substrate during deposition. For this, we need knowledge of the heat capacity of an uncured prepreg substrate. Differential scanning calorimetry (DSC) was performed [1] in order to determine the heat capacity of uncured (carbon/epoxy) pre-preg (Figure 4.5). During DSC, the difference in heat required to increase the temperature of a test sample compared to a sapphire sample is measured. Heating experiments are performed on 3 blank, 3 sapphire and 2 test samples. The mass of the test sample was 21.210 mg. A similar experiment was performed by Kalogiannakis et al. [8] in order to determine the heat capacity of both glass/epoxy and carbon/epoxy prepregs in a temperature range from -50 to 125 °C. Their results are also included in Figure 4.5 for comparison.

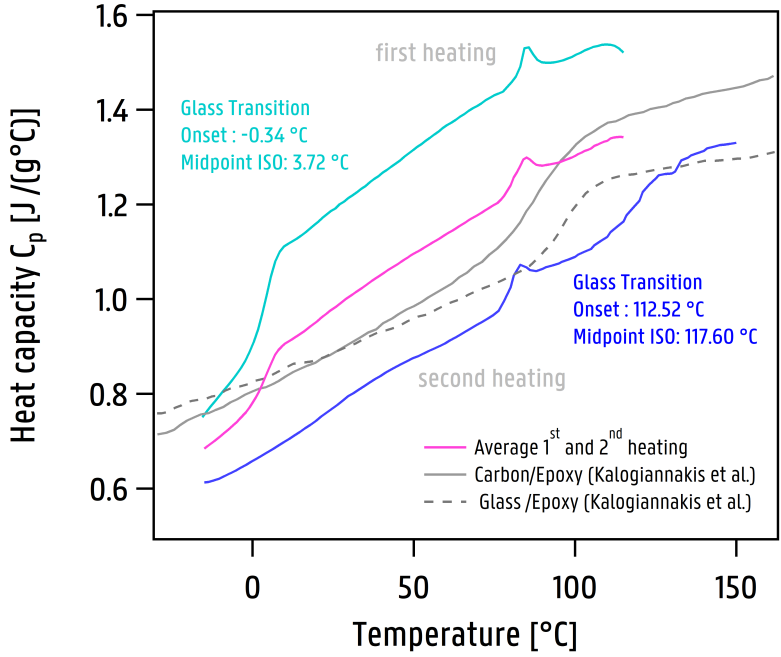

Figure 4.5. *Differential scanning calorimetry for the determination of the heat capacity of carbon fiber pre-preg.(Carbon fiber,21,2100 mg)*

Composite materials present a high variation of thermal properties as a function of temperature. The glass transition of the resin can significantly affect both the thermal conductivity and the heat capacity of the composite [8]. Glass transitions related to the polymer can be observed by the changes in the heat capacity. For the case of carbon/epoxy and glass/epoxy respectively [8], the glass transition temperature was identified at 89.1 °C and 97.0 °C, and the onset for transition at 77.7 °C and 89.3 °C. In the range from 10 °C to 70 °C, the behavior of the heat capacity C_p as function of temperature is linear. A fitting procedure of the averaged data in this temperature range yields

$$C_p(T) = (4.53 \pm 0.03) \times 10^{-3} T + (0.866 \pm 0.001) \tag{4.5}$$

with an R-squared value of 0.998. For sake of comparison, Kalogiannakis et al. obtained in this same temperature range

$$C_p(T) = (3.69 \pm 0.06) \times 10^{-3} T + (0.804 \pm 0.011) \tag{4.6}$$

and

$$C_p(T) = (2.71 \pm 1.20) \times 10^{-3} T + (0.829 \pm 0.036) \tag{4.7}$$

for carbon/epoxy and glass/epoxy respectively.

With knowledge of the heat capacity of a carbon prepreg, an estimation of the total temperature increase for a deposition of a specified thickness and deposition conditions can be given by

$$\Delta T = \frac{F_E}{v_D \rho_{pp} C_p\left(\Delta T\right)} d \tag{4.8}$$

with F_E the energy flux, v_D the deposition rate, ρ_{pp} the density of the carbon/epoxy prepreg, and C_p the temperature dependent heat capacity as determined by DSC. The density of the carbon prepreg was calculated as 1.6 g/cm^3 for a fiber-to-volume fraction of 65 %, with values for the density of 1.8 g/cm^3 for the carbon fiber and 1.2 g/cm^3 for the epoxy matrix. The calculated temperature increase as function of the layer thickness is shown in Figure 4.8. Both the heat load towards the substrate during deposition, and the mechanical properties of the final composite are affected by the film thickness. It is thus of importance to restrict the film thickness as much as possible. However, as will be discussed in Chapters 7 and 8, decreasing the overall layer thickness comes at a cost of deteriorated (thermo-)electrical film properties. Determining the optimal layer thickness requires a compromise between a restricted heat load and good film properties. Anticipating the results, once the layer thickness exceeds 100 nm, a more bulk-like behavior of the film is observed. If no compromise on film properties is allowed, at least a 100 nm film is, on average, required. An additional constraint to be considered is related to the intrinsic roughness of an (uncured) prepreg surface due to the presence of both fibers and the resin. Scanning electron microscopy (SEM) images of coated uncured prepregs are presented in Figures 4.6 and 4.7. A high degree of macroscopic surface roughness of the prepreg substrate can be observed. When deposited on such a rough surface, a too thin film risks to be discontinuous. Of course, this is detrimental when aiming for electrical applications. Furthermore, as the mobility of the polymer chains increases with temperature, local displacement of the epoxy is observed which can also deteriorate the continuity of the film. The probability for a breakage of the film pattern decreases with an increasing film thickness as the elastic properties of the film are improved. From the perspective of film continuity, somewhat thicker films are thus preferred.

Another point of attention is that the heat flux is not necessarily uniformly dissipated over the substrate. Regions of high energetic density can be present at the substrate, as example, due to the crossing of a magnetic field line with the substrate surface. This can cause a local spot on the substrate at much higher temperature as anticipated by the calculations. Therefore, it makes sense to limit the allowed heat load preventively.

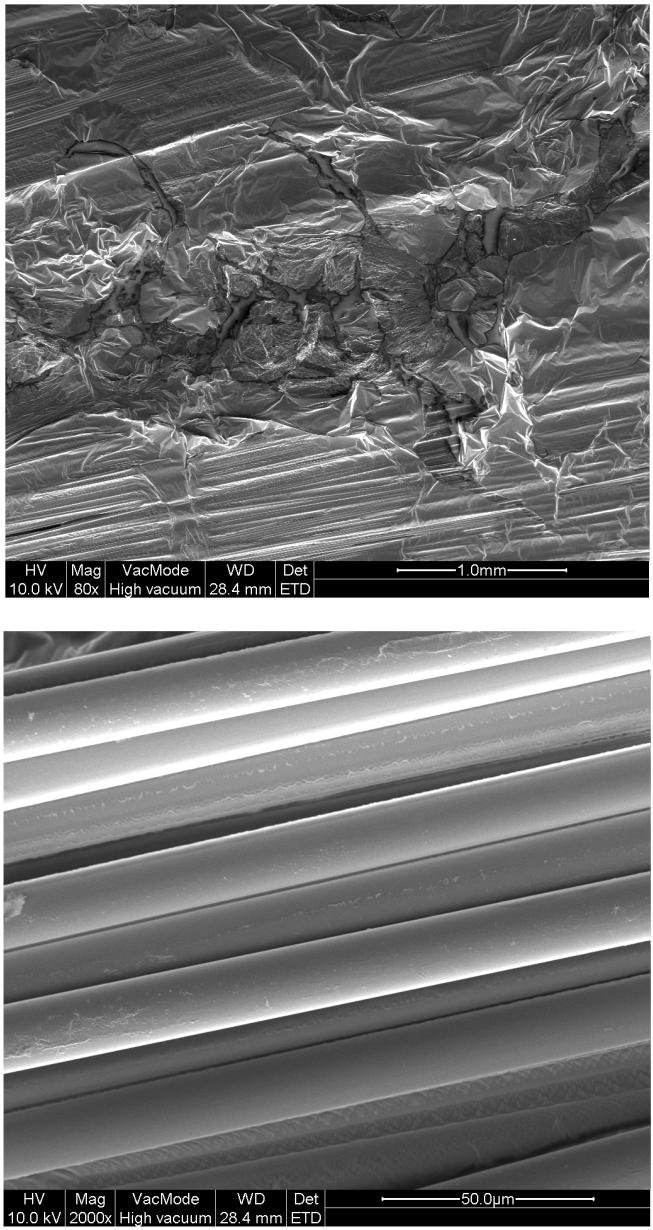

Figure 4.6. *SEM images of coated uncured prepreg layers.(top) SEM image at a scale of 1 mm. On the prepreg surface, fiber-rich and resin-rich areas can be observed. Escpecially the epoxy-rich areas show a high degree of surface roughness. (bottom) SEM image at a scale of 50 µm. The individual fibers, exposed at the surface of the prepreg are shown. On the fibers itself, no remarkable roughness is observed.*

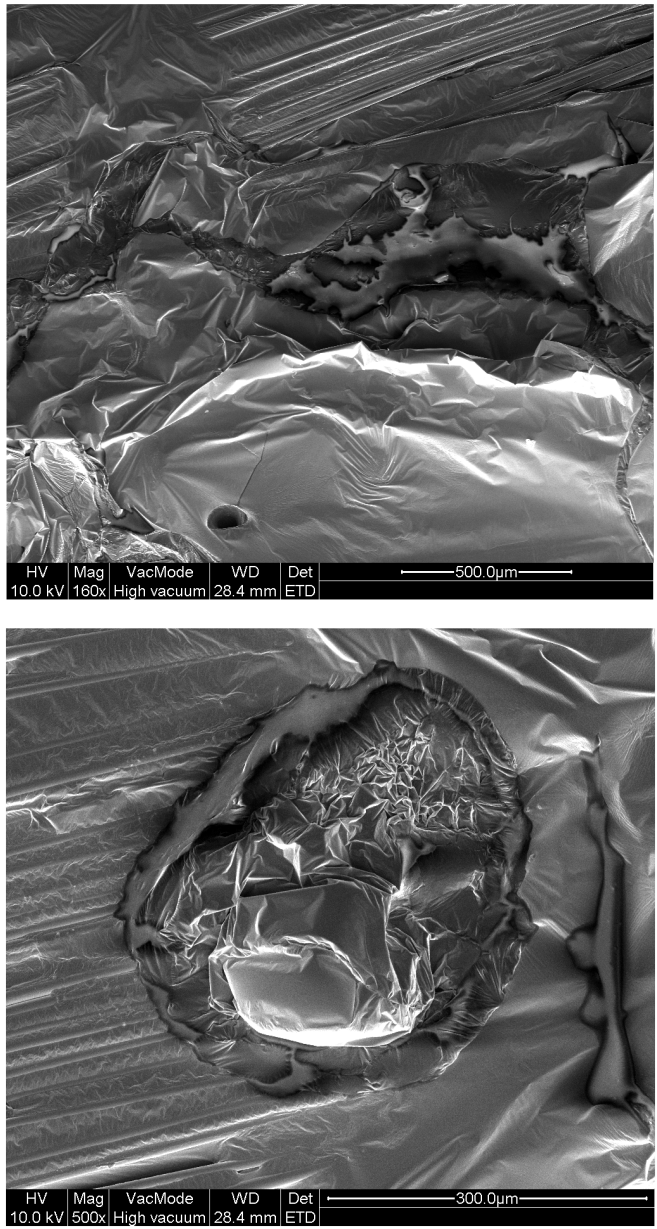

Figure 4.7. *SEM images of coated uncured prepreg layers.(top) SEM image at a scale of 500 µm. Outgassing of voids and bubbles contained in the epoxy can cause perforations of the epoxy. (bottom) SEM image at a scale of 300 µm. Craters of different dimensions can also be observed on the surface.*

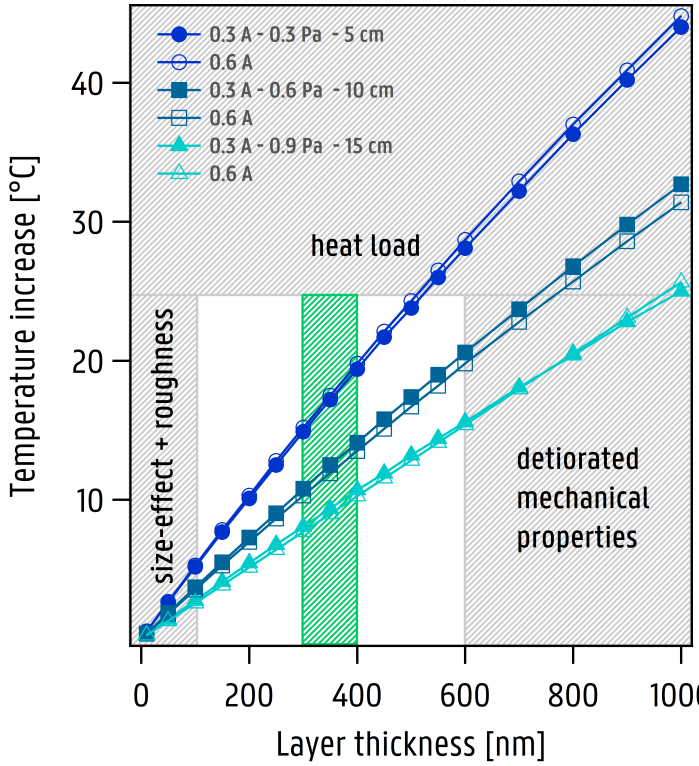

Figure 4.8. *The temperature increase of a carbon/epoxy prepreg as function of the deposited layer thickness for different deposition conditions. The gray patterned area represents excluded zones, i.e. not in line with the constraints. The preferential region in which depositions are mostly performed in this work is indicated by the green patterned area.*

Based on the DSC-measurements in Figure 4.5, we want to prevent the substrate temperature to exceed 70°C in order not to induce any phase transitions. If we preventively restrict the calculated temperature of the substrate by 20 degrees underneath the temperature barrier for a phase transition, a maximum temperature increase of 28°C is allowed (room temperature $\approx$ 22°C). This upper limit has no scientific ground, but is rather based on the practical experience obtained during this work. The constraints discussed above, are presented as patterned areas on Figure 4.8. As such, a region appears which fullfills all constraints and where deposition is allowed without affecting the mechanical properties of the composite, the properties of the film, or risking breaking of the film pattern. The preferential region in which depositions are mostly performed in this work is indicated by the green patterned area. Of course, it must be remarked that the constraints for the film and the material depend

on the application one bears in mind. As an example, for the digital volume correlation (DVC) applications discussed in the introduction, the constraint of discontinuous patterns was of no importance as no conductive path was necessary.

4.5. Conclusion

The heat flux and material flux towards the substrate during sputter deposition are characterized as function of the deposition conditions, i.e. discharge current, argon pressure and target-to-substrate distance. It was observed that, within our experimental range, both fluxes are mainly dependent on both the discharge current and the target-to-substrate distance, and only in a minor way by the argon pressure. The EPA was introduced as a more condition/environment-objective energy parameter. It was concluded that the EPA is mainly affected by the target-to-substrate distance, but is mainly independent of the discharge current and the argon pressure. The detailed quantification of the energies per arriving adatom as a function of the deposition conditions allowed to map the expected temperature increase as a function of the deposition conditions and the desired layer thickness. For this, first the heat capacity of a prepreg substrate was determined by means of digital scanning calorimetry. Given the constraints imposed on the film thickness by the size-effect and the surface roughness on the one hand, and the constraints related to the acceptable temperature increase of the prepreg prior to curing on the other hand, a favorable region for thin film deposition on an uncured prepreg substrate was determined.

References

[1] Test Method for Assignment of the Glass Transition Temperatures by Differential Scanning Calorimetry.

[2] M Andritschky, F Guimaraes, and V Teixeira, Energy deposition and substrate heating during magnetron sputtering, Vacuum **44** (1993), no. 8, 809–813.

[3] ZH Barber and RE Somekh, Magnetron sputtering of Cu55Ni45, Vacuum **34** (1984), no. 10-11, 991–994.

[4] G Buyle, D Depla, K Eufinger, J Haemers, W De Bosscher, and R De Gryse, Simplified model for the DC planar magnetron discharge, Vacuum **74** (2004), no. 3-4, 353–358.

[5] TP Drüsedau, T Bock, TM John, F Klabunde, and W Eckstein, Energy transfer into the growing film during sputter deposition: An investigation by calorimetric measurements and Monte Carlo simulations, Journal of Vacuum Science & Technology A: Vacuum, Surfaces, and Films **17** (1999), no. 5, 2896–2905.

[6] SD Ekpe and SK Dew, Investigation of thermal flux to the substrate during sputter deposition of aluminum, Journal of Vacuum Science & Technology A: Vacuum, Surfaces, and Films **20** (2002), no. 6, 1877–1885.

[7] GF Iriarte, JG Rodriguez, and F Calle, Effect of substrate–target distance and sputtering pressure in the synthesis of AlN thin films, Microsystem Technologies **17** (2011), no. 3, 381–386.

[8] G Kalogiannakis, D Van Hemelrijck, and G Van Assche, Measurements of Thermal Properties of Carbon/Epoxy and Glass/Epoxy using Modulated Temperature Differential Scanning Calorimetry, Journal of Composite Materials **38** (2004), no. 2, 163–175.

[9] H Kersten, GMW Kroesen, and R Hippler, On the energy influx to the substrate during sputter deposition of thin aluminium films, Thin Solid Films **332** (1998), no. 1-2, 282–289.
[10] Yu Kudriavtsev, A Villegas, A Godines, and R Asomoza, Calculation of the surface binding energy for ion sputtered particles, Applied surface science **239** (2005), no. 3-4, 273–278.
[11] MA Lieberman and AJ Lichtenberg, Principles of plasma discharges and materials processing, MRS Bulletin **30** (1994), no. 12, 899–901.
[12] J Lu and CG Lee, Numerical estimates for energy of sputtered target atoms and reflected Ar neutrals in sputter processes, Vacuum **86** (2012), no. 8, 1134–1140.
[13] E Lugscheider, C Barimani, C Wolff, S Guerreiro, and G Doepper, Comparison of the structure of PVD-thin films deposited with different deposition energies, Surface and Coatings Technology **86-87** (1996), 177–183.
[14] S Mahieu and D Depla, Reactive sputter deposition of TiN layers: modelling the growth by characterization of particle fluxes towards the substrate, Journal of Physics D: Applied Physics **42** (2009), no. 5.
[15] _____, An in-situ monitor to measure the momentum flux during physical vapour deposition, Surface and Coatings Technology **204** (2010), no. 12-13, 2085–2088.
[16] S Mahieu, K Van Aeken, and D Depla, Quantification of the ion and momentum fluxes toward the substrate during reactive magnetron sputtering, Journal of Applied Physics **104** (2008), no. 11, 113301.
[17] N Matsunami, Y Yamamura, Y Itikawa, N Itoh, Y Kazumata, S Miyagawa, K Morita, R Shimizu, and H Tawara, Energy dependence of the ion-induced sputtering yields of monatomic solids, Atomic Data and Nuclear Data Tables **31** (1984), no. 1, 1–80.
[18] DM Mattox, Particle bombardment effects on thin-film deposition: A review, Journal of Vacuum Science & Technology A: Vacuum, Surfaces, and Films **7** (1989), no. 3, 1105–1114.
[19] M Möller and W Eckstein, Tridyn — A TRIM simulation code including dynamic composition changes, Nuclear Instruments and Methods in Physics Research Section B: Beam Interactions with Materials and Atoms **2** (1984), no. 1-3, 814–818.
[20] I Petrov, PB Barna, L Hultman, and JE Greene, Microstructural evolution during film growth, Journal of Vacuum Science & Technology A: Vacuum, Surfaces, and Films **21** (2003), no. 5, S117–S128.
[21] J Thornton, Magnetron sputtering: basic physics and application to cylindrical magnetrons, Journal of Vacuum Science and Technology **15** (1978), no. 2, 171–177.
[22] _____, Substrate heating in cylindrical magnetron sputtering sources, Thin Solid Films **54** (1978), no. 1, 23–31.
[23] S Van Steenberge, WP Leroy, A Hubin, and D Depla, Momentum transfer driven textural changes of CeO2 thin films, Applied Physics Letters **105** (2014), no. 11, 111602.
[24] R Wendt, K Ellmer, and K Wiesemann, Thermal power at a substrate during ZnO: Al thin film deposition in a planar magnetron sputtering system, Journal of applied physics **82** (1997), no. 5, 2115–2122.
[25] Y Yamamura and H Tawara, Energy dependence of ion induced sputtering yields from monoatomic solids at normal incidence, Atomic Data and Nuclear Data Tables **62** (1996), no. 2, 149–253.

This page was intentionally left blank.

5 Thin film growth

It was observed in Chapter 2 that the impact of an embedded thin film on the structural properties of the composite decreases with decreasing layer thickness. Therefore, it is essential to develop a thorough understanding of the role of a reduced layer thickness on the microstructural evolution, and consequently, on the film properties. This chapter provides an overview of the microstructural evolution of sputter deposited films, from the early stage of nucleation to the stage of film thickening. Experimental data for the microstructural evolution during thickening are also presented and confronted with theoretical models and experimental data found in literature.

5.1. Nucleation

Thin film growth is initiated by the random deposition of adatoms on the bare substrate surface at a rate F_M. For magnetron sputtering, atoms arriving on the surface have a kinetic energy typically in the range of a few k_BT up to 50 eV (see Chapter 4), in contrast to evaporation where the gross of the adatoms arriving on the substrate are thermalized. Upon incidence, this energy is immediately dissipated to the substrate surface. This dissipated energy can cause atoms already chemically bound to the surface to be released. The latter atoms consequently migrate on the surface by successive hopping to adjacent lattice sites, a process referred to as adatom diffusion which enables dense and self-organizing thin film structures by adatoms rearranging on the substrate surface. In this context, the adatom surface diffusivity D is understood as a measure for the number of lattice sites an adatom visits per unit of time. The adatom surface diffusivity is given by

$$D \sim a^2 \nu exp(-E_D/kT_s) \qquad [\frac{m^2}{s}] \tag{5.1}$$

with ν the hopping frequency, a the lattice parameter of the substrate surface. The ratio E_D/kT_s compares the adatom energy, kT_s, to the energy barrier for diffusion E_D. Depending on the available energy, the adatom diffuses over the substrate surface and explores different energetic environments on the surface. At energetically favorable locations, the probability for adatom diffusion becomes low, i.e. large E_D, and the adatom becomes bounded. These locations can be kinks at step-terraces, impurities, or yet another diffusing adatom or cluster of adatoms. The critical nucleus size i^* indicates the number of constituting adatoms needed such that, after capture of another adatom, the cluster nucleates and is considered stable and immobile. In the case of depositions by magnetron sputtering at low substrate temperature, the size of a critical nucleus is only a few atoms or even $i^* = 1$, which means that collision of two hopping adatoms is sufficient to nucleate both into a stable and immobile island. Nucleation and island growth are competing processes as adatoms can either form new nucleation centers or can either contribute to island growth if captured by an already existing island [30]. Based on a balanced approach, we can rationalize a basic model describing the competition between adatom nucleation and island growth [6, 24, 33, 34, 41, 50, 51]. In its simplest form, the change in surface adatom density n with deposition time can be approached as:

$$\frac{dn}{dt} = F_M - 8Dn^2 - 4DNn \tag{5.2}$$

The first term F_M is the deposition flux towards the substrate, i.e. the influx of atoms. The second term represents the formation of a nucleation island by collision of two diffusing adatoms, and the third term represents island growth where a diffusing adatom is captured by an already existing island. The rate equation for the nucleation density N is given by

$$\frac{dN}{dt} = +4Dn^2 \tag{5.3}$$

The exclusion of mechanisms such as island coarsening and island desorption in our basic model are justified by the low substrate temperatures during deposition. In general, for a critical island size i^*, we yield the well-known expression:

$$N \sim \left(\frac{F}{D}\right)^{\chi} \tag{5.4}$$

with the exponent χ related to the size of the critical nucleus size i^*. If $N \gg n$, an exponent $\chi = \frac{i^*}{i^*+2}$ is found, whereas if $N \sim n$, the exponent becomes $\chi = \frac{i^*+1}{i^*+3}$. It is shown [34] that the existing islands merely grow in size after the moment where new island nucleation has been arrested by the efficient capture of adatoms by spatially extended islands but before island coalescence becomes significant. As the scaling properties of adatom nucleation and island growth have been recognized as

a tool for extracting characteristics of the atomic behavior, the scaling exponent χ can be used to determine the critical island size as well as activation energies for diffusion [1, 6, 25]. This is shown for molecular beam epitaxy of Cu on Ni(001) or for sputtered TiN/TiN(001), where in both cases $i^* = 1$. Note that the nucleation density depends on the process parameters through F and on the sputtered material through D. The ratio of the diffusion coefficient of an adatom to the deposition flux towards the substrate represents the competition between nucleation and growth. The higher the surface diffusion coefficient of an adatom – a material dependent parameter – the higher the probability the adatom is captured by an already existing island rather than another adatom is deposited in the vicinity of the diffusing adatom, providing a chance for adatom collision [30]. Therefore, high mobility materials are more likely to grow bigger islands. On the other hand, a high deposition flux favors the process of nucleation over island growth resulting in smaller islands. The average spacing between nucleated islands, i.e. the island center-to-center separation, distributed over a surface with an island density of N is given by [30, 34, 51]

$$L \sim \frac{1}{\sqrt{N}} \tag{5.5}$$

The separation between the different islands is determined by the average area an adatom explores on the surface within a fixed time frame, i.e. before arrival of another adatom forcing nucleation. We can define L as the characteristic length, i.e. the mean free path length of an adatom on the surface, prior to nucleation or attachment to an already existing island. Given equation (5.4) and (5.5), we find

$$L \sim \left(\frac{D}{F}\right)^{\chi/2} \tag{5.6}$$

From this point of view, every nucleation center has an adatom capture area of L^2 around its center, i.e. every adatom arriving in capture area is attached to the island. In this case, islands grow by adatom capture and at the stage of island impingement, $L \sim \frac{1}{\sqrt{(N)}}$ is a measure for the lateral island size [26] or, by relation, for the domain size.

5.2. Structure Zone Models

During the nucleation stage, different clusters of adatoms nucleate on the surface and grow in size by adatom capture. The formation of the small clusters of adatoms is driven by energy minimization. If the adhesion energy between the adatoms is larger than the binding energy of the adatom to the surface, the clusters of adatoms form small 3D islands or hills in order to reduce the free surface of the material. This growth-mode is

referred to as Volmer-Weber growth, and is typically the case when growing a metal on an amorphous substrate such as glass. Depositions at low substrate temperature T_s, i.e. low adatom surface diffusivity, on amorphous or randomly textured substrates leads to nucleation of islands with random orientation [47]. For higher adatom diffusivities, diffusion processes can allow to form more thermodynamically stable islands. The adatom diffusivity or the substrate temperature in combination with the deposition flux are therefore the driving parameter for the further structural and morphological evolution of a thin film. Structure zone models describe the microstructural evolution of a film by categorizing growth into different zones or growth modes as function of a driving parameter related to the deposition conditions. Structure zone models are the result of studying thin films with (cross-sectional) scanning microscopy and/or surface topography. Based on morphological properties, thin films can be categorized in different zones. The zone in which growth occurs and thus the related morphological properties of the film depend on the conditions during deposition. Movchan and Demshishin [31] were the first to categorize and describe the growth mode and related morphologies of evaporated thin films based on the evaluation of the homologuous temperature, i.e. T_s/T_M. As the energetic barriers for diffusion on the surface and in the bulk of different metals scale with the melting temperature T_M, and the diffusivity of the adatom scales with the substrate temperature T_s, the ratio T_s/T_M attemps to overcome the material dependency on the microstructure. Whereas the zone model of Movchan and Demshishin fairly well described the morphology of evaporated thin films, it has many shortcomings with regard to films grown by sputter deposition. The main differences between sputter deposition and evaporation are the enhanced (kinetic) energy of the arriving particles on the substrate and the presence of a sputter gas. Furthermore, as for evaporation high temperatures are needed inside the vacuum chamber, the amount of outgassing is expected to be significantly higher than in the case of sputtering. Efforts to meet these shortcomings were first done by Thornton by proposing a structure zone model for sputter deposited films [48], and later on by Mahieu et al. [28] and Anders [2]. The main rationale in all these models is that the resulting microstructure can be understood from the effect of deposition conditions on the adatom mobility (energy related), time available for surface diffusion (deposition speed-related) and possibly densification through momentum transfer or porosification by shadowing effects. In the latter case of Mahieu et al. for as-deposited films, i.e. deposited without any additional heating contribution to the substrate, the adatom surface energy kT_s is approximated by a fraction f of the EPA arriving of the substrate. With this, the adatom diffusivity becomes

$$D \sim a^2 \nu exp(-E_D/f\ EPA) \tag{5.7}$$

It was shown by Mahieu that variations in the reactive gas flow of the deposition of TiN resulted in changes of the microstructure as the EPA was varied. Of course, the changes in EPA under influence of the reactive gas flow are large [11] as a significant drop in deposition rate (material dependent but roughly order of magnitude) occurs when sputtering in reactive mode (see Chapter 9).

As presented in Figure 5.1 (a - f), the structure zone model proposed by Mahieu categorizes film growth by sputter deposition in mainly three zones, i.e. Zone I (a, b, and c), Zone T, and Zone II. Zone III is excluded from the discussion here as additional mechanisms are required to explain its presence. The growth conditions for the different zones are related to the adatom mobility. In order to properly understand the microstructural evolution during thickening of a film, it is important to look at film growth starting from the nucleation process. As mentioned in the introduction, the nucleated islands grow by adatom capture until they form a continuous layer at the stage of coalescence. The crystallographic orientation of the islands, called crystallites, depends on the crystallographic orientation of the substrate and the conditions during nucleation. In the case of epitaxial growth for example, the crystallographic orientation of the substrate is projected onto the orientation of the crystallites and a layer of crystallites with a preferential crystallographic orientation is formed. When a film grows on an amorphous or randomly textured substrate, it is more likely that the crystallographic orientation is randomly distributed over the surface, i.e. there is no preferential orientation of the crystallites. At the stage of island impingement, the formed crystallites touch one another and form a continuous layer. On average, a film becomes continuous, i.e. there is a continuous path between all island due to island impingement, at a thickness of around 10 nm. Further film growth now occurs by local epitaxy on the formed islands and strongly depends on the mobility of the adatoms (surface) and the grain boundaries (bulk).

5.2.1. Zone I: stages a, b and c

For the growth at low adatom mobility, or at low substrate temperatures, the film morphology is described as a Zone I microstructure. When the adatom diffusion is restricted, the arriving adatoms attach to the surface on their place of arrival and the initial (random) distribution of crystallites grows under influence of a "hit-and-stick" mechanism, also called a "ballistic" deposition. An analogous growth mode can however also arise at very high values for the deposition rate or material flux F towards the substrate. Indeed, as discussed in section 5.1, the ratio D/F embodies an available area which can be explored through unhindered adatom diffusion within the time frame between two subsequent arrivals of other adatoms within this area. At very high fluxes, the time frame for adatom diffusion becomes so small that adatoms are buried at the place they

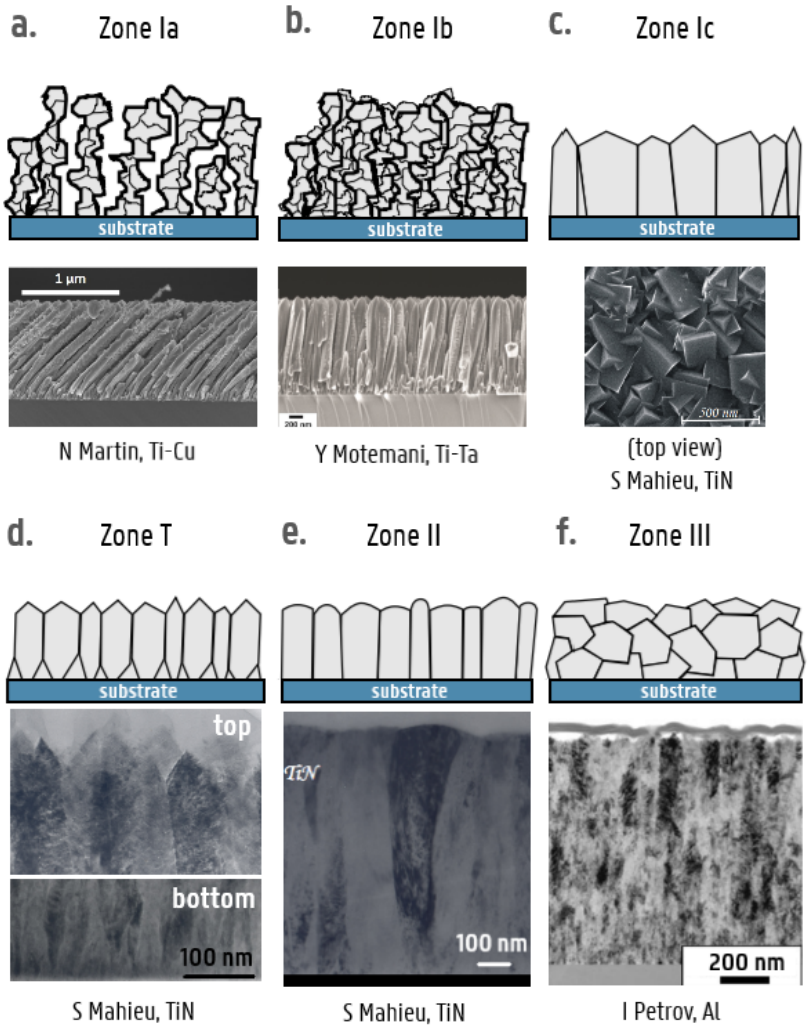

Figure 5.1. *Structure Zone Model for sputter deposited films as proposed by Mahieu et al [28]. Figure adapted from Ref. [28].*

land on the surface. Therefore, the effect of a very low adatom diffusivity at normal deposition rates is analogous as for a very high deposition rate at average adatom diffusivities, and both result in a hit-and-stick or ballistic growth mode. In this case, the crystallites grow into columns with an amorphous crystallographic nature. Shadowing of the impinging material flux onto the smaller columns by larger columns gives rise to an underdense structure of voided columns. This is presented by Figure 5.1a. In case the film is subjected to momentum transfer (knock-on events) during growth by impact of accelerated ions, reflected neutrals or

sputtered atoms (see Chapter 4), additional densification of the film can occur as is presented in Figure 5.1b. If the adatom energy is somewhat increased, adatoms can overcome the diffusion barrier and can diffuse on the underlying crystal or grain towards energetically favored locations. Adatoms arriving at crystallographic planes with a high sticking coefficient, i.e. a high number of dangling bonds or nearest neighbors offered to an adatom, and high diffusion barriers will have a restricted diffusivity and have a very low probability to leave this crystallographic plane. These planes will therefore collect more material and will thus show an enhanced perpendicular growth rate compared to the other crystallographic planes. Crystallographic planes with a high perpendicular growth rate get extinguished during the growth process and the crystallite surface is faceted by planes of the lowest crystallographic growth rate (Figure 5.1c). As the adatom energies in this "zone" are too low to allow diffusion from one grain to another, no interaction, apart from shadowing effects, exists between neighboring crystals or grains. Therefore, the largest columns will only overshadow the smaller ones, but no preferential out-of-plane orientation will arise.

5.2.2. Zone T

During Zone T growth, the adatom energy is high enough such that the adatom is no longer restricted to a single grain, but can diffuse from one grain to another, i.e. interaction between neighboring crystals or grains is now enabled. In this case, the randomly out-of-plane oriented grains, all faceted by their planes of lowest perpendicular growth rate, will grow uniformly in thickness under influence of the arriving flux. However, the different orientations of the faceted grains with respect to the substrate surface lead to an anisotropy of the growth rate perpendicular to the substrate surface. The grains with the most tilted facets with respect to the substrate will grow the fastest in the direction perpendicular to the substrate surface. Therefore, besides the effect of geometric shadowing, this gives rise to an additional overgrowth mechanism, or competition, between grains. The grains with the geometrically fastest growing directions perpendicular to the substrate overgrow the other grains until only one crystallographic out-of-plane orientation survives the competition. Initially, a small grained structure (corresponding mainly to the nucleation density) exist in the near-substrate region of the film. As soon as the out-of-plane alignment is completed at the free surface, a clearly faceted V-shaped columnar structure with a well defined out-of-plane orientation arises (see Figure 5.1d). The mechanism of competitive growth is discussed in more detail in the following section 5.3.

5.2.3. Zone II

In Zone II, i.e. at even higher values for the adatom energy or substrate temperature, growth is no longer initiated by randomly orientated

crystallites, but certain orientations are preffered. Chemisorbed particles can become mobile and give rise to island ripening, cluster diffusion and grain-boundary migration. In case of grain coarsening, driven by minimization of the overall edge and surface energy, crystallites with an orientation which has a low surface energy exposed to the surface will consume crystallites with higher surface energies and a (partial) distribution of crystallites with a preferential orientation can arise. Driven by minimization of the grain-boundary energy, larger grains with low surface energies can grow at the expense of smaller grains with an unfavorable orientation. The average grain size increases uniformly in size but the grain-size distribution is expected to be a time-invariant, monomodal distribution, indicating a self-similar growth, i.e. one cannot discriminate between microstructures if the magnification is unknown. This is known by normal grain growth. The grain size distribution is often fitted to a log-normal distribution [18, 36, 44] or a Weibull distribution [46]. Whereas the microstructure in zone T is determined by kinetic principles, i.e. growth rates, the growth mode in Zone II is thermodynamically driven, i.e. under influence of energy minimization. In this case, no evolutionary V-shaped overgrowth will develop, neither will shadowing have an influence due to the rapid surface diffusion. The observed microstructure consists of a dense structure of parallel columns with the plane of lowest surface energy exposed at the surface (see Figure 5.1e).

5.3. Grain growth during thickening

During competitive (zone T) or restructuring (zone II) growth modes, grains can grow in size at the expense of others. However, as film properties are strongly related to the underlying microstructure, this means that the properties of a film vary during growth. Knowledge of how the grain size is expected to vary with the layer thickness is therefore essential for models describing for example stress-evolution [7, 13, 14] or the size-effect in thin film resistivity [29].

5.3.1. Competitive grain growth (Zone T)

As we discussed in the previous section, the microstructure of a thin film during competitive growth is the consequence of an overgrowth mechanism between the initial set of crystallographic orientations originated on the surface during the nucleation phase [4]. Competitive polycrystalline growth can be viewed as a two-dimensional grain growth process in which the boundaries are mobile only at the surface of the film, and the mobility of the boundaries is related to the adatom diffusivities as well as to the time during which the adatoms can move before being buried by newly arriving adatoms [45]. Van der Drift [49] proposed a geometrical model that describes the principle of overgrowth and crystallographic se-

lection. In the model, growth is initiated by different crystalline nuclei equidistantly placed with different orientations on a 1D axis, i.e. (1+1)-growth, or on a flat ground plane, i.e. (2+1)-growth. The competition between crystallographic orientations during (1+1)-growth starting from randomly-oriented equidistant (10)-faceted square crystals is illustrated in Figure 5.2. The growth of the crystals is normal to their facets, with a growth rate which is equal for all facets and independent of the orientation. Van der Drift describes the increasing sharpness (V-shapes) during the vertical growth according to a principle of "evolutionary selection". The idea is that the vertical growth rates of the individual crystals, i.e. the rate at which the highest point rises, depend on their orientation with respect to the substrate surface. The bigger the vertical growth rate, the greater the probability for survival, or as stated by van der Drift "survival of the fastest". Therefore only a few favored orientations will remain at the surface, while others die out, hence the "evolutionary selection". Indeed, the crystals whose tops are pointing more or less normal to the surface will persist longer at the surface than those pointing in less favorable directions [42]. This is easily understood as, in the direction of a corner, the growth velocity of a square is by a factor $\sqrt{2}$ greater than in the direction perpendicular to a face. This preferentially rapid lateral growth will be further accentuated by a higher mobility of the atoms (or in effect a higher surface temperature) on such normally disposed faces, because these faces have the highest rate of arrival of energy per unit area from the incident atoms [12]. Because of evolutionary selection, a preferential orientation of the fastest growing crystallites develops [53]. Although a simplification of reality, the principle of evolutionary selection allows to predict the morphology of the film and the expected preferred orientations [53] which survive at the surface.

The Van der Drift model is however a geometrical selection model, initiated from clearly defined shaped crystallites placed in different orientations. In reality, the growth is rather initiated from clusters of atoms with a given crystallographic orientation but no definite geometrical shape. An atomistic view on competitive texture evolution is proposed by Gall et al. [15]. The model describes the transition from 111 to 001 texture observed in reactive sputter deposition of TiN under influence of incident low-energy (20 eV) N_2^+-ions. As this description offers a different perspective on competitive growth, a short description is given. During the initial growth stage of TiN, mainly 001- and 111-oriented grains nucleate with approximately equal number densities. For TiN, the 001 orientation corresponds to the lowest surface energy. Therefore, under growth conditions where thermodynamics rather than kinetics control texture formation, e.g. at high T_s/T_M, [001] is expected to be the dominant growth orientation. In most cases however, texture formation is controlled by kinetics. As the TiN(111) is always fully terminated by N, a Ti adatom can form strong N backbonds, and thus has a low surface mobility. The

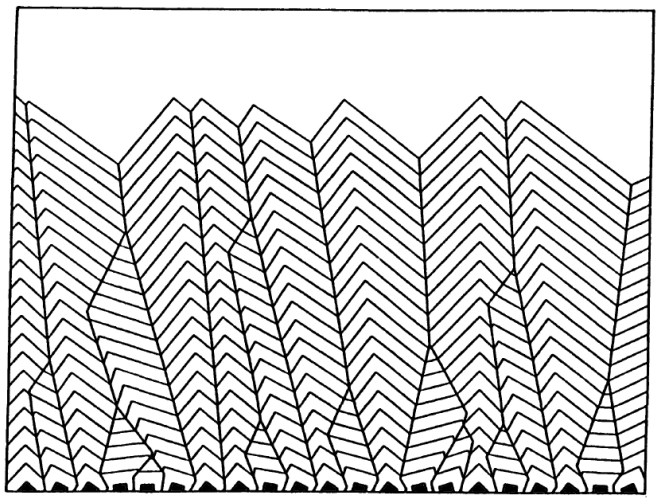

Figure 5.2. *(1+1) growth of randomly oriented cubic crystallites. The growth rates perpendicular to the facets are equal. Figure taken from [8].*

TiN(001) surface has only negligible nitrogen coverage and a high adatom mobility. The Ti adatoms on the (001) surface can nucleate with another Ti adatom or attach to an already existing TiN island. A significant part of the adatoms however will reach and cross the grain boundary towards the (111) surface after which their mobility is restricted. A net material flux thus flows from the (001) surface towards (111) surface, and thus the (111) surface grains grow at the expense of the (001) surface. The width of the [001] oriented grains decreases with layer thickness and the layer evolves towards a strong [111] preferred orientation. In case of incident low-energy N_2^+-ions on the surface, atomic nitrogen is present on the (001) surface due to the collisional dissociation of the ion. Ti adatoms are now more likely to form TiN bonds before reaching the grain boundary. Due to a change in the chemical potential of the surface, the Ti adatoms are more stable on the (001) surface in the presence of atomic nitrogen, and the [001] oriented grains will grow at the expense of the [111] oriented grains.

In comparison to the Van der Drift model, both texture evolution mechanisms depend on an overgrowth selection by growth anisotropy of crystallographic orientations. In the Van der Drift model, crystals oriented with tops normal to the surface are favored as the growth velocity in the direction of the top of the crystal is a factor $\sqrt{2}$ greater than in the direction perpendicular to a crystallographic face. The model proposed by Gall on the other hand describes a net material flux of adatoms crossing the grain boundaries towards adjacent crystallographic surfaces driven by a difference in chemical potential of the respective surfaces. In both cases however, the anisotropy in the normal growth rate of different crystal-

lographic planes favors a preferential crystallographic orientation as the film thickens. As can be observed in Figure 5.2, the average grain size related to the preferred out-of-plane orientations (in fact monocrystalline domains) increases with increasing layer thickness. The average lateral size of the domains D is determined by the number of crystals N surviving at the surface by $N \sim D^{-\alpha}$ for the (α+1) dimensional model, i.e. α=1 in the case of a line, i.e. (1+1), or α=2 in the case of a plane (2+1). Kolmogorov [23], who first envisioned the problem of evolutionary selection, predicted based on an analytical model that $D \sim t^{\alpha}$, with a value for the growth exponent α of 1/2 for both (1+1) and (2+1) growth. The same problem was also analyzed by Thijssen [43] who confirmed the exponent α=1/2 for the (1+1) growth, but found a growth exponent of 0.4 for the case of (2+1) growth. This latter exponent was also found by Ophus [32] with his analytical model for (2+1) growth. Computer simulations based on the Van der Drift model confirm these exponents. The exponent $\alpha = 1/2$ for (1+1) growth was confirmed by simulations of Dammers and Radelaar [8], and Paritosh [40], whereas the exponent $\alpha = 0.4$ for (2+1) growth could be confirmed by 3D simulations of Thijssen [42] and Smereka [39]. Even more examples can be found in the work of Thompson [44, 45].

5.3.2. Normal grain growth (Zone II)

The driving force for normal grain growth is the reduction in energy associated with a decrease in grain-boundary area. Individual grain-boundaries move towards their centers of curvature in order to reduce the boundary length and thus the total grain-boundary energy [9]. Grains larger than the average size grow, while smaller grains shrink. The grain boundary velocity is proportional to the curvature of the grain. When grain boundary energy reduction alone drives grain growth, it is expected that the rate of normal growth or the grain boundary velocity is given by (for an individual grain) [16]

$$\frac{d\bar{r}}{dt} \propto \bar{m}\bar{\gamma_{gb}}\Delta\kappa = \bar{m}\bar{\gamma}_{gb}\left(\frac{1}{\bar{r_{cr}}} - \frac{1}{\bar{r}}\right) \tag{5.8}$$

where $\bar{r}$ is the average in-plain grain radius, $\bar{r}_{cr}$ the critical grain radius $\kappa = \frac{1}{\bar{r}}$ the net curvature given by the inverse of the grain radius, $\bar{m}$ the average grain boundary mobility and $\bar{\gamma}_{gb}$ is the average grain boundary energy. Therefore, the incentive for grain boundary migration is inversely proportional to the size of the grain. If a grain has a radius smaller than the critical radius, i.e. $\bar{r} < \bar{r}_{cr}$, we find $\frac{d\bar{r}}{dt} < 0$ and thus the grain shrinks while other grains grow. From equation (5.8), it is thus expected that the average grain radius $\bar{r}$ will increase as:

$$\bar{r} \sim t^{1/2} \tag{5.9}$$

This kinetic power-law is also found for Monte Carlo simulations of both two- and three-dimensional grain growth during isothermal annealing [3]. For a film grown at constant deposition rate, the increase in thickness is proportional with time. The average grain size is thus expected to scale with the layer thickness as $D \sim h^{1/2}$. This scaling law is analoguous to the scaling expected for competitive growth. However, both approaches differ in nature. Normal grain growth is an energy-driven time effect, whereas competitive grain growth is a growth-driven thickness effect. An abundant source of analytical and computational approaches yielding this same result for normal grain growth, i.e. $D \sim t^{1/2}$, is given in the work of Thompson [46], describing grain growth and evolution of cellular structures in general, such as magnetic domains (Ising model for two crystallographic orientations), soaps froths or foams.

5.3.3. Experimental verification in thin films

The models described above which correlate film thickness with grains size are quite often only based on computational models but ample experimentally verified. Although our results (see further) confirm these trends, they are not a proof of the generality of the aforementioned models due

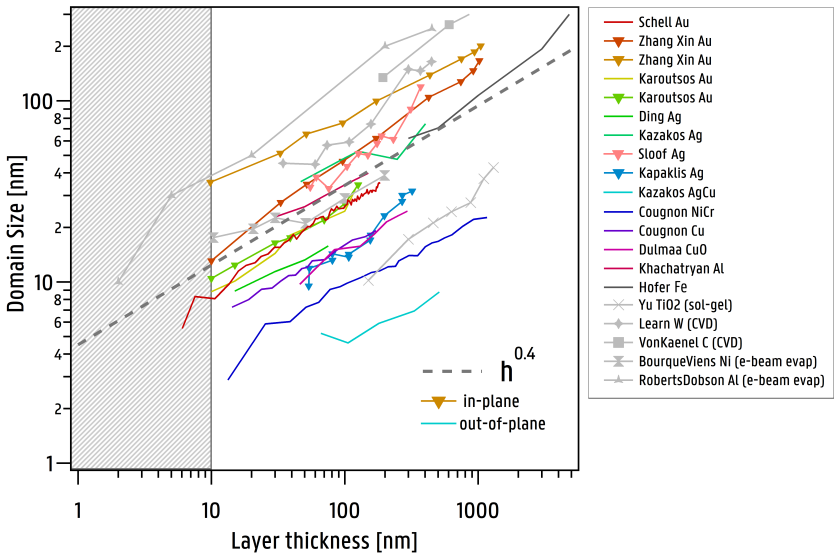

Figure 5.3. *Overview of experimental data (Cu and NiCr) and literature data for the grain growth during thicknening for films deposited with techniques. The colored lines represent deposition performed by sputtering, the gray lines are depositions performed with another technique as specified in the legend. The gray dotted line represents the prediction from theory, i.e.* $D \sim h^{0.4}$.

Table 5.1. *Overview of literature study and own experiments related to the variation in domain size with layer thickness*

Reference	Material	Method	T_s	annealed	Analysis	Orientation	Exponent	range	points
[37]	Au	sputtering	-30V	no	in-situ XRD	out-of-plane	0.44 ± 0.01	10 - 185	65
[54]	Au	sputtering	RT	no	AFM	in-plane	0.52 ± 0.02	10 - 1000	9
[54]	Au	sputtering	RT	300°C	AFM	in-plane	0.38 ± 0.01	10 - 1000	9
[20]	Au	sputtering	RT	no	STM	in-plane	0.48 ± 0.05	10 - 127	7
[20]	Au	sputtering	RT	no	XRD	out-of-plane	0.54 ± 0.07	10 - 127	6
[10]	Ag	sputtering	RT	no	XRD	out-of-plane	0.35 ± 0.02	15 - 75	4
[21]	Ag	sputtering	RT	no	XRD	out-of-plane	0.30 ± 0.10	35 - 75	5
[19]	Ag	sputtering	RT	no	XRD AFM	both	0.67 ± 0.04	50 - 350	12
[21]	AgCu	sputtering	RT	no	XRD	out-of-plane	0.58 ± 0.01	60 - 500	5
This work	Cu	sputtering	RT	no	XRD	out-of-plane	0.39 ± 0.01	14 - 170	15
[11]	CuO	sputtering	RT	no	XRD	out-of-plane	0.48 ± 0.04	50 - 300	7
This work	NiCr	sputtering	RT	no	XRD	out-of-plane	0.38 ± 0.01	13 - 1168	24
[22]	Al	sputtering	RT	no	XRD	out-of-plane	0.36 ± 0.02	30 - 150	5
[17]	Mo	sputtering	200 °C	no	XRD	out-of-plane	0.64 ± 0.07	300 - 5000	5
[38]	Fe	sputtering	RT	no	SEM	in-plane	0.73 ± 0.08	55 - 370	11
[35]	Al	e-beam evaporation	RT	no	TEM	in-plane	0.47 ± 0.06	2 - 450	5
[5]	Ni	e-beam evaporation	RT	no	SEM	out-of-plane	0.29 ± 0.04	10 - 199	6
[27]	W	CVD	300 - 400°C	no	TEM	in-plane	0.64 ± 0.07	30 - 450	8
[52]	C	CVD	850°C	no	SEM	in-plane	0.50 ± 0.03	200 - 10000	7
[55]	TiO_2	sol-gel	RT	500°C	XRD + TEM	combi?	0.66 ± 0.07	150 - 1300	7

to a lack of statistics. Indeed, the low amount of data and the restricted number of materials undermine the general applicability of these models. Therefore a different approach based on a dedicated literature study was performed to further test the proposed models. Table 5.1 shows the collected data for films deposited by different techniques such as sputtering, evaporation, CVD and sol-gel and both in-plane and out-of-plane measurements of the grain size. The data were fitted to a power-law $D = A\,t^{\alpha}$ within the specified thickness range and the resulting exponents are tabulated in Table 5.1. Depositions with a layer thickness smaller than 10 nm are excluded from the fitting procedure as it is not sure if this involves continuous films. Also data sets with less than 4 datapoints were not included in the analysis. When an error-weighted average of the exponents α is taken only for the data of sputter deposited metallic films, we find $\alpha = 0.449 \pm 0.001$. When the same procedure is applied for the non-sputter deposited films, i.e. 5 data sets including e-beam evaporation, CVD, and sol-gel (see Table 5.1), an exponent $\alpha = 0.485 \pm 0.010$ is found.

5.4. Conclusion

A thorough overview of the microstructural evolution of sputter deposited films from the early stage of nucleation to the stage of film thickening is given. In this context, structure zone models were discussed in order to demonstrate how the microstructure or film morphology is affected and classified into zones depending on the deposition conditions during growth. Finally, the topic of grain growth during the film thickening is treated. As the grain size is observed to increase with increasing film thickness, many film properties will be thickness-dependent. A literature study in search of different thickness-dependent grain sizes was performed. In general, the quantitative behavior of all data is very similar and show a power-like behavior. When only sputter-deposited films were considered, the grain size was observed to increase with the layer thickness as $D \sim h^{\alpha}$, with $\alpha = 0.449 \pm 0.001$. The exponent found for the non-sputter deposited films was comparable and given by 0.485 ± 0.010. These observations are also in agreement with theoretical predictions. In the upcoming chapters 7 and 8, the importance of the domain size on some thin film properties is demonstrated. In this light, the description of the thickness dependency of the domain size is essential knowledge.

References

[1] JG Amar and F Family, Critical cluster size: Island morphology and size distribution in submonolayer epitaxial growth, MRS Online Proceedings Library Archive **367** (1994).

[2] A Anders, A structure zone diagram including plasma-based deposition and ion etching, Thin Solid Films **518** (2010), no. 15, 4087–4090.

[3] MP Anderson, GS Grest, and DJ Srolovitz, Computer simulation of normal grain growth in three dimensions, Philosophical Magazine B **59** (1989), no. 3, 293–329.

[4] PB Barna and M Adamik, Fundamental structure forming phenomena of polycrystalline films and the structure zone models, Thin solid films **317** (1998), no. 1-2, 27–33.

[5] A Bourque-Viens, V Aimez, A Taberner, P Nielsen, and PG Charette, Modelling and experimental validation of thin-film effects in thermopile-based microscale calorimeters, Sensors and Actuators A: Physical **150** (2009), no. 2, 199–206.

[6] DD Chambliss and KE Johnson, Nucleation with a critical cluster size of zero: Submonolayer Fe inclusions in Cu (100), Physical Review B **50** (1994), no. 7, 5012.

[7] E Chason, AM Engwall, Z Rao, and T Nishimura, Kinetic model for thin film stress including the effect of grain growth, Journal of Applied Physics **123** (2018), no. 18, 185305.

[8] AJ Dammers and S Radelaar, Two-dimensional computer modelling of polycrystalline film growth, Texture, Stress, and Microstructure **14** (1991), 757–762.

[9] R Dannenberg, E Stach, and JR Groza, Phenomenological description of grain growth stagnation for nanocrystalline films and powders, Journal of Materials Research **16** (2001), no. 4, 1090–1095.

[10] G Ding and C Clavero, Silver-Based Low-Emissivity Coating Technology for Energy- Saving Window Applications, Modern Technologies for Creating the Thin-film Systems and Coatings, InTech, mar 2017.

[11] A Dulmaa, H Vrielinck, S Khelifi, and D Depla, Sputter deposition of copper oxide films, Applied Surface Science **492** (2019), 711–717.

[12] PK Dutta and H Wilman, Crystal growth and orientations in vacuum-condensed silver films and their systematic dependance on the residual air pressure, film thickness, rate of deposition and substrate temperature, Journal of Physics D: Applied Physics **3** (1970), no. 6, 839.

[13] AM Engwall, Z Rao, and E Chason, Origins of residual stress in thin films: Interaction between microstructure and growth kinetics, Materials & Design **110** (2016), 616–623.

[14] ———, Residual Stress in Electrodeposited Cu Thin Films: Understanding the Combined Effects of Growth Rate and Grain Size, Journal of The Electrochemical Society **164** (2017), no. 13, D828–D834.

[15] D Gall, S Kodambaka, MA Wall, I Petrov, and JE Greene, Pathways of atomistic processes on TiN(001) and (111) surfaces during film growth: anab initiostudy, Journal of Applied Physics **93** (2003), no. 11, 9086–9094.

[16] M Hillert, On the theory of normal and abnormal grain growth, Acta metallurgica **13** (1965), no. 3, 227–238.

[17] AM Hofer, J Schlacher, J Keckes, J Winkler, and C Mitterer, Sputtered molybdenum films: Structure and property evolution with film thickness, Vacuum **99** (2014), 149 – 152.

[18] M Huang, Y Wang, and YA Chang, Grain growth in sputtered nanoscale PdIn thin films, Thin Solid Films **449** (2004), no. 1-2, 113–119.

[19] V Kapaklis, P Poulopoulos, V Karoutsos, T Manouras, and C Politis, Growth of thin Ag films produced by radio frequency magnetron sputtering, Thin Solid Films **510** (2006), no. 1-2, 138–142.

[20] V Karoutsos, M Toudas, A Delimitis, S Grammatikopoulos, and P Poulopoulos, Microstructural evolution in nanostructured gold films, Thin Solid Films **520** (2012), no. 11, 4074–4079.

[21] AM Kazakos, DE Fahnline, R Messier, and LJ Pilione, Compositional dependence of grain size in silver copper alloys prepared by direct current magnetron sputtering, Journal of Vacuum Science & Technology A: Vacuum, Surfaces, and Films **10** (1992), no. 6, 3445–3450.

[22] H Khachatryan, SN Lee, KB Kim, and M Kim, Deposition of Al Thin Film on Steel Substrate: The Role of Thickness on Crystallization and Grain Growth,

Metals **9** (2019), no. 1, 12.
[23] A. N. Kolmogorov, Geometric selection of crystals, Doklady Akad Nauk Minerologia USSR (1976).
[24] M Kotrla, J Krug, and P Šmilauer, Submonolayer epitaxy with impurities: Kinetic Monte Carlo simulations and rate-equation analysis, Physical Review B **62** (2000), no. 4, 2889.
[25] _____, Effects of mobile and immobile impurities on two-dimensional nucleation, Surface science **482** (2001), 840–843.
[26] J Krug, Scaling regimes for second layer nucleation, The European Physical Journal B-Condensed Matter and Complex Systems **18** (2000), no. 4, 713–719.
[27] AJ Learn and DW Foster, Resistivity, grain size, and impurity effects in chemically vapor-deposited tungsten films, Journal of applied physics **58** (1985), no. 5, 2001–2007.
[28] S Mahieu, P Ghekiere, D Depla, and R De Gryse, Biaxial alignment in sputter deposited thin films, Thin Solid Films **515** (2006), no. 4, 1229–1249.
[29] AF Mayadas and M Shatzkes, Electrical-resistivity model for polycrystalline films: the case of arbitrary reflection at external surfaces, Physical review B **1** (1970), no. 4, 1382.
[30] YW Mo, J Kleiner, MB Webb, and MG Lagally, Activation energy for surface diffusion of Si on Si (001): A scanning-tunneling-microscopy study, Physical review letters **66** (1991), no. 15, 1998.
[31] BA Movchan and AV Demchishin, structure and properties of thick condensates of nickel, titanium, tungsten, aluminum oxides, and zirconium dioxide in vacuum, Fiz. Metal. Metalloved. 28: 653-60 (Oct 1969). (1969).
[32] C Ophus, EJ Luber, and D Mitlin, Analytic description of competitive grain growth, Physical Review E **81** (2010), no. 1, 011601.
[33] C Ratsch and JA Venables, Nucleation theory and the early stages of thin film growth, Journal of Vacuum Science & Technology A: Vacuum, Surfaces, and Films **21** (2003), no. 5, S96–S109.
[34] C Ratsch, A Zangwill, P Šmilauer, and DD Vvedensky, Saturation and scaling of epitaxial island densities, Physical review letters **72** (1994), no. 20, 3194.
[35] S Roberts and PJ Dobson, The microstructure of aluminium thin films on amorphous SiO2, Thin solid films **135** (1986), no. 1, 137–148.
[36] F Ruffino, MG Grimaldi, C Bongiorno, F Giannazzo, F Roccaforte, V Raineri, and C Spinella, Normal and abnormal grain growth in nanostructured gold film, Journal of Applied Physics **105** (2009), no. 5, 054311.
[37] N Schell, T Jensen, JH Petersen, KP Andreasen, J Bøttiger, and J Chevallier, The nanostructure evolution during and after magnetron deposition of Au films, Thin Solid Films **441** (2003), no. 1-2, 96–103.
[38] NR Shamsutdinov, WG Sloof, and AJ Böttger, A method for the experimental determination of surface photoemission core-level shifts for 3d transition metals, Journal of applied physics **98** (2005), no. 1, 014908.
[39] P Smereka, X Li, G Russo, and DJ Srolovitz, Simulation of faceted film growth in three dimensions: microstructure, morphology and texture, Acta Materialia **53** (2005), no. 4, 1191–1204.
[40] DJ Srolovitz, CC Battaile, X Li, JE Butler, et al., Simulation of faceted film growth in two-dimensions: microstructure, morphology and texture, Acta Materialia **47** (1999), no. 7, 2269–2281.
[41] LH Tang, Island formation in submonolayer epitaxy, Journal de Physique I **3** (1993), no. 4, 935–950.
[42] JM Thijssen, Simulations of polycrystalline growth in 2+ 1 dimensions, Physical Review B **51** (1995), no. 3, 1985.
[43] JM Thijssen, HJF Knops, and AJ Dammers, Dynamic scaling in polycrystalline growth, Physical Review B **45** (1992), no. 15, 8650.
[44] CV Thompson, Grain growth in thin films, Annual review of materials science **20** (1990), no. 1, 245–268.
[45] _____, Structure Evolution During Processing of Polycrystalline Films, Annual Review of Materials Science **30** (2000), no. 1, 159–190.
[46] _____, Grain growth and evolution of other cellular structures, Solid State Physics, vol. 55, Elsevier, 2001, pp. 269–314.

[47] CV Thompson and R Carel, Texture development in polycrystalline thin films, Materials Science and Engineering: B **32** (1995), no. 3, 211–219.
[48] JA Thornton, Influence of apparatus geometry and deposition conditions on the structure and topography of thick sputtered coatings, Journal of Vacuum Science and Technology **11** (1974), no. 4, 666–670.
[49] A Van der Drift, Evolutionary selection, a principle governing growth orientation in vapour-deposited layers, Philips Res. Rep **22** (1967), no. 3, 267.
[50] JA Venables and GDT Spiller, Nucleation and growth of thin films, Surface Mobilities on Solid Materials, Springer, 1983, pp. 341–404.
[51] J Villain, A Pimpinelli, L Tang, and D Wolf, Terrace sizes in molecular beam epitaxy, Journal de Physique I **2** (1992), no. 11, 2107–2121.
[52] Y Von Kaenel, J Stiegler, E Blank, O Chauvet, Ch Hellwig, and K Plamann, Microstructure evolution and defect incorporation in highly oriented and textured CVD diamond films, physica status solidi (a) **154** (1996), no. 1, 219–238.
[53] Ch Wild, N Herres, and P Koidl, Texture formation in polycrystalline diamond films, Journal of Applied Physics **68** (1990), no. 3, 973–978.
[54] Z Xin, S Xiao-Hui, and Z Dian-Lin, Thickness dependence of grain size and surface roughness for dc magnetron sputtered Au films, Chinese Physics B **19** (2010), no. 8, 086802.
[55] J Yu, X Zhao, and Q Zhao, Effect of film thickness on the grain size and photocatalytic activity of the sol-gel derived nanometer TiO2 thin films, Journal of materials science letters **19** (2000), no. 12, 1015–1017.

This page was intentionally left blank.

6 Impurities

When an uncured composite is introduced in a vacuum, the background pressure is severely affected due to the desorption of different species originating from the composite substrate, a process referred to as outgassing. One of the main reasons why thin film growth is preferentially performed at high vacuum is to reduce the presence of unwanted species or impurities during growth, as they can have a detrimental effect on the film properties. Therefore, especially in light of embedded sensor design, a quantified approach for the effect of impurities on the thin film growth is indispensable in order to properly evaluate the feasibility of the deposition of thin films with envisaged properties on a composite substrate. In this chapter, the outgassing products related to the presence of a composite in the vacuum chamber are determined, and fundamental insights on the influence of impurities on thin film growth are provided based on theoretical, experimental and computational results.

6.1. Introduction

Impurities are species present in the vacuum chamber that differ from the intended species. Examples are water molecules that desorb from the chamber walls, nitrogen and oxygen molecules entering the chamber through a vacuum leak, or unintended elements in the target [62, 72]. Impurities can also already be present on the substrate due to insufficient cleaning. Foreign atoms, or impurities, can affect the film growth on several levels. As an example, Figure 6.1 presents a beautiful visualization of the effect of surface contaminants, here accidentally applied body grease on a clean Mo_2S substrate, on the nucleation and growth of Au crystals. Clearly faceted Au crystals grow on the clean surface. On the contaminated surface however, as presented by the contoured area in Figure 6.1, the nucleation density is much higher and the randomly oriented crystals

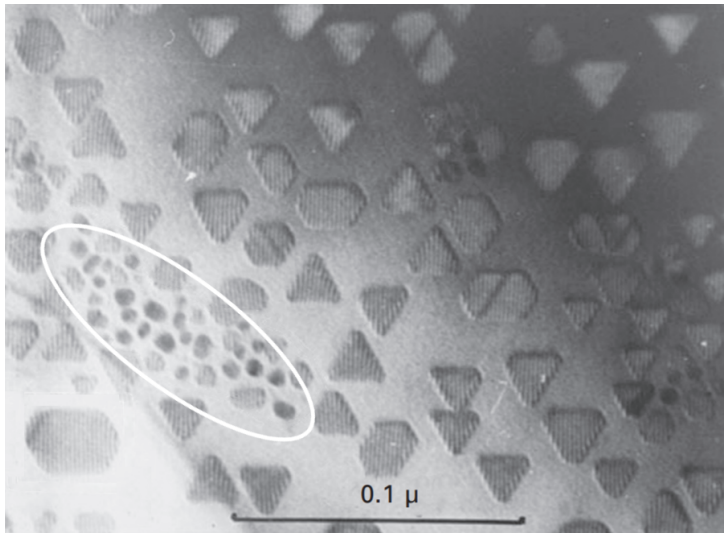

Figure 6.1. *Effect of substrate surface contamination (body grease) on the nucleation and growth of Au crystals on MoS_2 (0002) crystal face. Faceted Au crystals are grown on a clean surface with coherent epitaxial orientation as indicated by Moiré fringes. On the contaminated surface, the nucleation density is higher and the randomly oriented crystals have a rounded shape. Figure adapted from the work of P. Barna and G. Radnóczi [12].*

have a rounded shape. Given the high deposition rates used during magnetron sputtering, order 1 nm/s or 2 to 10 monolayers per second, surface contaminants are of a lesser concern compared to the continuous presence of gaseous impurities during growth. The residual background pressure in vacuum chambers for thin film deposition varies typically in the range of 1×10^{-7} Pa up to 1×10^{-3} Pa. The degree of vacuum obtained within a fixed time frame depends mainly on the volume of the chamber, the pumping equipment, the type of vacuum sealing, and the amount of outgassing from the chamber. Outgassing originates from impurities - mainly water vapor H_2O - trapped in porosities or accumulated as adsorbed monolayers on the chamber walls. Dealing with outgassing is mostly done by baking-out the vacuum system prior to deposition and to work in air-conditioned laboratories. During a bake-out, the pores of the vacuum chamber are thermally expanded under ohmic heating of the baking ribbons. As such the trapped impurities can be removed by the pump and do not gas-out during deposition. Heating the chamber walls requires copper sealing rings as rubber rings could melt. Compared to rubber sealings, also called *quick* or *klein* flanges (QF/KF), copper sealings or "ConFlat" flanges, also improve the vacuum as they do not allow water permeation. They are however less practical in usage, and more expensive. For applications in micro-electronics and more, many precautions, such as a clean rooms, are

taken to prevent impurities to interfere. As the overall price and operation efficiency are greatly affected by the desired degree of vacuum per volume, the demands for 24/7 industrial exploitation of thin film applications are barely reconcilable with maintaining coaters at high quality vacuum.

6.2. Impurities during film growth

The most abundant species present in the residual gas at a pressure of 1×10^{-4} Pa, as measured by mass spectrometry (see Figure 6.2), are H_2O, OH, H_2, N_2, and CO_2. When a leak is present in the system, there is mainly an increase of N_2 and O_2, reflecting of course the composition of the atmospheric air. As shown in Figure 6.2, the presence of a 5-layer prepreg laminate substrate ($6 \times 27 \times 0.1$ cm^3) into the vacuum chamber causes a strong increase of water vapor into the chamber (≈ 0.125 m^3). Although the prepreg was taken out of storage at -18 °C and left for over an hour to acclimatize, the water vapor is most likely the result of traces of condensation and adsorbed gases. Indeed, similar results are obtained in a study on the outgassing of cured (fiber-reinforced) epoxy resins in vacuum as measured by an electrobalance [19]. The authors report on a decreasing weight loss of the vacuum-exposed epoxy sample with time. A second vacuum exposure of the sample, after again nine days of exposure to the air, showed an identical weight loss. According to the authors, this indicates that the origin of the outgassing products are ad- or absorbed gases. Similar to our measurement presented in Figure 6.2, the outgassing

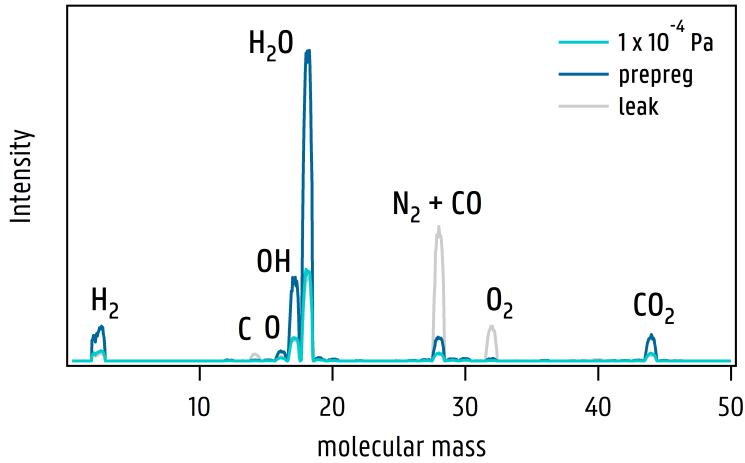

Figure 6.2. *Residual gas analysis for a background pressure of 1×10^{-4} Pa, a vacuum with a prepreg substrate introduced and a leak of atmospheric gas into the vacuum chamber. The vacuum chamber had a total volume of 0.125 m^3 and was sealed by means of rubber O-rings.*

products were identified by mass spectrometry measurements as mainly water vapor and small amounts of nitrogen, oxygen and carbon dioxide. H_2O is the main source of the H_2 and OH species present in the chamber [32, 74, 76]. The presence of these species during deposition will effectively influence the microstructure and film properties [32, 47, 75, 78, 86, 90]. As an example, Schneider et al. studied the effect of hydrogen on the growth of strontium titanate [75] and on the elastic properties of alumina thin films [76]. The results indicated that the hydrogen incorporation [74] is decisive for the composition and microstructure of the films. A more thorough study on the solubility of hydrogen in metals and alloys is found in Ref. [87]. CO_2, O_2 and N_2 are known to have high dissociation energies and are therefore less likely to chemisorb on the surface. However, during magnetron sputtering, these gas molecules can gain energy from the plasma and overcome the dissociation energy upon impact on the substrate. Also dissociation in the discharge will contribute to the flux of atomic species to the growing film surface. Atomic oxygen and nitrogen are now present on the surface. Because of their high reactivity, these species are very likely to chemisorb on the substrate surface. The effect of gaseous impurities, mainly oxygen and nitrogen, on thin film growth is a broadly studied topic. Starting from the nucleation process they influence the microstructural development and macroscopic properties. In what follows, a far from complete overview of different impurity-related studies on film growth and properties is given.

6.2.1. Literature overview of impurity-related studies

Barna and co-workers performed a dedicated study on the growth of evaporated aluminum thin films in the presence of oxygen [3–5, 8, 9, 11], resulting in a revised structure zone model for evaporated films. They discuss the influence of oxygen as an impurity and describe a change in the film texture together with a decrease in grain size as function of an increasing oxygen pressure. Similar effects were demonstrated by the same research group during the growth of TiN thin films [15] (see section 6).
Riedl et al. [72] studied the influence of oxygen impurities on the growth morphology and structure of TiAlN coatings. The oxygen impurity content was varied by three different routes: by the oxygen impurities contained in the target, by the residual background pressure in the system, and by adapted deposition conditions such as the deposition rate. A transition in preferred growth orientation occured from a small grain-sized random distribution at low impurity content to a pronounced [111] orientation with large grains at highest oxygen content ($\sim$1.3 at.%). Atomic probe tomography (APT) measurements showed that the oxygen impurities are rather homogeneously distributed in the film without any detectable concentration at grain boundaries.
Ghekiere et al. studied the growth of Cr under the presence of nitrogen

and oxygen impurities [58]. A strong similarity of the influence of nitrogen and oxygen on the film texture was reported.
Liu et al. [56] proposed a method for the deposition of stable β-W using N_2 as impurity gas. Molecules of the impurity gas are adsorbed on the substrate surface and act as nucleation sites for the growth of β-W. In areas free of nitrogen, large grained α-W grows ($\pm$ 70 nm). For increasing nitrogen coverage, the authors report a stronger contribution of β-W which is small grained (approx. 4 nm).
Chowdhury et al. [26] and Takahashi et al. [61] studied the influence of oxygen impurities on the magnetic properties of permalloy and Co/Cu films respectively. Dramatic changes in the magnetic properties are reported due to a reduction in grain size with increasing oxygen partial pressure. Coughlin et al. [27] showed how small additions of nitrogen or air leaked into the vacuum system induced a transformation from the hcp to the fcc crystallite phase for the growth of Co/Cr films and destroyed the magnetic anisotropy in the film. It was shown that very low background pressures were needed in order to obtain good orientation of the hcp c-axes normal to the film surface. A number of papers [18, 48, 66, 79] also report on changes of the intrinsic film stress as a function of the impurity content. Besides magnetic properties or stress, also (thermo-)electrical properties [18, 20, 91] are severely affected by the presence of impurities during thin film growth. This topic will be thoroughly discussed in Chapters 7 and 8.

In contrast to the detrimental effects contaminants can have on the film growth, they can also be used as a tuning mechanism to select desired thin film properties. For example Yu et al. [89] have shown that the film stress can be controlled by the impurity content. The improvement of the mechanical properties of high entropy alloys grown in a controlled contaminated environment was shown by Braeckman et al. [16, 17]. Other examples where impurities can act as beneficial tuning mechanisms are demonstrated by Gu et al. [40] for diffusion barrier applications, by Lee and Barabási [53] to control the spatial ordering of islands, or by Wu [88] to enhance nucleation. Firstov et al. [33] studied the hardness of Ti thin films as a function of the oxygen and nitrogen impurity content. The hardness of nanocrystalline films with a small content of oxygen ($\leq$2 at.%) and nitrogen ($\leq$1 at.%) remained approximately the same as for films deposited in a pure environment. A significant increase of the hardness however was observed from $\sim$4 to $\sim$10 GPa for an increase in oxygen/nitrogen content up to $\sim$6 at.%, as the average grain size decreased from $\sim$85 nm to $\sim$20 nm. A similar observation of an increase in hardness of evaporated Al films with increasing oxygen content was done by Barna et al. [10]. These results are in accordance with the Hall-Petch relation [41, 67] which describes the increased hardness of films with smaller grains, i.e. grain-refinement strengthening. The increased hardness of nanocrystalline met-

als is commonly explained by suppression of the dislocation activity with grain size reduction below ∼100 nm [33, 64, 73].

6.2.2. The impurity-to-metal impingement flux ratio

The enormous amount of available literature demonstrates the importance and wide-spread interest of the effects of impurities on thin film growth. Despite the beneficial tuning mechanisms described above, impurities generally have a degrading impact on the overall quality of the thin film and are undesired for many applications. Thin film growth is therefore often studied under ultra high vacuum conditions with base pressures lower than 1×10^{-5} Pa. From the perspective of the adatom however, the effective impurity level during growth should be evaluated by the amount of impurities as "seen" by the diffusing adatom, rather than just by the base pressure. Otherly stated, the amount of impurities impinging on the substrate per metal atom arriving on the particle is the parameter of interest to properly evaluate the base pressure. As the residual gas is uniformly distributed in the vacuum chamber, any surface present in the vacuum chamber experiences a continuous impingement flux of residual gas species. To calculate the impurity impingement flux F_i based on the measured background pressure, the following expression can be used

$$F_i = \sum_i \frac{z_i P_i}{\sqrt{2\pi m_i kT}} \qquad [\frac{atoms}{m^2 s}] \tag{6.1}$$

where P_i, z_i and m_i refer respectively to the partial pressure (in Pa), the stoichiometry, and the atomic mass of gas species i (in kg). The material flux F_m can be calculated as described by equation (4.4). The ratio between the impurity and metal impingement fluxes on the substrate is then given by

$$\tau = \frac{F_i}{F_m} \tag{6.2}$$

At a background pressure of around 1×10^{-5} Pa, and with the deposition rate during magnetron sputter deposition of metals and alloys in the range of 1 nm.s^{-1} or 1×10^{16} atoms cm^{-2} s^{-1} (see Chapter 3), τ is in the order of 0.01. For practical applications, i.e. in industrial vacuum systems, these conditions are often not reached, and the ratio τ will increase to 0.1.

As it was shown in Chapter 4, the average energy per arriving particle mainly depends on the target-to-substrate distance. In order to restrict the heat load towards the prepreg-substrate during deposition, and improve the uniformity in layer thickness, larger target-to-substrate values are preferred. However, when the target-to-substrate distance is increased, the material flux decreases (see Chapter 4), and thus the impurity-to-metal ratio τ increases in accordance to equation (6.2). Furthermore, τ is even more increased as the presence of the prepreg substrate

increases the background pressure due to the outgassing. Therefore, in order to develop a proper understanding of the film properties, it is important to study the influence of high τ values on the film growth.

6.3. Experiment

As discussed in the previous section, the presence of impurities due to the outgassing of the composite material, could have an influence on the envisaged properties of the embedded sensor. Therefore, we have studied the influence of impurities during the film growth of metals and alloys. To investigate the generality of the effect, additional elements and alloys were included in the study. With the same goal, the studied range for τ was taken quite large, i.e. between 0.01 and 10 or larger. More specific, four single elements systems (Al, Ag, Cr, and Cu) are studied together with two binary alloys ($Ni_{90}Cr_{10}$ and $Cu_{55}Ni_{45}$), and one complex alloy also known as a high entropy alloy (HEA) (CoCrCuFeNi). Colleague A. Dulmaa assisted in the numerous amount of depositions. The HEA series were deposited by colleague R. Dedoncker. To avoid any influence of the deposition system on the obtained results, the depositions were performed in three different vacuum chambers. A first chamber (volume: $0.021\,m^3$) was used for the HEA depositions, a second chamber (volume: $0.052\,m^3$) for Al, $Ni_{90}Cr_{10}$ and $Cu_{55}Ni_{45}$ depositions, and a third chamber (volume: $0.259\,m^3$) for all materials except the HEA. The residual gas pressure was each time lower than 5×10^{-4} Pa as measured by a Penning gauge. Two inch targets (Testbourne, purity 99.99%) were mounted on a home-built magnetron. Most depositions are performed at a constant argon pressure of 0.3 Pa, as measured with a capacitance gauge, while some series were deposited at 0.6 Pa. The silver depositions are performed at an argon pressure of 1 Pa. For all materials, series at constant current of 0.3 A and 0.6 A were performed. Only for the high entropy alloy, one series was performed at constant current (0.3 A) with increasing impurity flux, while another series was deposited at constant impurity flux but with increasing discharge current (range 0.04 A-0.69 A) and at an argon pressure of 1 Pa. The films were deposited on RCA cleaned silicon (100) substrates. For all materials two series with a film thickness of 100 nm and 300 nm were deposited (except the HEA had only one 300 nm series). The metal flux F_m was determined based on the measured thickness, film density and the deposition time (see Chapter 4). The deposition rate was approximately 1 $nm.s^{-1}$ for all materials, with exception of Ag with a deposition rate of 2 $nm.s^{-1}$. The impurity flux was controlled according to the following procedure. Before the magnetron discharge was ignited, atmospheric air was leaked into the chamber using a leak valve (Pfeiffer vacuum EVN 116) until a given pressure was reached. As atmospheric air was leaked

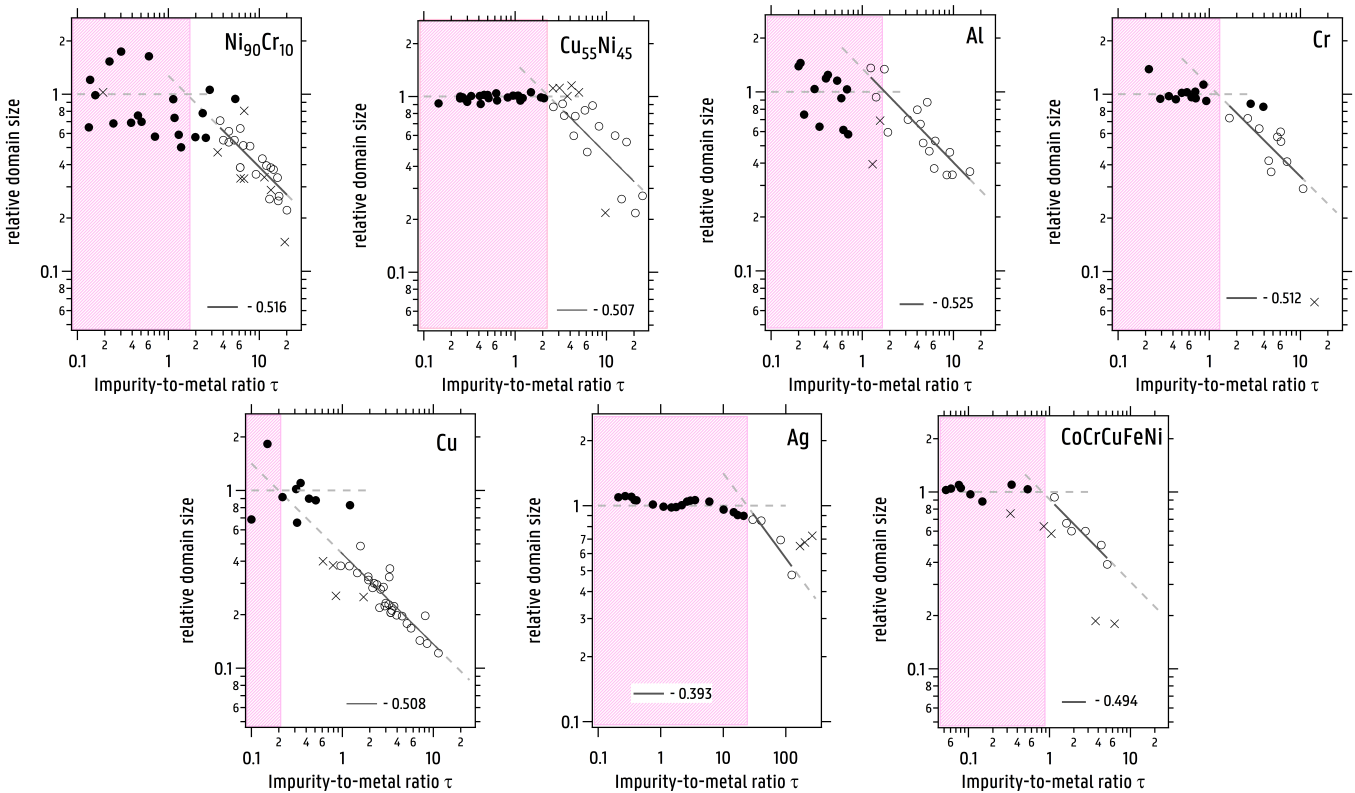

Figure 6.3. *The relative domain size as a function of the impurity-to-metal flux τ for a) chromel b) constantan c) aluminum and d) chromium e) copper f) silver and g) High Entropy Alloy. The closed markers refer to measurements where the domain size is not affected by the impurities (relative domain size equals one) while the open markers represent measurements for the regime of the impurity affected growth. The cross markers are used for measurements excluded from the analysis.*

into the chamber, oxygen (∼20%, $z = 2$) and nitrogen (∼80%, $z = 2$) were selected as gas species in equation (6.1) to calculate F_i. When the experiments were performed without additional leaking (HEA series with increasing current), the gas composition as measured with a residual gas analyzer (see Figure 6.2) was used in equation (6.1). X-ray diffraction (XRD) was performed with a Brüker D8, equipped with a line detector (LynxEye). To avoid any influence of the configuration on the observed trends, one series of samples was measured with a parallel beam configuration (Göbel mirror), while another series was measured in a classical Bragg-Brentano configuration. The instrumental broadening was determined by measuring the XRD pattern for both Cu and Al powder. The XRD peaks were fitted with a Pearson VII peak shape as described by Ida [44]. Based on the determined integral breadth, i.e. the ratio of the total area under the peak to the peak height, the domain size was calculated according to the Scherrer equation. In order to allow a better comparison of the different materials and conditions, the average values of the domain size in the low-impurity regime (∼ 10 - 23 nm) were used to normalize the domain size for each material respectively. The results are shown in Figure 6.3. The different plots show that for all seven materials and despite the differences in deposition conditions, the same trend in the domain size as a function of the ratio τ is observed. For low values of τ, the domain size is not significantly nor consistently affected by the presence of the impurities. To facilitate the discussion, this regime is indicated as the low-impurity regime and represented by the pink patterned areas and filled markers in the plots on Figure 6.3. Consequently, the high-impurity regime (open markers) refers to the regime where the domain size is significantly and consistently affected by an increased impurity-to-metal ratio τ. The cross markers represent measurements which were excluded from the analysis. Either the points could be considered as outliners based on a statistical analysis, or it was not possible to assign them to a specific regime. For 3 of the 7 materials, i.e. Al, Cu, and NiCr, the spread on the domain size in the low-impurity regime is large. As materials with a high melting point are expected to have a low mobility because of the strong cohesive bonds between the adatoms, a higher variability in domain size could be expected for these materials in the low-impurity regime. However, no specific correlation between metal properties such as melting temperature and elastic properties, and this high variability has been observed. It is, on the other hand, known that even at room temperature grain growth can occur for materials such as Cu [30, 31, 43] and Al [38]. The lower variability on the domain size in this high-impurity regime can probably be explained from the suppression of the driving forces for stress-assisted grain growth at higher background pressures as demonstrated by Gianola et al. [38]. In the high-impurity regime, it is remarkable to observe that the domain size becomes function of τ and can be described by a power law with an exponent -1/2. Furthermore,

this behavior is independent of the deposited material. The following exponents and respective errors (95% confidence interval) were found: Al: -0.525 ± 0.154, Cu: -0.508 ± 0.088, Cr: -0.512 ± 0.268, Ag: -0.393 ± 0.296, $Cu_{55}Ni_{45}$: -0.507 ± 0.174, $Ni_{90}Cr_{10}$: -0.516 ± 0.127, and HEA: -0.494 ± 0.225. When an error-weighted average of all the exponents of the different materials is taken, we find -0.50 ±0.07. Although the method as described by equation (6.1) was used for an absolute quantification of the impurity flux, the slope on the log-log plot is only susceptible to relative changes of the fluxes. It should be remarked that within the experimental range, no consistent influence of the film thickness, discharge current and argon pressure was observed on the reported trend. Also no remarkable variation of the film density as a function of τ was observed. Figure 6.4 a shows the film-to-bulk density ratio for chromel as a function of τ. The effect of an increased τ on the film density remains very limited, with a maximal 10% decrease compared to the bulk density. In light of the results presented in Figure 4.6, it is thus clear that the film density is mainly determined by variations in $P \times d$, but not severely affected by impurities. The density data for the series at reduced layer thickness (100 nm) are not present on the plot, as no density measurements were performed for this series. However, there is very little reason to assume that the layer thickness has any influence on the layer density. The data presented in Figure 6.4b are similar to the data as shown in Figure 6.3a, but only series with a difference in deposition conditions, i.e. discharge

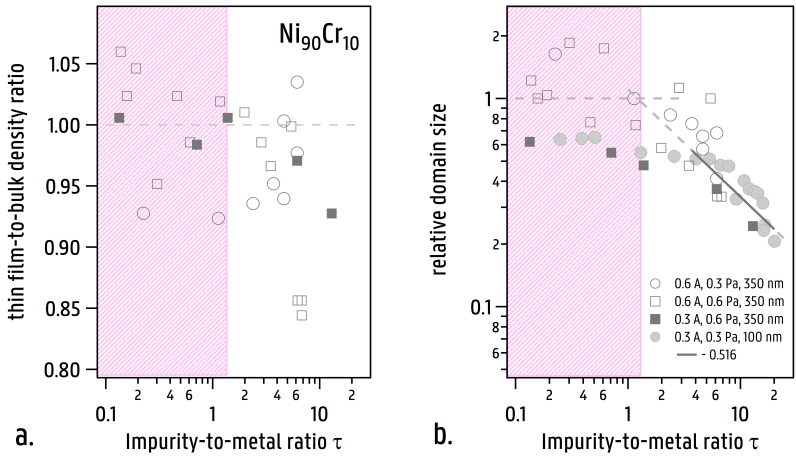

Figure 6.4. *a. The film-to-bulk density ratio and b. the relative domain size as a function of the impurity-to-metal ratio τ for films deposited at different deposition conditions and with different thickness. No systematic trends of the film density as a function of τ were observed. The deviation of the film density from the bulk value remained limited within 10% for almost all depositions. Also no influence of the film thickness, discharge current and argon pressure was noticed on the observed trend in grain refinement.*

current, argon pressure or layer thickness, are included and presented in a distinctive way. However, the variations within this experimental range did not affect the generality of the observed trend in grain refinement as a function of τ.

As mentioned before, gas molecules can overcome the dissociation energy upon impact on the substrate and dissociate in atomic species. Because of their high reactivity, these species are very likely to chemisorb on the substrate surface and act as nucleation sites for adatoms. From this perspective, the hypothesis originates that the observed grain refinement with increasing impurity-to-metal ratio could be attributed to the increased nucleation density on the substrate surface due to chemisorbed impurities.

6.4. Kinetic Monte Carlo Code

In order to demonstrate this mechanism of impurity-driven nucleation, a basic kinetic Monte Carlo code was developed [28]. The model is here firstly introduced for growth without the presence of impurities, i.e. homogeneous nucleation, afterwards impurities are added to the model resulting in heterogeneous nucleation.

6.4.1. Homogeneous Nucleation

The implementation of the model as described in Ref. [28], is shortly summarized here. Per time step, one or more adatoms, in accordance to the material flux F are randomly placed on a square lattice. The square lattice can be treated as a matrix with occupied and unoccupied positions. The adatoms move randomly over a given number of steps on the square lattice. This process represents adatom diffusion. As the diffusion rate is proportional with the number of steps, the ratio between the number of steps, and the number of cells filled per cycle is proportional to D/F. After each diffusion step, the surrounding of each adatom is checked. The critical nucleus size i^* defines the amount of neighboring adatoms needed such that, after addition of another adatom, i.e. $i^* + 1$, a stable nucleus is formed. When the amount of adjacent occupied cells is larger or equal to i^*, the total cluster becomes immobile and forms an island. This simulation cycle is repeated until a desired coverage of the substrate surface is reached. With increasing coverage, more small nuclei appear on the surface. At high surface coverage, the size of the existing nuclei increases and the number of adatoms decreases.

In the initial-stage regime, i.e. at low coverages, nucleation theory [36, 59, 85] indicates that the adatom density increases linearly with the deposition flux, i.e. $n \sim Ft = \theta_M$ (see equation (5.2)). With an increasing adatom density on the surface, the nucleation density increases as $N \sim n^2 \sim \theta_M^2$. In time, the free adatom density will increase initially to reach a maximum where after the adatom density decreases as the

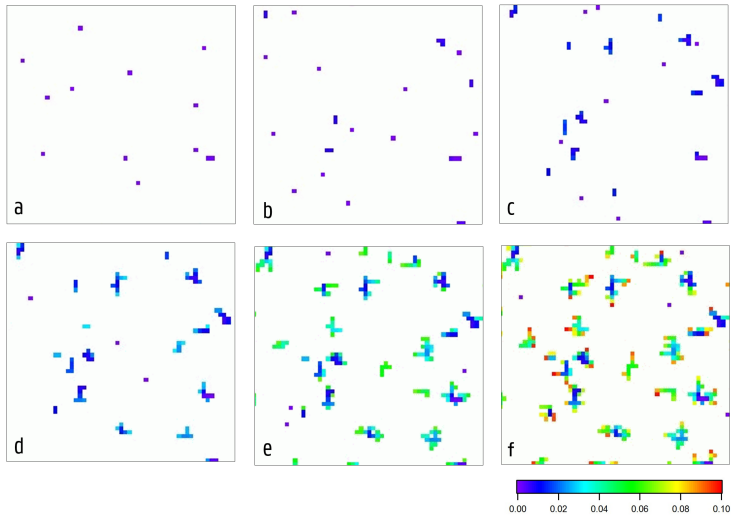

Figure 6.5. *Snapshots of KMC simulation with increasing coverage. The color scale represents the values for the surface coverage at the moment the adatom lands on the surface.*

adatoms easily adhere to the already existing islands, i.e. island capture dominates. The moment when mainly all adatoms are captured by already existing islands, i.e. when the rate at which monomers become immobile equals the deposition flux or $F \approx 4DnN$, the adatom density scales as $n \sim F/DN \ll N$. According to equation (5.3), the island density is then calculated as:

$$N \approx (\frac{F}{D})^{1/3}\theta_M^{1/3} \tag{6.3}$$

In general, the nucleation density N needs to scale with $(\mathrm{D/F})^{-\chi}$, with $\chi = i^*/i^* + 2$ for the case of irreversible homonucleation as described by equation (5.4).
As a test, the simple Monte Carlo model should be able to reproduce the results as obtained from nucleation theory. The adatom density and nucleation density scaling laws as simulated by the model are presented in Figure 6.6. The nucleation density was simulated for $i^* = 1$ and $i^* = 2$ over a wide range of D/F values. Clearly, the model succeeds in reproducing the predictions from nucleation theory. Although a 2D square lattice has been assumed for reasons of simplicity, this assumption has no effect on the conclusions derived from this model.

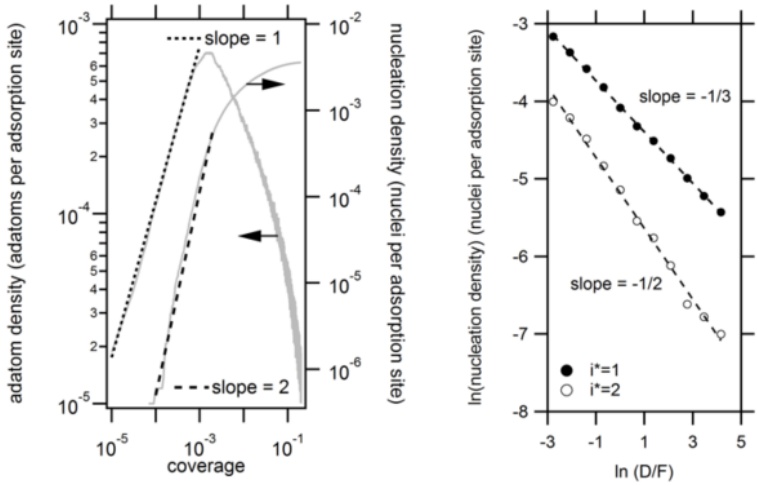

Figure 6.6. *(left) The adatom density per adsorption site (left axis) and the nucleation density per adsorption site (right axis) as a function of the coverage. For low coverages, the adatom density increase linearly, while the nucleation density increases quadratic with the coverage. Simulation conditions: D/F = 16/1. (right) The simulated island density per adsorption sites as a function of D/F for $i^* = 1$ and $i^* = 2$. The fitted line has a slope equal to -1/3 for $i^* = 1$, and -1/2 for $i^* = 2$.*

6.4.2. Heterogeneous Nucleation

In order to simulate the effect of impurities on the nucleation process, the same model structure is preserved with the only difference that the flux towards the substrate now consists of a mixture of impurities and adatoms in accordance to τ. The impurities are considered immobile, chemisorbed atoms, i.e. they freeze on the surface the moment they land, and can act as new nucleation centers. Kotrla [52] used the same strategy for the simulation of aluminum in the presence of oxygen impurities. The latter study started from the results of ab-initio calculations indicating that oxygen is essentially immobile on an Al(111) surface [51].
Figure 6.7 shows the results for $\ln(L)$, with L the characteristic length, as a function of $\ln(\tau)$ where the different traces represent different values for D/F_M (with decreasing values of D/F_M from top to bottom). For low τ values, i.e. the low-impurity regime, the characteristic length is greatly affected by different values for D/F_M and remains unaffected by the impurity flux. This is understood by a characteristic length of the adatoms which is smaller than the capture length based on the distribution of immobile impurities on the surface. In this case, the impurities are invisible for the adatoms and the grain size remains mainly unaffected. Otherly stated [52], if the deposition time, i.e. the time between two subsequent arrivals of a sputtered atom within the capture zone associated with a

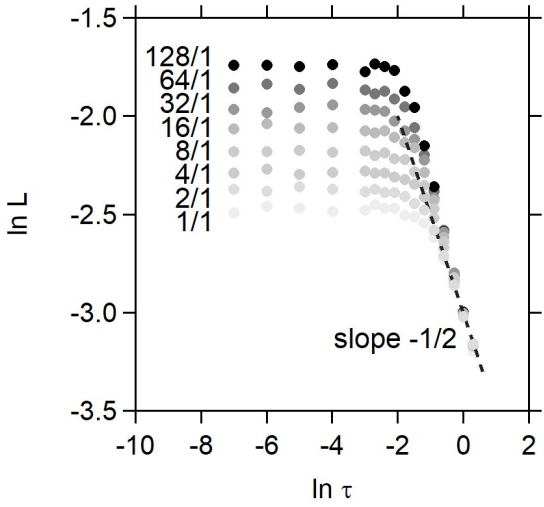

Figure 6.7. *Simulated island size as function of the impurity-to-metal impingement flux ratio for different values of D/F.*

single impurity, is smaller than the diffusion time, i.e. the time for an adatom to explore the complete capture zone and hence to get trapped at the impurity, the impurities are irrelevant for the nucleation process as the second adatom arrives in the capture zone before the first one has found the impurity. In this case homogeneous nucleation predominates.

When $F_i/F_M \gg 1$, i.e. the high contamination regime, the nucleation density is dominated by the freezing of monomer impurities into nucleation centra. The nucleation density thus scales with the impurity concentration on the surface, or $N \sim F_i/F_M$, with F_i/F_M interpreted as the number of nucleation densities formed after the growth of 1 monolayer. This was also rationalized by Yu et al. [89] for the impurity-controlled growth of Ni. With the characteristic length as a measure for the domain size, we find $d \sim L \sim \tau^{-1/2}$. The scaling in the high contamination regime is therefore solely determined by the random distribution of immobile impurity nucleation centers on the surface, and is independent on the choice of D/F, or stated differently, on the choice of the material and the deposition rate. Furthermore, the simulated transition point from the low-impurity regime to the high-impurity regime hardly depends on the choice of D/F. The same behavior is noticed in the experiment. The major exceptions are Ag and Cu, but this can probably be explained from their large difference in chemical reactivity to oxygen [32, 47].

The nucleation model as described here is consistent with $\chi = 0$ or a critical nucleus size $i^* = 0$ (see equation (5.4)). Indeed, the case $i^* = 0$ corresponds to an impurity dominated single-adatom nucleation model in

which the randomly deposited impurities spontaneously nucleate or freeze on the substrate and become immobile nucleation centra. Hence, the average spacing between the impurity atoms decreases with $\tau^{-1/2}$. At high values of τ, the characteristic length becomes dominated by the impurity spacing, and is therefore independent of the material. At low deposition temperatures, the adatom hopping rate for Cu is approximately 20 times lower than the value for Al [35]. Nevertheless, the observed behavior in the high-impurity regime for these two, and all other studied materials, is very similar.

A similar exponent for the power-law description of the grain refinement can be found in the work of P. Barna for evaporated aluminum oxide thin films (-0.518 ± 0.016) [10], in the work of B. Braeckman for sputter deposition of HEAs (-0.46) [16], by KMC simulations of Ni in the high-impurity tail [14], or in the work of T. Wu et al. (-0.48±0.08) [88] - see Figure 6.8 - where the authors introduce coronene as preferred nucleation sites to improve the homogeneity of a graphene monolayer grown by atmospheric-pressure CVD at low-temperatures. By introducing coronene seeds, they controlled the nucleation and domain growth, and supress uncontrolled nucleation and multilayer growth of graphene domains. Figure 6.8 (left) shows a AFM image of the coronene seeds on copper foil and the graphene grown at the nucleation seeds after 10 min. The graphene domain size as function of the concentration of coronene in toluene is shown in Figure 6.8 (left). The pink patterned area indicates, in analogy with the low-impurity regime, a region where the domain size is not too much affected by the increase in coronene concentration. At higher concentrations, and thus a higher nucleation density, the domain size decreases. The data in the unpatterned region are fitted to a power law $A\ x^{\alpha}$, and

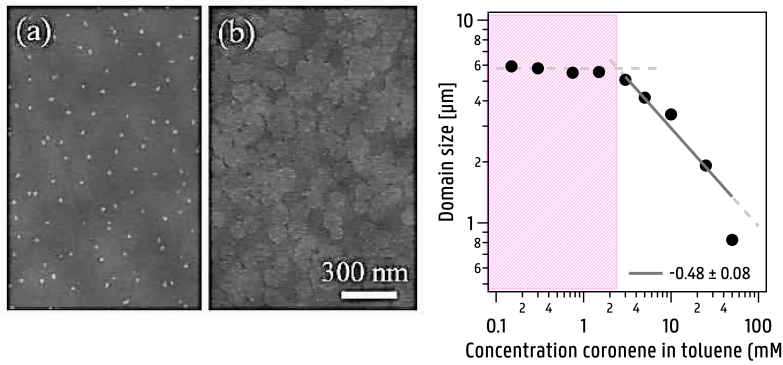

Figure 6.8. *(left) Graphene domain size as function of the concentration of coronene in toluene. The data in the unpatterned region are fitted to a power law $A\ x^{\alpha}$, and yielded an exponent $\alpha = 0.48 \pm 0.08$. The data are adapted from [88] (right)AFM image of a) coronene seeds on copper foil b)graphene grown for 10 min. Image taken from Ref. [88].*

yielded an exponent α = -0.48±0.08. The agreement of the behavior of grain refinement with the latter case, strengthens the hypothesis that the behavior, i.e. $D \sim \tau^{-1/2}$, can be understood from the perspective of an impurity-driven nucleation model.

The kinetic Monte Carlo model as presented here is one of bare simplicity. Although it represents the basic mechanism of adatom diffusion and nucleation and fulfills the prediction from nucleation theory, hardly any physics (such as inclusion of diffusion energy barriers, desorption rates, ...) is involved in the model. This approach was opted in order to reduce the amount of dependencies in the model and to stick to the bare minimum needed for a representation of nucleation. More elaborated kinetic Monte Carlo models or rate equation models, with a higher degree of complexity, can however be found in literature [6, 13, 22–24, 50, 52, 53, 57, 63, 68–71, 83, 85, 92].

6.5. Coalescence-hindered growth

It is assumed that the characteristic length correlates with the grain or domain size. This assumption implies that coalescence in the high-impurity regime is excluded. The idea of a nucleation-dominated regime without coalescence is based on the good agreement between the calculated characteristic lengths, i.e. in the range of 8-22 nm for all investigated materials, by the coalescence-free formalism described in the work of Braeckman et al. [29] and the observed domain sizes in the low-impurity regime for all materials. However, the observed power law and its exponent can also be explained from the perspective of a coalescence-hindered growth model. I want to thank G. Radnóczi from the Hungarian Academy of Sciences for addressing this.

Suppose that the contamination is accumulated only at the perimeter of a growing island. The covering layer on an island is described by a layer of height h along the perimeter of the island. If the accumulated material is collected from a diffusion area $D_I t\pi$ around the island of radius r and covers the island perimeter with one monolayer, the following relation holds

$$2\pi r h = D_I t \pi F_I \Omega_I^{2/3} t \qquad [m^2] \tag{6.4}$$

with F_I the impurity flux, D_I the impurity adatom mobility and Ω_I the atomic volume. Suppose the island grows according to a hemisphere, than within this time t, the volume of the island is given by

$$\frac{2\pi r^3}{3} = D_M t \pi F_M \Omega_M t \qquad [m^3] \tag{6.5}$$

with F_M the material flux, D_M the metal adatom mobility and Ω_M the atomic volume of the metal. Dividing equation (6.5) by (6.4), and solving

for r yields

$$r = \left(\frac{3hD_M\Omega_M}{D_I\Omega_I^{2/3}} \right)^{1/2} \left(\frac{F_I}{F_M} \right)^{-1/2} \qquad [m] \tag{6.6}$$

Therefore, in analogy to the nucleation-dominated growth model, a relation $r \sim \tau^{-1/2}$ is obtained in the case of the formation of a tissue layer covering the sidewalls of the grains. Coalescence is allowed in the model as long as the covering layer does not hinder it.
The observed power-law behavior of the grain refinement as a function of τ can thus either be explained from the perspective of island nucleation, or either from the effect impurities have on the later growth stages such as coalescence and grain growth. This latter argument is for example supported by the work of C.V. Thompson [81] and simulations of Kotrla [52]. A coalescence-hindered growth model by segregation of impurities is also proposed in the structure zone model of P. Barna which is mainly based on an elaborated study of the influence of oxygen on the growth of evaporated aluminum thin films [9]. It is reported that, as soon as $F_O/F_{Al} = \tau \sim 10^{-2}$, island coarsening is severely hindered due to segregated impurities at the grain boundaries, resulting in small grains and a decrease in crystallinity. This low value of τ affecting the film growth contrasts with our results. A possible explanation is the difference in the deposition technique. During evaporation it can safely be assumed that the impurities such as O_2 and N_2 are in their ground state. During magnetron sputtering, it is more likely that the same species are (partially) in an excited state and/or dissociated by the interaction with high energetic electrons in the discharge. The difference in adsorption behavior between the thermal and activated species could affect their influence on the growth. In the case of evaporation they will be initially physisorbed, and hence mobile, while during magnetron sputtering they will immediately chemisorb and hence be immobile. As such, it can be expected that the conditions for impurity segregation, and therefore coalescence hindered growth are thus more favorable for film deposited by evaporation. Furthermore, given the experimental conditions for the as-sputter deposited films studied here, the occurrence of island coalescence is not very likely. To illustrate this point, the results from another study are introduced first. Abadias et al. [2] performed a detailed study on the stress evolution during the initial growth stages of sputter-deposited thin metal films. They have determined the nominal film thickness at the moment the growing islands touch each other, i.e. continuous film formation. This phenomenon is correlated with a peak in the tensile stress. For DC magnetron sputtering under comparable deposition conditions, a nominal thickness of 6, 10.5 and 16.5 nm for respectively Pd, Au, and Ag is reported. The island radius can be determined from the nominal thickness based on the assumption of a densely packed array of touching

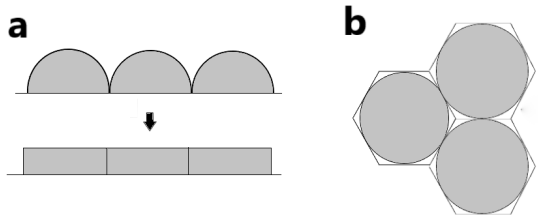

Figure 6.9. *Hemispherical island representation (left) and nominal thickness (right)*

hemispherical islands as presented in Figure 6.9. For a hexagon, we find

$$r = \frac{\sqrt{27}}{\pi} h^* \tag{6.7}$$

Using equation (6.7) and based on the reported nominal thicknesses [2], a radius of 10, 17, and 27 nm is calculated for Pd, Au, and Ag respectively. In the work of Abadias, the island radii were independently measured by means of AFM and were given by 9, 18, 23 nm. Therefore, given the good approximation between measurement and calculation, the assumption of hemispherical islands seems reasonable. With the material fluxes from the work of Abadias [2], the diffusion coefficient D calculated with equation (2) in Ref. [29], and the assumption of a critical nucleus size $i^* = 1$, the characteristic length L for Pd, Au and Ag was calculated as 11, 17 and 18 nm respectively. In this calculation, only island nucleation is included while coalescence is not accounted for. Nevertheless, the calculated values are in reasonably good agreement with the experiment. The deposition speeds reported in the paper of Abadias are around 0.2 nm/s, whereas the deposition speeds used in our experiments are of the order of 1 nm/s, i.e. around a factor five larger. With the characteristic length scaling with the deposition flux as $L \sim F^{-1/6}$, the expected grain sizes in our experiment in absence of coalescence should therefore be in the range of 6 – 16 nm (or approximately 70% of the values obtained by Abadias). This range also corresponds to the initial average grain size prior to coalescence, in the range of 10 - 20 nm, of evaporated silver islands calculated by Adamik et al. based on the saturation nucleation density [4]. The domain sizes in our experiments in the low-impurity regime (between 5 – 23 nm for all 7 materials) nicely correspond to both calculations. Therefore, it is likely that a dominant effect of coalescence can be ruled out for as-sputter deposited metal films as the calculations indicate that initial growth seems to be dominated by nucleation.

Another way to discriminate between a nucleation-dominated and a coalescence hindered growth model is to study the spatial distribution of impurities within a film. In case of a coalescence-hindered growth model, a clear segregation of impurities is expected at the grain boundaries within

the sample. Atom probe tomography (APT) was therefore performed to visualize the spatial distribution of the different atomic species present within the sample. The APT measurements, tip preparation, and data analysis was performed by postdoc-colleague I. Schramm [77]. Atom probe tips for the atom probe tomography (APT) measurements were prepared using a focused ion beam/scanning electron microscope (FIB/SEM – FEI xT Nova NanoLab 200). The needle-shaped specimens were produced using a standard lift-out technique [82] with a final cleaning step of 5 kV. The APT tip shape was optimized to reduce the thermal tails and to obtain a high quality mass spectrum. Several tips were produced per sample at different depth levels in the film. APT was performed using a local electrode atom probe (Cameca LEAP 5000 XR) in voltage mode and a controlled evaporation rate of 0.5% on samples held at a base temperature of 60 K. The pulse fraction was set to 30% and a repetition frequency of 200 kHz. Data reconstruction was carried out with the software package IVAS (version 3.8.0, Cameca) using an evaporation field of 30 V/nm, an image compression factor of 1.65 and a field factor between 3.3 and 4.0 depending on the tip shank angle. Parameters were obtained by using Kingham curves [82] and tip SEM images before and after the APT run.

Two APT measurements were performed on chromel samples. One measurement was performed on a sample deposited in the low-impurity regime, i.e. at $\tau = 0.26$, and another measurement was performed on a sample deposited in the high-impurity regime, i.e. at $\tau = 11.4$. The distribution of the atomic species is visualized in Figure 6.10 and the corresponding atomic composition (at. %) of the samples is presented in Table 6.1. When the values of incorporated nitrogen and oxygen between the low- and high-impurity regime from Table 6.1 are compared, it is observed that the impurity incorporation increases with τ. The ratio between the incorporated impurities to the impurity flux is however not a constant. This behavior could be expected if the impurity incorporation depends on τ as $a\tau + b$. However, the impurity incorporation does not necessarily have to scale linearly as a function of τ [7, 32, 47]. More data are needed in order to possibly conclude on this adsorption behavior as a function of τ. The important message here is that the impurity-to-metal ratio τ expresses a ratio of impingement fluxes and is thus not a compositional ratio.

Knowledge of the sticking coefficients of the different species, which is scarce, is needed in order to determine the fraction of impinging atoms which is incorporated in the film. No explanation however was yet found for the deviation from the $Ni_{90}Cr_{10}$ stoichiometry from the original target in the film. From Figure 6.10, it is clear that the measurements for the low and the high-impurity regime are very similar and indicate a uniform distribution of the impuritive species over the sample. There is

Table 6.1. *Chemical composition by atom probe tomography of both chromel samples.*

	Low-impurity regime sample $\tau = 0.26$	High-impurity regime sample $\tau = 11.4$
Element	Composition (at. %)	Composition (at. %)
Chromium	14.010 ± 0.008	13.431 ± 0.011
Nickel	79.904 ± 0.023	75.999 ± 0.033
Nitrogen	3.429 ± 0.004	5.753 ± 0.007
Oxygen	2.631 ± 0.003	4.480 ± 0.006
Carbon	0.0062 ± 0.00015	0.0025 ± 0.0001
Aluminum	0.01760 ± 0.00026	0.0044 ± 0.0002
Argon	0.00110 ± 0.00006	0.0047 ± 0.0002

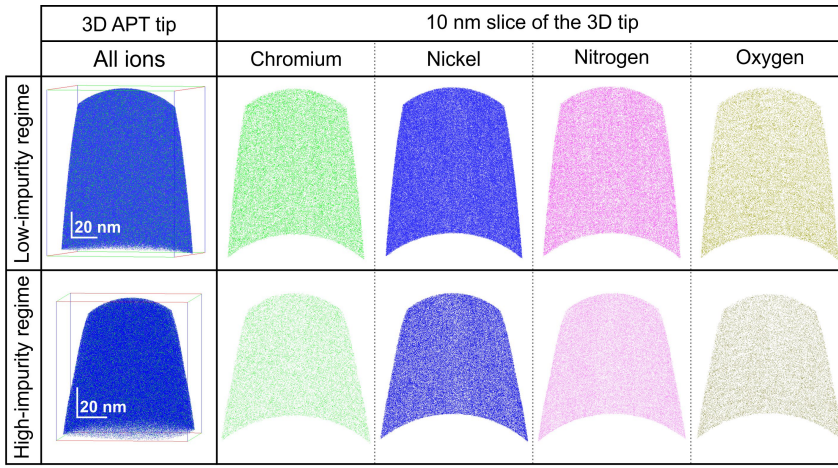

Figure 6.10. *APT measurements for two chromel samples showing the distribution of the constituent elements. The top panels are related to chromel thin film deposited at an impurity-to-metal flux ratio of 0.26 (low contamination regime), while the bottom panels represent the elemental distribution for a thin film deposited at an an impurity-to-metal flux ratio of 11.4 (high contamination regime)*

however no indication for segregation of impurities at grain-boundaries. Therefore, this result again favors the explanation of grain refinement in high-impurity regime through nucleation at impurities rather than by coalescence-hindered growth.

6.6. Texture change

Texture development is associated with an enhanced level of atomic mobility on the growing crystals. For growth of high-melting materials, i.e. inherently low adatom mobility, on amorphous substrates, there is a ran-

dom polycrystalline growth up to about 50 nm [47]. Afterwards, preferred orientation is developed due to anisotropy in growth rate of different crystallographic faces and predominance of favorable oriented crystals [47]. As already mentioned, impurities can greatly affect the crystallographic texture. Figure 6.11 shows different diffractograms as function of an increasing impurity-to-metal ratio in a waterfall representation for $Cu_{55}Ni_{45}$, $Ni_{90}Cr_{10}$, Cu, and Ag. For all materials, all fcc-metals, a preferential crystallographic (111) out-of-plane orientation is observed. For metals with an fcc crystal structure, the (111) crystallographic plane is the most densely packed plane and consequently the plane of lowest surface tension. In case of thermodynamically driven growth, for example at very high deposition temperatures, the plane of the lowest surface tension will be exposed at the surface to minimize the overall energy and the (111) plane thus becomes the preferred out-of-plane orientation (at least for cubic materials). As the impurity-to-metal ratio is increased, the intensity of the (111) Bragg reflection peak drops while the (200) Bragg peak remains unaffected or slightly increases. The reduced diffraction intensity with increasing impurity-to-metal ratio indicates a decrease in the preferential (111) out-of-plane orientation and an evolution towards a more random crystallite orientation. The variation of the intensity ratio for the (111)-peak to the total peak intensity, i.e. $I_{111}/(I_{200} + I_{111})$, as func-

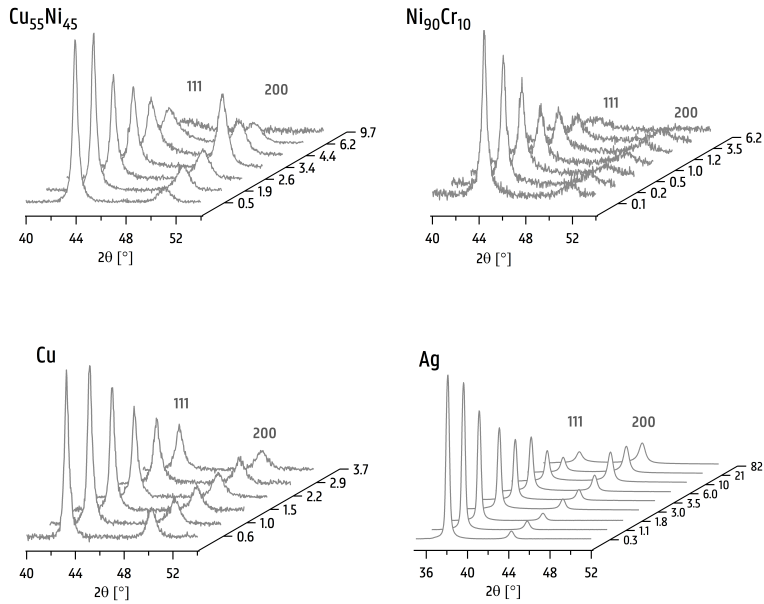

Figure 6.11. *Waterfall plot of XRD diffractograms as function of an increasing impurity-to-metal ratio. All films had a thickness of 350 ± 30 nm.*

tion of an increased impurity-to-metal ratio τ is shown in Figure 6.12. The measured I_{111} and I_{200} intensities were only corrected for the layer thickness, but not for the structure factor. Similar observations for the decreases of the (111) texture appearance with increasing residual gas pressure are reported in literature. To illustrate two, Kakati et al. [47] describe the variation of the (111) orientation in evaporated gold, silver, and copper films as function of the residual gas pressure and the film thickness. Jhingan et al. studied the effect of oxygen and nitrogen on the crystal texture of sputtered Ni-Fe films [45, 46], and observed for both gas species a decrease from the (111) crystal texture upon increasing the nitrogen or oxygen content in the vacuum chamber. In case of nitrogen addition, a similar transition - as observed in Figure 6.11 - to a (200) preferred crystallographic orientation occured. It was also observed by microstructural analysis that the presence of nitrogen in the sputtering gas promotes grain refinement. The average grain size of the films decreased from 65 nm to 25 nm with addition of nitrogen (from 0 to 1% partial pressure). Jhingan et al. attributed the fine grain-sized films to the increased number of nuclei. The influence of the nitrogen on the crystal texture was therefore attributed to the variation of the crystallites nucleation behavior, or growth pattern.

As mentioned in section 2, Barna and co-workers correlate the texture transition to the change in grain size, for example, for evaporated Ag [4], Al/O_2 [10] and TiN in an O_2 environment [15]. In case of the latter, the texture change from (111) to (001) with increasing oxygen level is attributed to competitive growth by the different ways the oxygen impurities can segregate or incorporate on the crystal faces. According to the authors, the oxygen is preferentially segregated as a surface layer on the (111) crystal face, and thus growth of this orientation is hindered. On the 001 faces on the other hand, major part of the oxygen species are dissolved into the crystal lattice and thus the 001 orientation is less hindered and evolves towards a preferential orientation. The texture transition is therefore related to a decrease of the grain size as coalescence is hindered due to the formation of a surface covering layer. The results as presented in Figure 6.13 however do not indicate any general behavior for the texture change in the high-impurity regime, in contrast to the consistent grain refinement observed for all of the studied materials in the high-impurity regime in Figure 6.3. Only for $Cu_{55}Ni_{45}$, $Ni_{90}Cr_{10}$, and the HEA the texture change coincides with the change in domain size. For Cr, the out-of-plane orientation was (110), but did not change as a function of τ and is thus not included in the plots. Therefore, it can be concluded that, at least no straightforward correlation exists between the texture change and the variations in grain size. Consequently, the observations of a texture change correlated to a change in grain size for evaporated films can not be generalized. The other way around, although the domain size

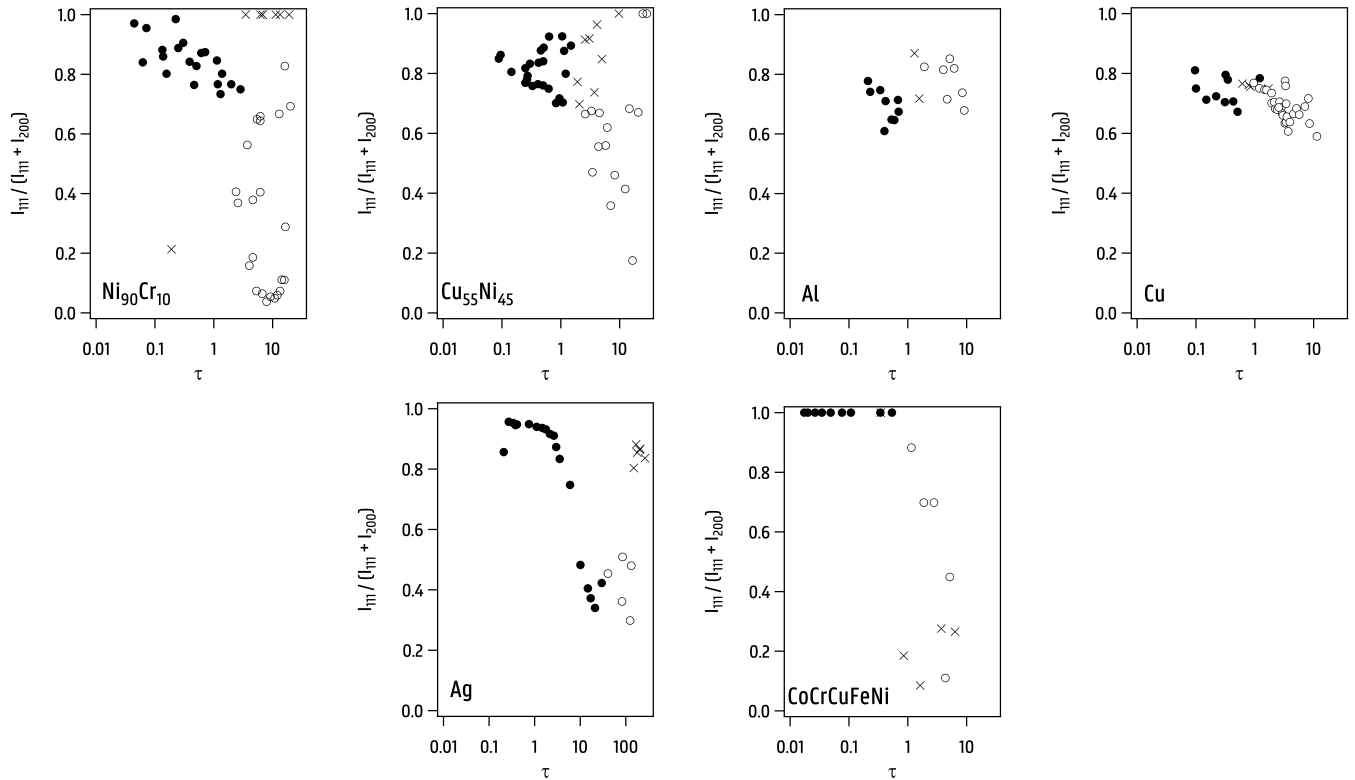

Figure 6.12. *The ratio between the intensity of the (111) Bragg reflection and the intensity of both the (111) and (200) Bragg reflection for a) chromel, b) constantan, c) aluminum, and d) copper e) silver, and f) a high-entropy alloy. The closed markers refer to measurements in the low-impurity regime, while the open markers represent measurements performed in the high-impurity regime. The cross markers are used for measurements excluded from the analysis.*

was always determined based on the 111 peak (for fcc metals), the conclusions on the grain refinement in the high-impurity regime seem to hold irrespective of the texture of the film. The different results obtained between texture transitions for sputtered and evaporated films might again be attributed to the unfavorable conditions for impurity segregation in as-sputter deposited films (see Figure 6.10). Indeed, impurities that are soluble into the crystal lattice have no effect on the crystallographic texture because they are dissolved into the crystal lattice without building up their own phase [37]. Therefore, the absence of impurity segregation and thus coalescence hindered growth, is in line with the absence of a correlation between texture transition and grain refinement for the as-sputter deposited films in the high-impurity regime. However, caution should be taken to generalize this statement as it seems to contradict with the report of Biro et al [15]. As already mentioned, the latter work reports on a texture change in sputter deposited TiN films caused by a competition between incorporation and segregation of impurities [42]. A possible cause which can explain impurity segregation in sputter-deposited films is the combination of the low deposition rates used (0.2 nm/s in contrast to 1 nm/s in this work) together with the elevated substrate temperatures (400°C in contrast to as-deposited in this work). Indeed, in case of a low deposition rate and enhanced substrate temperature, the chance for desorption together with the time for impurity diffusion is increased. Therefore, for sputter-deposited films under these conditions, it is possible that impurity segregation is facilitated.

6.7. Lattice Expansion

When an additional impurity flux impinges on the substrate, the impurity species can either be adsorbed and segregated on the growing crystal phases or be dissolved in the crystal lattice. Yu et al. [89] discussed that incorporation of impurities on metal surfaces or on the surface sites of grain boundaries introduces stress into the film. Stress development in a thin film [1] can be reflected by a change in the lattice parameter. When impurities are incorporated as interstitials, the model of Yu predicts that the induced stress, and consequently the lattice expansion, is proportional to the impurity concentration and the ratio between the atomic volume of the impurities and the host metal.
The impurity concentration on the surface is proportional to the ratio between the impurity flux F_{imp} and the total flux towards the growing film, i.e. $F_{imp}/(F_m + F_{imp})$, or $\tau/(1+\tau)$. The chemical reactivity of the metal will however define the final concentration (see Table 6.1). The relative change of the unrelaxed lattice parameter as measured by XRD is shown in Figure 6.13 as a function of $\tau/(1+\tau)$. The filled and open markers represent depositions performed in the low and the high-impurity regime respectively. The cross markers again represent measurements which were

excluded from the analysis. The lattice expansion as a function of the impurity concentration is only studied in the low-impurity regime. This because stress development in a thin film can find different contributions. Among others, the origin of stress can either be intrinsically related to the film-substrate properties, such as a difference between the thermal expansion coefficient of the substrate compared to the film, or is either related to the conditions during growth [34, 39, 49]. As an example of the latter, it was shown that variations in grain size induce variations in growth stress [21, 25, 65, 80, 84]. In the low-impurity regime, it was previously shown that the domain size keeps in good approximation a constant value. Therefore, in this regime, the influence of a varying domain size on the stress development is excluded. Also, as the target-to-substrate distance was fixed for all the depositions at 10 cm, the heat flux is comparable and thus the influence of thermal effects can be ruled out.
In this low-impurity regime, it can be confirmed from Figure 6.13 that the lattice parameter increases proportionally to the impurity concentration. Therefore, the impurity incorporation can be evaluated from the slope of the line fitting the increase in the lattice parameter with impurity concentration. Only for Ag (see Figure 6.13f), the slope of the lattice expansion as a function of $\tau/(1+\tau)$ is within the error equal to zero, i.e. the lattice parameter is not affected by the impurity concentration on the surface. This seems in contrast with the predictions by the model of Yu. However, the latter model does not account for the size of octahedral/tetrahedral positions in the fcc or bcc lattice. The octahedral positions within Ag have a radius similar to the atomic radius of oxygen, and hence no strain can be induced. As discussed above, also the chemical reactivity of the element will define the actual concentration of impurities in the thin film, and consequently also the lattice parameter change. Leroy et al. [54, 55] showed that the incorporation coefficient should also depend linearly on the electronegativity difference between the impurity and the host metal . Hence, the measured slope between the lattice parameter and $\tau/(1+\tau)$ should scale with

$$\frac{r_{imp}}{r_M c_{void}}\Delta\epsilon \tag{6.8}$$

where r_{imp} and r_M are respectively the radius of the impurities, taken as an average value of nitrogen and oxygen atomic radius, and the metal radius. For the alloys, a weighted average of the radii of the components was taken. The electronegativity difference is represented by $\Delta\epsilon$, and c_{void} is a constant which relates the void size with the metal radius. For fcc lattices c_{void} equals 0.414, while for bcc lattices a value of 0.291 is found [60]. Figure 6.14 shows that the prediction of equation (6.8) can be fairly well validated. The good agreement between the slope of the lattice parameter with the radius of the impurity , the void volume between the crystal lattice and the chemical reactivity of the host metal, indicates that, in the low-impurity regime, the impurities are presumably dissolved

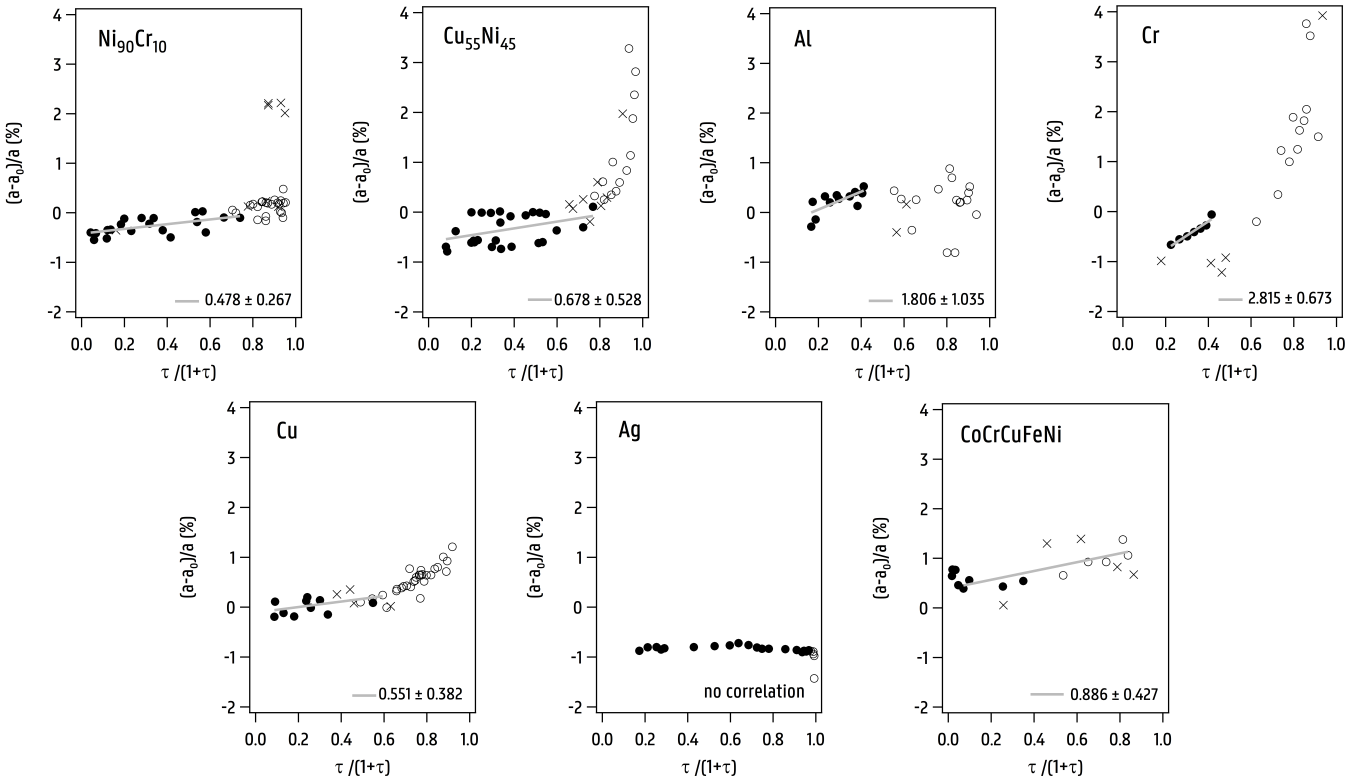

Figure 6.13. *The relative change of the lattice parameter presented as a function of the impurity concentration, i.e. $\tau=(1+\tau)$, for a) chromel b) constantan c) aluminum d) chromium e) copper f) silver g) the CoCrCuFeNi high-entropy alloy. The closed markers refer to measurements in the low-impurity regime, while the open markers represent measurements performed in the high-impurity regime. The cross markers are used for measurements excluded from the analysis.*

in the lattice and not segregated at the grain boundaries.
The stronger increase of the lattice parameter in the high-impurity regime for some materials such as Cr, Cu, and $Cu_{55}Ni_{45}$, is more difficult to quantify, as many other processes should be taken into account. In this case, it is known that the domain size varies as a function of the impurity incorporation, and it is thus less straightforward to discriminate between the effects of impurity incorporation and stress development on the lattice parameter. Also, although no crystalline oxide or nitride phases have been observed in XRD, under influence of high impurity contamination, the formation and presence of amorphous oxide phases cannot be ruled out. Furthermore, for most materials a texture change occurs in the high-impurity regime (see previous section), and thus it is unclear what lattice parameter should be interpreted in this regime.

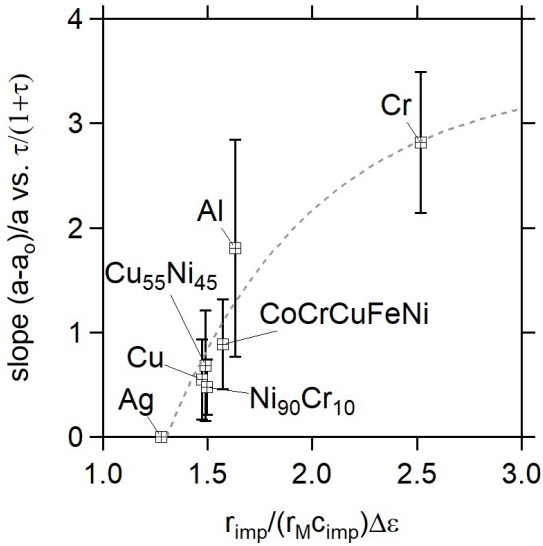

Figure 6.14. *The slope of the lattice parameter change in the low-impurity regime as a function of the parameter derived in equation (6.8). The line is a guide for the eye.*

6.8. Conclusion

The effect of impurities originating from the residual gas in the chamber, from leaks, or from the outgassing products of an epoxy substrate was discussed. The principal gas species present in the system are identified as N_2 and O_2 in the case of a leak, whereas H_2O, H_2, and OH are the principal species observed when outgassing of the chamber walls or an epoxy substrate is the main source of contamination. The outgassing products from the prepreg substrates most likely originate from adsorbed gases after exposure to the air. The observed outgassing of the prepreg

also indicates the importance of maintaining the exposed surface area at a minimum, especially if the sample is to be repeatedly subjected to readily adsorbable gases present in the air. It was shown that the presence of O_2, N_2, or H_2O species during deposition can severely affect thin film growth. The impact of impurities on the film growth can be evaluated from the impurity-to-metal impingement ratio τ, i.e. the relative amount of impurities impinging on the surface per arriving adatom. It was shown that, in the low-impurity regime, i.e. when $\tau < 1$, the domain size was not significantly or consistently affected by the presence of impinging impurities. This was understood as the spatial distribution between chemisorbed impurity species is larger than the characteristic length of the metal adatoms. For larger impurity-to-metal ratios, i.e. $\tau > 1$, the spatial distribution between the chemisorbed species will be smaller than the characteristic length of the diffusing adatoms. In this case, the explored diffusion area of the adatom is restricted by the presence of different nucleation sites within this area, promoting nucleation and consequently grain-refinement. A power-law behavior $D \sim \tau^{\alpha}$ is observed, which describes the decrease in domain size with increasing impurity-to-metal ratio τ for all seven studied materials. When the exponent α is averaged over the different materials, a value $\alpha = -0.50 \pm 0.07$ was found. This material-independent power-law behavior was also successfully simulated by means of a kinetic Monte Carlo code for a nucleation-dominated growth model. Also a coalescence-hindered growth model could explain this observed power-law behavior. However, for as-sputter deposited films, i.e. deposited without any additional heating contribution to the substrate, the conditions for impurity segregation are less favorable and its occurrence is debatable. This was illustrated by means of the APT measurements, the observed texture changes and lattice expansions which are not in line with the idea of impurity segregation.

References

[1] G Abadias, E Chason, J Keckes, M Sebastiani, GB Thompson, E Barthel, GL Doll, CE Murray, CH Stoessel, and L Martinu, Review Article: Stress in thin films and coatings: Current status, challenges, and prospects, Journal of Vacuum Science & Technology A: Vacuum, Surfaces, and Films **36** (2018), no. 2, 020801.

[2] G Abadias, A Fillon, JJ Colin, A Michel, and C Jaouen, Real-time stress evolution during early growth stages of sputter-deposited metal films: influence of adatom mobility, Vacuum **100** (2014), 36–40.

[3] M Adamik, PB Barna, and I Tomov, Columnar structures in polycrystalline thin films developed by competitive growth, Thin Solid Films **317** (1998), no. 1-2, 64–68.

[4] ———, Correlation between texture and average grain size in polycrystalline Ag thin films, Thin Solid Films **359** (2000), no. 1, 33–38.

[5] M Adamik, I Tomov, and PB Barna, Texture evolution in stratified Al thin films, Solid State Phenomena **56** (1997), 213–218.

[6] JG Amar and F Family, Critical cluster size: Island morphology and size distribution in submonolayer epitaxial growth, MRS Online Proceedings Library Archive **367** (1994).

[7] N Ayawei, AN Ebelegi, and D Wankasi, Modelling and Interpretation of Adsorption Isotherms, Journal of Chemistry **2017** (2017), 1–11.

[8] A Barna, PB Barna, G Radnoczi, FM Reicha, and L Toth, Formation of aluminum thin films in the presence of oxygen and nickel, Physica Status Solidi A-Applied Research **55** (1979), no. 2, 427–435.
[9] PB Barna and M Adamik, Fundamental structure forming phenomena of polycrystalline films and the structure zone models, Thin solid films **317** (1998), no. 1-2, 27–33.
[10] PB Barna, M Adamik, U Kaiser, S Laux, H Bangert, M Pulliainen, and KA Pischow, Structure related optical and mechanical properties of oxygen doped Al films, Surface and Coatings Technology **100-101** (1998), 72–75.
[11] PB Barna, Z Bodo, YG Gergely, P Croce, J Adam, and P Jakab, Ellipsometric and X-ray specular reflection studies on naturally grown overlayers on aluminum thin films, Thin Solid Films **120** (1984), no. 4, 249–256.
[12] PB Barna and G Radnóczi, Metallic Films for Electronic, Optical and Magnetic Applications, Elsevier, 2014.
[13] MC Bartelt and JW Evans, Nucleation and growth of square islands during deposition: Sizes, coalescence, separations and correlations, Surface Science **298** (1993), no. 2-3, 421–431.
[14] CC Battaile and JJ Hoyt, Modeling the effects of impurities on microstructure formation in nanocrystalline nickel thin films, JOM **57** (2005), no. 9, 71–73.
[15] D Biro, MP Hasaneen, L Szekely, M Menyhard, S Gurban, P Pekker, I Dodony, and PB Barna, Texture change of TiN films due to anisotropic incorporation of oxygen, Vacuum **103** (2014), 78–86.
[16] BR Braeckman, P Djemia, F Tetard, L Belliard, and D Depla, Impurity-controlled film growth and elastic properties of CoCrCuFeNi thin films, Surface and Coatings Technology **315** (2017), 475–483.
[17] BR Braeckman, F Misják, G Radnóczi, M Caplovicova, P Djemia, F Tetard, L Belliard, and D Depla, The nanostructure and mechanical properties of nanocomposite Nbx-CoCrCuFeNi thin films, Scripta Materialia **139** (2017), 155–158.
[18] SH Brongersma, E Kerr, I Vervoort, A Saerens, and K Maex, Grain Growth, Stress, and Impurities in Electroplated Copper, Journal of Materials Research **17** (2002), no. 3, 582–589.
[19] RD Brown, Outgassing of epoxy resins in vacuum, Vacuum **17** (1967), no. 3, 168.
[20] A Canizo-Cabrera, E Gomez-Barojas, C Tabares-Munoz, R Silva-Gonzalez, and V Garcia-Vazquez, Figures of merit for niobium thin films grown on sapphire substrate, Modern Physics Letters B **15** (2001), no. 17-19, 639–642.
[21] L Cao, A Sengupta, D Pantuso, and M Koslowski, Effect of texture and grain size on the residual stress of nanocrystalline thin films, Modelling and Simulation in Materials Science and Engineering **25** (2017), no. 7, 075004.
[22] J Carrey and JL Maurice, Scaling laws near percolation during three-dimensional cluster growth: A Monte Carlo study, Physical Review B **65** (2002), no. 20.
[23] J Carrey, JL Maurice, F Petroff, and A Vaurès, Growth of Au Clusters on AmorphousAl2O3: Evidence of Cluster Mobility above a Critical Size, Physical Review Letters **86** (2001), no. 20, 4600–4603.
[24] DD Chambliss and KE Johnson, Nucleation with a critical cluster size of zero: Submonolayer Fe inclusions in Cu (100), Physical Review B **50** (1994), no. 7, 5012.
[25] Y Choi and S Suresh, Size effects on the mechanical properties of thin polycrystalline metal films on substrates, Acta Materialia **50** (2002), no. 7, 1881–1893.
[26] P Chowdhury, HC Barshilia, KS Rajam, PK Mishra, CL Prajapat, and DV Rao, Role of oxygen impurity in growth and magnetic properties of Ni83Fe17 permalloy thin films, Journal of Magnetism and Magnetic Materials **322** (2010), no. 21, 3266–3270.
[27] TM Coughlin, ER Wuori, and JH Judy, Nitrogen-induced fcc phase in rf sputtered Co–Cr films having the hcp phase and perpendicular magnetic anisotropy, Journal of Vacuum Science and Technology **20** (1982), no. 2, 171–174.
[28] D Depla, Magnetrons, reactive gases and sputtering, 2017.
[29] D Depla and BR Braeckman, Quantitative correlation between intrinsic stress and microstructure of thin films, Thin Solid Films **604** (2016), 90–93.
[30] C Detavernier, D Deduytsche, RL Van Meirhaeghe, J De Baerdemaeker, and C Dauwe, Room-temperature grain growth in sputter-deposited Cu films, Applied Physics Letters **82** (2003), no. 12, 1863–1865.

[31] C Detavernier, S Rossnagel, C Noyan, S Guha, C Cabral, and C Lavoie, Thermodynamics and kinetics of room-temperature microstructural evolution in copper films, Journal of Applied Physics **94** (2003), no. 5, 2874–2881.
[32] PK Dutta and H Wilman, Crystal growth and orientations in vacuum-condensed silver films and their systematic dependance on the residual air pressure, film thickness, rate of deposition and substrate temperature, Journal of Physics D: Applied Physics **3** (1970), no. 6, 839.
[33] S Firstov, V Kulikovsky, T Rogul, and R Ctvrtlik, Effect of small concentrations of oxygen and nitrogen on the structure and mechanical properties of sputtered titanium films, Surface & Coatings Technology **206** (2012), no. 17, 3580–3585.
[34] JA Floro, E Chason, RC Cammarata, and DJ Srolovitz, Physical Origins of Intrinsic Stresses in Volmer–Weber Thin Films, MRS Bulletin **27** (2002), no. 1, 19–25.
[35] CP Flynn, Point defect reactions at surfaces and in bulk metals, Physical Review B **71** (2005), no. 8, 085422.
[36] DR Frankl and JA Venables, Nucleation on substrates from the vapour phase, Advances in Physics **19** (1970), no. 80, 409–456.
[37] P Ghekiere, Structure evolution of biaxially aligned thin films deposited by sputtering, Ph.D. thesis, Ghent University, 2007.
[38] DS Gianola, S Van Petegem, M Legros, S Brandstetter, H Van Swygenhoven, and K.J Hemker, Stress-assisted discontinuous grain growth and its effect on the deformation behavior of nanocrystalline aluminum thin films, Acta Materialia **54** (2006), no. 8, 2253 – 2263.
[39] SY Grachev, FD Tichelaar, and GCAM Janssen, Stress in sputter-deposited Cr films: Influence of Ar pressure, Journal of Applied Physics **97** (2005), no. 7, 073508.
[40] GH Gu, SM Park, and CG Park, Impurity-controlled Mo films as diffusion barriers for Cu metallization, Metals and Materials International **18** (2012), no. 3, 517–520.
[41] EO Hall, The Deformation and Ageing of Mild Steel: III Discussion of Results, Proceedings of the Physical Society. Section B **64** (1951), no. 9, 747–753.
[42] M.F. Hasaneen, D. Biro, L. Székely, P. Nemes-Incze, and P.B. Barna, Substructure in the columnar crystals of the Ti0.45O0.20N0.35 oxynitride thin film, Vacuum **86** (2012), no. 12, 2105–2108.
[43] SP Hau-Riege and CV Thompson, In situ transmission electron microscope studies of the kinetics of abnormal grain growth in electroplated copper films, Applied Physics Letters **76** (2000), no. 3, 309–311.
[44] T Ida, New measures of sharpness for symmetric powder diffraction peak profiles, Journal of Applied Crystallography **41** (2008), no. 2, 393–401.
[45] AK Jhingan, Effect of nitrogen on the crystal texture and microstructure of sputtered Ni-Fe films, Journal of applied physics **57** (1985), no. 8, 3991–3993.
[46] AK Jhingan, RR Dubin, and LF Herte, Film growth characterization of an underlayer for perpendicular magnetic recording, IEEE transactions on magnetics **20** (1984), no. 5, 779–781.
[47] KK Kakati and H Wilman, The development of oriented crystal growth during condensation of gold, silver and copper films in vacuum, and its systematic dependence on the residual gas pressure and adsorption, and the film thickness, atomic mobility and chemical reactivity, Journal of Physics D: Applied Physics **6** (1973), no. 11, 1307.
[48] LP Kendig, ZU Rek, SM Yalisove, and JC Bilello, The role of impurities and microstructure on residual stress in nanoscale Mo films, Surface & Coatings Technology **132** (2000), no. 2-3, 124–129.
[49] R Koch, The intrinsic stress of polycrystalline and epitaxial thin metal films, Journal of Physics: Condensed Matter **6** (1994), no. 45, 9519–9550.
[50] M Kotrla, J Krug, and P Šmilauer, Submonolayer epitaxy with impurities: Kinetic Monte Carlo simulations and rate-equation analysis, Physical Review B **62** (2000), no. 4, 2889.
[51] _____, Effects of Adsorbates on Submonolayer Growth, Collective Diffusion on Surfaces: Correlation Effects and Adatom Interactions, Springer Netherlands, 2001, pp. 247–257.
[52] _____, Effects of mobile and immobile impurities on two-dimensional nucleation, Surface science **482** (2001), 840–843.

[53] C Lee and AL Barabási, Spatial ordering of islands grown on patterned surfaces, Applied Physics Letters **73** (1998), no. 18, 2651–2653.
[54] WP Leroy, S Mahieu, R Persoons, and D Depla, Method to Determine the Sticking Coefficient of O_2 on Deposited Al During Reactive Magnetron Sputtering, Using Mass Spectrometry, Plasma Processes and Polymers **6** (2009), S342–S346.
[55] ———, Quantification of the incorporation coefficient of a reactive gas on a metallic film during magnetron sputtering: The method and results, Thin Solid Films **518** (2009), no. 5, 1527–1531.
[56] J Liu and K Barmak, Topologically close-packed phases: Deposition and formation mechanism of metastable beta-W in thin films, Acta Materialia **104** (2016), 223–227.
[57] S Lucas and P Moskovkin, Simulation at high temperature of atomic deposition, islands coalescence, Ostwald and inverse Ostwald ripening with a general simple kinetic Monte Carlo code, Thin Solid Films **518** (2010), no. 18, 5355–5361.
[58] S Mahieu, P Ghekiere, D Depla, and R De Gryse, Biaxial alignment in sputter deposited thin films, Thin Solid Films **515** (2006), no. 4, 1229–1249.
[59] T Michely and J Krug, Islands, Mounds and Atoms, Springer Berlin Heidelberg, 2012.
[60] EK Mittemeijer, Fundamentals of Materials Science: The Microstructure–Property Relationship Using Metals as Model Systems, Chapter 9, p. 405, Springer Berlin Heidelberg, 2010.
[61] S Miura, M Tsunoda, and M Takahashi, Role of oxygen in the film growth and giant magnetoresistance of Co/Cu multilayers, Journal of Applied Physics **89** (2001), no. 11, 6308–6313.
[62] M Moriyama, T Morita, S Tsukimoto, M Shimada, and M Murakami, The effect of target purities on grain growth in sputtered copper thin films, Materials Transactions **46** (2005), no. 5, 1036–1041.
[63] P Moskovkin and S Lucas, Computer simulations of the early-stage growth of Ge clusters at elevated temperatures on patterned Si substrate using the kinetic Monte Carlo method, Thin Solid Films **536** (2013), 313–317.
[64] TG Nieh and J Wadsworth, Hall-petch relation in nanocrystalline solids, Scripta Metallurgica et Materialia **25** (1991), no. 4, 955–958.
[65] WD Nix and BM Clemens, Crystallite coalescence: A mechanism for intrinsic tensile stresses in thin films, Journal of Materials Research **14** (1999), no. 8, 3467–3473.
[66] LJ Parfitt, OP Karpenko, ZU Rek, SM Yalisove, and JC Bilello, Origins of residual stress in Mo and Ta films: The role of impurities, microstructural evolution, and phase transformations, Thin Films: Stresses and Mechanical Properties VI (WW Gerberich, HJ Gao, JE Sundgren, and SP Baker, eds.), Materials Research Society Symposium Proceedings, vol. 436, 1997, pp. 505–510.
[67] NJ Petch, The cleavage strength of polycrystals, Journal of the Iron and Steel Institute **174** (1953), 25–28.
[68] A Pimpinelli and R Ferrando, Reentrant morphological instability of epitaxial islands, Physical Review B **60** (1999), no. 24, 17016–17022.
[69] C. Polop, H. Hansen, W. Langenkamp, Z. Zhong, C. Busse, U. Linke, M. Kotrla, Peter J. Feibelman, and T. Michely, Oscillatory interaction between O impurities and Al adatoms on Al(111) and its effect on nucleation and growth, Surface Science **575** (2005), no. 1-2, 89–102.
[70] C Ratsch and JA Venables, Nucleation theory and the early stages of thin film growth, Journal of Vacuum Science & Technology A: Vacuum, Surfaces, and Films **21** (2003), no. 5, S96–S109.
[71] C Ratsch, A Zangwill, P Šmilauer, and DD Vvedensky, Saturation and scaling of epitaxial island densities, Physical review letters **72** (1994), no. 20, 3194.
[72] H Riedl, CM Koller, F Munnik, H Hutter, FM Martin, R Rachbauer, S Kolozsvari, M Bartosik, and PH Mayrhofer, Influence of oxygen impurities on growth morphology, structure and mechanical properties of Ti-Al-N thin films, Thin Solid Films **603** (2016), 39–49.
[73] J Schiøtz, FD Di Tolla, and KW Jacobsen, Softening of nanocrystalline metals at very small grain sizes, Nature **391** (1998), no. 6667, 561–563.
[74] JM Schneider, A Anders, B Hjörvarsson, I Petrov, K Macák, U Helmersson, and JE Sundgren, Hydrogen uptake in alumina thin films synthesized from an aluminum plasma stream in an oxygen ambient, Applied Physics Letters **74**

(1999), no. 2, 200–202.
[75] JM Schneider, B Hjörvarsson, X Wang, and L Hultman, On the effect of hydrogen incorporation in strontium titanate layers grown by high vacuum magnetron sputtering, Applied Physics Letters **75** (1999), no. 22, 3476–3478.
[76] JM Schneider, K Larsson, J Lu, E Olsson, and B Hjörvarsson, Role of hydrogen for the elastic properties of alumina thin films, Applied Physics Letters **80** (2002), no. 7, 1144–1146.
[77] IC Schramm Benítez, Defect-engineered (Ti,Al)N thin films, Ph.D. thesis, 2017.
[78] F Shojik, K Sumitomo, T Kinoshita, Y Tanaka, K Oura, and I Katayama, Hydrogen Adsorption Effects on Thin Film Growth Mode Studied by Ion Scattering, MRS Proceedings **237** (1991).
[79] C Kishan Singh, S Ilango, SR Polaki, S Dash, and AK Tyagi, On the evolution of residual stress at different substrate temperatures in sputter-deposited polycrystalline Mo thin films by x-ray diffraction, Materials Research Express **1** (2014), no. 3, 036401.
[80] CV Thompson, The yield stress of polycrystalline thin films, Journal of Materials Research **8** (1993), no. 2, 237–238.
[81] ———, Structure Evolution During Processing of Polycrystalline Films, Annual Review of Materials Science **30** (2000), no. 1, 159–190.
[82] K Thompson, D Lawrence, DJ Larson, JD Olson, TF Kelly, and B Gorman, In situ site-specific specimen preparation for atom probe tomography, Ultramicroscopy **107** (2007), no. 2-3, 131–139.
[83] JA Venables and GDT Spiller, Nucleation and growth of thin films, Surface Mobilities on Solid Materials, Springer, 1983, pp. 341–404.
[84] R Venkatraman and JC Bravman, Separation of film thickness and grain boundary strengthening effects in Al thin films on Si, Journal of Materials Research **7** (1992), no. 8, 2040–2048.
[85] J Villain, A Pimpinelli, L Tang, and D Wolf, Terrace sizes in molecular beam epitaxy, Journal de Physique I **2** (1992), no. 11, 2107–2121.
[86] FH Wang, CF Yang, JC Liou, and IC Chen, Effects of Hydrogen on the Optical and Electrical Characteristics of the Sputter-Deposited Al2O3-Doped ZnO Thin Films, Journal of Nanomaterials **2014** (2014), 1–7.
[87] H Wipf, Solubility and Diffusion of Hydrogen in Pure Metals and Alloys, Physica Scripta **T94** (2001), no. 1, 43.
[88] T Wu, G Ding, H Shen, H Wang, L Sun, Y Zhu, D Jiang, and X Xie, Continuous graphene films synthesized at low temperatures by introducing coronene as nucleation seeds, Nanoscale **5** (2013), no. 12, 5456–5461.
[89] HZ Yu and CV Thompson, Stress engineering using low oxygen background pressures during Volmer–Weber growth of polycrystalline nickel films, Journal of Vacuum Science & Technology A: Vacuum, Surfaces, and Films **33** (2015), no. 2, 021504.
[90] K Zhang, F Zhu, C Huan, and A Wee, Effect of hydrogen partial pressure on optoelectronic properties of indium tin oxide thin films deposited by radio frequency magnetron sputtering method, Journal of Applied Physics **86** (1999), no. 2, 974–980.
[91] YM Zhou, Z Xie, HN Xiao, PF Hu, and J He, Effects of deposition parameters on tantalum films deposited by direct current magnetron sputtering, Journal of Vacuum Science & Technology A **27** (2009), no. 1, 109–113.
[92] G Zinsmeister, Theory of thin film condensation. Part B: Solution of the simplified condensation equation, Thin solid films **2** (1968), no. 5-6, 497–507.

7 Electrical Properties

In this chapter, the influence of the layer thickness together with the influence of deposition conditions and impurities on the thin film resistivity is discussed. In light of the constraint imposed on the layer thickness in order not to deteriorate the mechanical properties of the laminate (see Chapters 2 and 4), it is essential to properly evaluate the impact of a restricted layer thickness on the (electrical) properties of the film.

7.1. Introduction

The electrical properties of thin films are of importance in many technical applications such as in microelectronics, solar panels, optical filters, or sensor design. In addition to the scattering mechanisms already present in the bulk material, electrical conduction in a thin film is also troubled by other scattering contributions. When one of the dimensions of a conductor is restricted in the order of the mean free path length of an electron - typically in the order of tens of nanometers for metals - the film resistivity ρ_f increases vastly. This is known as the size-effect for conductors. The size effect sets a physical boundary to applications such as for interconnect paths in microelectronics [11] or coatings for low E-glass [30, 44] because the dimensions of the conducting film are already below the electron mean free path of most metals. Indeed, the size of interconnect paths in modern integrated circuits are of the order of 10 to 30 nm, while the film thickness of the silver layers for low E-coatings is typically 5 nm. Several theoretical models have been proposed in order to describe the main mechanisms responsible for this size effect. A good overview is given by M.A. Angadi [1]. Assuming each mechanism is described by an independent relaxation time, the different contributions to the total resistivity can be summed in accordance to Matthiessen's rule

$$\rho_f = \rho_0 + \rho_{ss} + \rho_{gb} \tag{7.1}$$

with ρ_0 the resistivity of the bulk metal with the same lattice fault density as the film, ρ_{ss} the external surface scattering contribution, and ρ_{gb} the grain boundary scattering contribution.

7.2. Influence of layer thickness

7.2.1. The Fuchs-Sondheimer model

The idea of an additional contribution attributed to electron scattering at external surfaces to explain the size-effect in thin film conductors was elaborated by Fuchs and Sondheimer, resulting in the Fuchs-Sondheimer (FS) model [34]. Briefly, this model describes the thin film resistivity as a function of a specularity parameter p, and the ratio between the film thickness h and the electron mean-free path l_0, i.e. $\lambda = h/l_0$. The parameter p ([0,1]) represents the fraction of electrons which are specularly reflected at the thin film surface, whereas $(1-p)$ represents the complementary fraction of diffusely scattered electrons. The Fuchs-Sondheimer equation can be summarized as

$$\rho_f = \rho_0 + \rho_{ss} \tag{7.2}$$

$$\rho_f = \rho_0 \, [1 - \frac{3}{2\lambda}(1-p)\int_1^\infty (\frac{1}{u^3} - \frac{1}{u^5})\frac{1-e^{-\lambda u}}{1-pe^{-\lambda u}}du]^{-1} \tag{7.3}$$

with $u = 1/cos(\theta)$ $(0 \leq \theta \leq \pi)$ the integration variable. In the case of total specular reflection, i.e. $p = 1$, the FS equation reduces to $\rho_f = \rho_0$. For the case $p \neq 1$, a size-effect is expressed by the fraction $(1-p)$ of diffusively scattered electrons. For thick films compared to the mean free path, i.e. $\lambda > 1$, the FS equation is simplified to [41]

$$\rho_f = \rho_0(1 + \frac{3}{8\lambda}(1-p)) \qquad \text{for } \lambda > 1 \tag{7.4}$$

Practically, and especially for sputter-deposited films, the reported layer thicknesses are restricted to 10 nm as the continuity of the films below this thickness is doubtful. For copper, with a relatively high mean-free path of 39 nm, this yields a lower limit for λ, i.e. $\lambda > 0.25$. Therefore, as very small values for λ are experimentally not obtained, equation (7.4) (with p=0) is an often used approximation for the full FS equation [31]. The equation thus predicts a $1/h$-dependency on the thickness.
Ezzat et al. showed that the thickness-dependent resistivity behavior of a single-crystal sputtered Ru film is properly approximated by the FS-model [13]. This is understood from the perspective that, within the FS-model, a thin film is modeled as a single-grained epitaxial layer and does not account for any contributions from defects, impurities or grain boundary scattering. As the grain sizes for as-sputter deposited thin films are of the same order of magnitude as the electron mean free path length in

metals [14], the additional electron scattering mechanism at grain boundaries can significantly contribute to the thin film resistivity. This latter effect was described by Mayadas and Shatzkes and summarized under the Mayadas-Shatzkes (MS) model.

7.2.2. The Mayadas-Shatzkes model

In the MS-model, the isotropic background scattering ρ_0, and the scattering contribution of the external surfaces ρ_{ss}, are combined with a contribution of grain boundary scattering ρ_{gb}, i.e. scattering at internal surfaces. The model approaches grain boundary scattering in a film by repetitive scattering of electrons to grain boundaries of parallel columnar grains oriented normal to the electrical field. This is reflected in the parameter α

$$\alpha(h) = \frac{l_0}{D(h)} \frac{R}{(1-R)} \tag{7.5}$$

where $D(h)$ represents the thickness-dependent grain size (see Chapter 5), l_0 the electron mean free path, and $0 \leq R \leq 1$ the grain boundary reflection coefficient. Figure 7.1 shows an illustration of how the electrical field is oriented in the film (cross-sectional view) respective to the orientation of the grains when the film resistivity is measured with a four-point probe. The electrical field, and consequently the electron transport, is parallel to the substrate and perpendicular to the grain orientation. The value for

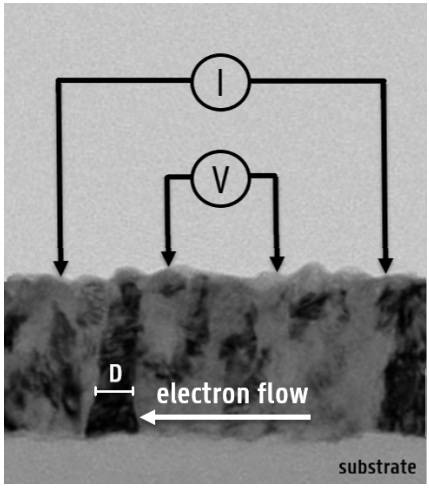

Figure 7.1. *Illustration of a four-point probe measurement on a thin film. The dimensions of the probes are not on the same scale as the film. The TEM image shows a cross-sectional view of a sputtered aluminum film (approx. 250 nm thick) grown in a contaminated environment of water vapor. Different grains are clearly distinguishable. D illustrates the in-plane grain size. TEM image adapted from [25].*

D in equation (7.5) thus refers to the in-plane grain size. When an XRD-measurement is performed on a sample, we typically measure the crystallographic coherence of different crystallographic domains through the thickness of the sample [38], i.e. the out-of-plane domain size. Atomic force microscopy (AFM), transmission electron microscopy (TEM) or scanning tunneling microscopy (STM) are techniques which are used to determine the in-plane dimension of grains. Based on the observations at the end of Chapter 5, the relation $D \sim h^{\alpha}$ was hardly affected by whether the in-plane domain sizes or the out-of plane domains sizes are reported [21]. Consequently, a comparable qualitative behavior between both can be expected. Different studies indicate however that, for sputter-deposited films, the out-of-plane domain sizes measured by XRD are also in good quantitative agreement with the in-plane domain sizes as measured by AFM [19], TEM [6], or STM [21]. Therefore, in what follows, the out-of-plane domain size as measured by XRD is used as a representative measure for the in-plane domain size and both in-plane and out-of-plane are simply referred to as the domain size D. In the MS model, the contribution of grain boundary scattering ρ_{gb} to the overall thin film resistivity ρ_f is given by

$$\frac{\rho_0}{\rho_{gb}} = 3\,[\frac{1}{3} - \frac{1}{2}\alpha + \alpha^2 - \alpha^3 ln(1+\frac{1}{\alpha})] \tag{7.6}$$

$$\begin{aligned} \frac{\rho_0}{\rho_{gb}} &\approx \left(1+\frac{3}{2\alpha}\right)^{-1} && \text{for } \alpha \gg 1 \\ \frac{\rho_0}{\rho_{gb}} &\approx \frac{3}{4\alpha} && \text{for } \alpha \ll 1 \end{aligned}$$

When the grain boundary contribution ρ_{gb} is combined with the Fuchs-Sondheimer contribution, the authors obtain (expression (15b) in Ref. [24])

$$\rho_f = [\frac{1}{\rho_{gb}} - \frac{6}{\pi\kappa_0\rho_0}(1-p)\int_0^{\frac{\pi}{2}} d\phi \int_1^{\infty} \frac{cos^2(\phi)}{H^2(u,\phi)}(\frac{1}{u^3} - \frac{1}{u^5})\frac{1-e^{-\beta}}{1-pe^{-\beta}}\,du]^{-1}$$

with

$$\begin{aligned} \beta &= \kappa_0 u H(u,\phi) \\ \kappa_0 &= t/l_0 \\ H(u,\phi) &= 1 + \alpha/cos(\phi)\sqrt{1-\frac{1}{u^2}} \end{aligned} \tag{7.7}$$

As an example, when combining the limiting case $\lambda > 1$ (equation (7.4)) with $\alpha \ll 1$ (equation (7.6)), the thin film resistivity is approximately given by [10]

$$\rho_f = \rho_0\left(1 + \frac{3}{8\lambda}(1-p) + \frac{3\alpha}{2}\right) \tag{7.8}$$

The FS contribution to the overall film resistivity scales as $1/\lambda \sim 1/h$. The MS contribution scales with $\alpha \sim 1/D(h)$ with $D(h) \sim h^{0.45}$ as shown in Chapter 5. With exception of very small thicknesses (< 30 nm), this behavior can however be fairly well approximated by a linear relationship, i.e. $D(h) \sim h$. As such, over a broad range of layer thicknesses, both the FS and MS contributions to the film resistivity yield approximately a $1/h$-behavior [3, 31]. It is therefore not always straightforward to distinguish between the relative magnitudes of the two mechanisms of interface scattering and grain boundary scattering in polycrystalline thin films. As pointed out in an extensive review by Sambles [31] and also by van Attekum et al. [36], separating the respective contributions of surface and grain-boundary scattering can be done by measuring the resistivity over a sufficiently large temperature range [42]. However, within polycrystalline thin films, the predictions by the FS-model vastly underestimate the measured resistivity [5] and in most cases grain boundary scattering is the dominant contribution to the film resistivity [11, 24, 35]. Similar observations can also be confirmed for as sputter-deposited films as outlined in the next sections.

7.2.3. Experiment

The applicability of the MS model was tested on the experimental data of the resistivity as a function of the layer thickness for copper and silver as presented in Figure 7.1. The MS equation (7.7) was numerically solved using MatLab. When fitting the MS model to the experimental data, it is important to choose physically relevant input parameters [31]. Besides the film thickness t, the electron mean free path l_0, and the specularity parameter p, all embedded in the Fuchs-Sondheimer (FS) model, the MS model demands an additional input for the domain size D and the grain boundary reflection coefficient R (see equation (7.4)). The experimental data of the thickness-dependent domain size for Cu and Ag as presented in Figure 5.3 are used as input for D. The product of $\rho_0 l_0$, a material dependent parameter, was kept constant and set to 16.7 $\Omega\ nm \times 39\ nm$ and 15.9 $\Omega\ nm \times 52\ nm$ for Cu and Ag respectively [44]. This embodies the thought that the chemical purity is not a function of the thickness. The experimental data were here fitted with only the grain boundary reflection coefficient R as fitting parameter. The value for p is affected by the interfaces and the atomic level surface roughness. As an example, the Soffer-model [32] introduces an angle-dependent specularity parameter based on the roughness of the scattering surface. For the fitting procedure presented here, the specularity parameter for the FS-model was set to zero, i.e. entirely diffuse scattering, which is common for sputter deposited thin films [10, 24, 34].

The MS model, with $p = 0$, could be properly fitted to the experimental data with a Pearson correlation coefficient > 0.99. The best fit

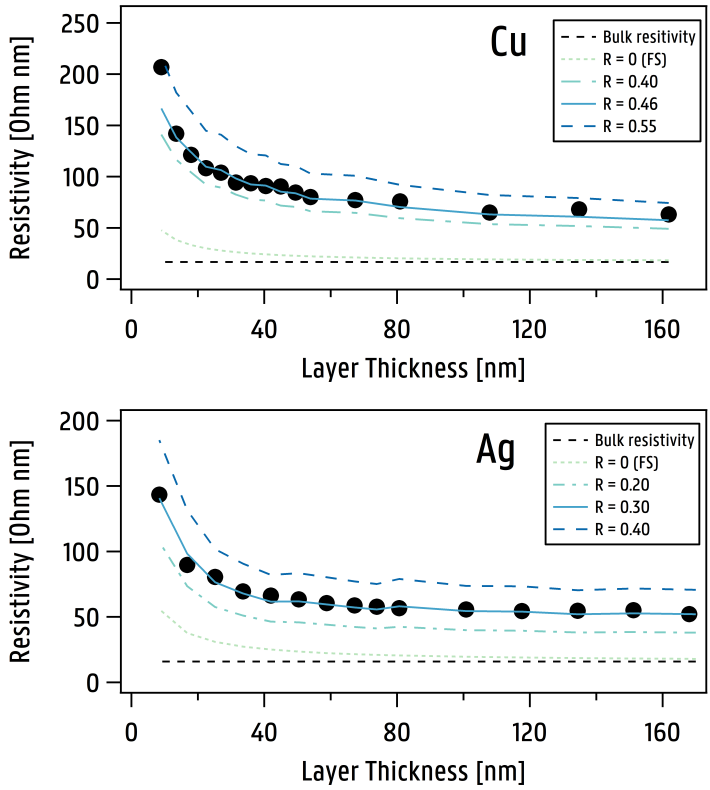

Figure 7.2. *The MS-model fitted to the resistivity as a function of the layer thickness for copper and silver.*

was found with $R = 0.46$ for Cu, and $R = 0.30$ for Ag as presented in Figure 7.1. These findings are in very good agreement with other values found for sputtered-deposited copper films in literature, i.e. $R = 0.44$ [35], $R = 0.46$ [44], or $R = 0.42$ [23]. A broad variation in the reported values for the reflection coefficient R of copper can however be found, in the range from $0.20 - 0.80$ [3, 10, 11, 42–44]. Many reasons can be given for this spread. At first, the implementation of the thickness-dependency of the grain size into the MS model (see equation 7.4) can largely affect R. In some cases experimental values are used [35], whereas in other cases the domain size is set equal to the layer thickness or is estimated by a relation, like $D \sim h$ [3, 24] or $D \sim h^{\alpha}$, with $\alpha = 0.43$ [1] as in the case of Chawla et al. [10]. Secondly, R depends on the deposition technique and the conditions during growth, which result in different types of grain-boundaries [42–44]. The grain size however seems not to affect the reflection coefficient [3, 10]. Finally, also the choice for p can strongly

[1] Notice the good agreement with the growth exponent derived in Chapter 5.

influence the obtained value for R [42]. For the case of silver, no reported values could be found to compare the obtained result other than "it appears to be smaller than 0.46" [44]. At least, this statement can be confirmed.

For the other materials studied in this work, i.e. constantan or chromel, a similar experiment as described above was performed. For these materials, no size-effect was however observed within our experimental thickness range. This could be explained by a smaller mean free path of the electrons in these materials. Metals with short mean-free paths l_0 are inherently less sensitive to surface or grain boundary scattering for a given layer thickness. As a result, such metal films may exhibit lower resistivities than Cu for sufficiently small dimensions despite their larger bulk resistivity (for example Cu (l_0 = 40nm) and Al (l_0=16 nm)) [11, 20, 28]. This opens perspectives for the use of material alternatives to copper such as aluminum or platinum-group metals [11].

7.3. Influence of deposition conditions

7.3.1. Experiment

Besides the layer thickness, the film resistivity is also affected by the deposition conditions during growth. In order to study the influence of the deposition conditions on the film resistivity, the effect of the layer thickness must first be ruled out. Therefore, all films in this experiment had a thickness of (350 ± 30) nm. Figure 7.3a summarizes the film resistivity of chromel thin films, deposited under different experimental conditions, as a function of $P \times d$, i.e. the product of the argon pressure P times the target-to-substrate distance d. The measurements were again repeated for constantan and showed a similar behavior (see Figure 7.3b). The resistivity measurements are presented as function of $P{\times}d$, as the resistivity is influenced by both the argon pressure P and the target-to-substrate distance d, but not unambiguously described by either of them. This behavior could be understood from the transport of the sputtered atoms. For an atom travelling through the gas phase, the probability for a collision event with a gas atom scales with the product of target-to-substrate distance and the argon pressure (see Figure 4.1). $P{\times}d$ is a direct measure for the thermalization of energetic species such as sputtered atoms and reflected neutrals. Therefore, $P{\times}d$ is a process parameter often related to energy and momentum flux towards the substrate [26, 33]. With this, it seems obvious to relate the resistivity behavior to the energy per arriving adatom (EPA, see Chapter 4). However, one has to be cautious to interpret these results solely from the perspective of energy. Indeed, the experiments show that the discharge current has a significant influence on the resistivity. The behaviour as function of the discharge current for both material systems is very comparable. However, the large difference

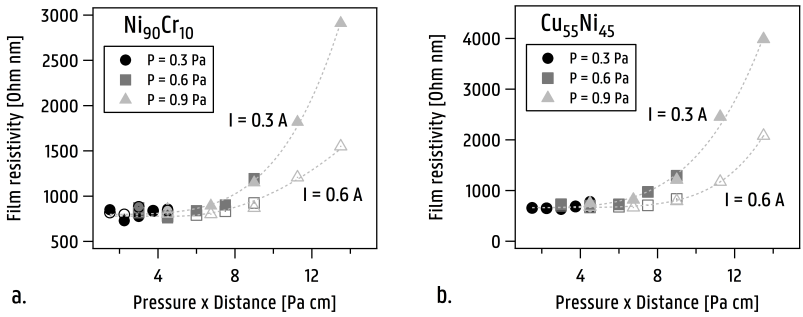

Figure 7.3. *The thin film resistivity of a) chromel and b) constantan as a function of argon pressure times target-to-substrate distance at two different deposition currents (closed markers: 0.3 A, open markers: 0.6 A).*

in resistive behaviour between the series deposited at different currents (0.3 A and 0.6 A) cannot be explained from the perspective of EPA as the influence of the current on EPA was shown to be very small (see Figure 4.4 Chapter 4). Inclusion of additional mechanisms or new driving parameters are thus needed to enable a complete understanding of this behavior. We focus on this topic in the next section.

7.4. Influence of impurities

When thin film growth occurs in a contaminated environment, impurities are incorporated into the growing film. It was concluded from Chapter 6 that incorporation of impurities into the growing film characterizes the grain refinement in a material-independent way when operating in the high-impurity regime, i.e. the impurity-to-metal ratio $\tau \gg 1$. From the perspective of the MS-model, small domain sizes account for a major contribution to the total thin film resistivity due to grain-boundary scattering. When the target-to-substrate distance is varied, one simultaneously changes the EPA and the impurity-to-metal impingement flux ratio. In order to discriminate between the effects of EPA and impurities on the thin film resistivity, it must be verified 1) how the resistivity is affected by variations in impurity-to-metal impingement flux ratio when variations in EPA are excluded 2) how the resitivity together with the domain size is affected by variations in EPA when the influence of impurities is excluded, and 3) how the resistivity evolves when both EPA and impurity-to-metal ratio are simultaneously changed.

Firstly, the resistivity as function of τ at constant EPA was investigated. The data are presented by the black round markers in Figure 7.4c. It is observed that the film resistivity is greatly affected in the high-impurity regime, but remains mainly unaffected in the low-impurity regime. Note that the resistivity data are presented here as the ratio of the bulk re-

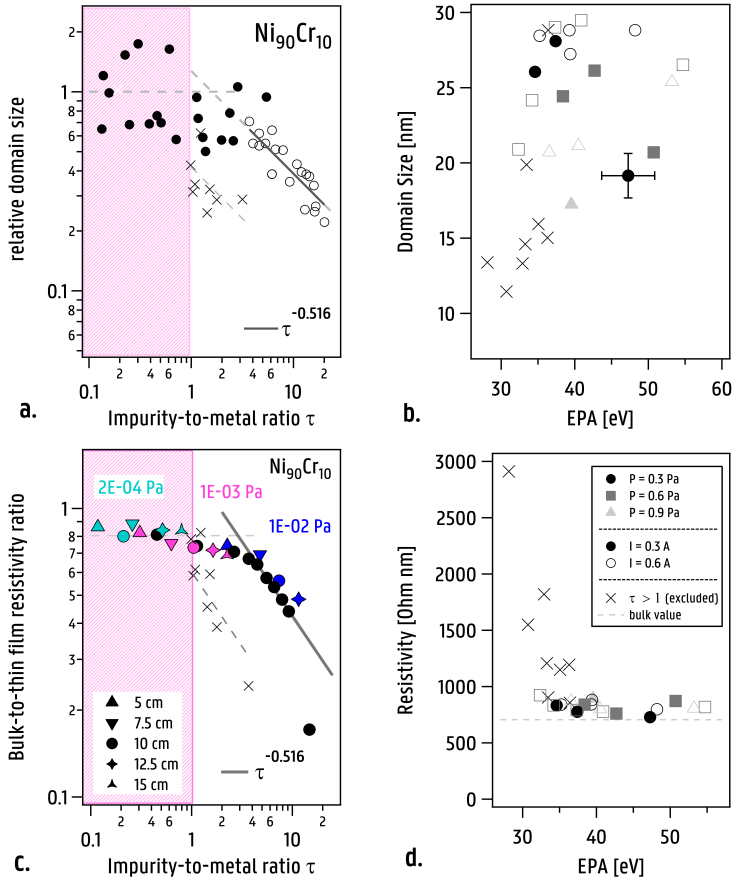

Figure 7.4. *(a) Domain size as function of the impurity-to-metal ratio. Data taken from Chapter 6. The gray line represents a fit to the data in the high-impurity regime.(b) The domain size as function of the EPA. The cross markers represents data for which $\tau > 1$. The error bars are valid for all data points but only presented on a single marker.(c) The bulk-to-thin film resistivity ratio as function of the impurity-to-metal ratio. The colored sets represent depositions at fixed argon pressure (0.3 Pa) and discharge current (0.3 A) and varying target-to-substrate distance. The gray line represents the power-law behavior of the domain size (see Chapter 6) and is a guide for the eye.(d) The resistivity as function of the EPA. The cross markers represent data for which $\tau > 1$.*

sistivity ρ_0 to the thin film resistivity ρ_f, i.e. ρ_0/ρ_f. In this way, the importance of the grain-boundary contribution to the film resistivity due to grain refinement in the high-impurity regime can be emphasized. As presented in equation (7.5), the ratio ρ_0/ρ_{gb} scales with D for large α. As depositions in the high-impurity regime result in small-grained films, it is expected that grain-boundary scattering is the dominant contribution to the total resistivity, and thus $\rho_0/\rho_{tf} \propto D$ [3]. This relation can indeed

be validated and is shown by the full gray line in Figure 7.4c. The line represents the relation $A\tau^{-0.516}$, with the proportionality factor A fitted to the resistivity data in the high-impurity regime. The exponent -0.516 originates from Chapter 6 (see Figure 7.4a).

Secondly, the influence of the EPA on both the domain size and the resistivity is studied for the data presented in Figures 7.4b and d. The data originate from the same depositions presented in Figure 7.3. The variations in EPA are caused by a variation of deposition parameters and thus different impurity-to-metal ratios. Therefore, only samples with $\tau < 1$ during growth, i.e. the low-impurity regime, should be included in order to exclude the influence of impurities on the domain size and film resistivity. The samples for which $\tau > 1$ are excluded from the test and represented by a cross marker. A Kendall-tau rank test is applied to evaluate a correlation between the domain size and EPA for the filtered data. The test indicates that no correlation exists between the EPA and the domain size ($\tau_K = 0.012$; $N = 19$) or between the resistivity and the EPA ($\tau_K = -0.193$; $N = 19$). However, when a Kendall-tau rank test [22] is applied on the entire dataset, the test indicates that the domain size and the EPA are clearly correlated ($\tau_K = 0.355$; $N = 27$), as well as the resistivity and the EPA ($\tau_K = -0.493$; $N = 27$). The observed correlation in the latter case is an example of a spurious correlation between the domain size and the EPA, driven by the deposition rate which acts as the confounding variable. It thus becomes clear that an evaluation of the impurity-to-metal ratio is essential in order to properly disentangle energy effects from impurity effects. Based on our observations, no influence of the EPA could be found in absence of impurity effects. Possibly, the EPA variations during as-deposited sputter deposition are too small to activate grain growth [16].

Finally, we added three additional data sets on the graph presented in Figure 7.4c. Each data set is deposited at a given background pressure while the target-to-substrate distance within each set was varied from 5 cm up to 15 cm. The variation in target-to-substrate distance causes a simultaneous variation in EPA and impurity-to-metal ratio (see Chapter 4). In the low-impurity regime (2×10^{-4} Pa - green markers), i.e. in abscence of impurity effects, it is again confirmed that the variations in target-to-substrate distance, and hence in EPA, have no influence on the resistivity. At a somewhat higher contamination level (1×10^{-3} Pa - pink markers), there is a small effect following the course of the increased impurity-to-metal ratio but again no distinguishable effect of energy is observed. In the high-impurity regime (1×10^{-2} Pa - blue markers), the behavior of the resistivity as function of an increased target-to-substrate distance is very similar to the behavior of the resistivity with increasing

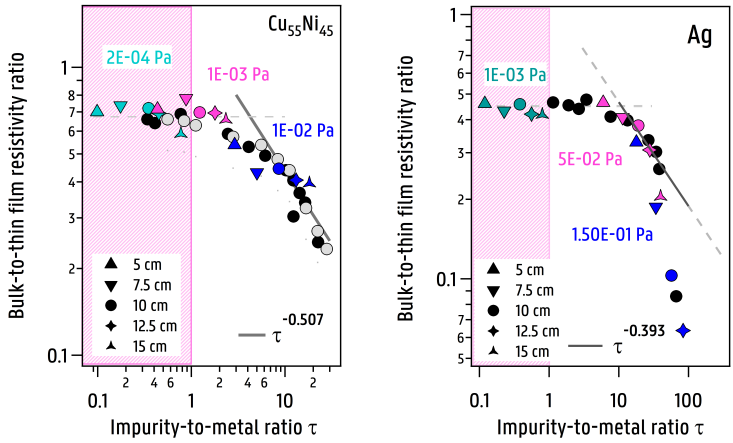

Figure 7.5. *The bulk-to-thin film resistivity ratio as function of the impurity-to-metal ratio for constantan (left) and silver (right). The colored sets represent depositions at fixed argon pressure (0.3 Pa) and discharge current (0.3 A) and varying target-to-substrate distance. The gray line represents the power-law behavior of the domain size (see Chapter 6) and is a guide for the eye.*

impurity-to-metal ratio. Analoguous results for constantan and silver are presented in Figure 7.5. In the case of silver however, a strong deviation from the predicted trend is observed for the extreme case of $\tau \approx 100$. Under these extreme conditions, island isolation by impurities and thus hindrance of a conductive path, or oxidation of the silver might contribute to this observation.

The excluded datapoints from Figures 7.4b and d, i.e. the cross markers for which $\tau > 1$, are also included in Figures 7.4a and c. In case of the latter, the data are however shifted towards lower impurity-to-metal ratios. The reason for this originates from a different experimental approach. The background pressures were only noted prior to the opening of the load lock and not prior to the deposition. As the load lock is pumped by a small rotation pump (a valve between the rotation pump and the vacuum chamber prevents oil from being sucked up), the obtained pressure in the load lock before opening towards the vacuum chamber remains relatively high, i.e. around 5×10^{-1} Pa, in comparison with the pressure in the vacuum chamber. Therefore, when the sample is introduced in the vacuum chamber for deposition, the actual background pressure is significantly higher than the value reported prior to the opening of the load lock. This explains the shift in impurity-to-metal ratio between both sets of data. Although the load lock was consistently pumped for all depositions until a pressure of 5 Pa was reached before opening, and thus the data points could be rescaled, it was chosen to present the data unaltered. However, in order to compare the behavior with the other datapoints already present on the graph, the relation $A \times \tau^{-0.516}$ was rescaled to fit

the data, with A the fitting parameter. This is presented by the dotted lines in Figures 7.4b and d. Despite the broad variation in deposition conditions present in the crossed markers, the overall behavior as a function of τ is again very analogous. Therefore, we can conclude that the effect of a varying target-to-substrate distance, or more general of varying deposition conditions, on the resistivity is not related to energetic effects but can be attributed to the changes in impurity-to-metal ratio linked to these variations in deposition conditions. Within our studied range, the effect of different deposition conditions can thus in good approximation be evaluated by projecting the conditions on the corresponding τ value.

When the literature is studied in this context, it is clear that a quantified treatment of impurities, in contrast to a qualitative treatment, is an often neglected aspect during thin film growth. Some studies which quantitatively report on the role of impurities during growth under the form of the ratio of impingement fluxes are the work of P. Barna et al. [4] on optical and mechanical properties of evaporated aluminum, the work of K. Ino et al. [17] on the effects of ion energy and ion flux on tantalum thin films, or more recently in a study by McClure presented in the 2019 Summer Bulletin of the society of vacuum coaters (SVC) [25]. However, the number of similar studies is very limited. In contrast, there is an abundant source of papers available where the influence of deposition conditions (here we focused on variations in the target-to-substrate distance and discharge power) on the structural, electrical, mechanical or optical properties of thin films are studied and explained from the perspective of energetic principles, but without any record of the deposition speed or base pressure prior to deposition which impedes a proper evaluation of the impurity-to-metal flux ratio. In many other cases, even with the good practice of the authors of reporting all details of base pressure and deposition speed, the possible effect of impurities is often overlooked. Table 7.1 gives an overview of the ranges over which the impurity-to-metal ratio τ has been (unintentionally) varied for some examples. The calculations for the range of τ are based on the data provided in the publications for the base pressure prior to deposition and the minimal and maximal deposition speeds. Note that the presented examples involve non-reactive depositions, i.e. reactive gas species are not intentionally present in the system. The results in Table 7.1 indicate that the range over which the impurity-to-metal ratio is varied can be very broad. For example, Duygulu et al. [12] performed experiments in a very clean environment at high deposition rates which causes the impurity-to-metal ratios to be small (low-impurity regime), whereas the deposition speeds reported by Anthony et al. [2] and Gopikishan et al. [15] are so low that, even at a residual gas pressure of 5×10^{-4} Pa, the impurity-to-metal ratios become very high. In case the variations in impurity-to-metal ratio are

Table 7.1. *Overview of different works linking a given property to a given deposition parameter and their respective unintentional variation in impurity-to-metal flux ratio τ.*

Reference	Material	Technique	Parameter	Property	τ
Duygulu et al. [12]	ZnO	RF-sputtering	T-S distance	grain size/resistivity	0.05-0.10
Nanto et al. [27]	ZnO	RF-sputtering	Substrate position	resistivity	0.24-2.32
Vopsaroiu et al. [39]	Cr	HiTUS	Cathode bias voltage	grain size	0.50-1.50
Pandharkar et al. [29]	Mo	DCMS	T-S distance	grain size/resistivity	1.03-2.06
Jeong et al. [18]	AZO	RF-sputtering	T-S distance	grain size/resistivity	0.67-5.81
Vasant Kumar et al. [37]	ITO	RF-sputtering	T-S distance	resistivity	0.67-10.2
Lee et al. [8]	ITO	RF-sputtering	Background pressure	resistivity	1.13-79.9
Antony et al. [2]	ITO	RF-sputtering	T-S-distance	grain size/resistivity	42.8-124.71
Gopikishan et al. [15]	Cu	DCMS	T-S distance	grain size	53.6-536.2

so large that we end up in a high-impurity regime, the results must be interpreted with great caution. Even for the smaller variations in impurity-to-metal flux ratio, the effect can be relevant. For example, Vopsaroiu et al. [39] reports on a technique to control the grain size by means of a bias voltage applied on the cathode. They report on an increase of the domain size of Cr from 12.3 nm to 16.2 nm by tuning the bias voltage on the cathode from -200 V up to -800 V. These latter authors correlate the grain size growth to an increased energy of the ions [40]. However, the observed increase in domain size can as well be described by the decreased impurity-to-metal ratio when the bias voltage on the cathode, and thus the deposition rate, is increased. Indeed, the reported deposition conditions allows us to calculate the variation in impurity-to-metal ratio from τ=0.50 (-800 V) up to τ=1.50 (-200 V). Based on the measurements of the domain size of chromium as function of the impurity-to-metal ratio presented in Chapter 6, a decrease of the domain size from 16.1 nm (τ=0.50) up to 12.7 nm (τ=1.50) is expected solely from the perspective of an increased impurity-to-metal ratio at constant EPA. These predicted variations in domain size are in good agreement with the reported values by Vopsaroiu et al., but are here explained from the point-of-view of an increased impurity-to-metal ratio and not from the perspective of energetic principles. This example again emphasizes the importance for a quantitative approach with regard to impurities.

A last remark in this context is related to pulsed deposition processes. DC magnetron sputtering (DCMS) as a continuous deposition technique has evolved the last years towards more complex oscillatory and pulsed processes such as pulsed magnetron sputtering (p-DCMS) or high power impulse magnetron sputtering (HiPIMS). p-DCMS is mainly suited for the deposition of non-conductive dielectric materials (silica, alumina, ...), whereas the use of HiPIMS is attractive for applications depending on high-density films. These latter processes, especially HiPIMS, are finding their way into industry, for example in the hard-coating industry. No studies have however been performed on the impact of the impurity-to-metal flux ratio during a pulsed deposition process such as HiPIMS or pulsed laser deposition as compared to a continuous deposition process as DC magnetron sputtering (DCMS). For example, a recent study [9] investigated the electrical resistivity of copper films (20-800 nm) deposited by HiPIMS. The electrical and microstructural properties were then compared to films deposited by DCMS under comparable conditions. The base pressure in their system was 3×10^{-4} Pa, the target-to-substrate distance was fixed at 9 cm and an average power of 100 W was kept constant for both HiPIMS and DCMS. The deposition rate was found to be 0.47 nm/s for the HiPIMS samples, compared to 1.0 nm/s for the samples deposited by DCMS. At the same average film thickness, the HiPIMS Cu

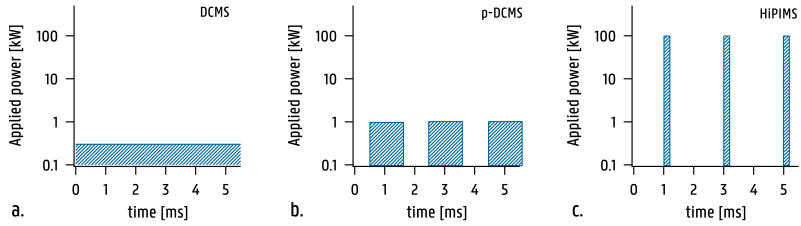

Figure 7.6. *The applied power as a function of time during a) DC magnetron sputtering (DCMS), b) pulsed magnetron sputtering (p-DCMS), and c) high power impulse magnetron sputtering (HiPIMS). During DCMS the power is continuously applied. During p-DCMS, the power is pulsed with an on-time of a few milliseconds (ms), with a duty cycle between 10 to 90 %. For HiPIMS, the on-time is between 10 to 500 microseconds (μs), with a duty cycle between 0.5 to 2 %. Figure adapted from Ref. [7].*

films have larger grains (≈ factor 2) compared to the DCMS samples. The electrical resistivity of the samples deposited by HiPIMS were consistently lower than for DCMS. The authors explain the differences based on the impingement of high energetic species present in the HiPIMS discharge which affect the adatom mobility and grain-boundary diffusion. Of course, this is an interesting and convincing argument. However, in light of the discussion above, an additional argument can be thought of. Whereas DCMS is a continuous process, HiPIMS is a pulsed process (see Figure 7.6). If one would calculate the deposition rate based on the on-time (duty cycle of 2%) instead of the total growth time, one ends up with much higher deposition rates in the case of HiPIMS, i.e. 23.33 nm/s. Therefore, the impurity-to-metal ratios are much lower, i.e. $\tau = 0.01$, as we have a much more concentrated material flux during pulsed processes compared to a continuous process. This lower τ-value, i.e. almost 20 times smaller than the τ-value for the DC case, could also contribute to the observations done by Cemin et al. [9]. However, during the off-time (98%) of the HiPIMS discharge, the film is exposed to the impurity flux. This difference in interaction with impurities could also result in a difference in growth. Whether this is a valid argument, asks for further studies.

7.5. Conclusion

As the conclusions from Chapter 2 indicated that a reduced layer thickness restricts the impact of the embedded film on the mechanical properties of the laminate, the effect of a reduced layer thickness on the electrical properties was studied in the first section of this chapter. It was shown that, for as-sputter deposited films, the increase in resistivity with decreasing layer thickness is mainly attributed to enhanced grain boundary scattering as described by the Maydas-Shatzkes model. For copper and silver, the best fitting results obtained $R = 0.46$, and $R = 0.30$ respectively,

with R the grain-boundary reflection coefficient. Sections 3 and 4 discuss the effect of the deposition conditions on the resistivity from the perspective of energy per arriving particle (EPA) and impurity-to-metal ratio τ. It was shown that a proper evaluation of the impurity-to-metal ratio is essential in order to disentangle energy effects from impurity effects. Within the studied experimental range, the changes in film resistivity under influence of varying deposition conditions could not be related to energetic effects, but rather to the effect of impurities. The effect of different deposition conditions can in good approximation be evaluated by projecting the conditions on the corresponding τ value. The resistivity was not significantly affected by the deposition conditions as long as the impurity-to-metal ratio is low. In the high-impurity regime, enhanced grain-boundary scattering due to the grain-refinement was shown to be the dominant contribution to the film resistivity.

References

[1] MA Angadi, Some transport properties of transition metal films, Journal of materials science **20** (1985), no. 3, 761–796.

[2] A Antony, M Nisha, R Manoj, and MK Jayaraj, Influence of target to substrate spacing on the properties of ITO thin films, Applied Surface Science **225** (2004), no. 1-4, 294–301.

[3] N Artunc and ZZ Ozturk, Influence of grain-boundary and surface scattering on the electrical resistivity of single-layered thin copper films, Journal of Physics: Condensed Matter **5** (1993), no. 5, 559–566.

[4] PB Barna, M Adamik, U Kaiser, S Laux, H Bangert, M Pulliainen, and KA Pischow, Structure related optical and mechanical properties of oxygen doped Al films, Surface and Coatings Technology **100-101** (1998), 72–75.

[5] M Birkett and R Penlington, Electrical resistivity of CuAlMo thin films grown at room temperature by dc magnetron sputtering, Materials Research Express **3** (2016), no. 7, 075021.

[6] BR Braeckman, F Misják, G Radnóczi, M Caplovicova, P Djemia, F Tetard, L Belliard, and D Depla, The nanostructure and mechanical properties of nanocomposite Nbx-CoCrCuFeNi thin films, Scripta Materialia **139** (2017), 155–158.

[7] N Britun, S Konstantinidis, and R Snyders, Diagnostics of Magnetron Sputtering Discharges by Resonant Absorption Spectroscopy, Plasma Science and Technology - Progress in Physical States and Chemical Reactions, InTech, apr 2016.

[8] HL Byung, LG Kim, SW Cho, and SH Lee, Effect of process parameters on the characteristics of indium tin oxide thin film for flat panel display application, Thin Solid Films **302** (1997), no. 1, 25 – 30.

[9] F Cemin, D Lundin, D Cammilleri, T Maroutian, P Lecoeur, and T Minea, Low electrical resistivity in thin and ultrathin copper layers grown by high power impulse magnetron sputtering, Journal of Vacuum Science & Technology A: Vacuum, Surfaces, and Films **34** (2016), no. 5, 051506.

[10] JS Chawla, F Gstrein, KP O'Brien, JS Clarke, and D Gall, Electron scattering at surfaces and grain boundaries in Cu thin films and wires, Physical Review B **84** (2011), no. 23, 235423.

[11] S Dutta, K Sankaran, K Moors, G Pourtois, S Van Elshocht, J Bömmels, W Vandervorst, Z Tőkei, and C Adelmann, Thickness dependence of the resistivity of platinum-group metal thin films, Journal of Applied Physics **122** (2017), no. 2, 025107.

[12] NE Duygulu and AO Kodolbas, Investigation of DTS effect on rf magnetron sputtered ZnO thin films, Crystal Research and Technology **51** (2016), no. 3, 189–196.

[13] SS Ezzat, PD Mani, A Khaniya, W Kaden, D Gall, K Barmak, and KR Coffey, Resistivity and surface scattering of (0001) single crystal ruthenium thin films, Journal of Vacuum Science & Technology A: Vacuum, Surfaces, and Films **37**

(2019), no. 3, 031516.
[14] D Gall, Electron mean free path in elemental metals, Journal of Applied Physics **119** (2016), no. 8, 085101.
[15] S Gopikishan, I Banerjee, Anand Pathak, and SK Mahapatra, Axial distribution of plasma fluctuations, plasma parameters, deposition rate and grain size during copper deposition, Radiation Effects and Defects in Solids **172** (2017), no. 7-8, 545–554.
[16] CRM Grovenor, HTG Hentzell, and DA Smith, The development of grain structure during growth of metallic films, Acta Metallurgica **32** (1984), no. 5, 773–781.
[17] K Ino, T Shinohara, T Ushiki, and T Ohmi, Ion energy, ion flux, and ion species effects on crystallographic and electrical properties of sputter-deposited Ta thin films, Journal of Vacuum Science & Technology A: Vacuum, Surfaces, and Films **15** (1997), no. 5, 2627–2635.
[18] SH Jeong and JH Boo, Influence of target-to-substrate distance on the properties of AZO films grown by RF magnetron sputtering, Thin Solid Films **447** (2004), 105–110.
[19] V Kapaklis, P Poulopoulos, V Karoutsos, T Manouras, and C Politis, Growth of thin Ag films produced by radio frequency magnetron sputtering, Thin Solid Films **510** (2006), no. 1-2, 138–142.
[20] P Kapur, JP McVittie, and KC Saraswat, Technology and reliability constrained future copper interconnects. I. Resistance modeling, IEEE Transactions on Electron Devices **49** (2002), no. 4, 590–597.
[21] V Karoutsos, M Toudas, A Delimitis, S Grammatikopoulos, and P Poulopoulos, Microstructural evolution in nanostructured gold films, Thin Solid Films **520** (2012), no. 11, 4074–4079.
[22] MG Kendall, Rank Correlation Methods., Biometrika **44** (1957), no. 1/2, 298.
[23] H Marom, J Mullin, and M Eizenberg, Size-dependent resistivity of nanometric copper wires, Physical Review B **74** (2006), no. 4, 045411.
[24] AF Mayadas and M Shatzkes, Electrical-resistivity model for polycrystalline films: the case of arbitrary reflection at external surfaces, Physical review B **1** (1970), no. 4, 1382.
[25] DJ McClure, Contamination in Vacuum Coatings Due to Water Vapor, 61st Annual Technical Conference Proceedings, Society of Vacuum Coaters, oct 2018.
[26] T Motohiro and Y Taga, Monte Carlo simulation of the particle transport process in sputter deposition, Thin solid films **112** (1984), no. 2, 161–173.
[27] H Nanto, T Minami, S Shooji, and S Takata, Electrical and optical properties of zinc oxide thin films prepared by rf magnetron sputtering for transparent electrode applications, Journal of applied physics **55** (1984), no. 4, 1029–1034.
[28] C Pan and A Naeemi, A proposal for a novel hybrid interconnect technology for the end of roadmap, IEEE Electron Device Letters **35** (2013), no. 2, 250–252.
[29] SM Pandharkar, SR Rondiya, AV Rokade, BB Gabhale, HM Pathan, and SR Jadkar, Synthesis and Characterization of Molybdenum Back Contact Using Direct Current-Magnetron Sputtering for Thin Film Solar Cells, Frontiers in Materials **5** (2018), 13.
[30] M Philipp, Electrical transport and scattering mechanisms in thin silver films for thermally insulating glazing, Ph.D. thesis, Saechsische Landesbibliothek-Staats- und Universitaetsbibliothek Dresden, 2011.
[31] JR Sambles, The resistivity of thin metal films—some critical remarks, Thin Solid Films **106** (1983), no. 4, 321–331.
[32] SB Soffer, Statistical model for the size effect in electrical conduction, Journal of Applied Physics **38** (1967), no. 4, 1710–1715.
[33] RE Somekh, The thermalization of energetic atoms during the sputtering process, Journal of Vacuum Science & Technology A: Vacuum, Surfaces, and Films **2** (1984), no. 3, 1285–1291.
[34] EH Sondheimer, The mean free path of electrons in metals, Advances in physics **1** (1952), no. 1, 1–42.
[35] T Sun, B Yao, AP Warren, K Barmak, MF Toney, RE Peale, and KR Coffey, Dominant role of grain boundary scattering in the resistivity of nanometric Cu films, Physical Review B **79** (2009), no. 4, 041402.
[36] PM Van Attekum, PH Woerlee, GC Verkade, and AAM Hoeben, Influence of grain boundaries and surface Debye temperature on the electrical resistance of thin gold films, Physical Review B **29** (1984), no. 2, 645.

[37] CVR Vasant Kumar and A Mansingh, Effect of target-substrate distance on the growth and properties of rf-sputtered indium tin oxide films, Journal of Applied Physics **65** (1989), no. 3, 1270–1280.
[38] Y Von Kaenel, J Stiegler, E Blank, O Chauvet, Ch Hellwig, and K Plamann, Microstructure evolution and defect incorporation in highly oriented and textured CVD diamond films, physica status solidi (a) **154** (1996), no. 1, 219–238.
[39] M Vopsaroiu, G Vallejo Fernandez, MJ Thwaites, J Anguita, PJ Grundy, and K O'grady, Deposition of polycrystalline thin films with controlled grain size, Journal of Physics D: Applied Physics **38** (2005), no. 3, 490.
[40] M Vopsaroiu, MJ Thwaites, G Vallejo Fernandez, S Lepadatu, and K O'Grady, Grain size effects in metallic thin films prepared using a new sputtering technology, Journal of Optoelectronics and Advanced materials **7** (2005), no. 5, 2713–2720.
[41] F Warkusz, Size Effects in Metallic Films, ElectroComponent Science and Technology **5** (1978), no. 2, 99–105.
[42] W Wu, SH Brongersma, M Van Hove, and K Maex, Influence of surface and grain-boundary scattering on the resistivity of copper in reduced dimensions, Applied physics letters **84** (2004), no. 15, 2838–2840.
[43] AE Yarimbiyik, HA Schafft, RA Allen, MD Vaudin, and ME Zaghloul, Experimental and simulation studies of resistivity in nanoscale copper films, Microelectronics Reliability **49** (2009), no. 2, 127–134.
[44] W Zhang, SH Brongersma, O Richard, B Brijs, R Palmans, L Froyen, and K Maex, Influence of the electron mean free path on the resistivity of thin metal films, Microelectronic Engineering **76** (2004), no. 1-4, 146–152.

8 Thermoelectric properties

Temperature sensors for real industrial applications must survive hostile environments, provide high accuracy, long-term stability and reliability, and cannot interfere or obstruct the operation of the host component. In contrast to conventional wire thermocouples which are mostly attached to the surface, an approach of an embedded thin films sensor seems therefore favorable to protect the sensor from oxidation, chemical corrosion, wear or contamination [39]. Furthermore, an embedded sensor guarantees minimal interference of the sensor with the mode of operation of the host structure. Thin film thermocouples (TFTCs) are a promising approach to operate as an embedded temperature sensor inside composite materials. Additionally, because of their very small thermal mass, they have a very fast response time (order of nanoseconds). The sensitivity of the thin film thermocouples depends however on the process conditions during deposition. In analogy to the discussion on the electrical properties in the previous chapter, this chapter discusses the influence of the layer thickness, the deposition conditions and residual gas impurities on the Seebeck coefficient of sputter-deposited metal thin films.

8.1. Introduction

The Seebeck effect is a thermoelectric effect which describes the build-up of an electric potential difference over the ends of a conductor under influence of a temperature difference. The working principle of a thermocouple is based on this effect. A thermocouple consists of two dissimilar conductors connected in an open-circuit junction. The open-circuit voltage over the unpaired ends allows to measure a relative temperature difference between the junction and the environment. Thermocouples are a convenient approach to measure temperature in ranges or environments - from outer space, to temperature measurements within living cells or

combustion engines - where more classical thermometers are hindered to operate. Nickel-based alloys are a widely used material choice for thermocouples because they are inexpensive, have a high melting point, a good long-term thermal stability, and a good resistance against corrosion at elevated temperatures. Some of the most commonly used types of nickel-based alloy thermocouples are the K-type: chromel ($Ni_{90}Cr_{10}$) - alumel ($Ni_{95}Al_2Mn_2Si_1$), J-type: iron (Fe) - constantan ($Cu_{55}Ni_{45}$) or E-type: chromel - constantan, and can measure in a temperature range of -200 $°C$ up to 1350 $°C$, -40 $°C$ up to 750 $°C$, and -50 $°C$ up to 740 $°C$, respectively. The sensitivities of K, J, and E-type thermocouples are respectively given by $\approx$ 38.7, 50.4, and 67.3 $\mu V/°C$. Thermocouples are mostly fabricated from wires. Thermocouples in a thin film format however can be very attractive for numerous applications as they have reduced dimensions, a very low mass and a very fast response time [8, 22, 23, 33]. To give some examples, thin film thermocouples are used for monitoring local temperature distributions [24] on solid oxide fuel cells [16], on integrated-circuits [25], or are applied for monitoring sudden temperature changes [17] such as in turbine engines for aerospace applications [28], or in cutting tools for machining explosive materials [38].

8.2. Seebeck coefficient

The Seebeck effect describes the observation of an induced electrical potential difference δV when a temperature difference δT is applied over a metal or semiconductor. The Seebeck coefficient is defined as the change in thermoelectric potential with temperature, i.e.

$$S = \frac{\delta V}{\delta T} \qquad [\frac{V}{^\circ C}] \tag{8.1}$$

The buildup of a thermoelectric potential difference ΔV, typically in the micro- to millivolt range, is a consequence of the diffusion of charge carriers [13]. As the average energy of electrons in the hot region is higher than in the cold region, charges move from the hot to the cold side, leading to a gradient in the number of charge carriers. At equilibrium, the charge carrier transport is balanced by the buildup of an internal electrical field. An analytical expression for the Seebeck coefficient can be derived [21]. Suppose that a small temperature difference δT results in a thermoelectric potential δV. For an electron diffusing from the hot region to the cold region, an amount of work $-e\delta V$ has to be delivered, decreasing the average electron energy δE_{avg}. At equilibrium [21]

$$-e\delta V = E_{avg}\,(T + \Delta T) - E_{avg}\,(T) \tag{8.2}$$

with

$$E_{avg}\,(T) = \frac{3}{5} E_F \left[1 + \frac{5\pi^2}{12}\left(\frac{kT}{E_F}\right)^2\right] \tag{8.3}$$

Substituting equation (8.3) into equation (8.2), expanding $(T + \Delta T)$ and neglecting δT^2 obtains

$$-e\delta V \approx \frac{\pi^2 k^2 T \delta T}{2E_F} \tag{8.4}$$

Substituting equation (8.1) into equation (8.4), an expression for the Seebeck coefficient S can be given by

$$S \approx -\frac{\pi^2 k^2 T}{2eE_F} \tag{8.5}$$

Typically, metals have a high charge carrier concentration and thus a high electrical conductivity but a low Seebeck coefficient, whereas semiconductors have a low charge carrier concentration and a low electrical conductivity, but a high Seebeck coefficient [1]. The type of majority charge carriers, i.e. holes or electrons, determines the sign of the Seebeck coefficient. A superconductor below its transition temperature shows no thermoelectric effect at all. Consequently, the absolute Seebeck coefficient of a conductor can be measured by connecting it in a circuit with a superconductor below its transition temperature [26]. In practice, the absolute Seebeck coefficient of a conductor is measured in comparison to tabulated standard metals.

When two dissimilar conductors are connected in a closed circuit with a temperature difference over both ends, a thermoelectric current will flow in the circuit. When a similar circuit is composed of the same conductor, no current will flow in the circuit due to symmetry. In order to observe thermoelectricity in a circuit, it is thus necessary to have a circuit composed of two different conductors [26], or the same material in two different states (for an example see Chapter 9). The thermoelectric potential over the circuit is a consequence of the difference in the work function, i.e. the energy needed to remove an electron from a solid, of the constituting conductors in the junction. In case of a thermocouple, an open-circuit is used and the total current in the circuit is zero. With the total electric current density J given by the sum of the ohmic and thermoelectric contribution, we obtain

$$J = \sigma(-\Delta V - S\Delta T) = 0 \tag{8.6}$$

and thus

$$\Delta V = \Delta S \Delta T \tag{8.7}$$

[1] Although semiconductors have higher Seebeck coefficients than metals, these materials are not studied in this work as these materials can quite often only be RF-sputter deposited which hinders to upscale the obtained results to industrial applications. Furthermore, they are more expensive and have a more complex charge carrier transport mechanism.

with

$$\Delta S = S_1 - S_2 \tag{8.8}$$

where S_1 and S_2 represent the absolute Seebeck coefficients of the constituting conductors in the thermocouple. Given equation (8.6), the thermoelectric potential over a thermocouple circuit, consisting of two conductors 1 and 2, is given by

$$V_{12} = \int_{T_0}^{T} (S_1 - S_2) dT = \int_{T_0}^{T} (S_{12}) dT \tag{8.9}$$

Substituting equation (8.5) into (8.9), yields - after integration - the following relation [21]

$$V_{12} = a\Delta T + b\,(\Delta T)^2 \tag{8.10}$$

According to equation (8.6), the thermocouple output is not linear with the temperature difference. However, if $\Delta T/T \ll 1$ (with T in Kelvin), the relation is in good approximation linear [26].

8.2.1. Experimental determination of the film Seebeck coefficient

In order to measure the Seebeck coefficient of a thin film, the thin film is brought in a thermocouple junction with a wire with a known Seebeck coefficient. This is illustrated for the measurement of the Seebeck coefficient for a constantan thin film in Figure 8.1(left). At first, the thin film is deposited on glass and patterned using a sputter mask (35 mm $\times$ 90 mm) in a shape as presented in Figure 8.1. After deposition, a complementary bulk wire is soldered onto the thin film in order to form a E-type thermocouple (in case of the example $Cu_{55}Ni_{45}$(film) + $Ni_{90}Cr_{10}$(wire)). The Seebeck measurements are performed with a home-built system. The setup consists of a heating element (MeiVac substrate heater) and a water-cooled copper block, separated over a distance of $\approx$ 8 cm. The bimetallic film-wire junction of the sample is centered on the heating element, whereas the electrodes are centered on the copper block. Thermal paste (Dow Corning) was applied at both ends of the glass substrate in order to enhance the heating or cooling transfer. The water-cooled copper block is kept at a constant temperature, i.e. $T_{cold} \approx 11\ ^\circ C$. The heating element is PID-controlled and ramps from room temperature to 60 °C at a rate of 1 °C/min, i.e. T_{hot}. Due to the imposed temperature difference, an open-circuit thermoelectric voltage arises at the electrodes of the film-wire thermocouple. The output of the thermocouple is logged by means of a TC01 (National Instruments), a thermocouple measurement device with built-in software for data acquisition. In order to provide a good electrical contact with the film for the read-out, a fine copper brush is clamped onto the thin film. The wires from the electrodes towards the input terminals of the TC01 are also made out of copper. The hot junction and cold junction temperature are measured by means of a conventional

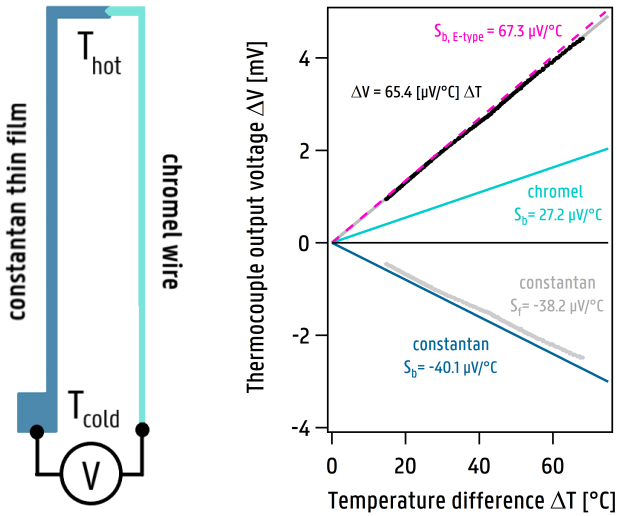

Figure 8.1. *(left) Representation of the film-wire thermocouple used to measure the Seebeck coefficient of the film. (right) Example of a voltage-temperature output data of a constantan film - chromel wire thermocouple (black markers). Within the experimental temperature range, the behavior is in good approximation linear. The slope determines the Seebeck coefficient and is found to be 65.4 ± 1.76µV/°C. The pink, green and blue lines represent the calculated output for the bulk E-type thermocouple, for a chromel wire and a constantan wire respectively. The gray markers represent the calculated output data of the constantan film based on the black markers and corrected for the Seebeck contribution of chromel. The slope of the gray data yields the Seebeck coefficient of the constantan film, i.e. -38.2 ± 1.76µV/°C.*

K-type thermocouple. A Labview code manages all the data and plots the measured voltage as a function of the temperature difference between the hot and cold junction. In accordance to equation (8.1), a straight line is fitted to the data (≈ 200 measurement points) and the slope of this line is used to determine the Seebeck coefficient.
An example of a voltage-temperature output of a constantan film - chromel wire thermocouple is shown in Figure 8.1 (right). The output of the film-wire thermocouple is represented on the graph by the black dots. Within the temperature range of the experiment, the voltage-temperature behavior is in good approximation linear. A fit to the data yields a value for the Seebeck coefficient of 65.4 $\mu V/°C$. With an absolute Seebeck coefficient of a chromel wire and a constantan wire of 27.2 (green line) and -40.1 $\mu V/°C$ (blue line) respectively, the Seebeck coefficient of an E-type wire thermocouple is given by 67.3 $\mu V/°C$ (pink striped line) [15]. The Seebeck coefficient of the constantan film is then calculated as $S_{f,CuNi} = S_{b,NiCr} - S_{fb,E-type} = -38.2\ \mu V/°C$ as presented by the gray markers. The error on the determined Seebeck coefficient is 1.76 $\mu V/°C$. The reported value for the thin film Seebeck coefficient in

this example is thus in close vicinity of the reported value for the bulk wire. The value for the thin film Seebeck coefficient is however strongly dependent on the process conditions during deposition. This will be the topic of section 8.4. First, the influence of the layer thickness on the Seebeck coefficient is discussed.

8.3. Role of Layer Thickness

It was discussed in Chapter 7 that the electrical properties of a thin metal film deviate from the bulk as soon as one of the dimensions of the film is restricted in the order of the electron mean free path length, a phenomenon referred to as a size-effect. In case of the thermoelectric film properties, the discussion is similar as for the electrical film properties. In analogy to the Fuchs-Sondheimer model describing the size-effect in thin film conductors, a similar model was proposed by Mayer [27] in order to describe the size-effect in thermoelectric film properties. According to the model of Mayer, the deviation of the thin film Seebeck coefficient from the bulk value scales with the inverse of the layer thickness, i.e. $|S_B - S_F| = |\Delta S_F| \sim l_0/t$. This behavior can indeed be verified by an abundant amount of experimental data present in literature. For example, this is reported for sputtered $Ni_{90}Cr_{10}$ [39], for evaporated Cu [8, 31, 35, 37], Ag [20, 32, 37], Au [20], Al [10], Fe [33], Sn [1], Sb [6], Bi films [6, 9, 29], or electron-beam evaporated Ni [5].
It was already shown in Chapter 5 that, for thin films grown by physical vapor deposition, the domain size increases with the film thickness, i.e. $D \sim t^{\chi}$, with χ a value between 0.4 and 0.5. Variations in film thickness are thus linked with variations in the domain size. The thinner the film, the smaller the resulting domains. Typically, for as-sputter deposited thin films, $D < t$ (see Chapter 5). As already discussed in Chapter 7, when electrons flow through a thin film under influence of an electric field (resistivity) or temperature difference (thermoelectricity), the net flow of diffusing electrons is parallel to the substrate and thus perpendicular to the out-of-plane growth direction of the grains (see Figure 7.1 Chapter 7). In analogy to the Mayadas-Shatzkes model, Deschacht et al. [12] elaborated an analytical model for the description of the thermoelectric power of polycrystalline films, taking into account the effects of grain boundary scattering. The possibility of a strong effect of grain boundary scattering on the Seebeck coefficient was also already noted by other authors [3–5]. Therefore, in analogy to the electrical properties discussed in the previous chapter, the size-dependent effects are likely to be related to variations in D [34]. Elaborated experimental studies on the Seebeck coefficient of sputtered thin films presenting the influence of the deposition conditions, or proofing the dominant character of the domain size, are however scarce [2, 3].

8.4. Effect of deposition conditions and impurities

The influence of the deposition conditions on the Seebeck coefficient are experimentally investigated for sputter deposited copper (Cu) and constantan ($Cu_{55}Ni_{45}$) thin films. Both materials are chosen as they exhibit a large difference in electrical properties and are the constituting materials of T-type thermocouples. In what follows, the layer thickness is kept constant (350 ±30 nm) for all depositions in order to exclude the influence of the layer thickness from the discussion.

8.4.1. Experiment

In a first experiment, the influence of the presence of impurities on the Seebeck coefficient is studied. In analogy to the experiments performed in Chapter 6 and 7, this was done by leaking atmospheric air into the chamber by means of a mass flow controller (MKS). In a second series of experiments, thin films were deposited at different discharge currents, and the impact on the Seebeck coefficient was studied. The discharge current was varied between 0.1 and 0.6 *A*. The experiments were repeated for two different background pressures (3.5×10^{-3} Pa and 7.5×10^{-3} Pa). To exclude any effects related to target erosion and/or chamber heating, the discharge current experiments were performed in a random way.
The samples discussed in both experiments are deposited in a cuboid stainless steel vacuum chamber with a volume of approximately 0.25 m^3. The used sputter targets are two inch circular planar copper and constantan targets (Testbourne, purity 99.99%). If not otherwise specified, the discharge current is 0.6 *A* and the background pressure lower than 5×10^{-4} Pa. The target-to-substrate distance and the argon pressure were kept constant during all depositions at 10 cm and 0.6 Pa. Also the pumping speed was kept constant (≈ 75 l/s) and the substrate was grounded and not externally heated or cooled. All films had a comparable layer thickness of 350 ± 30 nm. The films are simultaneously grown on acetone-cleaned glass substrates (VWR International) for the Seebeck measurements as on RCA-cleaned silicon wafers for other characterization techniques. The films for the Seebeck measurements are patterned using a sputter mask (35 mm × 90 mm) in a shape as presented in Figure 8.1. After deposition, a complementary bulk wire is attached to the thin film in order to form a conventional E-type, i.e. $Cu_{55}Ni_{45}$(film) + $Ni_{90}Cr_{10}$(wire), or T-type thermocouple, i.e. Cu(film) + $Cu_{55}Ni_{45}$(wire) in analogy to the approach presented in Figure 8.1. The $Cu_{55}Ni_{45}$ and $Ni_{90}Cr_{10}$ wire (Goodfellow) had a diameter of 0.125 mm and a polyimide insulation.

8.4.2. Influence of impurities

Figure 8.2 presents the results for the deviation of the thin film Seebeck coefficient from the bulk value, i.e. $|\Delta S| = |S_b - S_f|$, plotted as func-

tion of an increasing impurity-to-metal ratio τ for both copper (left) and constantan (right). For both figures, error bars are included on a single marker but are valid for all data points in the respective plots. The full gray lines in Figure 8.2 represent the maximal deviation $|\Delta S|_{max}$ which is found when $S_f \rightarrow 0$ and thus $|\Delta S|_{max} = |S_b|$. We find for copper and constantan a value of 6.2 μV/°C and 40.1 μV/°C respectively [15]. In the low-impurity regime, i.e. $\tau \ll 1$, the Seebeck coefficient is not significantly affected by an increased background pressure. The average deviation from the bulk value in this regime is represented by the dotted line for both copper (1.9 μV/°C) and constantan (2.61 μV/°C). In the high-impurity regime, i.e. $\tau \gg 1$, the Seebeck coefficient is strongly affected by an increasing degree of contamination. Again, this behavior is very comparable to the behavior of the domain size (see Chapter 6) or the thin film resistivity (see Chapter 7) over the entire range of τ. The striped lines in the figures represent the relation $|\Delta S| \sim \tau^{1/2}$, where the

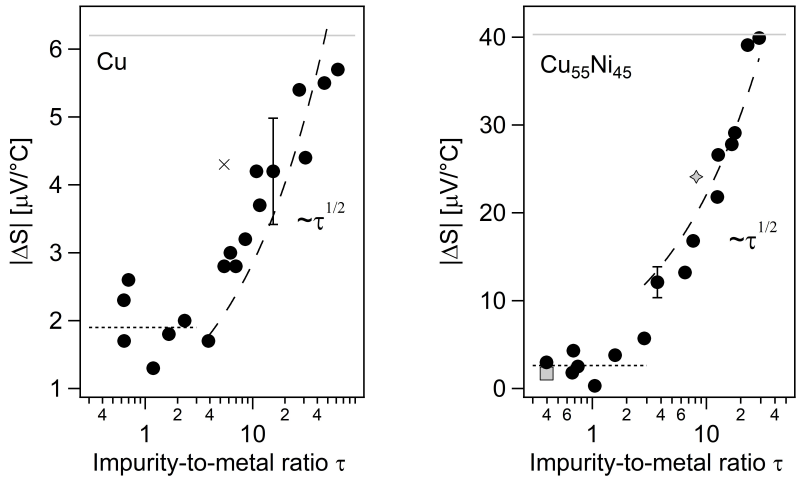

Figure 8.2. *The deviation of the thin film Seebeck coefficient from the bulk value plotted as a function of the impurity-to-metal impingement flux ratio for (left) copper and (right) constantan. The depositions are performed at a discharge current of 0.6 A, an argon pressure of 0.6 Pa and a target-to-substrate distance of 10 cm. The impurity-to-metal ratio was increased by leaking atmospheric impurities inside the vacuum chamber. The full gray lines in the figures indicate the maximal deviation $|\Delta S|_{max}$ for copper (6.2 $\mu V/^\circ C$) and constantan (40.1 $\mu V/^\circ C$). The dotted lines represent the average deviation from the bulk value in the low-impurity regime for copper (1.9 $\mu V/^\circ C$) and constantan (2.61 $\mu V/^\circ C$) and the striped lines represent the power law $|\Delta S| \sim \tau^{1/2}$. Error bars are included on a single marker but valid for all data points in the respective plots. The data point represented by the cross marker (left figure) was excluded from the fit for the proportionality factor. The gray square and diamond markers (right figure) represent data points from the experiment discussed in section 8.4.3.*

proportionality factor is fitted to coincide with the data in this high-impurity regime. The agreement between the experimental results and the proposed relation $|\Delta S| \sim \tau^{1/2}$ is evaluated by means of a chi-squared test. For copper and constantan, $\chi^2 = 1.98$ (12 data points) and $\chi^2 = 3.21$ (9 data points) are found respectively. In both cases, the significance of the description by the relation $|\Delta S| \sim \tau^{1/2}$ is guaranteed within the 95% confidence interval. Given the result obtained from Chapter 6, i.e. $D \sim \tau^{-1/2}$, this specific agreement of the experimental data with the relation $|\Delta S| \sim \tau^{1/2}$ embodies the thought of a relation between $|\Delta S|$ and the domain size D, more specifically $|\Delta S| \sim 1/D$.

In the next experiment, the domain size is tuned by means of a variation in deposition conditions (see Chapter 6) in order to verify if this hypothesis can indeed be validated. As copper has a much smaller Seebeck coefficient in comparison to constantan, this hinders the electronic Seebeck measurement and results in a high signal-to-noise ratio. Therefore, further experiments on copper were not performed, but focussed on constantan as the latter material has a higher Seebeck coefficient.

8.4.3. Discharge current

The results for the influence of the discharge current on the thin film Seebeck coefficient are presented in Figure 8.3. The square markers and diamond markers represent depositions performed at a background pressure of 3.50×10^{-4} Pa and 7.50×10^{-3} Pa respectively. The values for $|\Delta S|$ are significantly larger for the series deposited at a high background pressure compared to the series deposited at a low background pressure, an observation in accordance to the results discussed in Figure 8.2. For both series, the measurements indicate an increasing deviation of the film Seebeck coefficient from the bulk value with decreasing discharge current. For completeness, the data points obtained in this experiment which correspond to the same deposition conditions as the previous experiment, i.e. the samples deposited at a discharge current of 0.6 A, are also included on the plot in Figure 8.2 for $Cu_{55}Ni_{45}$ and represented by the gray (square and diamond) markers.
As already mentioned, the discharge current is varied in order to verify if the induced variation in domain size is reflected in the Seebeck measurement and coincides with the hypothesis $\Delta S \sim 1/D$. As the discharge current is varied from 0.6 A up to 0.1 A, the deposition speed was varied from 1.28 nm/s up to 0.23 nm/s respectively. The variation in background pressure between both series did not have any influence on the deposition speed. Given the constant background pressure used within each series, the value for τ thus increases with decreasing discharge current. In the high impurity regime, the domain size is thus expected to decrease as $D \sim \tau^{-1/2}$. The domain sizes corresponding to the series deposited at varying discharge current at both low and high background

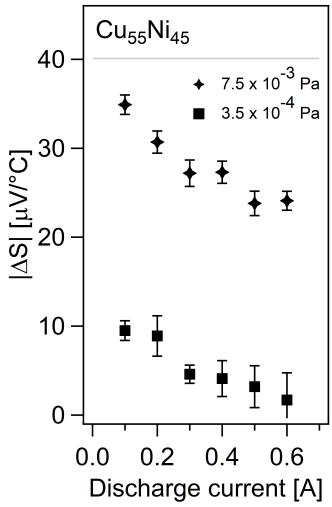

Figure 8.3. *The deviation of the thin film Seebeck coefficient from the bulk value measured as function of the discharge current for 2 different background pressures: 3.50×10^{-4} Pa (■) and 7.50×10^{-3} Pa (♦). The argon pressure was set to 0.6 Pa and the target-to-substrate distance was 10 cm. The full gray line indicates the maximal deviation* $|\Delta S|_{max}$.

pressure are plotted in Figure 8.4 (left). The domain size decreases with increasing background pressure and decreasing discharge current. Figure 8.4 (right) is based on the same data for the domain size as in Figure 8.4 (left), but now presented in a normalized way and as a function of the respective τ-values. It can be observed that the predicted relation from Chapter 6, i.e. $D \sim \tau^{-1/2}$, can again be consolidated. This relation is represented by the striped line and further embodied by the gray markers taken from Figure 6.3 (Chapter 6). In line with the previous chapter, it is again observed that a good estimation of the change in domain size is allowed when the variations in deposition conditions are projected on the corresponding τ-values (see Chapter 7).

8.4.4. Confrontation with literature

As already mentioned, based on the observed trend of grain-refinement in the high-impurity regime, i.e. $D \sim \tau^{-1/2}$ (see also Chapter 6), the specific agreement of the experimental data with the relation $|\Delta S| \sim \tau^{1/2}$ in the high-impurity regime, as presented in Figure 8.2, embodies the thought of a relation between $|\Delta S|$ and the domain size D, more specifically $|\Delta S| \sim 1/D$ for $\tau \gg 1$. Figure 8.5 summarizes the effect of the background pressure (■ vs ♦) and discharge current (■ and ♦) on $|\Delta S|$, described as a function of $1/D$. For the depositions performed in the high-impurity regime (♦), the predicted behavior, i.e. $|\Delta S| \sim 1/D$, can indeed be validated. This confirms the hypothesis that the thin film

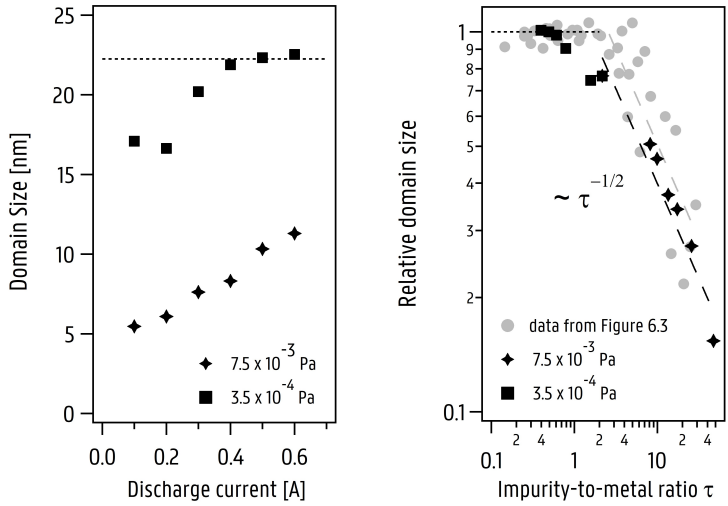

Figure 8.4. *(left) Domain size as a function of the discharge current. (right) Domain size presented as a function of the impurity-to-metal impingement flux ratio. The square markers represent the deposition performed at low background pressure (3.50×10^{-4} Pa), the diamond markers represents the depositions performed at high background pressure (7.50×10^{-3} Pa). The gray round markers are the data for $Cu_{55}Ni_{45}$ already presented in Figure 6.3. The dotted lines in the figures represents the average domain size in the low-impurity regime. The striped lines (right) represent the relation $D \sim \tau^{-1/2}$.*

Seebeck coefficient is a strong function of the domain size. In the low-impurity regime (■), the variation in domain size - see data related to the square markers in Figure 8.4 - is also reflected in $|\Delta S|$. A steep increase of $|\Delta S|$ is observed for the transition from the low-impurity regime towards the high-impurity regime. This is probably related to the size-effect, i.e when the average domain size becomes of the same magnitude as the electron mean free path.

A similar study was performed by Barber et al [3]. In the latter work, the influence of the layer thickness and P×d on the Seebeck coefficient of sputter deposited constantan films was studied. The depositions for which enough information was available to recalculate their respective domain size D using the Scherrer-equation, are added on the plot in Figure 8.5. The influence of the layer thickness on the thin film Seebeck coefficient at fixed P×d-values is presented by the unfilled green round markers, and the influence of P×d at constant layer thickness is represented by the unfilled blue square markers. The round filled gray markers in Figure 8.5 represent combinations of a varying thickness together with an unspecified P×d-value (thickness range 2000 nm - 90 nm). The results of Barber show that, for a fixed P×d-value, there is an increasing deviation

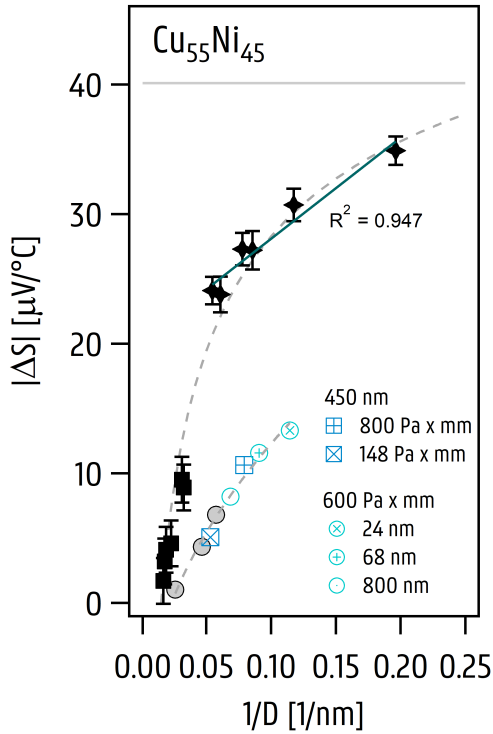

Figure 8.5. *Deviation of the thin film Seebeck coefficient from the bulk value as function of the inverse of the domain size. The data derived from the work of Z. Barber et al. [3] on sputter deposited constantan films are represented by the blue square unfilled markers (varying P×d, constant thickness), the blue round unfilled markers (varying thickness, constant P×d) and the round gray filled markers (combinations of a varying thickness (range 2000 nm - 90 nm) together with unspecified P×d-values). The full gray line represents the value for the maximal deviation $|\Delta S|_{max}$. The gray dotted lines are a guide to the eye.*

|ΔS| from the bulk value as the film grows thinner. This is in agreement with the classic observation of the size-effect as discussed in section 8.3. Inversely, at fixed layer thickness, |ΔS| increases with increasing P×d-values. It was shown by Barber et al. that a linear relation could be found between |ΔS| and the full width at half maximum (FWHM), irrespective of the value for the layer thickness or $P \times d$. This can also be observed for the blue, green and gray markers presented in Figure 8.5. Although no explanation could yet be given for the difference in the observed slopes between the presented data in this work and the work of Barber et al., the experimental data fulfill the same qualitative response of the Seebeck coefficient to the variations in domain size, i.e. $|\Delta S| \sim 1/D$.

The dependency of the Seebeck coefficient on the FWHM as observed by Barber et al. indicates that the Seebeck coefficient is strongly related to the microstructure of the film. In this respect, the conclusions are in agreement with the observations done in this work. A major difference however between this work and the work of Barber et al. consists in the argumentation for the origin of these microstructural changes. In the latter work, the dependency of the Seebeck coefficient on P×d is explained by thermalization effects affecting the microstructure. Arguments can however be given that the changes in microstructure, or FWHM, with $P \times d$ are more likely attributed to impurities rather than to thermalization effects. It was demonstrated that the main effect of varying deposition conditions such as the discharge current I, is the related variation the impurity-to-metal ratio τ. This variation in τ-value affects the domain size according to $D \sim \tau^{-1/2}$. Analogously, the impurity-to-metal ratio τ also increases with increasing P×d (see Chapter 4). It can be found in literature that large P×d-values result in smaller grains [7, 14, 30]. The P×d-values used in the work of Barber, i.e. in the range of 150 - 800 $Pa \times mm$, are however very high in comparison to the P×d-value used in this work, i.e. 60 $Pa \times mm$. The EPA values in the work of Barber are thus expected to be much lower than for the depositions performed in this work (see Chapter 4). According to SiMTra simulations [36] presented in Figure 4.1, the energy of the sputtered particles in the range of 150 - 800 $Pa \times mm$ is estimated between 1.5 eV and $3/2kT$ (T at 300 K) respectively, and around 6 eV for the P×d-value used in this work (60 $Pa \times mm$). The simulations indicate fully thermalized sputtered particles, i.e. $E = 3/2kT$, at a P×d-value close to 400 $Pa \times mm$. Therefore, it seems less likely that the variations in $|\Delta S|$ as function of P×d (see Figure 2 in [3]) could be attributed to thermalization effects, especially when P×d $>$ 400 $Pa \times mm$. Of course, as outlined in Chapter 4, other contributions to the energy balance for the adatoms are possible. However, for this material-sputter gas combination, the amount of reflected neutrals is expected to be low [11, 19], and a dominant electronic and radiative contribution is not expected to scale as function of P×d. Furthermore, it was also shown in Chapter 4 that the EPA is not significantly affected by a variation in the discharge current. The experimental results presented in Figure 8.5 can thus not be compatible with the idea of a variation in film Seebeck coefficient caused by thermalization effects. Our observations therefore indicate that a more consistent description for the effect of the deposition conditions on the thin film Seebeck coefficient can be given from the perspective of refined grains - in coherence with the change in microstructure as reported in the work of Barber - but caused by an increased impurity-to-metal impingement flux τ rather than caused by thermalization effects.

A critical reader could argue that the base pressure reported in the work of Barber are way to too low for the growth process to be possibly affected by impurity effects. As reported, the base pressure was 2×10^{-7} Pa with an outgassing rate of 0.2 10^{-6} dm^3s^{-1}, resulting in an impurity level in the ppm range for the lowest deposition rates. A very small cylindrical vacuum chamber was used with a volume[2] of 3.5 10^{-3} m^3. The ultra high vacuum was obtained by cooling the chamber walls by liquid nitrogen. This is a common approach for obtaining lower pressures by gettering impurities from the vacuum through condensation of the impinging species on the chamber walls. As such, a large amount of monolayers is accumulated on the chamber walls. During magnetron sputtering however, as soon as the magnetron discharge is ignited, energy is dissipated towards the chamber walls under the form of radiation and impact of energetic species. In case of an unbalanced magnetron, many magnetic field lines cross the chamber walls. As such, energetic electrons gyrating around the magnetic field lines are easily directed towards the chamber walls. Under influence of electron bombardment, adsorbed gases on the chamber walls are stimulated to desorb from the surface, an effect known as electron-stimulated desorption [18]. As lots of impurities are condensed on the surface, the electron flux towards the chamber walls will result in a vast desorption of the condensed monolayers. Especially for small vacuum chambers, as in the latter case, this electron flux will be significant. As such, the effective base pressure during deposition will be much higher as the base pressure noted prior to the deposition. In this respect, interference of impurity effects during the film growth in the work of Barber et al. cannot be excluded.

8.5. Conclusions

This chapter discusses the effect of the layer thickness, the deposition conditions, and the presence of impurities during growth on the thin film Seebeck coefficient. Under pure deposition conditions, the obtained thin film Seebeck coefficients are in close vicinity of their respective bulk values. Variations in deposition conditions can however severely affect the thin film Seebeck coefficients. Also the layer thickness affects the Seebeck coefficient as described by the size-effect. It was emphasized here how these variations in layer thickness or deposition conditions can both affect the domain size. In view of the diversity of experimental variations which could be summarized as function of the domain size, more specifically, $|\Delta S| \sim 1/D$, the domain size was found to be a key parameter in understanding the behavior of the thin film Seebeck coefficient. Consequently, the influence of the deposition conditions and the layer thickness on the Seebeck coefficient can be understood by evaluating their effect on

[2]For comparison, the vacuum chamber used for the depositions performed in this chapter has a volume of 1.25 10^{-1} m^3

the domain size. Finally, it was concluded that the origin of variations in domain size with varying deposition conditions can be attributed to an increased impurity incorporation during growth, rather than to thermalization effects. These conclusions are also in line with the discussion on the electrical thin film properties in the previous chapter where it was shown that the variations in EPA, in absence of impurity effects, could not be correlated to the changes in electrical properties.

References

[1] MA Angadi and LA Udachan, Thermoelectric power measurements in thin tin films, Journal of Physics D: Applied Physics **14** (1981), no. 7, L103.

[2] M Arab Pour Yazdi, N Martin, C Petitot, K Neffaa, F Palmino, F Cherioux, and A Billard, Influence of Sputtering Parameters on Structural, Electrical and Thermoelectric Properties of Mg–Si Coatings, Coatings **8** (2018), no. 11, 380.

[3] ZH Barber and RE Somekh, Magnetron sputtering of Cu55Ni45, Vacuum **34** (1984), no. 10-11, 991–994.

[4] G Beensh-Marchwicka, S Osadnik, E Prociów, and W Mielcarek, Structure and morphology of Ge (Au) sputtered films with useful Seebeck effect, Vacuum **50** (1998), no. 1-2, 207–210.

[5] A Bourque-Viens, V Aimez, A Taberner, P Nielsen, and PG Charette, Modelling and experimental validation of thin-film effects in thermopile-based microscale calorimeters, Sensors and Actuators A: Physical **150** (2009), no. 2, 199–206.

[6] A Boyer and E Cisse, Properties of thin film thermoelectric materials: application to sensors using the Seebeck effect, Materials Science and Engineering: B **13** (1992), no. 2, 103–111.

[7] KY Chan and BS Teo, Effect of Ar pressure on grain size of magnetron sputter-deposited Cu thin films, IET Science, Measurement & Technology **1** (2007), no. 2, 87–90.

[8] KL Chopra, SK Bahl, and MR Randlett, Thermopower in Thin-Film Copper—Constantan Couples, Journal of applied physics **39** (1968), no. 3, 1525–1528.

[9] VD Das and N Soundararajan, Size and temperature effects on the Seebeck coefficient of thin bismuth films, Physical Review B **35** (1987), no. 12, 5990.

[10] D De, S K. Bandyopadhyay, S Chaudhuri, and AK Pal, Thermoelectric power of aluminum films, Journal of Applied Physics **54** (1983), no. 7, 4022–4027.

[11] D Depla, S Mahieu, et al., Reactive sputter deposition, vol. 109, Springer, 2008.

[12] D Deschacht, A Boyer, and E Groubert, The thermoelectric power of polycrystalline semimetal films, physica status solidi (a) **71** (1982), no. 2, K205–K209.

[13] TH Geballe and GW Hull, Seebeck effect in silicon, Physical Review **98** (1955), no. 4, 940.

[14] G Gordillo, F Mesa, and C Calderón, Electrical and morphological properties of low resistivity Mo thin films prepared by magnetron sputtering, Brazilian Journal of Physics **36** (2006), no. 3B, 982–985.

[15] A Guan, H Wang, H Jin, W Chu, Y Guo, and G Lu, An experimental apparatus for simultaneously measuring Seebeck coefficient and electrical resistivity from 100 K to 600 K, Review of Scientific Instruments **84** (2013), no. 4, 043903.

[16] E Guk, M Ranaweera, V Venkatesan, and JS Kim, Performance and durability of thin film thermocouple array on a porous electrode, Sensors **16** (2016), no. 9, 1329.

[17] H Guo, JY Jiang, JX Liu, ZH Nie, F Ye, and CF Ma, Fabrication and Calibration of Cu-Ni Thin Film Thermocouples, Advanced Materials Research, vol. 512, Trans Tech Publ, 2012, pp. 2068–2071.

[18] J Herring-Captain, GA Grieves, A Alexandrov, MT Sieger, H Chen, and TM Orlando, Low-energy(5 - 250eV) electron-stimulated desorption of H,H2, and H2O from low-temperature water ice surfaces, Physical Review B **72** (2005), no. 3.

[19] DW Hoffman and JA Thornton, Internal stresses in Cr, Mo, Ta, and Pt films deposited by sputtering from a planar magnetron source, Journal of Vacuum Science and Technology **20** (1982), no. 3, 355–358.

[20] M Hubin and J Gouault, Resistivity and thermoelectric power between -100C

and+100C of gold and silver thin films formed and studied in ultrahigh vacuum, Thin Solid Films **24** (1974), no. 2, 311–331.
[21] S Kasap, Thermoelectric effects in metals: thermocouples, Canada: Department of Electrical Engineering University of Saskatchewan (2001).
[22] KG Kreider, Sputtered high temperature thin film thermocouples, Journal of Vacuum Science & Technology A: Vacuum, Surfaces, and Films **11** (1993), no. 4, 1401–1405.
[23] M Laugier, The construction and use of thin film thermocouples for the measurement of surface temperature: Applications to substrate temperature determination and thermal bending of a cantilevered plate during film deposition, Thin Solid Films **67** (1980), no. 1, 163–170.
[24] G Li, Z Wang, X Mao, Y Zhang, X Huo, H Liu, and S Xu, Real-time two-dimensional mapping of relative local surface temperatures with a thin-film sensor array, Sensors **16** (2016), no. 7, 977.
[25] H Liu, W Sun, A Xiang, T Shi, Q Chen, and S Xu, Towards on-chip time-resolved thermal mapping with micro-/nanosensor arrays, Nanoscale research letters **7** (2012), no. 1, 484.
[26] DKC MacDonald, Thermoelectricity: an introduction to the principles, Courier Corporation, 2006.
[27] H Mayer, Structure and properties of thin films, by CA Neugebauer, JW Newkirk, and DA Vermilyea, Wiley, New York (1959), 225.
[28] RD Meredith, JD Wrbanek, GC Fralick, LC Greer, GW Hunter, and L Chen, Design and operation of a fast, thin-film thermocouple probe on a turbine engine, 50th AIAA/ASME/SAE/ASEE Joint Propulsion Conference, 2014, p. 3923.
[29] P Mikolajczak, W Piasek, and M Subotowicz, Thermoelectric power in bismuth thin films, physica status solidi (a) **25** (1974), no. 2, 619–628.
[30] H Qiu, F Wang, P Wu, L Pan, and Y Tian, Structural and electrical properties of Cu films deposited on glass by DC magnetron sputtering, Vacuum **66** (2002), no. 3-4, 447–452.
[31] VVRN Rao, S Mohan, and PJ Reddy, Electrical resistivity, TCR and thermoelectric power of annealed thin copper films, Journal of Physics D: Applied Physics **9** (1976), no. 1, 89.
[32] ———, The size effect in the thermoelectric power of silver films, Thin Solid Films **42** (1977), no. 3, 283–289.
[33] L Scarioni and EM Castro, Thermoelectric power in thin film Fe–CuNi alloy (type-J) couples, Journal of applied physics **87** (2000), no. 9, 4337–4339.
[34] T Sun, B Yao, AP Warren, K Barmak, MF Toney, RE Peale, and KR Coffey, Surface and grain-boundary scattering in nanometric Cu films, Physical Review B **81** (2010), no. 15, 155454.
[35] AP Thakoor, R Suri, SK Suri, and KL Chopra, Electron transport properties of copper films. II. Thermoelectric power, Journal of Applied Physics **46** (1975), no. 11, 4777–4783.
[36] K Van Aeken, S Mahieu, and D Depla, The metal flux from a rotating cylindrical magnetron: a Monte Carlo simulation, Journal of Physics D: Applied Physics **41** (2008), no. 20, 205307.
[37] HY Yu and WF Leonard, Thermoelectric power of thin silver films, Journal of Applied Physics **44** (1973), no. 12, 5324–5327.
[38] QY Zeng, T Hong, L Chen, and YX Cui, Magnetron sputtering of NiCr/NiSi thin-film thermocouple sensor for temperature measurement when machining chemical explosive material, Key Engineering Materials, vol. 467, Trans Tech Publ, 2011, pp. 134–139.
[39] X Zhang, H Choi, A Datta, and X Li, Design, fabrication and characterization of metal embedded thin film thermocouples with various film thicknesses and junction sizes, Journal of Micromechanics and Microengineering **16** (2006), no. 5, 900.

9 Applications

In this final chapter, different insights obtained during this work are acquired to present some new perspectives and possible applications. Besides a new approach for the development of a single-metal thin film thermocouple that is proposed, a feasibility study of the use of thin films for heating applications and antenna fabrication is presented as well as insight is given on how ceramic films could be deposited on composite substrates. It is however not the purpose of this chapter to elaborate or to optimize applications, but rather to demonstrate how a proper understanding of film growth on composites enables new perspectives and benefits in the development of sensing applications.

9.1. Single-metal thermocouples

Due to its simplicity, the structure of a thermocouple, i.e. a couple of two dissimilar conductors, has remained unquestioned and invariant for a long time. More recently, Liu et al. [19] proposed a very simple, alternative approach for the production of thin film thermocouples (TFTCs) constituted out of the same material, i.e. a single metal thermocouple. They demonstrated that the size-effect in metallic thin films can be exploited to fabricate TFTCs constituted of films of the same material, but with different thermoelectric properties. As such, a single-metal TFTC was constructed, composed of two sputter-deposited Ni thin films with different spatial dimensions and with sensitivities around $1\mu V/^{\circ}C$. Zhang et al. [44] also demonstrated that the thinner the films used in the TFTC, the faster the response time (≈ 52 ns). However, given the constraint on the layer thickness due to the intrinsic roughness of the prepreg substrate (see Chapter 4), the approach for the production of single-metal thermocouples based on the size-effect seems not applicable for the deposition on composites.

However, based on the results presented in Chapter 8, an alternative approach can be proposed. It was shown in Chapter 8 that the film Seebeck coefficient deviates from its bulk value according to the inverse of the domain size, i.e. $|\Delta S| \sim 1/D$. In Chapter 6, it was shown that the domain size D is severely affected for films deposited with a high impurity-to-metal ratio τ during growth, i.e. $D \sim \tau^{-1/2}$. An increased impurity concentration present in the vacuum chamber during deposition can thus be used to tune the thermoelectric properties of the film. As will be demonstrated, a single-metal TFTC can be created by combining two thermocouple legs of the same material, but with one leg deposited in the low-impurity regime, and another leg in the high-impurity regime. In Chapter 6, mass spectrometry of outgassing products indicated that the presence of the composite in the vacuum is already a source of impurities itself. Therefore, whereas initially the outgassing related to the presence of the composite was considered as a negative situation, the usage of the high-impurity regime in the deposition process of a single-metal thermocouple allows for an opportunity to turn the outgassing into a useful tool for tuning film properties.

9.1.1. Fabrication and validation

Figure 9.1 shows the evolution of the total base pressure in the system as a function of time, but recalculated to a corresponding impurity-to-metal ratio τ for metallic films deposited at a rate of 1 nm/s (approx. 10^{16} atoms $cm^{-2}s^{-1}$). The pressure evolution in the system was measured by monitoring the output voltage of the pressure gauge measurement unit (Pfeiffer DualGauge TPG 262) and recalculated to the background pressure by the provided calibration functions in the measurement unit manual. This was done for four different situations: only the vacuum chamber (with an opened loadlock), the vacuum chamber with an empty substrate stick, and the vacuum chamber with a substrate stick foreseen of a laminate (5 cm × 17 cm) with a stacking of 2 and 10 prepreg layers. The step-wise increase in τ-value coincides with the opening of the load lock to introduce the substrate stick into the vacuum. The presence of the composite laminate, together with the number of prepreg layers integrated in the laminate, have a clear and distinguishable effect on the outgassing. A large amount of outgassing in the chamber can also be attributed to the presence of the substrate stick.
In case of the presence of the laminate with only 2 prepreg layers, the low-impurity regime is reached after 2660 s, i.e. approximately 45 minutes. Even longer times are expected for the case of 10 prepreg layers. The transition towards the low-impurity regime can however be facilitated by increasing the total pumping capacity of the system. As an illustration, for a perfect vacuum vessel, i.e. zero leakage, gas permeability and

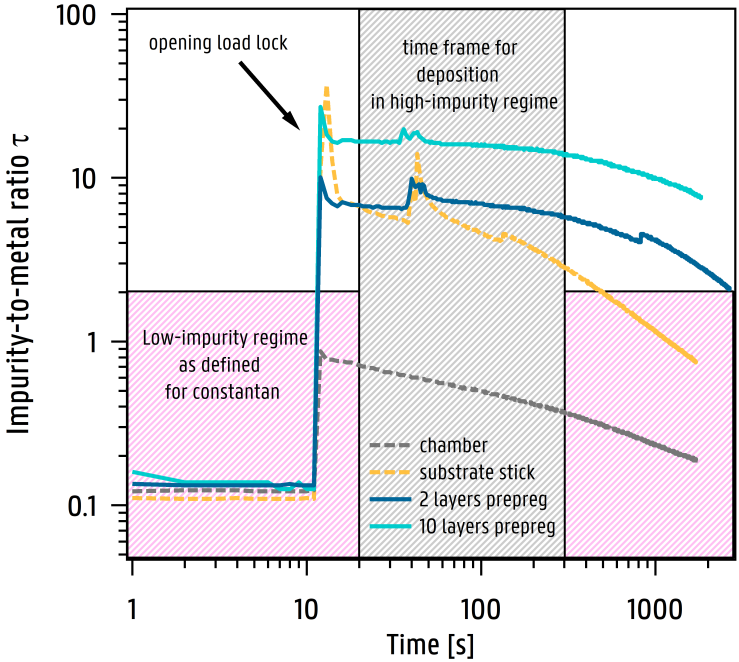

Figure 9.1. *The evolution of the total base pressure (τ-value) in the system as a function of time, but recalculated to the corresponding impurity-to-metal ratio τ for constantan deposited at a rate of 1 nm/s. Four different pressure-time evolutions are presented: the vacuum chamber (with an opened loadlock (volume: 0.00157 m^3)), the vacuum chamber with an empty substrate stick, and the vacuum chamber with a substrate stick forseen of a laminate with a stacking of 2 and 10 prepreg layers. The gray area represents the available time-frame to perform a deposition in the high-impurity regime, the pink area represents the low-impurity regime as defined for constantan in accordance to Figure 6.3. The vacuum chamber in which the measurement was performed differed from the system used for the depositions discussed in previous chapter due to availability reasons. The volumes of both chambers are equivalent, the full pumping speed in the original chamber (model THM1600 with 1500 l/s) is a factor three higher than in the latter system (model TMU521 520 l/s).*

outgassing, with a volume V and pumped by a pumping speed S, the pressure-time relation is given by

$$V\frac{dp}{dt} = -Sp(t) \tag{9.1}$$

and thus solving for $p(t)$ gives

$$p = p_0 exp(-\frac{S}{V}t) \tag{9.2}$$

with p_0 the pressure at the beginning of the pumping. The ratio V/S can be considered the time constant of the system. The vacuum chamber in

which the measurement presented in Figure 9.1 was performed, differed from the system used for the depositions discussed in previous chapter due to availability reasons. The volumes of both chambers are equivalent, but the full pumping speed in the original chamber (model THM1600 with 1500 l/s) is a factor three higher than in the latter system (model TMU521 520 l/s). Therefore, the time constant of the system with the low pumping speed (520 l/s) will be around three times larger than for the system with the high pumping speed (1500 l/s). This is indeed reflected by the large times required to enter the system into the low-impurity regime in Figure 9.1. For a good control of the process, it is thus essential to have enough pumping capacity. Initially, when the composite is introduced, the impurity level and the time for deposition can be regulated by means of the pumping speed. Afterwards, i.e. after the deposition in the high impurity regime is finished, the transient towards the low-impurity regime can be facilitated by switching towards a higher pumping speed.
The deposition of the single metal thermocouple was performed on a laminate stacking of 2 prepreg layers. As indicated by the gray patterend area in Figure 9.1, a time-frame in the high-impurity regime of around 300 s can be defined with a relatively constant τ -value, $\tau \approx 17$. A 300 nm constantan film, patterned as a thermocouple leg, was deposited in this regime onto a laminate of 2 prepreg layers at a deposition speed of 1 nm/s. After the deposition of the first thermocouple leg in the high-

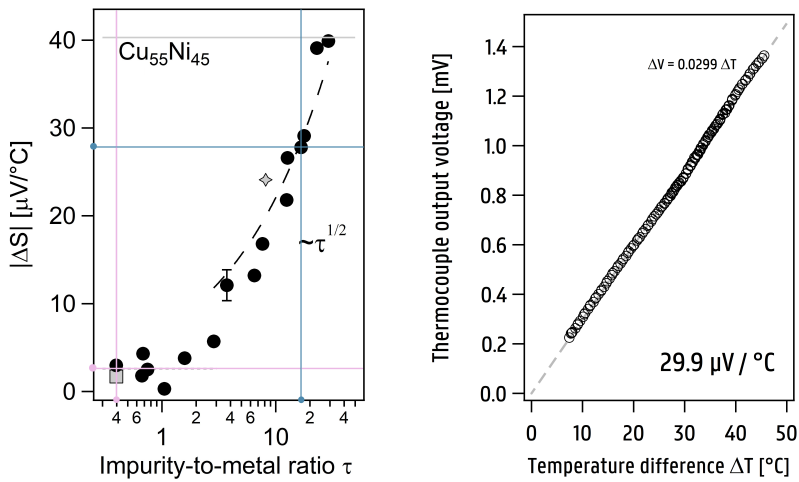

Figure 9.2. *(left) Deviation of the thin film Seebeck coefficient from the bulk value as a function of the impurity-to-metal ratio τ. The blue line represents the $(\tau, |\Delta S|)$ combination for the deposition of the thermocouple leg in the high-impurity regime, and the pink line represents the $(\tau, |\Delta S|)$ combination for the deposition of the thermocouple leg in the low-impurity regime.(right) The temperature-voltage output of the single-metal thermocouple. The Seebeck coefficient of the single-metal TFTC is 29.9 μ V/°C.*

impurity regime, the system is given time to move into the low-impurity regime. Here, at $\tau = 0.4$, the second leg of the thermocouple, i.e. again a 300 nm constantan film, is deposited. The expected sensitivity of the single-metal thermocouple is given by the difference between the thermoelectric properties of the first themocouple leg deposited in the high-impurity regime (blue line) and the second thermocouple leg deposited in the low-impurity regime (pink line). From Figure 9.2 (based on Figure 8.2 from previous chapter), the sensitivity of the single-metal thermocouple is thus estimated as $|\Delta S| \approx 27 \mu V/°C$. Figure 9.2 (right) shows the experimentally measured thermocouple output voltage as a function of the applied temperature difference. From the measurement, the sensitivity of the thermocouple is found to be 29.9 $\mu V/°C$, which is very close to the predicted value of 27 $\mu V/°C$ [1]. It is thus possible to fabricate single-metal thin film thermocouples by tuning the thermoelectric properties of the films by means of impurities. The obtained sensitivities are also far larger than the sensitivities of the single metal TFTCs reported by Liu et al. [19]. Single-metal TFTCs allow for a much simpler fabrication process compared to bimetallic thermocouples as only one target material has to be present in the vacuum chamber.

9.2. Heat generation in composite materials

The possibility of a controlled heat generation in the bulk of a composite laminate is very attractive with regard to different applications such as in-flight deicing of components in aerospace, in-situ electroresistive curing [16, 28], or the use of calibrated heat fluxes for non-destructive thermographic defect inspection in composites [17].
In order to first illustrate the principle of thin film heaters, a 10-layer glass/epoxy laminate was produced foreseen of a fully coated prepreg sheet (300 nm $Cu_{55}Ni_{45}$) in the midplane for heating purpose. A single-metal thin film thermocouple was embedded just underneath the laminate surface, i.e. 4 prepreg layers above the heating film for monitoring the surface temperature. A potential difference of 5 V was applied over the film, resulting in a current of 0.11 A ($R = 181\ \Omega$) and thus a dissipated power of $P = 0.14\ W$. Under influence of ohmic heating, the temperature at the surface of the laminate increases. The temperature evolution at the surface as measured by the single-metal TFTC is presented in Figure 9.3. When the power is on, a typical heating curve is observed, when the power is off, a typical cooling curve is observed. As an illustration, the fitted equations to the heating and cooling curves are also included in the graph. For the measurement presented here, the time constant is given by $1/9.7 \times 10^{-3} \approx 10^2 s^{-1}$. For homogeneous materials, the time constant can be used to derive information about the heat transfer coefficient.

[1] The sensitivities of K, J, and E-type thermocouples are respectively given by ≈ 38.7, 50.4, and 67.3 $\mu V/°C$.

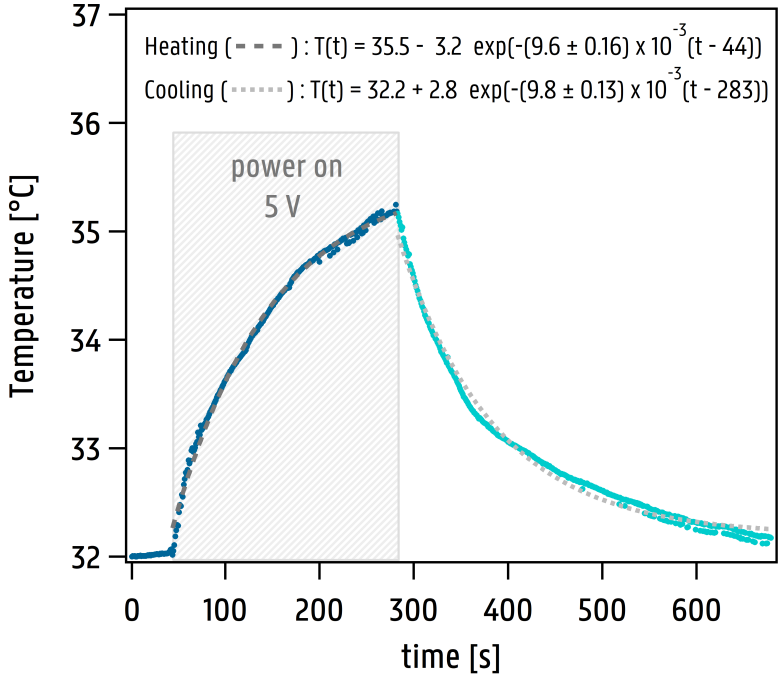

Figure 9.3. *The temperature evolution at the surface of a composite laminate under influence of a heating element integrated in the mid-plane of the 10-layer composite laminate. The surface temperature was measured by an embedded single-metal TFTC embedded just underneath the surface. The sensitivity of the single-metal TFTC was* $\approx 30\ \mu V/°C$*. During the heating period, i.e. power on, a typical heating curve is measured. During the cooling period, i.e. power off, a typical cooling curve is observed. The heating and cooling curves were fitted only for illustration.*

However, as most composites are thermally anisotropic and inhomogeneous, the heat transport is more complex. Although some analytical approaches for the heat conduction in a non-homogeneous medium can be given [5, 14], computational solution are commonly applied for solving the heat transfer inside the composite. Integration of properly calibrated networks of TFTCs into different layers of the composite laminate is however a feasible and interesting approach for detailed measurements of the temperature distribution through the thickness of the laminate as minimal impact of the temperature sensor on the heat transfer is expected. Another interesting feature arises when the single-metal TFTC is connected in a feed-back loop with the power supply of the thin film heating element. In this case, a constant temperature in time could be obtained in the bulk of composite. It is interesting to note that this entire functionality was deposited with only one constantan target present in the vacuum system.

With regard to deicing applications in aerospace, different types of heating systems are used. Most commonly, heating wires (for example, NiCr-alloys as chromel) or carbon fabric-based heating systems are used. The use of heating wires is a very simple and effective approach, but can however not be applied for aerospace applications as the related weight increase involves compromises on speed and fuel. Carbon-fiber on the other hand is often used due to its beneficial properties in terms of weight, flexibility, and coverage area. In this context, also thin films should be a promising approach, especially because of the even smaller weight, and thus the very fast ramp times, and the minimal impact on structural properties. In the following, the feasibility of thin films for embedded electro-thermal deicing applications is evaluated.

9.2.1. De-icing

Ice formation on a plane during flight causes an increased weight and drag and decreases the lift of the plane. Many accidents with airplanes could be attributed to effects directly or indirectly related to ice accumulation on the plane's surfaces. The primary objective of anti-icing and de-icing is therefore to prevent or (periodically) remove accumulated ice formation on the plane surfaces. Icing may be categorized as light, moderate, and severe [33]. In severe icing conditions, the rate of formation ($>$ 4 cm per hour) is such that anti-icing and deicing may fail to control the ice accumulation. In moderate icing, the rate of ice formation (approximately 2 to 4 cm per hour) is such that there is potential for a hazardous situation. Light icing is usually not a problem unless the aircraft is exposed for a lengthy period (rate of ice formation approx. 0.1 to 2 cm per hour). Some common approaches for de-icing are either based on pneumatic boot systems, i.e. a rubber membrane attached to the wing is inflated by means of compressed air in order to break the formed ice layer, on chemical fluids, or on electrical heating system (electro-thermal deicing).

9.2.2. Power requirements for deicing

For electro-thermal deicing applications on less critical parts such as the airplane wings, it is not necessary to evaporate or to melt all of the impinging droplets on the surface. By periodic melting of the surface-air interface, typically with a power on-time of 9 seconds and an off-time of 3 minutes, the ice droplets no longer adhere to the surface and the accumulated ice is consequently removed by aerodynamic forces. A simple calculation allows to estimate the power requirements for deicing [25]. Assuming an ice layer ($\rho_{ice} = 900\ kg/m^3$) of 0.5 mm has to be melted to separate the ice from the surface, this corresponds to a total mass of 0.45 kg of ice. In order to melt the ice, energy has to be supplied to heat the ice first to the zero point, and afterwards latent heat has to be applied to

melt the ice. With an average environmental temperature of -17.78 $°C$, the latent heat for melting ice given by 332.5 kJ/kg, and the heat capacity of ice $c_{ice} = 2.1\ J/g$, the total power required to melt this mass within a time frame of 9 seconds can be calculated as 18.5 kW. Under the assumption that only 50 % of the generated power is dissipated at the surface, the heating system must be able to deliver 37 kW/m^2, or 3.7 W/cm^2. This value is in agreement with prescriptions of the SAE standards AIR 1168/4 [2] which are based on empirical results (34.10 kW/m^2).
A test is performed in order to evaluate if these prescribed power densities are feasible for thin film heaters. For this, three different 10-layer laminates (approx. 30 cm^2) were produced. Two laminates are produced with a line pattern coated onto the prepreg layer integrated in the midplane of the laminate. One laminate had a line pattern with a film thickness of 100 nm, while the other laminate had a 350 nm thick line pattern. For a third laminate, a fully coated (350 nm) prepreg ply was integrated in the midplane. The films were all deposited at the same sputter conditions, i.e. $I = 0.6$ A, $P = 0.6$ Pa, $d_{TS} = 10$ cm, $v_d = 1$ nm/s, and $P_B = 2 \times 10^{-3}\ Pa$. Copper was chosen as the deposited material because of the good electrical properties. A higher background pressure was however chosen in order to add some resistance to the heating circuit in order to prevent a short-circuit. After curing the samples, the contacting to the thin films was obstructed by a thin layer of epoxy. Copper tape was therefore applied onto the contact and perforated through the epoxy film in order to make electrical contact with the film. The power to the thin films was provided by means of a home-built DC voltage supply. The

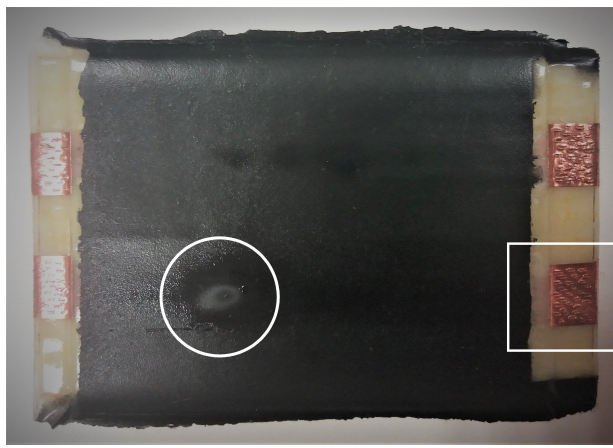

Figure 9.4. *Example of a laminate foreseen of two line heating patterns. A black spray coating is applied onto the surface in order to set the emissivity of the surface to one. The white circle indicates a burning mark due to a local hot spot. The square indicates the edge region at the electrodes where an elevated pressure arises during curing.*

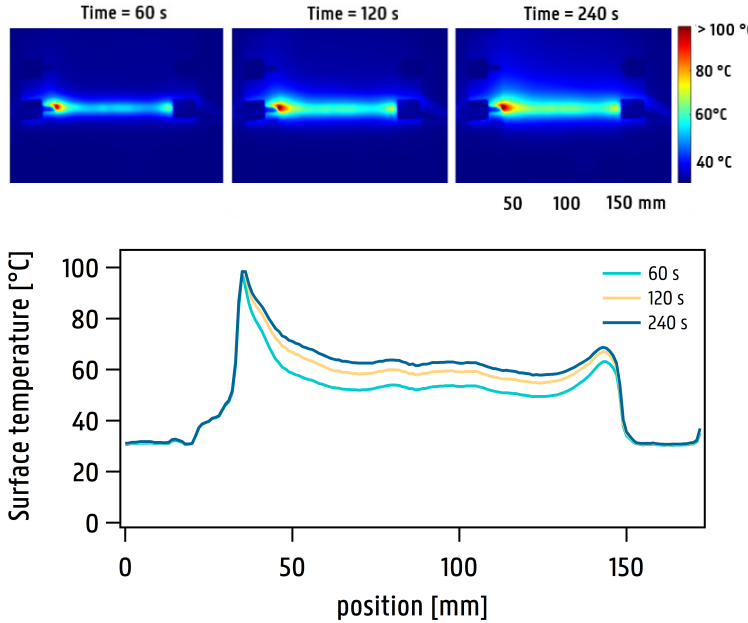

Figure 9.5. *Infrared inspection (top) and the temperature profile at the surface along a 300 nm line heating element, i.e. from end to end (bottom). The applied voltage was 4.5 V, the resistance of the line heating pattern 9.6 Ω and the current in the circuit was 0.46 A. The total amount of dissipated power by the heater is calculated as approximately 2 W. Averaged over the total surface area of the sample, the average dissipated power density by the heating element yields 0.07 W/cm^2 or 0.22 W/cm when only accounting for the line element.*

heat generation on the surface of the composite was monitored by means of a high-end thermographic camera (FLIR A6750sc). A black spray coating was therefore applied onto the surface in order to set the emissivity of the surface to one (see Figure 9.4). Voltages in the range from 1 to 40 V were applied over the film circuit. Figure 9.5 shows the evolution of the surface temperature as measured by the thermographic camera after 1, 2 and 4 minutes of ohmic heating for the 300 nm thin film heater in line pattern. The applied voltage in this example was 4.5 V, and with a resistance of the thin film heater of $R = 9.6\ \Omega$, this results in a current of 0.46 A. Consequently, the dissipated power in the bulk of the composite is $P = 2\ W$. When averaged over the surface area ($\approx\ 30\ cm^2$) of the sample, this yields 0.07 W/cm^2. When averaged over the line element, this yields 0.22 W/cm. The infrared inspection on the surface temperature indicates a strong but non-uniform temperature increases in the surrounding of the heating element. The surface temperature along the length of the heating element, i.e. from end to end, is shown in Figure 9.5. Increased temperatures are observed at both ends of the heating element, just before the

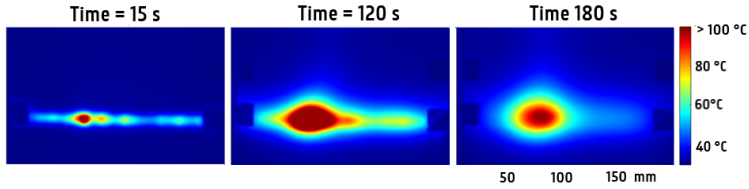

Figure 9.6. *Infrared inspection of a 100 nm line heating element. The applied voltage was 10 V, the resistance of the line heating pattern 13.6 Ω and the current in the circuit was 0.73 A. The total amount of dissipated power by the heater is calculated as approximately 7.2 W. Averaged over the total surface area of the sample, the average dissipated power density by the heating element yields 0.24 W/cm^2. Averaged over the line element yields 0.8 W/cm. A non-uniformity in the layer thickness caused a local hot spot and consequently failure of the heating element (indicated be the white circle in Figure 9.4).*

electrodes. The points of elevated heat production indicate regions with a higher resistance. Non-uniformities in the layer thickness are related to a higher local resistance and can thus also easily be observed by means of infrared inspection. The points of enhanced temperature at the ends of the heater are however not a consequence of non-uniformities in the layer thickness during deposition, but rather a consequence of the composite production process. The electrodes onto the thin film have to be exposed, i.e. not embedded in the composite, in order to allow physical contacting to the power supply. As such, as presented by the square indication in Figure 9.4, a step edge is created at this point. During the manufacturing process of the laminate (see Figure 2.4), after stacking of the lay-up, a vacuum is applied for the consolidation of the laminate. During the curing process, the laminate is thus subject to a large force. Especially at edges of the laminate, this gives rise to regions of elevated pressure. Therefore, also the film located underneath this edge will experience this local pressure field. This can cause a local deterioration of the embedded film which gives rise to points of enhanced resistance and consequently increased heat generation.

Figure 9.6 shows an analoguous measurement but in this case for the 100 nm thin film line heater. The applied voltage in this case was 10 V. With a resistance of the thin film heater of 13.6 Ω and a current in the circuit of 0.73 A, the dissipated power in the sample is 7.2 W. When the power is dissipated uniformly over the sample, the dissipated power density of the heater would be 0.24 W/cm^2. As most heat is dissipated along the line element, the dissipated power density along the heating element yields 0.8 W/cm. Again, the temperature increase on the substrate surface was very fast but strongly inhomogeneous. In this case, again a point of elevated temperature is observed, but this time not located at the edge of the electrodes but in the film itself. The temperature of this hot spot increased above the predefined calibrated range for the thermocamera,

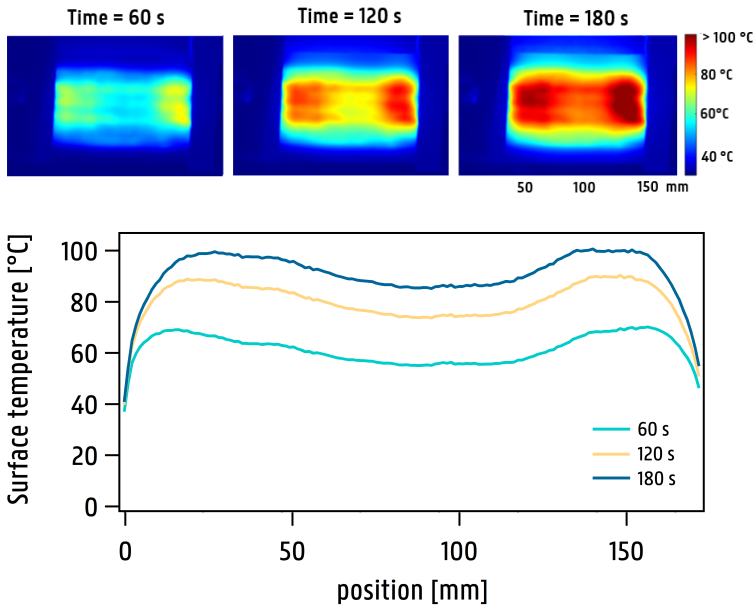

Figure 9.7. *Infrared inspection (top) and the temperature profile at the surface of a 300 nm fully coated prepreg ply (bottom). The applied voltage was 40 V, the resistance of the line heating pattern 8.4 Ω and the current in the circuit was 4.6 A. The total amount of dissipated power by the heater is calculated as approximately 178 W. Averaged over the total surface area of the sample, the average dissipated power density by the heating element yields 5.9 W/cm^2. In case of a full coated layer, the uniformity of the temperature distribution across the surface is much improved.*

i.e. $> 100°C$, until failure occured. In the time evolution, the failure can be observed in between 2 and 3 minutes after the heating started. After 3 minutes, the circuit is already broken and only the afterglow of the heating process is observed. The failure of the film is probably attributed to cracks under influence of thermal stresses. Local melting of the solid film is, given the heat generation, however less likely but not excluded. The hotspot can also be observed on the surface of the composite sample as indicated by the white circle 9.4. The origin of the hot spot in this case was a non-uniformity in layer thickness. Small deviations on a 100 nm thick layer can result in very thin regions in the film, and given the size-effect, very high local resistances. This is again in line with the constraint on the layer thickness as discussed in Chapter 4.

In both approaches based on the line patterns, the average dissipated power density by the heater was clearly insufficient to meet the requirements for deicing, i.e. 0.07 and 0.24 W/cm^2 vs. the prescribed 3.7 W/cm^2. The main limitation for this are the points of enhanced resisitance in the heating film. As a consequence, this point limits the total current in the

heating system, becomes a hot spot and is detrimental for the uniformity of the generated heat flux in the composite. Therefore, although it compromises on the structural integrity, a third test was performed with a fully coated (300 nm) prepreg ply as heating element, in order to reduce the impact of non-uniformities in the film. The evolution of the surface temperature in case of a full coated heater ply is shown in Figure 9.7. It can indeed be observed that the surface temperature is more homogeneously distributed. However, regions of elevated temperature are still observed at the ends of the electrode. As the contacting area to the film was larger in case of the line pattern (contacting is possible over the entire width of the composite samples), much higher powers could be applied to the film. In the latter case, a voltage of 40 V was applied over the 8.4 Ω heating film, resulting in a circuit current of 4.6 A. Consequently, the dissipated power by the heater is 178 W, or expressed as a power density dissipated over the samples surface yields 5.9 W/cm^2. The dissipated power density in this case, in contrast to the previous cases, clearly fulfills the requirements as outlined by the SAE standard (AIR 1168/4) [2]. The higher obtained power densities are attributed to the decrease of the impact of non-uniformities and to larger and thus enhanced contacting area. With the exception of the 100 nm layers, failure of the sample with increasing power applied over the heater occured due to failure at the contacts rather than failure in the film. Therefore, if contacting is not limited, power densities in accordance to the prescription of the SAE standard (AIR 1168/4) [2] can indeed be dissipated by the thin film heating elements. Although the first results and numbers are thus in favor, currently the main challenges towards application are related to the homogeneity of the deposited film and the electrical contacting to the film.

Contacting is a major obstacle for embedded sensing applications in general [3, 9, 30, 36, 40]. In case of physical electrical contacting to the film, the film has to come out of the laminate stacking (as presented in Figure 9.4) and needs to be exposed at the surface in one way or another. As discussed, this created film inhomogenities due to local pressure points during the curing process. As a consequence, this point becomes a hot spot, limits the total current in the heating system and is detrimental for the uniformity of the generated heat flux in the composite. A much more convenient approach would be based on passive sensor elements and wireless power transfer through induction instead of physical contacting. In this case, the sensors or functionalities can be completely embedded in the composite which reduces the chances for the initiation of delamination and neutralizes the problem of the pressure points during curing. Therefore, in the next section, the feasibilty of a wireless sensing approach by means of coupled antennas is evaluated.

9.3. Antennas

Many difficulties have to be overcome when conventional wired sensors or heating elements have to be embedded inside a structure [10] such as the need for a power supply and the complexity of connecting and wiring sensors, especially when the structure has moving parts. A possible solution is provided by coupled antennas as they have the ability to inductively transfer power and communicate without any physical connection. Many examples of sensing by means of embedded passive wireless sensors can be found in review literature [10, 20]. Planar coil resonators or inductive loop antennas are used for near-field communication (NFC) applications such as ticketing, radio-frequent identification or near-field communication (NFC). Related to the antenna design, the circuit can be attributed an intrinsic resistance R related to the material and the conductor dimensions, an inductance L related to the coil shape, and a parasitic capacitance C related to the conductor spacing and substrate type. The resonance frequency of an antenna, or RLC-circuit, is a property solely defined by the inductance L and capacitance C, and thus dependent on the geometrical design of the circuit. For NFC applications, antennas are often designed to operate in the high-frequency range with a resonance at 13.56 MHz. Power can be delivered to an antenna circuit by radio-frequent (RF) inductive coupling [24]. The antennas can be found in several shapes and materials, such as copper, aluminum or conductive (silver) paste, and can be produced in various ways. For commercial applications, the most often used techniques are basic copper wire winding, etching, electroplating, stamping or (inkjet) printing with silver ink [31, 43], but in literature also examples for PVD processes such as evaporation [34] or sputtering [32, 41] can be found. Furthermore, it was shown by different authors that an antenna circuit can be used as a sensor [26, 29] as the resonance frequency can change when subjected to variations such as in pressure [30], humidity [30, 37] or strain [15]. Therefore, thin film antennas can operate as passive sensors, and behold the potential, at least from a theoretical perspective, to inductively generate heat in the bulk of the composite. Similar feasibility studies are already performed on embedded foil antennas for structure health monitoring in carbon fiber composites. [23, 35], or more recently, Gleason et al. [42] reported on an embedded a wireless electronic sensor system for measuring pressure and temperature during an infusion process. In all studies, it was shown that power could effectively be transmitted through the composite, towards the embedded antenna. At least this was confirmed for more bulk-like antenna designs. In the case of commercial foil circuits however, thicknesses usually in the range of a few micrometers up to hundreds of micrometers can be expected. The response and behavior of thin film antennas, i.e. with a thickness $< 1\ \mu m$, is therefore hardly documented.

9.3.1. Experiment

The feasibility of a resonating thin film antenna circuit is evaluated for purposes of embedded sensing and power induction. The antenna circuits are measured on their resonance properties when coupled to a reference antenna in the high-frequency range (MHz). Thin films of Cu, Ag and $Ni_{90}Cr_{10}$ with different thicknesses (50, 100, 150, and 200 nm) were shaped into an antenna design as presented in Figure 9.8. In order to evaluate the effect of the layer thickness on the antenna, the depositions were this time not performed on prepreg substrates. This was done initially to rule out surface roughness effects. In order to keep the analogy with a temperature sensitive substrate, the depositions were performed on 0.1 mm thick Mylar® plastic. The argon pressure inside the system was kept constant at 0.6 Pa for all Cu and $Ni_{90}Cr_{10}$ depositions and at 0.3 Pa for Ag. The target-to-substrate distance was fixed at 8.5 cm. During deposition, the discharge current was fixed at 0.6 A for Cu and $Ni_{90}Cr_{10}$ depositions and at 0.3 A for Ag. The deposition speeds obtained for Cu, Ag and $Ni_{90}Cr_{10}$ are 1.1, 2.7 and 1.0 nm/s respectively. For all depositions, the background pressure was kept lower than 5×10^{-4} Pa.

Depending on the application, different antenna designs can be found [15]. The geometry of the antenna circuit in Figure 9.8 is based on a Confidex busticket (ISO/IEC 7810 ID-1/Class-1) and shaped in a way that allows easy masking for sputter deposition. This was thought to be sufficient as a design for a feasibility study towards thin film antennas. Therefore we cannot say that the antennas are optimized to operate at a certain frequency. Different analytical expressions allow however to estimate the resonance frequency based on the geometry of the antenna design [4, 6, 13, 15, 18, 21, 22, 27]. For the design here presented, the resonance frequency is predicted to be located at around 15 MHz. The shaping of the antenna circuit was done by masking the substrate with a laser cut mask. In order to ensure the stability of the mask, stability bridges between the cuts needed to be placed. Therefore an additional deposition under the exact same conditions was performed with a complementary mask to connect the interrupted connection paths. A piece of copper tape was used as overpass conductor (see Figure 9.8) and the conductive paths are protected from the tape by Mylar foil in order to prevent short circuits. In a later stage, this connection can be replaced by an isolating ceramic film and a copper film as overpass. An even better approach however would be to completely redesign a more sputter-friendly antenna geometry, i.e. no overpass conductors, easy shaping by means of one single mask and no too small conductor paths ($> 1\ mm$). The latter constraint is again related to the intrinsic roughness of the prepreg, but also to the rigidity of the mask, as high aspect ratio trenches in the mask are obstructed in time due to sputter deposition on the sidewalls.

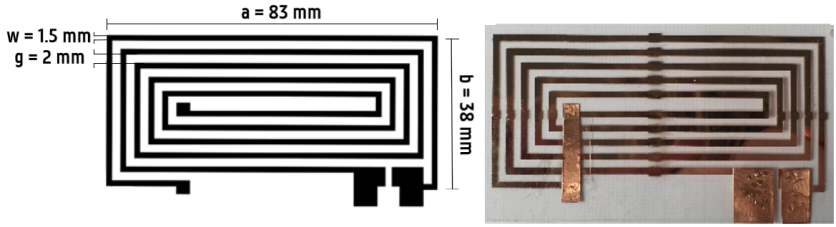

Figure 9.8. *(left) Geometrical parameters of the antenna design (right) Thin film Cu antenna. The overpass connection paths are preliminary done by copper tape and isolated from the rest of the circuit by Mylar.*

The antenna response on the variation of the frequency of the inducer signal was tested with the setup as presented in Figure 9.9. As inducer antenna, always the same 400 nm thick Cu antenna was used which acted as the reference. A function generator was used to apply a sinusoidal 10 V peak-to-peak signal on the electrodes of the reference antenna. The frequency was varied in the range from 1 MHz up to 25 MHz and the receiver antenna was placed at a fixed distance from the source. Measurements at separations of 10, 30 and 50 mm were performed while the frequency was sweeped between 0 and 25 MHz. The signal generated over the electrodes of the receiving antenna was captured by an oscilloscope (Agilent Technologies DSO1024A). The output impedance of the function

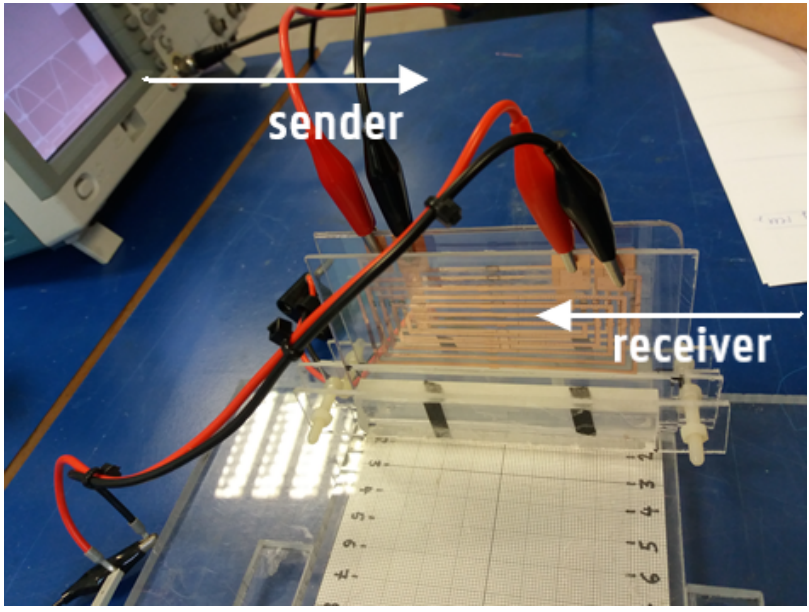

Figure 9.9. *Experimental setup with the coupled sender and receiver antenna.*

generator was set at 50 Ω, and the input impedance and capacitance of the oscilloscope were 1 MΩ and 18 pF respectively. The measured peak-to-peak voltage of the induced signal was consequently plotted as function of the increasing frequency for different distance (10, 30, and 50 mm) between the coupled antennas.

The results of the antenna response for three different materials at three different distances from the source are shown in Figure 9.10. Different trends can be observed. The thicker the film, the higher the peak-to-peak voltage induced in the antenna. The larger the separation between the sending and receiving antenna, the lower the induced voltages. For a peak-to-peak signal of 10 V applied over the sender antenna, the maximal peak-to-peak voltages were found for the thickest (200 nm) antennas located closest (10 mm) to the source. Values of 4, 1.2, and 0.20 V are found for silver, copper and chromel respectively. For all materials, a certain response is noticed at a frequency in the vicinity of 15 MHz. The effect becomes more expressed at larger distances between sending and receiving antenna, i.e. when the signal amplitude is low, but the frequency at which the circuit resonates is unaltered by the distance from the source. The frequency at which the response occurs is close to the predicted resonance frequency of 13.56 MHz for which the original antenna was designed to operate, and to the predictions, i.e. in the range of 14.49 to 15.29 MHz for a thickness range from 50 to 200 nm, based on the analytical models [21, 22]. The resonance frequency is a property determined by the capacitance and inductance of the circuit, i.e. both design properties. The resonance frequency is therefore not expected to depend on the material choice. This can also be confirmed by the measurements. The resonance behavior is however not what we would expect from textbook examples. This behavior is not yet understood. Also the difference in behavior for the chromel antenna, which inhibits a much higher intrinsic resistance compared to the other metals, is currently unclear. The antenna seems to respond in a different way on variations through the frequency range compared to the other measurements. This response is also in comparison with the output voltage of printed antenna circuits as reported by Ong et al. [30], and can also be observed when the film thickness of the antennas was decreased to small values, as is observed for the 50 nm Cu antennas, or as shown in Figure 9.10 i for a 32 nm thick silver antenna. If this effect is related to the resistance of the sputtered circuit, and thus to a restricted electron mean free path, is currently unclear. However, although this behavior is not yet fundamentally understood and far more detailed impedance measurements are recommended, it is a very interesting observation with regard to sensing applications that a consistent resonance response from the antennas could be obtained.

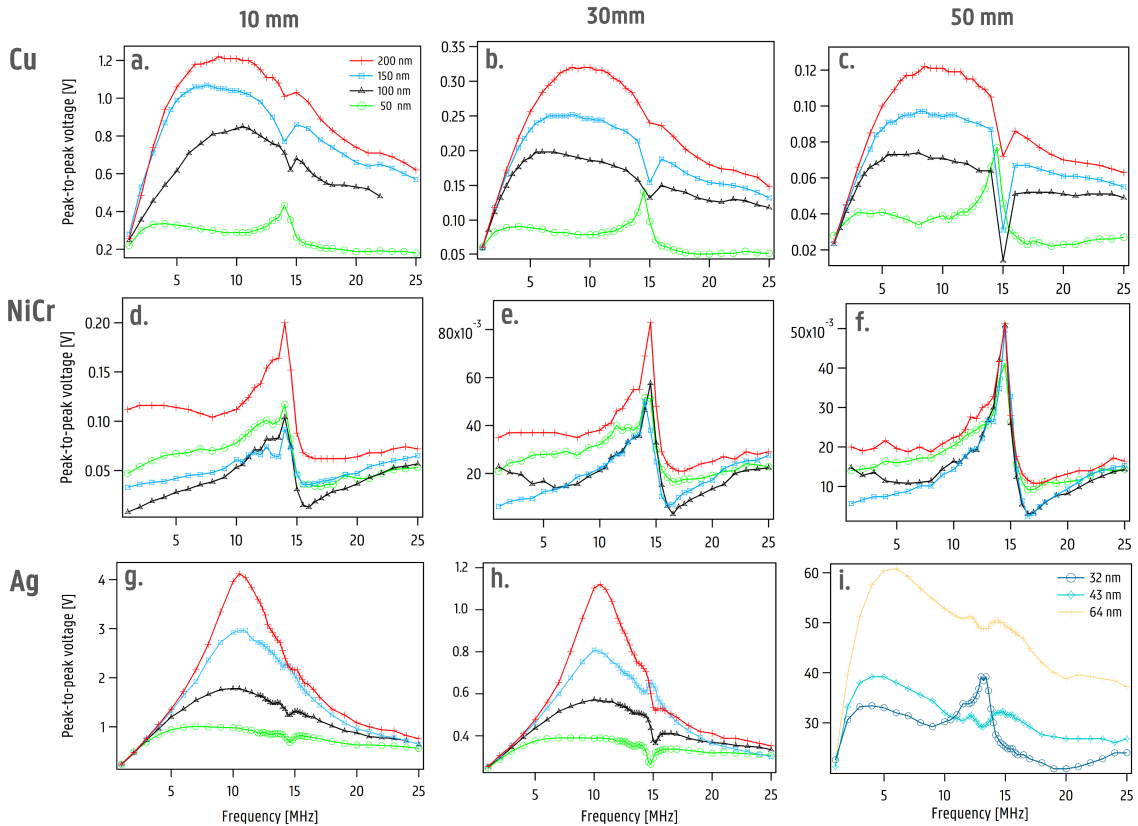

Figure 9.10. *Induced peak-to-peak voltage on the receiver antenna as function of the frequency of the AC signal on the sender antenna for chromel (top) copper(middle) and silver (bottom). For each material system, different layer thicknesses of 50, 100, 150,and 200 nm for the receiving antenna were tested.*

The results thus indicate that two sputter-deposited antennas can be coupled and that a specific frequency-dependent response, or resonance, can be measured. This opens perspectives and possibilities for embedded sensing applications. Up to 40 % of the applied peak-to-peak voltage on the sender antenna could be induced in the receiver antenna in the case of silver. This indicates that inductive heating by means of embedded thin film antenna patterns could be considered as a feasible approach. Transferring high power through induction into the composite, as needed in the case of deicing, seems currently less straightforward. Optimization of the antenna design, material choice and film properties could still further improve the power induction. However, for thermographic defect inspection for example, even small heat fluxes generated in the bulk of the composite can already be very useful. In the latter approach, anomalies in the heat distribution through the composite, as visualized by a very sensitive thermographic camera, can be used to localize internal defects. To this end, a network of embedded antennas could possibly also operate as a calibrated, passive heat source located in the bulk of the composite. Of course, a cautious approach is recommended as the preliminary tests are not performed for antennas embedded in a composite. Furthermore, due to the electrical conductivity of the fibers, electromagnetic shielding could be a detrimental side-effect for antenna applications in carbon-based composites. However, for an explorative study, these are promising first results and numbers.

9.4. Deposition of ceramic thin films

It was already briefly mentioned in the previous section that ceramic isolating layers could prove useful as buffer layers for antenna designs requiring an overpass conductor. This specific need is however not critical as the overpass conductor can still be neutralized by redesigning the antenna geometry. A more pressing obstacle however is the electrical isolation of metallic films deposited onto carbon fiber prepregs in order to prevent shortcircuits and leaking currents. With carbon fibers as the most common of all fibers for use in high-end applications, the demand for the deposition of isolating ceramic layers such as alumina (Al_2O_3) or tantalum pentoxide (Ta_2O_5) is imposed.

Oxide and nitride layers can be deposited by reactive magnetron sputtering. During reactive magnetron sputtering, a reactive gas such as oxygen or nitrogen is introduced in the chamber. Part of the reactive gas, depending on the total pressure, is pumped while another part chemically reacts with the sputter deposited metallic particles on the substrate and the chamber walls, as well as with the metallic sputter target. If the introduced reactive gas flow remains lower than the flow required to fully oxidize the deposited material, the formed layer is not stoichiometric. Operation under these conditions is referred to as the metallic mode. When

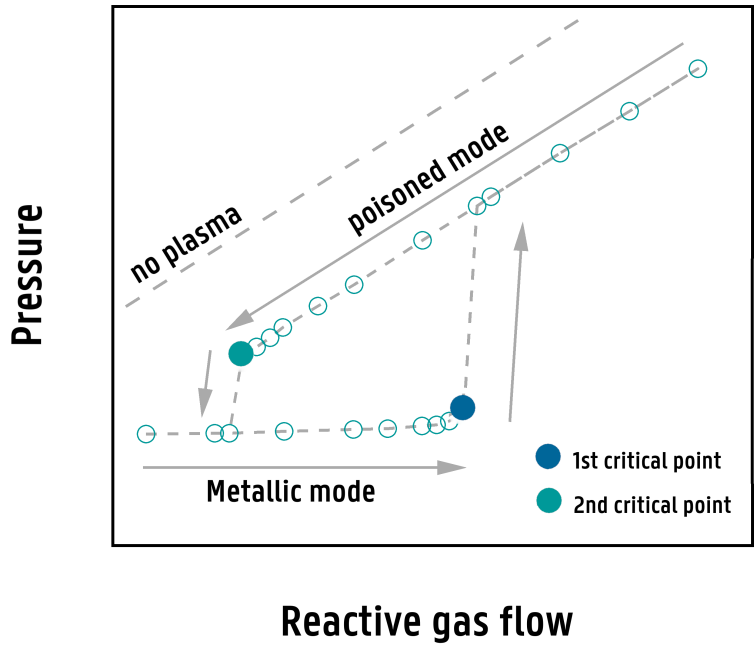

Figure 9.11. *Hysteresis behavior during reactive magnetron sputtering with indication of the metallic and the poisoned mode. The blue point indicates the first critical point, the green point indicates the second critical point.*

the gas flow entering the vacuum chamber exceeds the rate of gas consumption by the metallic deposits and the pump, the target surface and sub-surface are chemically bound with the reactive gas. We refer to this target state as poisoned or reactive mode. The point at which the transition from the metallic to the poisoned mode occurs is referred to as the first critical point. When operating in poisoned mode, the material deposited on the substrate is fully stoichiometric. As no metallic material is deposited anymore, the reactive gas consumption drops and the total pressure increases even more, i.e. an avalanche effect. In order to bring the target state back into the metallic mode, the reactive gas flow has to be decreased to a lower value than originally triggered poisoning. By doing so, the rate of compound formation is decreased compared to the erosion rate of the target due to the sputter process, which allows to erode the target back into the metallic state. The point at which the system returns into metallic mode is referred to as the second critical point. This non-linear behavior is known as hysteresis and is sketched for the reactive gas pressure as a function of reactive gas flow in Figure 9.11.With respect to deposition rate and gas consumption, highest efficiency for depositions in the reactive mode is obtained when operating as close to the second critical point as possible. In this case however, instabilities in the process

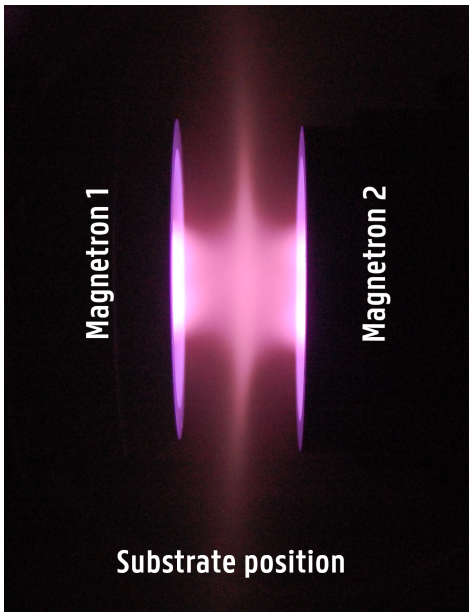

Figure 9.12. *A close-up picture of the target geometry during facing target sputtering with a target-to-target separation of 3.5 cm.*

can easily trigger a transition back to the metallic mode, a detrimental event that is avoided at all cost. Knowledge of the hysteresis behavior, characterized by the first and second critical point (see Figure 9.11), is thus essential for a stable operation in the reactive mode and to guarantee the stoichiometry of the deposited material. More details on reactive magnetron sputtering and its modeling can be found in a recently published tutorial paper [11, 39].

It is clear that the process behavior during reactive sputtering differs significantly from sputter deposition of pure metals. Therefore, the constraint imposed on the film properties and deposition process by the composite substrate (see Chapter 4) have to be re-evaluated. As an example, for reactive depositions, the effect of the substrate outgassing will be of less importance as reactive gas is intentionally introduced in the chamber. The constraint on the limited heat flux towards the substrate on the other hand becomes more severe. This is related to the much lower deposition rates (approx. one order of magnitude) during reactive sputtering. Therefore, the EPA is much higher during reactive depositions than in the case of metallic depositions [12]. Reactive sputter deposition of thick, isolating ceramic layers seem thus not compatible with the constraint of the restricted heat load towards the composite substrate. Solutions must therefore be found in order to tackle this limitation.

A way to reduce the heat load towards the substrate is by placing the

substrate perpendicular to the axis of two facing magnetrons, a process referred to as facing target sputtering. As presented in Figure 9.12, the plasma is sufficiently confined within the region of the targets which makes it possible to achieve film growth on temperature sensitive substrates. When two magnetrons are facing one another, part of the material sputtered from one target is deposited onto the other target and vice versa, i.e. cross-deposition between targets. Of course, the larger the distance between the cathodes, i.e. the target-to-target distance, the larger the material fraction escaping into the vacuum chamber and thus towards the substrate. In this context, contributions were also made to the field by studying the effect of the target-to-target distance on the hysteresis behavior during facing target sputtering by means of experiment and simulations [8]. As presented in Figure 9.13, it was demonstrated that a decreasing target-to-target distance results in a shift of the first critical point towards lower reactive gas flows, while only a minor effect is observed on the position of the second critical point. The main mechanisms for these shifts of the critical points are elucidated by means of simulations performed with an extended version [7][2] of the RSD model [38], i.e. a time-dependent and spatially-resolved simulation model for reactive sputtering developed at the DRAFT research group (download from Ref. [1]).

The shift of the first critical point under influence of a decreasing target-to-target distance is governed by the decrease in the effective gettering area, i.e. the surface area in the chamber covered by metal species readily to react with, and thus getter, the reactive gas. Indeed, when the target separation during reactive facing target sputtering is lowered, two conditions are changed. Firstly, there is a higher cross-deposition between the targets. Secondly, the effective gettering area for the reactive gas is decreased as the spread of the deposited metallic material in the system is decreased. The shift of the first critical point can be understood from the latter effect. When the two targets are brought closer to one another, more (metallic) material is deposited from one target surface onto the other magnetron and vice versa. As such, we can say that the smaller the distance between the targets, the smaller the total substrate area seen by the sputtered particles, and thus the smaller the effective reactive gas gettering area. Therefore, the gas consumption for a given reactive gas flow will decrease with decreasing target separation, enhancing the increase in reactive partial pressure in the system. As the first critical point corresponds to the condition where the reactive gas flow overcomes the getter capacity of the system, it can be expected that this first effect explains the shift in the first critical point towards lower reactive flows with decreasing target-to-target distance.

[2]The extension of the RSD simulation code towards multiple magnetrons was the topic of my master's thesis *'Simulation of multiple reactive magnetron sputtering'* [7].

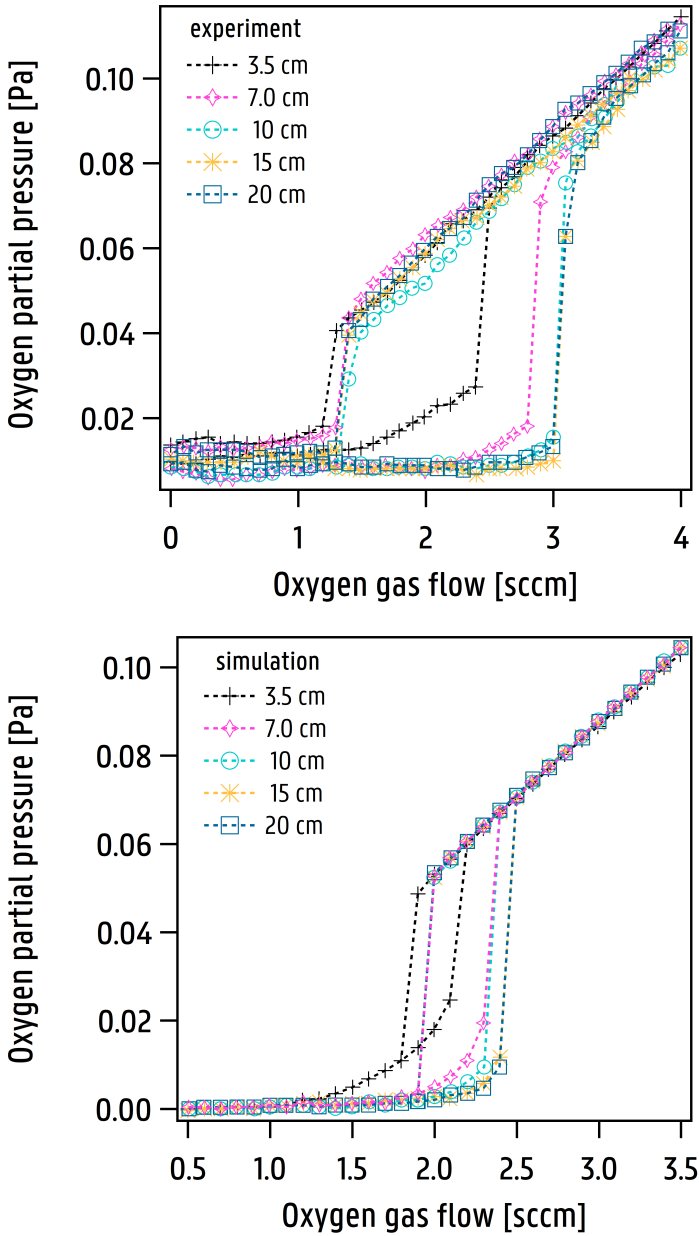

Figure 9.13. *(left) The simulated oxygen partial pressure as a function of the oxygen flow for different target separations. For details about the simulation parameters see Ref. [8]. (right) The experimentally measured oxygen partial pressure as a function of the oxygen flow for different distances between both targets. The target-to-target distance was increased from 3.5 cm to 20 cm. For experimental details, see Ref. [8].*

The behavior of the second critical point is not controlled by gas gettering as both substrate and target are fully poisoned. The slight difference in position of the second critical point can be understood from the effect of the cross-deposition between the targets. The increased cross-deposition at shorter target-to-target distances causes a reduction in the surface erosion speed on the target as reacted material is continuously supplied from the other target. The smaller the target surface speed, the more time implanted reactive ions get to chemically react with the metal in the sub-surface of the target, and therefore, the less efficient the target surface is "cleaned" or eroded to return to the metallic state. Consequently, a lower reactive gas flow is needed to decrease the rate of target poisoning (keeping the system in poisoned mode) compared to the rate target erosion (pushing the system back to metallic mode).

The insight acquired in the hysteresis behavior as a function of the target-to-target distance during facing target sputtering allows to optimize the deposition rate of the ceramic layers while guarantying full stoichiometric films.

9.5. Conclusion

In this chapter the feasibility of some potential applications and new perspectives is evaluated. It is however not the goal of this chapter to elaborate and optimize different applications, but rather to demonstrate the benefits of a fundamental understanding of thin film growth with regard to sensor design for composite materials. As an example, the outgassing products of the composite were employed to tune the thermoelectric properties of a metallic film for the fabrication of single-metal thermocouples. Thin films were also used for the fabrication of heating elements and antennas. Knowledge and proper control of the resistance will here be essential for providing calibrated heat fluxes or desired power outputs. Finally, in case of reactive depositions, the constraints for the growth of ceramic films on composite substrates have to be re-evaluated. Given the insights provided in the interplay between substrate properties and metallic film growth in this work, a much better evaluation of the critical aspects can be made and consequently refined solutions can be proposed.

References

[1] Download RSD from www.draft.ugent.be.

[2] SAE Aerospace Applied Thermodynamics Manual, Ice, Rain, Fog, and Frost Protection.

[3] JL Abot, Y Song, MS Vatsavaya, S Medikonda, Z Kier, C Jayasinghe, N Rooy, VN Shanov, and MJ Schulz, Delamination detection with carbon nanotube thread in self-sensing composite materials, Composites Science and Technology **70** (2010), no. 7, 1113–1119.

[4] A Ammouri, T Ben Salah, and H Morel, A spiral planar inductor: An experimentally verified physically based model for frequency and time domains, International Journal of Numerical Modelling: Electronic Networks, Devices and Fields **31** (2018), no. 1.

[5] KA Antonopoulos and C Tzivanidis, Analytical solution of boundary value problems of heat conduction in composite regions with arbitrary convection boundary conditions, Acta Mechanica **118** (1996), no. 1-4, 65–78.

[6] HE Bryan, Printed inductors and capacitors, Tele-Tech & Electronic Industries **14** (1955), no. 12, 68.

[7] FG Cougnon, Simulation of multiple reactive magnetron sputtering, Master's thesis, Ghent University, 2015.

[8] FG Cougnon, K Strijckmans, R Schelfhout, and D Depla, Hysteresis behavior during facing target magnetron sputtering, Surface and Coatings Technology **294** (2016), 215–219.

[9] NK Das, F Khorrami, and S Nourbakhsh, New integrated piezoelectric-dielectric microstrip antenna for dual wireless actuation and sensing functions, Smart Structures and Materials 1998: Smart Electronics and MEMS, vol. 3328, International Society for Optics and Photonics, 1998, pp. 133–147.

[10] A Deivasigamani, A Daliri, CH Wang, and S John, A review of passive wireless sensors for structural health monitoring, Modern Applied Science **7** (2013), no. 2, 57.

[11] D Depla, K Strijckmans, A Dulmaa, F Cougnon, R Dedoncker, R Schelfhout, I Schramm, F Moens, and R De Gryse, Modeling reactive magnetron sputtering: Opportunities and challenges, Thin Solid Films **688** (2019), 137326.

[12] A Dulmaa, H Vrielinck, S Khelifi, and D Depla, Sputter deposition of copper oxide films, Applied Surface Science **492** (2019), 711–717.

[13] HM Greenhouse, Design of planar rectangular microelectronic inductors, IEEE Transactions on parts, hybrids, and packaging **10** (1974), no. 2, 101–109.

[14] DW Hahn and MN Özişik, Heat Conduction, John Wiley & Sons, Inc., aug 2012.

[15] Yi Jia, Ke Sun, Fredrick Just Agosto, and Manuel Toledo Quinones, Design and characterization of a passive wireless strain sensor, Measurement Science and Technology **17** (2006), no. 11, 2869.

[16] C Joseph and C Viney, Electrical resistance curing of carbon-fibre/epoxy composites, Composites Science and Technology **60** (2000), no. 2, 315–319.

[17] M Kersemans, E Verboven, J Segers, S Hedayatrasa, and W Van Paepegem, Non-Destructive Testing of Composites by Ultrasound, Local Defect Resonance and Thermography, Proceedings **2** (2018), no. 8, 554.

[18] Y Lee, Antenna circuit design, Application manual of Microchips Technology (1999).

[19] H Liu, W Sun, and S Xu, An extremely simple thermocouple made of a single layer of metal, Advanced Materials **24** (2012), no. 24, 3275–3279.

[20] JP Lynch and KJ Loh, A summary review of wireless sensors and sensor networks for structural health monitoring, Shock and Vibration Digest **38** (2006), no. 2, 91–130.

[21] S. Bernard V. Kerzérho F. Azaïs M. Renovell T. Kervaon P. H. Pugliesi-Conti M. Dieng, M. Comte, Accurate and efficient analytical electrical model of antenna for NFC applications, 2013 IEEE 11th International New Circuits and Systems Conference (NEWCAS) (2013), 1–4.

[22] O. Pop M. Zolog, D. Pitica, Characterization of Spiral Planar Inductors Built on Printed Circuit Boards, 2007 30th International Spring Seminar on Electronics Technology (ISSE) (2007), 308–313.

[23] I Mayordomo, T Drager, JA Alayon, and J Bernhard, Wireless power transfer for sensors and systems embedded in fiber composites, 2013 IEEE Wireless Power Transfer (WPT), IEEE, may 2013.

[24] I Mayordomo, T Drager, P Spies, J Bernhard, and A Pflaum, An Overview of Technical Challenges and Advances of Inductive Wireless Power Transmission, Proceedings of the IEEE **101** (2013), no. 6, 1302–1311.
[25] O Meier and D Scholz, A handbook method for the estimation of power requirements for electrical de-icing systems, DLRK, Hamburg **31** (2010).
[26] A Mita and S Takahira, Health monitoring of smart structures using damage index sensors, Smart Structures and Materials 2002: Smart systems for bridges, structures, and highways, vol. 4696, International Society for Optics and Photonics, 2002, pp. 92–100.
[27] SS Mohan, M del Mar Hershenson, SP Boyd, and TH Lee, Simple accurate expressions for planar spiral inductances, IEEE Journal of solid-state circuits **34** (1999), no. 10, 1419–1424.
[28] C Nolet, Composite wind blade engineering and manufacturing.
[29] LJ Novak, KM Grizzle, SL Wood, and DP Neikirk, Development of state sensors for civil engineering structures, Smart Structures and Materials 2003: Smart Systems and Nondestructive Evaluation for Civil Infrastructures, vol. 5057, International Society for Optics and Photonics, 2003, pp. 358–364.
[30] KG Ong and CA Grimes, A resonant printed-circuit sensor for remote query monitoring of environmental parameters, Smart materials and structures **9** (2000), no. 4, 421.
[31] I Ortego, N Sanchez, J Garcia, F Casado, D Valderas, and JI Sancho, Inkjet printed planar coil antenna analysis for NFC technology applications, International Journal of Antennas and Propagation **2012** (2012).
[32] BS Park, JM Lee, SG Lee, MS Kang, and JI Choi, Design of sputter-deposited multilayer thin films planar inverted-F antenna for mobile terminals, IEEE Antennas and Wireless Propagation Letters **8** (2009), 1143–1145.
[33] MK Politovich, Aviation meteorology and Aircraft Icing, Encyclopedia of Atmospheric Sciences, Elsevier, 2015, pp. 160–165.
[34] C Ramade, S Silvestre, F Pascal-Delannoy, and B Sorli, Thin film HF RFID tag deposited on paper by thermal evaporation, International Journal of Radio Frequency Identification Technology and Applications **4** (2012), no. 1, 49–66.
[35] M Salas, O Focke, AS Herrmann, and W Lang, Wireless Power Transmission for Structural Health Monitoring of Fiber-Reinforced-Composite Materials, IEEE Sensors Journal **14** (2014), no. 7, 2171–2176.
[36] J Sebastian, N Schehl, M Bouchard, M Boehle, L Li, A Lagounov, and K Lafdi, Health monitoring of structural composites with embedded carbon nanotube coated glass fiber sensors, Carbon **66** (2014), 191–200.
[37] G Stojanović, M Radovanović, M Malešev, and V Radonjanin, Monitoring of water content in building materials using a wireless passive sensor, Sensors **10** (2010), no. 5, 4270–4280.
[38] K Strijckmans and D Depla, A time-dependent model for reactive sputter deposition, Journal of Physics D: Applied Physics **47** (2014), no. 23, 235302.
[39] K Strijckmans, R Schelfhout, and D Depla, Tutorial: Hysteresis during the reactive magnetron sputtering process, Journal of Applied Physics **124** (2018), no. 24, 241101.
[40] Z Su, X Wang, Z Chen, L Ye, and D Wang, A built-in active sensor network for health monitoring of composite structures, Smart Materials and Structures **15** (2006), no. 6, 1939.
[41] NA Tran, HN Tran, MC Dang, and E Fribourg-Blanc, Copper thin film for RFID UHF antenna on flexible substrate, Advances in Natural Sciences: Nanoscience and Nanotechnology **1** (2010), no. 2, 025016.
[42] MG Vargas Gleason, R Jedermann, A Dimassi, and W Lang, Embedded Wireless Sensor Systems for Resin Flow Monitoring In Glass and Carbon Fiber Composites, IEEE Sensors Journal (2019), 1–1.
[43] L Yang, A Rida, R Vyas, and MM Tentzeris, RFID tag and RF structures on a paper substrate using inkjet-printing technology, IEEE Transactions on Microwave Theory and Techniques **55** (2007), no. 12, 2894–2901.
[44] X Zhang, H Choi, A Datta, and X Li, Design, fabrication and characterization of metal embedded thin film thermocouples with various film thicknesses and junction sizes, Journal of Micromechanics and Microengineering **16** (2006), no. 5, 900.

This page was intentionally left blank.

Scientific Contributions

Publications

- The Seebeck coefficient of sputter deposited metallic thin films, **F.G. Cougnon** and D. Depla, Coatings 9 (2019) 299
- On the electrical properties of sputter deposited thin films: The role of energy and impurity flux, **F.G. Cougnon**, I. Schramm, and D. Depla, Thin Solid Films 690 (2019) 137540
- Modeling reactive magnetron sputtering: opportunities and challenges, D. Depla, K. Strijckmans, A. Dulmaa, **F.G. Cougnon**, R. Dedoncker, R. Schelfhout, I. Schramm, F. Moens, and R. De Gryse, Thin Solid Films 688 (2019) 137326
- Impurity dominated thin film growth, **F.G. Cougnon**, A. Dulmaa, R. Dedoncker, R. Galbadrakh, and D. Depla, Appl. Phys. Lett. 112 (2018) 221903
- Hysteresis behavior during facing target magnetron sputtering, **F.G. Cougnon**, K. Strijckmans, R. Schelfhout, and D. Depla, Surface and Coatings Technology 294 (2016) 215-219

Conferences

Papers

- Development of a new generation of embedded sensors for monitoring structural composites, A. Lamberti, A. Feng, **F.G. Cougnon**, J. Missinne, D. Depla, and W. Van Paepegem, ECCM18 - 18th European Conference on Composite Materials 2018

Posters

- F.G. Cougnon at SURFOCAP2017 (Besançon, France): Embedded thin-film thermocouples for self-sensing composite materials.
- F.G. Cougnon at PSE2016 (Garmisch-Partenkirchen, Germany) : Embedded thin-film thermocouples for self-sensing composite materials

- F.G. Cougnon at RSD2016 (Ghent, Belgium) : Embedded thin-film thermocouples for self-sensing composite materials

Orals

- F.G. Cougnon at ICMCTF2019 (San Diego, USA): Sputtered Thin Film Sensors for Self-sensing Composite Materials
- F.G. Cougnon at E-MRS 2017 (Strasbourg, France): Sputter deposition of $Cu_{55}Ni_{45}$ and $Ni_{90}Cr_{10}$ for thin film thermocouple applications.